Department of Biosciences and Biotechnology

PhD program: Chemical, Geological and Environmental Sciences

Cycle: XXXVI

Curriculum in: Chemistry

Development of New Toll-Like Receptor 4-directed adjuvants and Clarification of their Mechanism of Action

Surname: Franco   Name: Ana Rita

Registration number: 876473

Supervisor: Prof. Francesco Peri

Coordinator: Prof. Marco Malusà

ACADEMIC YEAR 2022/2023

" I'm just beginning, the pen is in my hand, ending unplanned.

Today is when my book begins, the rest is still unwritten."

Natasha Bedingfield, Unwritten

Table of Contents

Abstract

Antimicrobial resistance microorganisms are now a permanent concern in global health systems, causing high number of infection-associated morbidity and mortality. While the pipeline for new antibiotics has been halted, investing in this strategy does not tackle the resistance problem. Vaccines have been decreasing disease burden since their creation in the 18th century. Undeniably, their contribution to public health has been dramatic, contributing to the decrease of severity and incidence of infectious diseases.

Subunit vaccines are of particular interest since they can contain a desired antigen, responsible for eliciting a pathogen-specific response. While safer than whole pathogen vaccines, they are often less immunogenic. Accordingly, subunit vaccines should be formulated with an adjuvant. An adjuvant is a chemical entity capable of enhancing and/or modulating the antigen's immune response and overall vaccine efficacy. Adjuvant development is slow and for several decades, alum remained the only approved adjuvant for human use. Thus, there is still a need for novel chemical entities. Considering the role of an adjuvant in a vaccine, clarification of its mechanism of action is essential for the formulations' success.

Toll-like receptors are important innate immune receptors that recognize microbial components and trigger a downstream of cellular events leading to a proinflammatory immune response and modulation of the adaptive memory. Particularly, TLR4, whose natural ligand is lipopolysaccharide from gram negative bacteria, has been extensively studied and several new agonists have been developed as vaccine adjuvants. MPLA, a detoxified analog of the bioactive portion of LPS, is a TLR4-agonist that has been approved as vaccine adjuvant for human use. It is now incorporated into different marketed vaccines in different presentations.

The aim of this work was to design and synthesize new glycolipid TLR4-directed adjuvants and clarify their mechanism of action using different cell-biology techniques. New TLR4 agonists have been synthesized based on lipid X and its TLR4-stimulating analogs. Their biological characterization was carried out using a human macrophage-like cell line and by employing ELISA and western blot techniques to measure cytokine

production and protein expression. High throughput imaging techniques were also used to follow intracellular targets using fluorescence labelling.

FP20 and its derivatives have demonstrated to be active and selective TLR4 agonists with activity both *in vitro* and *in vivo*. Interestingly, its C6 functionalized derivatives, FP20Glyco and FP20Hmp, have demonstrated a dramatic increase in activity compared to the parent compound. In particular, FP20Hmp was formulated with an *Enterococcus faecium* antigen, in a novel vaccine formulation, and it enhanced the production of antigen-specific antibodies. Additionally, a novel FTIR screening method for proinflammatory compounds was developed using LPS and applied to the project in order to identify new proinflammatory TLR4-stimulating molecules. Overall, this project combined a multidisciplinary approach for the development of new TLR4-directed adjuvants and clarification of their mechanism of action.

Acknowledgments

As these intense 3 years culminate in the writing of this thesis, it only fitted to acknowledge people who allowed me to pursue my PhD. First of all, I would like to thank Professor Francesco Peri for selecting me to join his lab. Thank you for the risk you took on taking me and for allowing me to have an international PhD experience. Thank you for giving me independence and for listening to my point of views during the projects. It was truly a life-changing experience that I'm very grateful of.

Thank you also to all the BactiVax network. All the meetings, courses, and experiences transformed my PhD and the way I see science. It was a privilege to share science and fun times with such amazing scientists. Particularly, a special thanks to Professor Jesús Jiménez-Barbero and Professor Juan Anguita for having me in their labs at CIC bioGune in Bilbao for my secondment. I really appreciated all the knowledge and experience I was able to get there. Thank you also to Siobhán for welcoming me in Dublin.

To all my colleagues that shared good and bad moments with me during this time, I can only say thank you for your help, your time, your friendship, and for all the moments we shared. Particularly, I would like to thank Valentina for everything she taught me. It wouldn't be possible for me to achieve this work without her. Our time in the lab was so fun and I couldn't ask for a better colleague and mentor. Thank you, Vale, for everything! To Andrea, thank you for welcoming me into the lab, for mentoring me and for being a great friend! Thank you to Alessio for sharing this journey with me. Thank you to Nicole for all the good times, even though time was short, it was great! To Monsoor and Federico, my dear friends, a special thanks for always making me laugh and listen to all my worries and stories. And finally, but not least, to Alice for accepting to learn from me in such a humble way, for always giving a hand even when she was already busy and for being such a great colleague.

Fortunately, friendships grow even outside of our lab, and I was fortunate enough to have such a great group of people around me. Thank you, Mati, for all your kindness and help. To Federica for all your mentoring and fun times. To Monica for all the late

afternoon conversations that turned into a great friendship. And to Francesca with who I unexpectedly but fortunately crossed paths and shared such good moments.

Participating in a European network allowed me to meet great people everywhere. Sara, Marcos, and Unai, thank you for being great friends and for making my experience in Bilbao one I'll never forget. Thank you to all my BactiVax colleagues but particularly to Sam, Paulina and Chiara for all the great times we had! It was amazing to meet you and share happy moments!

And now, in Portuguese, I would like to thank my family and friends.

Primeiro, gostava de deixar um agradecimento especial ao Fernando por me inspirar a ser sempre melhor cientista e por me mostrar todas as oportunidades que podia agarrar.

Em geral, obrigada a todos que fazem parte da minha vida e que me apoiaram nesta jornada. Obrigada os meus amigos que, mesmo à distância, sempre se mantiveram presentes. Em particular, obrigada aos meus amigos Vasco e Julião que sempre acreditaram em mim e que estiveram lá nos bons e nos maus momentos.

Obrigada às minhas amigas de sempre por serem sempre família. Catarina e Ritinha, obrigada pela vossa amizade, pelo vosso apoio e por sempre me darem força para atingir os meus objetivos. Sou o que sou hoje porque partilhei a vida com vocês. Um obrigado especial também ao Eduardo por todo o apoio que me foi dando ao longo destes anos. Ao Pedro, obrigada por seres um bom amigo e por celebrares todas as conquistas com tanto entusiasmo.

Obrigada à minha família, por me apoiarem enquanto perseguia meus sonhos. À minha mãe e ao meu irmão, obrigada por toda a paciência, apoio e por aceitarem a distância. Obrigada, também aos meus avós que, sem entenderem bem o que faço, sempre estiveram do meu lado, apesar de estarem longe. À minha madrinha, obrigada por sempre te preocupares comigo. Não poderia não agradecer ao Francisco e à Delfina por toda a ajuda e disponibilidade. A todos obrigada.

Por fim, obrigada Francisco. Por estares sempre do meu lado, onde quer que isso fosse. Por me dares todo o apoio em todos os momentos. Sem ti não seria possível concluir esta tese, nem sequer iniciá-la. Obrigada, não é sequer suficiente.

List of Abbreviations

AIM2R - Absent in Melanoma 2-like Receptors

AMR - Antimicrobial resistance

AP-1 – Activator Protein 1

APC – Antigen Presenting Cell

AS – Adjuvant System

ASC - Apoptosis-associated Speck-like protein

BCG - Bacillus Calmette-Guérin

BEEC - Bacterial Enzymatic Combinatorial Chemistry

CARD - Caspase Activation and Recruitment Domain

cGAMP - 2',3'-cyclic-GMP-AMP

CMC – Critical Micellar Concentration

CpG - Cytidine-phosphate Guanosine

CTLD – C-type Lectin Domain

DAMP - Danger-Associated Molecular Pattern

DMAP - *N,N*-dimethylaminopyridine

dsDNA - Double-stranded DNA

dsRNA – Double-stranded RNA

EDC - 1-Ethyl-3-(3-dimethylaminopropyl)carbodiimide

ELISA - Enzyme-linked Immunosorbent Assay

ER - Endoplasmic Reticulum

FA – Fatty Acid

FMT - Fecal Microbiota Transplantation

FTIR - Fourier Transform Infrared

GAG - Glycosaminoglycans

GLA - Glucopyranosyl Lipid A

GMF-γ - Glia-Maturation Factor -γ

GSDMD - Gasdermin D

HGT - Horizontal Gene Transfer

Hib - *Haemophilus influenzae* type b

HPV – Human Papilloma Virus

IFN – Interferon

IR – Infrared

IRAK - Interleukin-1 Receptor Associated Kinase

IRF – Interferon regulatory factor

ISGF3 - IFN-stimulated genes 3

IV - Inactivated Vaccines

JAK1 - Janus kinase 1

JNK - c-Jun N-terminal Kinase

KDO - 3-deoxy-d-manno-octulosonic acid

LAV - Live-attenuated Vaccine

LGP2 - Laboratory of Genetics and Physiology 2

LPS - LPS Binding Protein

LPS – Lipopolysaccharide

LRR - Leucine Rich Repeats

LUV – Large Unilamellar Vesicles

MAPK - Mitogen-Activated Protein Kinase

MAVS – Mitochondrial Antiviral Signaling adaptor protein

Md – Molecular dynamics

MD2 - Myeloid Differentiation protein 2

MDA5 - Melanoma Differentiation factor 5

MDR - Multidrug Resistant

MHC – Major Histocompatibility Complex

HMP - 2,2-Bis(hydroxymethyl) propionic acid

MPLA - Monophosphoryl lipid A

MRSA - Methicillin Resistant *Staphylococcus aureus*

MTT - 3-(4,5- dimethylthiazol-2-yl)-2,5-diphenyltetrazolium bromide

MyD88 - Myeloid Differentiation primary-response protein 88

NEMO - NF-κB Essential Modulator

NF-κB - Nuclear factor-κB

NK - Natural Killer cells

NLR - NOD-like Receptor

NO – Nitric Oxide

NOD - Nucleotide-binding Oligomerization Domain

ODN – oligodeoxynucleotides

OMV - Outer Membrane Vesicles

OVA - antigen chicken ovalbumin

PAMP - Pathogen-Associated Molecular Pattern

PRR - Pattern-Recognition Receptor

PBMC – Peripheral Blood Mononuclear Cell

PBP - Penicillin-Binding Protein

PG – Proteoglycan

PLS-DA - Partial Least-Squares Discriminant Analysis

PMA - Phorbol 12-myristate- 13-acetate

PpiC - Peptidyl-prolyl cis-trans isomerase

QS-21 - *Quillaja Saponaria* Molina: fraction 21

R-LPS – Rough LPS

RD – Repressor Domain

RIG1 - Retinoic acid-inducible Gene I

RLR - RIG1-like Receptor

RND - Resistance-Nodulation-Division

S-LPS – Smooth-LPS

SagA - secreted antigen A

SEAP - secreted embryonic alkaline phosphatase

SMOC – Supramolecular Organizing Center

ssDNA – Single-stranded DNA

ssRNA – Single-stranded RNA

STAT – Signal Transducer and Activator of Transcription

TB - Tuberculosis

TBDMS - *tert*-butyldimethylsylyl

TDM - THP-1 X-Blue Derived Macrophages

TEA – triethylamine

TGF- β – Tumor Growth Factor β

Th - T-helper

TIR - Toll/Il-1R

TLC – Thin-layer Chromatography

TLR - Toll-like Receptor

TNF - Tumor Necrosis factor

TRAF6 - TNF receptor-associated factor 6

TRAM - TRIF-related adaptor molecule

TRIF - TIRAP-inducing IFN-β

TYK2 - tyrosine kinase 2

VLP - Virus-like Particle

VRE - Vancomycin-resistant *Enterococcus faecium*

WHO - World Health Organization

List of Figures

List of Tables

1. Introduction

1.1. Antimicrobial Resistance

Antimicrobial resistance (AMR) is one of the biggest health concerns of our century. The World Health Organization (WHO) has named AMR one of the main global threats and estimates that nearly five million people died due to resistance in 2019[1]. Moreover, it is estimated that ten million people a year will die in 2050 due to AMR[2]. The main pathogens involved are *Escherichia Coli*, *Staphylococcus aureus*, *Klebsiella pneumoniae*, *Streptococcus pneumoniae*, *Acinetobacter baumannii* and *Pseudomonas aeruginosa*[3]. Four of these pathogens belong to a class of bacteria described as ESKAPE pathogens which includes *Enterococcus faecium*, *Staphylococcus aureus*, *Klebsiella Pneumoniae*, *Acinetobacter baumannii*, *Pseudomonas aeruginosa* and *Enterobacter spp*[4]. Over the years, ESKAPE pathogens have shown increasing multidrug resistance and have been responsible for most of the nosocomial infections[4]. Besides this group of pathogens, another growing concern is multidrug resistant tuberculosis (MDR-TB) which accounted for 78% of overall tuberculosis infections in 2019[5]. MDR-TB is associated with poor treatment outcomes due to the duration of treatment, as well as detrimental side effects[6], and the global burden of TB remains a priority concern[7]. The impact of AMR goes beyond the treatment of active infections, as antibiotics are part of prophylactic treatment for a number of procedures, such as organ transplantation, cancer treatment, surgeries, among others[8]. Indeed, the WHO released a report, in 2016, where it was shown that about 200 000 new-born babies died every year due to multidrug resistant (MDR) bacteria[9].

1.1.2. Mechanisms of Resistance

Mechanisms of resistance have been present in bacteria long before the development of antibiotics and contributed over time to competitiveness between microbes[10]. However, human intervention has exacerbated this phenomenon to a point where it is threatening global health and it is particularly concerning in ESKAPE pathogens[11]. Nevertheless, in order to understand the impact of AMR and develop new strategies is important to understand how bacteria survived in nature[12]. Resistance can be

intrinsic, derived from mutations or acquired though horizontal gene transfer (HGT). Natural selection derived from phages, competitors and predators contribute to the persistence of bacteria with these improved mechanisms[12]. In fact, antibiotic resistance genes are a growing concern due to their abundance, mobility and ability to be expressed in different bacteria, although interestingly, these genes already existed before antibiotics but had different functions[13].

There are different molecular mechanisms of antibiotic resistance that can be categorized in different ways as, for example, accordingly to how it prevents the drug to have its therapeutic effect. Accordingly, we can group these mechanisms into prevention of access to target, target site changes and inactivation of antibiotics (**Figure 1**)[14].
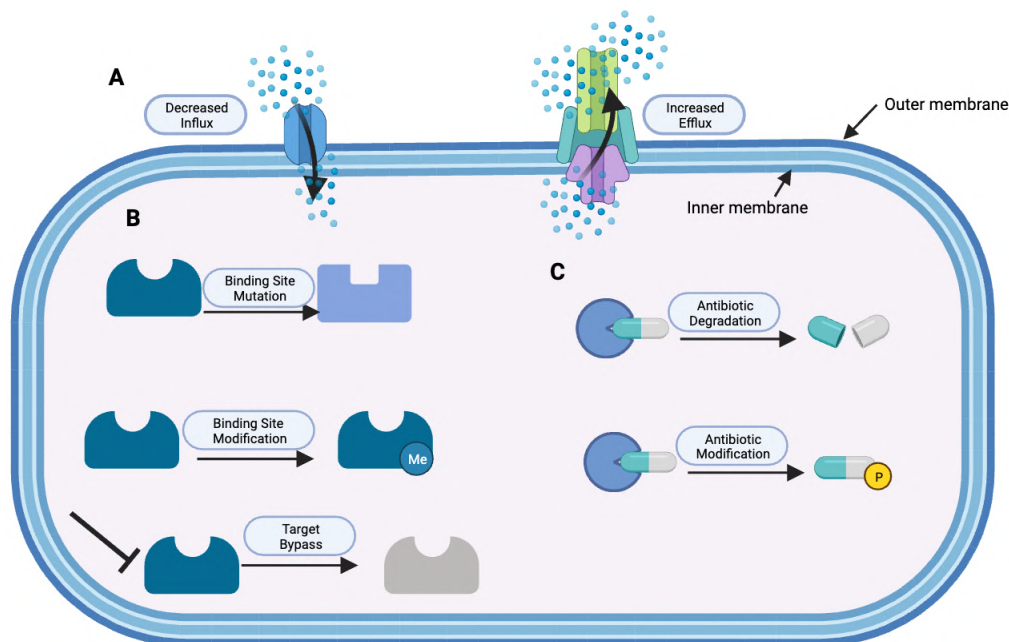
Figure 1. Mechanisms of Resistance – A. Mechanisms that prevent access to target – decreased influx through porin downregulation or increased efflux though efflux pumps upregulation. B. Mechanisms that lead to target changes – Binding site mutations leading to change in binding; Binding site modifications leading to protection of the target and Target bypass through a homologous protein with the same function but lower affinity towards the antibiotic. C. Inactivation of antibiotics – Enzyme catalyzed degradation or modification of the drug.

In the first group, we can identify mechanisms that decrease the ability of the biocidal compound to reach the target. This can happen due to reduced permeability or increased efflux. The latter is intrinsic to gram-negative bacteria that contain an outer membrane, making it difficult for antibiotics to penetrate the bacterial wall and reach the target[15]. Additionally, these bacteria also decrease the number of channels through which antibiotics can enter the cell, named porins, increasing its resistance. For example,

Pseudomonas aeruginosa's loss of OprD porins is associated with high level resistance to carbapenems[16]. In MDR bacteria, while porins are decreased in response to antibiotic exposure, once the drug enters the cell, some bacteria increase other type of active transmembrane transport proteins in order to expel the antibiotics[15]. These channels are called efflux pumps and are one of the major concerns when it comes to mechanisms of resistance in MDR, since most of them can transport a wide range of substrates. Furthermore, it has been found that genes encoding for AMR efflux pumps have been mobilized into plasmids, allowing for HGT and spread of this mechanism of resistance between bacteria[15]. These pumps are of particular importance in Gram negative bacteria and one of the most studied families of these proteins are resistance-nodulation-division (RND). RND interact with other proteins and coat the entire cell envelope conferring additional resistance to several species such as *E. coli*, *P. aeruginosa* and *A. baumannii*[16]. Overall, these transport proteins are associated with multivariate regulators and several genes associated with bacterial survival under stress, making it an appealing but difficult target to fight AMR[16].

In the second group of resistance mechanisms, modifications to the target site are described. The majority of antibiotics are high affinity antagonists of their targets, leading to decrease or loss of activity and, ultimately, to cell death[15]. This means that if there is a change in the binding site, efficacy is compromised. Indeed, if a strain has a mutation on the binding site that prevents substrate binding, resistance is highly probable[15]. For example, in the case of β-lactam antibiotics that bind to penicillin-binding proteins (PBPs) and prevent cell-wall synthesis, resistance has been associated with mutations in PBP3 in *E.coli* strains resistant to aztreonam and avibactam[16]. Not only mutations can alter a binding site, but also decoration with another chemical group can lead to important changes in drug-target interactions[15]. The latter does not require a mutation in the genes that encode the target. One example of this type of resistance is chloramphenicol-florfenicol resistance in both Gram-negative and Gram-positive bacteria such as *E. coli* and *S. aureus,* respectively[15]. Methylation, via a methyltransferase enzyme, of 23S rRNA leads to altered binding in the ribosome, compromising the activity of macrolides[15]. Furthermore, these genes are often carried in plasmids leading to HGT and dissemination of this type of resistance. Another example is decoration of bacterial lipopolysaccharide (LPS) in Gram negative bacteria as a counterattack to the mechanism of action of colistin[16]. Modification of the overall charge of LPS by transferring a

phosphoethanolamine, decreases the interaction with colistin and bacteria can survive by maintaining its membrane intact[16]. Additionally, bacteria can also have the ability to bypass the target by synthesizing a new protein with the same ability as the one that was inactivated by the antibiotic[16]. This is the case of methicillin resistant *S. aureus* (MRSA). These bacteria acquire an exogenous PBP with lower affinity for β-lactams, allowing the maintenance of cell wall synthesis and bacterial survival[16].

In the final group explored in this chapter we find the ability of bacteria to modify the antibiotic molecule by degradation or transfer of hindering groups. Direct degradation of antibiotics is one of the older described resistance mechanisms. Indeed, in 1940 the first β-lactamase, an enzyme capable of degrading the β-lactam ring of antibiotics such as penicillin and cephalosporins derivatives, was described[15]. Since then, several bacterial enzymes with the ability to degrade antibiotic molecules have been described, namely carbapenemases. KPC, NDM and OXA enzymes can hydrolyze penicillins, cephalosporins and carbapenems and have become increasingly prevalent in MDR strains isolated worldwide[16]. Inactivating enzymes go beyond β-lactam antibiotics and, for example, tetracycline oxidases have been found in MDR isolates from patients[16]. Moreover, bacteria can inactivate or decrease a compound's activity by transferring chemical groups such as acyl, phosphates, nucleotidyl, among others[15]. One of the most susceptible groups are aminoglycosides that, due to their size, expose a significative number of hydroxyl and amino groups. The enzymes responsible for these modifications are often mobile and found in both Gram negative and Gram positive bacteria[16]. Not only aminoglycosides are chemically modified by bacteria but also lincosamide, macrolides, and rifamycin can suffer inactivation and modifications to its structure. The latter is of particular concern since it is the first line treatment for M. tuberculosis infection[16].

1.1.3. Causes and Consequences of AMR

From the discovery of penicillin until the current state of AMR, several different factors contributed to the rise of resistance. Besides natural reasons such as genetic mutation, genetic material transfer and selective pressure[17], the over consumption of antibiotics, together with inadequate prescriptions, are important contributors. By using indiscriminately antibiotics, resistant bacteria survive, while drug-sensitive bacteria are eliminated. In turn, these resistant species can proliferate and even transfer resistance to

other species through HGT[18]. Nevertheless, human consumption is not the only contributor since the widespread use of antibiotics in livestock accounts for most of the antibiotic sales. Animals are exposed to these drugs daily, leading to the emergence of new resistant strains and increasing the chances of HGT on an exponential level. Indeed, it has been found that resistant strains are transmitted to humans through meat products, confirming their persistence on these animals. Furthermore, the excretion of antibiotics through urine and feces exposes even more microorganisms to antibiotics, increasing yet again resistances[19].

Nonetheless, antibiotics are still an important weapon on the arsenal against bacteria. Ultimately, one of the main causes for the increase of resistant strains is the lack of new effective antibiotics. In 2019, WHO released a bulletin with updates on new antibiotics against priority pathogens[20]. In this report, they highlight the lack of new compounds when considering the spread of AMR. From all the 50 antibiotics on the pipeline only six of these fulfil at least one of the innovation criteria and only two are active against MDR Gram-negative bacteria[20]. The criteria revolve around the novelty of the drug, focusing on the identification of new classes, new targets and new mechanism of action. Furthermore, it is expected that there are no known cross resistances to it[21].

The difficulty of finding new and effective antibiotics, that are not just performing as its predecessors, has led to a decrease in private funding, namely from big pharmaceutical coHmpnies[21]. Indeed, most of the above mentioned compounds are being developed by small or medium-size coHmpnies[20]. Accordingly, several funding initiatives have been put in place in order to promote antibiotic development, such as CARB-X, INCATE, REPAIR Impact Fund and AMR Action Fund[22]. Furthermore, some governments, namely in the UK, are trialing a subscription model, paying companies a regular fee for last-resource antibiotics, instead of relying on usage-based profits, in an attempt to keep these drugs on the market[23]. Although this strategy aims to mitigate the risks of big companies pulling out of the antibiotic scene, there are concerns if funding a few drugs with public money is going to promote innovation or just influence companies to bet on safe and easy to market compounds, such as slightly improved old antibiotics and combination of existing drugs[24].

The lack of investment in research and development of new antibiotics is clear by looking at the numbers from recent years. Since 2013 until December 2022, 19 small

antibacterial molecules have been approved and, amongst them, none was first-in-class[22]. Interestingly, during that period, two monoclonal antibodies against Gram-positive bacteria, obilotxaximab and bezlotoxumab, and one biotherapeutic drug, Rabyota, were approved. The latter is a liquid suspension of fecal microbiota with activity against gram positive bacteria[22]. Fecal Microbiota transplantation (FMT) can be found in dozens of clinical trials mainly for approval of treatment against *Clostridium difficile*, the most prevalent pathogen of nosocomial diarrhea and one of the top antibiotic resistance threats named by the center for disease control and prevention[25]. Another current strategy is the reproposing of existing drugs market for other therapeutic indications. Classes such as non-steroidal anti-inflammatory drugs, local anesthetics, opioids, antipsychotics, antidepressants, antiplatelets drugs, antihistamines and statins have been studied as possible treatments against MDR bacteria, namely ESKAPE pathogens[26]. Other approaches involve targeting of bacterial mechanisms of resistance, namely efflux pumps inhibitors[27,28].

Nevertheless, there are several small-molecule clinical trials ongoing, most of them phase I and II, with new structures and new mechanisms of action. These structures were extensively reported by Butler et al[22]. Furthermore, there is an effort to develop compounds with different targets in order to potentiate effectiveness and decrease chances of resistance[29]. Alternatively, some researchers have been trying to develop new antibiotics inspired by marine structures in an effort to increase structural diversity[30].

1.2. Vaccines against AMR

Considering all the issues associated with AMR, the cost of using antibiotics to treat infections is increasing rapidly. Not only there is a need to consider the cost of the antibiotic itself but also longer hospitalization periods, more expensive second and third line antibiotics, isolation procedures and ultimately morbidity and death[31]. Together, data on AMR shows that prioritizing hygiene and correctly using available antibiotics, as well as the development of new and effective vaccines against bacteria might be the best approach[32]. Vaccines are effective against non-resistant and resistant strains, and they can both decrease the number of infections and antibiotic consumption, thus also decreasing resistance due to the minimization of selective drug pressure[33]. It is possible to establish that vaccines can influence AMR at a direct level, by targeting bacteria; at a populational

level, by decreasing transmission between individuals; at a pathogen level, by decreasing HGT, mutations and emergence of new resistance; at a public health level, by lowering infection and disease incidence; and at a healthcare level, by decreasing pressure on health systems, preventing improper prescription of antibiotics and lowering its overall consumption[34].

Not only bacteria-targeting vaccines are important for decreasing the impact of AMR. Viral vaccines target AMR by decreasing the chance of secondary bacterial infections and by decreasing the overuse and misuse of antibiotics[35,36]. Accordingly, influenza, rotavirus and varicella vaccines have proven to be important in fighting AMR[35].

Vaccines are formulations that contain live, attenuated, or killed pathogens, or parts or products from them, such as protein epitopes or mRNA, for example. They are able to stimulate the immune system to produce antigen-specific antibodies that, in turn, offer protection through different mechanisms such as facilitating complement-mediated lysis, promoting opsonophagocytosis, neutralizing the pathogen and its toxins or increasing mucosal barriers and preventing adherence to these structures[37] (**Figure 2**). Furthermore, vaccines elicit an immune response and do not affect the commensal bacteria that colonizes the body, unlike antibiotics, thus preserving the microbioma[37]. Historically, vaccines have proven to be successful in controlling and even eradicating infectious diseases, as it is the case of smallpox[35].
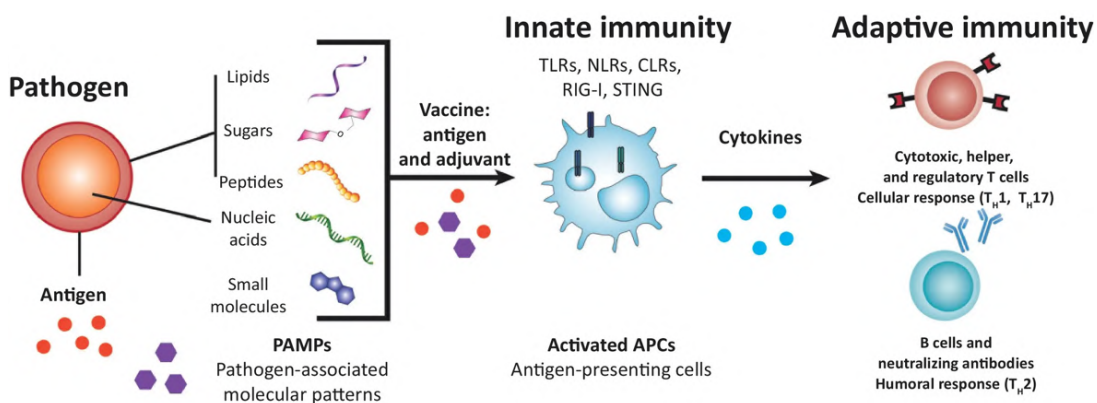
Figure 2. How vaccines work[38]

There are success cases of vaccines against AMR in the clinic such as the pneumococcal conjugate vaccine, that has not only decrease disease incidence and severity but also reduced antibiotic prescription and number of resistant pneumococci[39].

Pneumococci are responsible for morbidity and mortality worldwide, particularly in children under five years old, although elderly individuals are also affected by this disease[40]. Introduction of this vaccine in vaccination programs led to a decrease in the number of infections and cases of severe disease[41]. Indeed, in Africa it was found that vaccinated individuals had 67% less penicillin-resistant pneumococci severe disease compared to non-vaccinated individuals[41]. Currently, expert recommendations focuses on the widespread use of existing vaccines against bacteria, the investment on early stage research on new vaccines and the maintenance of a viable market for them[2].

1.2.1. Types of Vaccines

Vaccines can be categorized according to their manufacturing technology (**Figure 3**). Live-attenuated vaccines (LAVs) and inactivated vaccines (IVs) are called "conventional" vaccines due to their established position on the vaccine market[42]. These types of vaccine started to be developed since the 19th century when Pasteur described the idea of "isolate, inactivate and inject" the pathogen. In this strategy, virus or bacteria are attenuated to make them able to incite an immune response and train immunity without causing severe disease[32]. One good example of a LAV is the Bacillus Calmette-Guérin (BCG) vaccine against TB that has been used since 1921 and although it has been demonstrated that its efficacy is low for some strains and in some endemic countries, it is still considered a crucial weapon against TB[42]. However, LAVs and IVs offer some disadvantages namely due to their safety profile and possibility of reversion to virulence, costs of production and safety of the agents used to inactivate the pathogen[42].
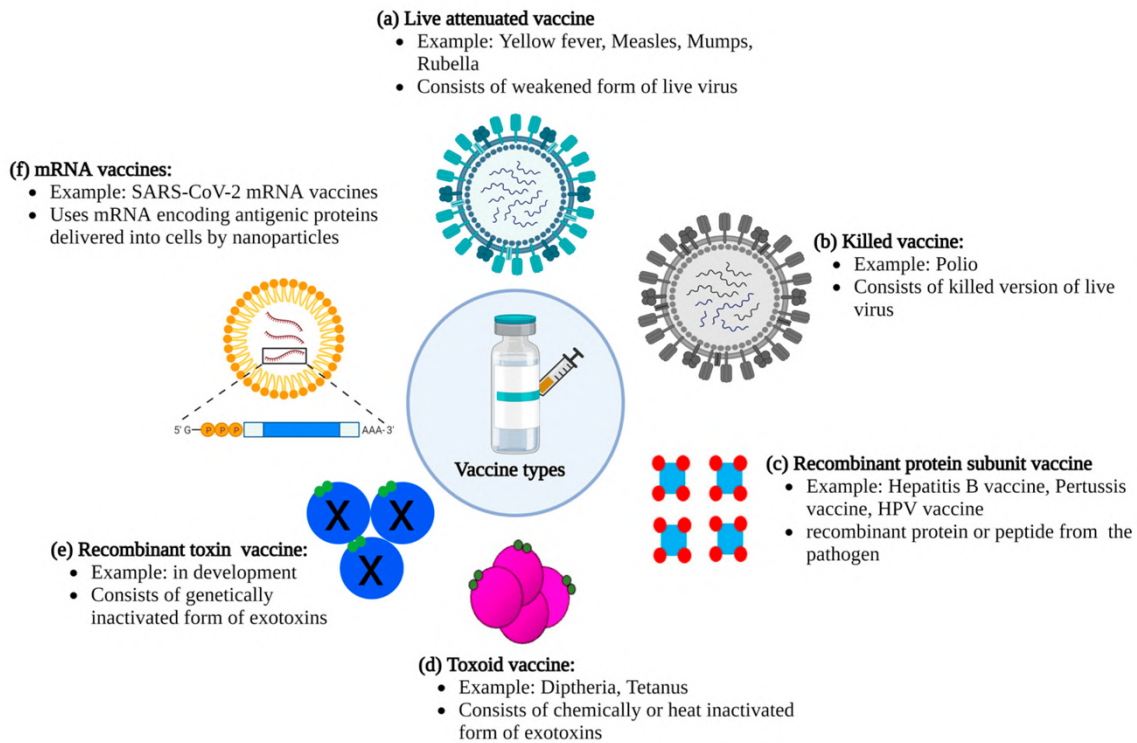
Figure 3. Types of vaccines[43]

With the advance of science and technology, vaccine research evolved from working with the whole pathogen to finding a smaller immunogenic protein portion of bacteria or virus, an antigen. Accordingly, subunit vaccines started to be developed due to their improved safety profile and target activity[44]. However, since they contain fewer antigens than the whole pathogen, they are often less immunogenic and require the use of an adjuvant[45]. Inside this group of vaccines, we can find different types of antigens such as proteins, toxoids, polysaccharide vaccines and virus-like particles (VLPs).

Protein vaccines can me manufactured with isolated proteins or, more often, with recombinant proteins most commonly produced in *E. coli*, since it allows for the production of massive quantities of the antigenic protein[45]. The meningococcal B vaccines are examples of subunit recombinant protein vaccines targeting bacteria.

Toxoid vaccines are made through the detoxification of toxins produced by pathogenic bacteria such as *Clostridium tetani* or *Corynebacterium diphtheriae* responsible for tetanus and diphtheria, respectively[32]. Toxoid vaccines protect against disease but not prevent infection or transmission. Indeed, they require multiple doses to ensure protection and not protect non-vaccinated individuals[45].

Polysaccharide vaccines are based on polysaccharide capsules that certain bacterial pathogens contain and that are essential for their pathogenesis[45]. When formulating polysaccharides, from different pathogens, alone, it was found that immunogenicity was not high enough and that the vaccines were not effective in children under 2 years old[32]. Accordingly, in order to enhance the immunostimulanting properties of these vaccines and extend their coverage to all age groups, polysaccharides were conjugated with carrier proteins, such as tetanus toxoid and a non-toxic cross-reacting mutant of diphtheria toxoid (CRM197). This approach changed the immune response to a T-cell-dependent response with immune memory and high-affinity antibodies and, furthermore, decreased nasopharyngeal carriage by infected patients, decreasing disease transmission[45]. *Haemophilus influenzae* type b (Hib), *Streptococcus pneumoniae* and *Neisseria meningitidis* are examples of pathogens covered by this type of vaccines.

Finally, VLPs are able to imitate the structure of native viruses while lacking the viral genome which means that they are not able to cause infection[46]. Since they maintain most of the antigenic portions of the virus, their immunogenic profile is better compared to protein antigens[45]. Human papilloma virus vaccines are successful cases of application of this technology.

With new techniques and medical needs, new types of vaccines have emerged in the last few years, such as RNA vaccines[32]. These vaccines offer advantages compared to LAVs and IVs as they offer no risk of infection. Furthermore, they have no risk of insertional mutagenesis and their immunogenicity can be tailored[47]. Furthermore, they have commercial advantages as they can be produced rapidly, at a large scale and inexpensively, when compared to other types of vaccines[47]. Their safety has been assessed on millions of individuals due to the massive vaccination campaign during the COVID-19 pandemic[48]. Stability was a big concern in early development, but new techniques yielded stable mRNA vaccines even though they are inherently susceptible to degradation[48,49]. For example, mRNA vaccines often require -80ºC freezing storage[50]. The latter is a limitation to the distribution of the vaccine and its ability to reach all communities. Additionally, the number of doses required to offer protection might rely on the half-life of the encoded protein. Nevertheless, dosing must be tailored considering not only the latter, but also the immune response and the clearance of the vehicle that can

be, for example, a lipid nanoparticle[50]. Overall, this technology is very promising in the field of vaccination and might offer a paradigm shift in the next decade.

1.2.2. Challenges in Vaccine Development targeting AMR bacteria

Even though we have seen a boost in vaccine development in the last decades, it faces a number of challenges. These are aggravated when it comes to vaccines against bacterial diseases since, in most cases, there is commercialized cure[39]. Indeed, by 2019 FDA had approved 32 vaccines against bacteria and 65 against viral pathogens and none of them included ESKAPE pathogens[51]. These numbers illustrate the challenges in developing a bacteria-targeting vaccine. First of all, vaccines are subjected to several regulatory evaluations and require extensive research and clinical trials before being implemented by governments[52]. Moreover, the investment on new vaccines targeting bacteria is much less than the one for new drugs, showing that even though it is known that vaccines are a valuable weapon against AMR, decision making policies are not supportive[39].

One of the challenges when it comes to decision making on vaccines is deciding the target population. For example, previously developed vaccines such as Hib and meningococci focused on pathogens responsible for a high burden of disease[41]. While universal vaccination is suitable for this type of pathogens that infect a big portion of the population, that might not be the case for some AMR strains that affect mostly hospitalized patients or individuals with co-morbidities[37]. In those cases, target vaccination might be the best approach for a fast and reliable intervention. However, these populations have very particular immune systems or, as it is the case of transplant patients, a compromised one. In that case, there might be a hurdle in the response incited by the vaccine, as it might not be enough to induce the production of protective antibodies[37].

Economic challenges are present throughout the vaccine development process. Available data in Europe shows that there are around 670 thousand infections each year due to AMR bacteria and that, from those, 30 thousand people die. The cost of these infections are estimated at 1.1 billion euros[35]. Previous reports have also calculated that by 2050 the cost of AMR to economy might be around 100 trillion dollars worldwide[2]. However, from an investment point of view, if the target populations are individuals susceptible to resistant strains and not the overall population, the number of patients might

not be large enough to attract investment and resources[37]. Therefore, government incentives are important to promote research and development in this field as regulatory boards can estimate economic and social savings in the local health systems. One effective approach for decision-making might be the use of mathematical models to predict both the vaccine's impact on AMR as well as its economic advantages, a combination that was not taking into account in published models so far[34]. It is suggested that analyzing AMR and economic impact together might change the cost-effectiveness evaluation of a given vaccine[34]. Furthermore, vaccine hesitancy also plays a role in decision-making. While in some countries there is an overall acceptance and understanding of the protective role of vaccines, in others there is a growing wave of anti-vaccination due to concerns about efficacy and safety[53]. This hesitancy arise from personal, cultural and religious beliefs as well as mistrust in health authorities[54].

Global coverage is also a hurdle difficult to overcome. While distribution and access to vaccines is not a problem in Europe and other developed parts of the world, reaching developing countries through licensing and appropriate coverage presents as a challenge[36]. For example, in highly successful vaccines such as Hib and pneumococcal conjugate vaccine, global coverage does not reach 50% of the population[36]. Moreover, most mathematical models used as predictors for vaccine outcome do not take into account low and middle-income countries and focus mostly in the United States of America and Europe[34].

1.2.3. Targeted ESKAPE Pathogens – What is on the Pipeline

Even though the impact of vaccines targeting bacterial pathogens is estimated to be crucial in fighting AMR, there is a need to specify the pathogen and scenario to target in order to produce a real and measurable outcome[52]. Current techniques, such as transcriptomics, genomics and proteomics allow for the identification of novel specific antigens that can be possible vaccine candidates[37]. These bioinformatic techniques are often combined with reverse vaccinology. The latter refers to the identification of epitopes, which are specific proteins segments from the pathogen, able to induce a protective immune response[42]. This identification is achieved using genetic information of the bacteria together with omics techniques, allowing for a targeted and faster development when compared to traditional methods such as pathogen inactivation or

attenuation[42]. Recently, these strategies have been applied, together with immunoinformatics and molecular docking, to develop an *in silico* promising broad-spectrum vaccine candidate against 18 MDR pathogens based on a multi-epitope antigen construct[55].

Historically, there have been different vaccine candidates targeting ESKAPE pathogens and other concerning bacteria. However, most of the clinical trials failed due lack of efficacy or safety concerns[37]. Nevertheless, researchers continue to search for a promising vaccine that targets these concerning pathogens. The following paragraphs will focus on vaccines that target ESKAPE pathogens.

Enterococci are Gram-positive anaerobic bacteria present in the commensal flora of the human gastrointestinal tract[56]. However, considering that enterococci can survive in extreme pH, wide range of temperatures and tolerate high concentration of salts, and, additionally, that there are several resistant and virulent strains described, they present themselves as important nosocomial pathogens that target immunocompromised patients[56,57]. A possible approach towards the development of enterococci vaccines could be to explore the capsular polysaccharides since it has been shown that antibodies against them promoted killing of *E. faecalis* and *E. faecium,* although no clinical advancements were pursued[57]. A few enterococcus proteins have also been explored as possible antigens, namely secreted antigen A (SagA), which is a protein secreted during biofilm formation by *E. faecium*[56]. It was shown that immunization with this antigen resulted in the production of antibodies capable of killing vancomycin-resistant E. Faecium strains, demonstrating its potential as a vaccine component against these bacteria[58,59]. Unfortunately, there are no current clinical or preclinical trials of a vaccine formulation against Enterococci[33]. Nevertheless, omic techniques and bioinformatic tools have been applied to develop a multiepitope-based vaccine against *E. faecium* based on SagA and peptidyl-prolyl cis-trans isomerase (PpiC) with promising immunological predictions that can eventually evolve to preclinical studies[60].

S. aureus is a Gram-positive bacterium commensal to the human skin. However, when there is loss of mucosal and skin integrity, it can cause disease[61]. Moreover, it is one of the most critical pathogens associated with AMR due to its high morbidity and mortality, which reaches nearly 18% in developed countries[62]. These bacteria have the ability to quickly develop resistance to antibiotics and MRSA is one of the most

problematic nosocomial pathogens worldwid[42]. The effort to tackle multi-resistance in these bacteria has led to the preclinical development of several vaccine candidates, leading to a few ongoing clinical trials[33]. In the past, most of the candidate failed due to the lack of translation from preclinical to clinical trials and lack of definition of correlates of protection[62]. Indeed, *S. aureus* has a complex host-pathogen interaction that is difficult to replicate in mice models[62]. Accordingly, new strategies are being explored. Namely, the use of organoids to create *in vitro* organ models that mimic natural infections and the use of organs-on-chips, which are micro-scale organs with their own microfluid system originated from either cell culture or *ex vivo* patient samples[62]. StaphVAX was a *S. aureus* vaccine candidate that contained two capsular polysaccharides, CP5 and CP8. It reached phase III trials but failed due to lack of reduction in number of infections when compared to the placebo group[63]. Another candidate, the V710 vaccine, was formulated with iron surface determinant B which is highly conserved. Although it reached phase IIb/III trials, it failed due to lack of protection in patients undergoing surgery[63]. Most recently, SA4Ag, developed by Pfizer, failed in phase IIb trials[62]. Currently, there is one vaccine candidate in phase II trials containing recombinant toxic shock syndrome toxin-1 variant and other two in early clinical development phases[33].

K. pneumoniae are ubiquitous Gram-negative bacteria found in animals, plants, and humans where it is part of the normal gastrointestinal flora. It is a major cause of nosocomial infections, namely pneumonias, bacteremia, urinary tract infections and skin infections in burned victims and it is one of the 6 pathogens with highest mortality due to AMR[33,64]. It is also a frequent cause of newborn sepsis in low-income countries[42]. Even though there is a clear burden of *K. pneumoniae* in health systems worldwide, investment in vaccine development for this ESKAPE pathogen is conditioned due to commercial demand, since most of its expression is in low-income countries[33]. Furthermore, it has an important impact on newborn babies and there is very difficult to assess effectiveness and safety in this population[33]. Extended spectrum β-lactamases, carbapenemases and different hypervirulent strains have been identified in *K. pneumoniae*, and these bacteria possess different virulence factors such as pili, siderophores, lipopolysaccharide and capsule[42]. The latter has been extensively characterized and flagged as a possible vaccine target[42] although no candidate went past preclinical stages due to no significant effects in infection or protection[64]. A tetravalent vaccine, KlebV4, based on LPS, more specific the

O-antigen polysaccharides of the most prevalent *K. pneumoniae* strains, is currently being evaluated in a phase I/II trial with and without adjuvant AS03[65].

A. baumannii is a Gram-negative coccobacillus associated with MDR and nosocomial infections in immunocompromised individuals[66]. It has been flagged by the WHO as a critical priority due to its high carbapenem resistance and ability to form biofilms and persist in hospital settings[66]. Infections are usually pneumonia, sepsis, skin infections and meningitis[67]. Due to its high resistance, different strategies have been employed, using different technologies such as LAVs, outer membrane vesicles (OMVs), DNA based vaccines and subunit protein vaccines, with the aim of controlling *A. baumannii* infections[67]. *A. baumannii* ATCC 19606 was inactivated and administered to mice intramuscularly with 85-100% survival rates after a lethal sepsis challenge and a favorable immune profile[66]. Although promising, LAVs are not the technology of choice due to the risk virulence reversion in the immunocompromised target population[67]. Accordingly, several virulence-associated proteins were explored as possible vaccine antigens targeting these Gram-negative bacteria. Outer membrane proteins are conserved proteins involved in different steps of *A. baumannii* pathogenesis and associated with virulence[66]. A few mice studies revealed some protection against induced sepsis but overall the purification process and costs associated with producing such vaccines have proven difficult to advance past preclinical steps[67] and there are currently no ongoing clinical trials[33].

P. aeruginosa is a motile Gram-negative bacillus responsible for an important number of opportunistic infections in immunocompromised patients and it was identified as one of the critical pathogens by the WHO[68]. It is if particular clinical significance for patients with chronic pulmonary diseases, such as cystic fibrosis[68]. Indeed, half of the patients with this disease, in the United States of America, were colonized with P. aeruginosa[68]. These bacteria are critical nosocomial pathogens since they possess the ability of forming biofilms, making it difficult their removal from hospital surfaces[69]. Furthermore, different virulence factors were identified, namely, flagellum, type IV pili, LPS and Type 3 secretion system which is important to directly secrete virulent compounds[70]. Moreover, its low permeability and high efflux contribute significatively to its resistance to antibiotics[69]. Over the years, several preclinical vaccine candidates were developed based on different important virulence factors such as LPS, flagellum,

outer membrane proteins and there were even whole-pathogen candidates[70]. Even though most candidates showed promising results in this stage of development, translation into clinical development was difficult due to the adaptation characteristics of *Pseudomonas* and high heterogeneity of proteins[42]. Therefore, a promising strategy could be to combine different proteins associated with different mechanisms of virulence using current techniques such as reversed vaccinology[69,71]. As in other Gram-negative pathogens, outer-membrane proteins were highly exploited as vaccine candidates due to their high immunogenicity and conserved status among strains. Accordingly, OprF and OprI were formulated together in vaccine candidate IC43[70]. The latter showed promising results in phase I/II trials but failed to show benefit in phase III since it only induced IgG production following initial colonization which was not early enough in the studied conditions. Nevertheless, this candidate can be exploited as a possible prophylactic vaccine for high-risk population with recurrent admissions to intensive care units[70]. A mucosal IC43 formulation was also evaluated as a possible effective vaccine due to the involvement of mucosal immunity in the *P. aeruginosa* infection[70]. Currently, there are no vaccines in clinical development, although preclinical development continues to search for a promising candidate using different approaches including multiepitope vaccines and DNA vaccines[33,68].

1.3. Innate Immunity

The development of vaccines has been always followed by an attempt to fully understand the immunological responses responsible for protection[72]. Accordingly, it is crucial to understand innate immune responses. The innate immune system is the first-line of defense against everything non-self[73]. Immune cells, such as macrophages, monocytes, dendritic cells, neutrophils, and natural killer cells (NK) possess a recognition system able to start a non-specialized immune response[73].

Particularly, macrophages are important immune cells with phagocytic functions.[74] These cells derive form monocytes after these cross the capillary walls into connective tissue due to a stimulus[74]. Langerhans cells and brain microglia are exceptions since they do not derive from monocytic cells[74]. On site differentiation leads to an increase in size, organelle complexity and phagocytic ability and, additionally, to a site-specific adaption[75]. Depending on the stimuli, macrophages can polarize into different phenotype

that are classified as classically activated (M1) or alternatively activated (M2) [76] (**Figure 4**). M1 phenotype is also called Proinflammatory and M2 as Anti-inflammatory[76].
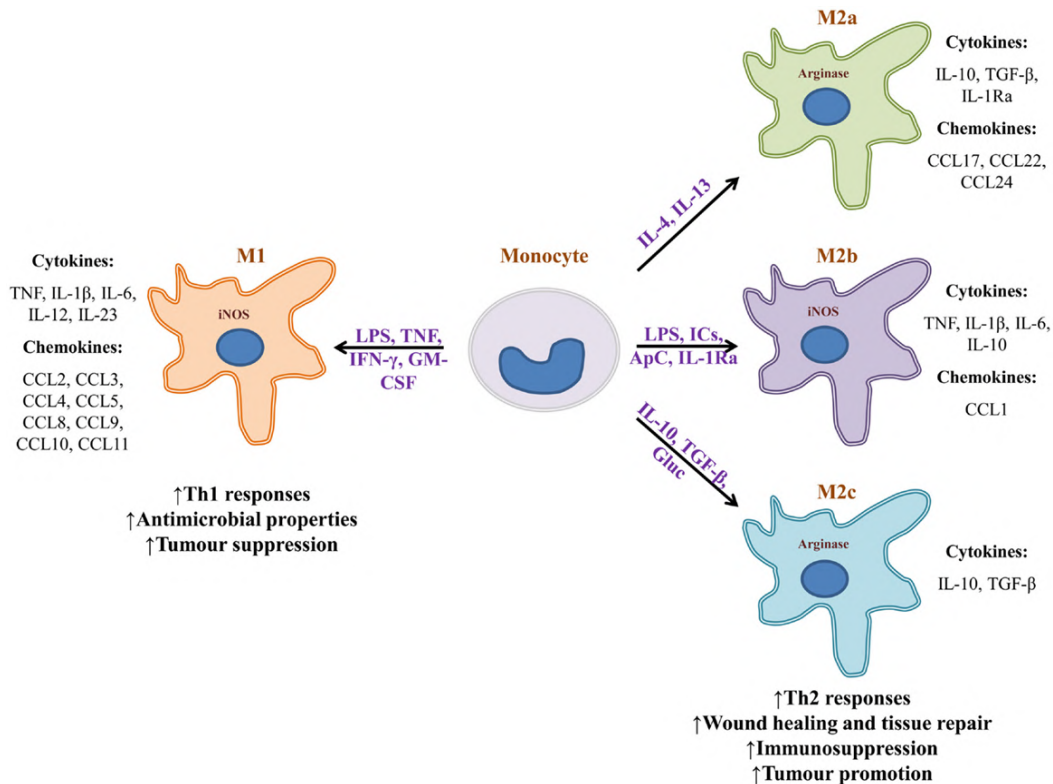
Figure 4. Macrophage polarization[74]

Macrophage polarization is an ongoing event during an inflammatory process and it depends on the amount of cytokines, time of exposure and competition for the cytokine by the membrane receptors on the cell[77]. M1 macrophages are polarized by inflammatory stimulus such as LPS, tumor necrosis factor (TNF) and others, and they secrete proinflammatory cytokines such as IL-1β IL-6, IL-12, IL-23 and TNF[78]. On the other hand, M2 macrophages are polarized in response to IL-4 and IL-13 and they produce anti-inflammatory cytokines such as IL-10 and TGF-β, that can, themselves, polarize other macrophages or induce monocyte differentiation into M2 macrophages[78]. Interestingly, M1 macrophage also express higher levels of nitric oxide (NO), leading to vasodilation and increased inflammatory responses, while M2 macrophages produce NO in low concentrations, and instead secrete arginase, which is involved in healing and proliferation[75].

Cells associated with early immune response, such as macrophages, express pattern-recognition receptors (PRRs) that bind to different molecules, namely pathogen-

associated molecular patterns (PAMPs) and endogenous danger-associated molecular patterns (DAMPs)[79]. Known receptor families include Toll-like receptors (TLRs), retinoic acid-inducible gene I (RIG1)-like receptors (RLRs), nucleotide-binding oligomerization domain (NOD)-like receptors (NLRs), C-type lectin receptors (CLRs) and absent in melanoma 2-like receptors (AIM2Rs)[79]. TLRs and CLRs are found on the cell surface or endocytic compartments, while RLRs, NOD-like receptors and AIM2Rs are located in the cytoplasm, thus being important for intracellular pathogens[80]. Besides cellular mechanisms of defense, the innate immune system also relies on humoral mechanisms that are important for recognition and response, such as LPS binding protein (LBP), C-reactive protein and others[81]. Although its role in defense against microorganisms is crucial, the innate immune system is also involved in the pathogenesis of different inflammatory diseases, such as asthma, type I diabetes, inflammatory bowel disease and systemic lupus erythematosus[81].

1.3.1. NOD-like Receptors

NLRs are present in the cytosol in order to recognize not only intracellular pathogens but also byproducts of infectious and inflammatory processes[82]. DAMPs associated with NLRs include ATP, hyaluronic acid, sodium urate, uric acid and cholesterol crystals[83]. NLRs are part of the AAA+ family of ATPases and have a conserved tripartite domain structure with an N-terminal protein-protein interaction domain, a central nucleotide-binding and oligomerization domain (NOD) and a variable number of C-terminal leucine-rich repeats[84]. According to their N-terminal effector domains, NLRs can be divided into NLRA, NLRB, NLRC and NLRP. Respectively, the N-terminal domain is either a acidic transactivation domain, a three tandem baculovirus inhibitor of apoptosis repeats, a caspase activation and recruitment domain or a PYRIN domain[84]. The latter, is present in 14 of the described receptors and it is important for initiating a pyroptotic response or starting an inflammatory signalling[83]. So far, 22 receptors have been described although not all of them have a clear function yet.[83] Nevertheless, as described in

Table 1, NOD-like receptors are involved in different immune and non-immunological functions.

Table 1. NOD-like receptors and their known functions.[83,84]

Subfamily	Examples	Function
NLRA	CIITA	Activates MHC II.
NLRB	NAIP	Recognizes flagellin and T3SS.
NLRC	NOD1	Activate NF-κB, autophagy mechanisms, type I interferon, and MAPK. Recognizes diaminopimelic acid.
	NOD2	Involved in autophagy mechanisms. Recognizes muramyl dipeptide, viral ssRNA.
	NLRC3	Negatively regulates T-cell and TLR activation.
	NLRC4	Involved in inflammasome formation. Recognizes flagellin and rod proteins.
	NLRC5	Activates MHC I expression and inhibits Type I interferon and NF-κB.
	NLRX1	Involved in autophagy and inhibits Type I interferon and NF-κB.
NLRP	NLRP1	Involved in inflammasome formation. Recognizes muramyl dipeptide and anthrax toxin.
	NLRP2	Inhibitor of NF-κB signaling. Involved in embryonic development.

Subfamily	Examples	Function
	NLRP3	Involved in inflammasome formation. Recognizes DAMPs.
	NLRP4	Negatively regulates Type I interferon. Involved in autophagy mechanisms.
	NLRP5	Involved in Embryonic development.
	NLRP6	Involved in regulating NF-κB and in responses to intestinal virus.
	NLRP7	Recognizes lipopeptides.
	NLRP10	Involved in dendritic cell migration and T-cell maturation.
	NLRP12	Negatively regulates NF-κB in T-cells.
	NLRP14	Involved in spermatogenesis. Inhibitor of STING signal.

As described in the table above, the NLRP subfamily NLRC4 are associated with the formation of inflammasomes. Inflammasome is a term to describe a multi-protein complex that consists of an NLR, and adaptor protein named apoptosis-associated speck-like protein (ASC) containing a caspase activation and recruitment domain (CARD) and the effector protein pro-caspase-1[85]. NLRP recruits ASC through interaction with the pyrin domain and starts a downstream signaling. Afterwards, pro-caspase-1, which is a member of the cysteine-aspartic acid protease family, is recruited to the complex and cleaved, originating activated caspase-1[85]. Subsequently, caspase-1 cleaves the precursors of proinflammatory cytokines pro-IL-1β and pro-IL-18 into its mature forms[85]. These two cytokines belong to the IL-1 family, which has important innate immune functions, increasing antigen recognition and lymphocyte function which in turns augments the host's immune response to pathogens[86]. Co-activation of caspase-1 and caspase-4/5 activates gasdermin D (GSDMD) leading to pyroptosis, a proinflammatory and non-

apoptotic form of programmed cell death[87]. The latter constitutes the non-canonical inflammasome, while canonical inflammasome refers to activation of caspase-1 only[88]. It is noteworthy that AIM2 and Pyrin are also able to assemble inflammasomes[83] (**Figure 5**).
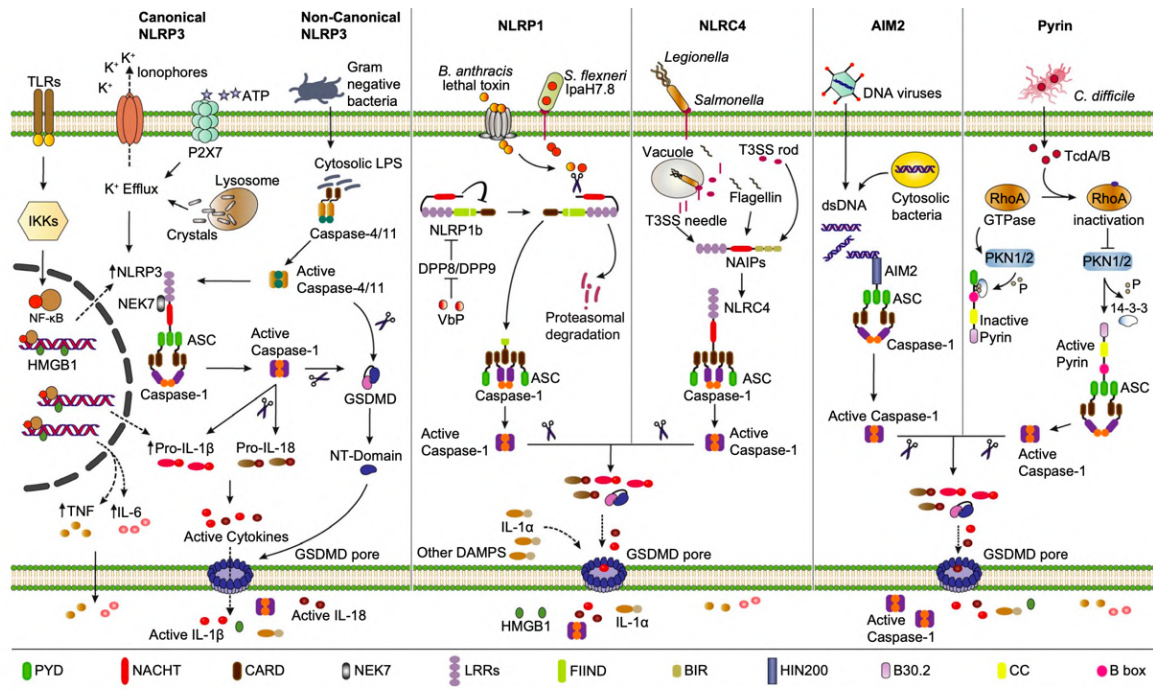
Figure 5. Overview of different inflammasomes[89]

As shown in **Figure 5**, different inflammasomes are assembled depending on the stimuli and on the receptor that is triggered. NLRP3 is the most studied inflammasome and it has a quite complex signaling, as it possesses both a canonical and a non-canonical activation through caspase-4/5[89]. It can also be activated through TLR signaling.[85] Its canonical activation requires a priming signaling followed by an activation signaling. Priming occurs through the stimulation of PRRs by PAMPs and DAMPS and subsequent NF-κB signaling. This step increases the expression of NLRP3 and pro-IL-1β and deubiquitinates NLRP3, which is essential for inflammasome assembly[85]. The activation step is mainly mediated by a potassium efflux derived from the recognition of different DAMPs.

Non-canonical activation of NLRP3 occurs with LPS stimuli, independent from TLR4 activation, followed by caspase-4/5 activation in humans that in turn leads to the assembly of the inflammasome and the activation of caspase-1[88]. Both activations result in pyroptosis and IL-1β and IL-18 release. However, in the non-canonical activation,

caspase-4/5 can also activate the canonical NLRP3 inflammasome through the efflux of ions[90]. Caspase 4 is able to cleave GSDM, leading to the formation of pores and pyroptosis which further enables the release of pro-inflammatory cytokines and other cellular products such as DAMPs and ions[90].

Although it is still not clear their role in pathogenesis, inflammasome function is associated with different diseases. For example, NLRP1 is genetically associated with vitiligo, Addison's disease, and autoimmune diseases such as type I diabetes and thyroid disease[85]. Immune responses against some intracellular pathogens are also mediated by inflammasomes. *Salmonella typhimurium, Shigella flexneri, P. aeruginosa* and *Legionella pneumophila* release PAMPs into the cytoplasm that are recognized by NLRC4 through a NAIP protein signaling[85]. While not part of NOD-like family of receptors, AIM2 recruits ASC to form an inflammasome that activates caspase-1 in response to double-stranded DNA (dsDNA) from virus[91].

1.3.2. RIG-1-like Receptors

RLRs are intracellular receptors able to sense viral RNA and transcriptional intermediates in the cytoplasm[92]. Structurally, RLRs consist in three parts, a DexD/H helicase domain with ATPase and helicase activity that stands in the middle, an N-terminus with two CARD domains that are able to induce downstream signaling and a C-terminus responsible for self-regulation through a repressor domain (RD)[82] (**Figure 6**). Indeed, if there is no stimulus, the C-terminus and the helicase domain are folded and RIG-1 activity is inhibited. When viral RNA is recognized by the C-terminus, there is a conformational change leading to the exposure of the receptor as well as multimerization[82]. So far, three different families have been identified: RIG-1, melanoma differentiation factor 5 (MDA5) and laboratory of genetics and physiology 2 (LGP2). As shown in **Figure 6**, LGP2 does not contain a CARD domain and, thus, it cannot transmit signals while MDA-5 does not have a RD and therefore does not have a self-inhibitory function[82]. It is speculated that LGP2 has regulatory functions over RIG-1 and MDA5 receptors[83].
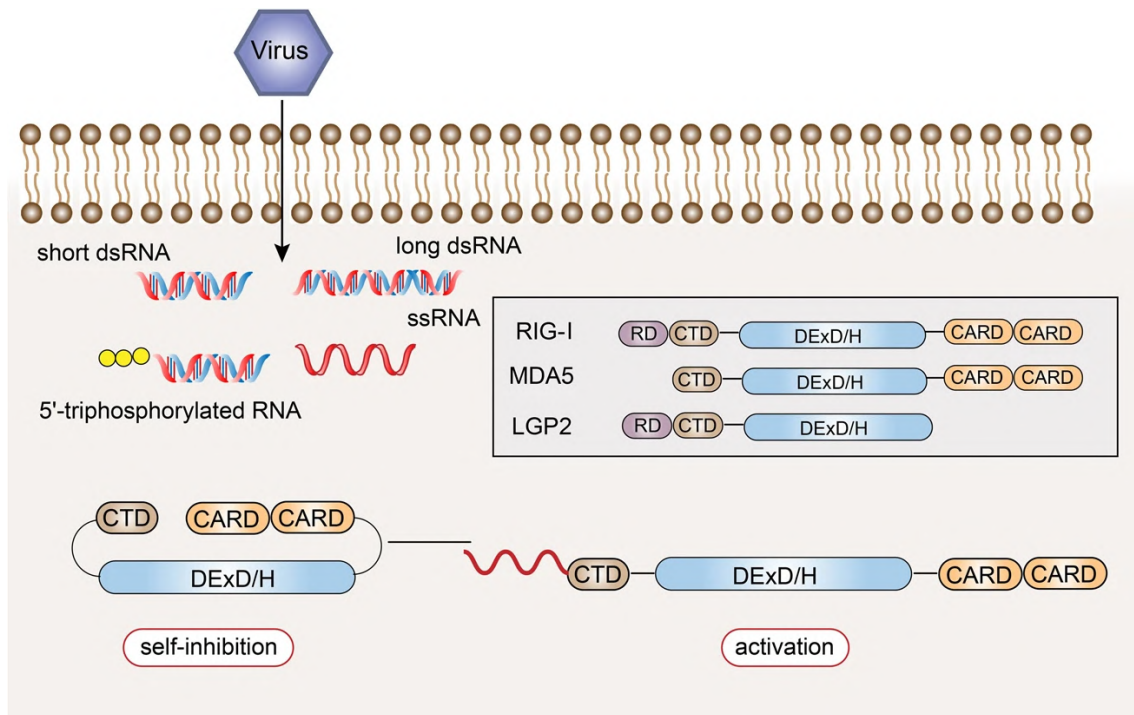
Figure 6. RLRs structure and ligand recognition[82]

After activation and multimerization, RIG-1 receptors interact with a mitochondrial antiviral signaling (MAVS) adaptor protein located in the outer membrane of the mitochondria[93]. Afterwards, there is the formation of a prion-like filament structure that initiates a downstream signaling cascade, called the MAVS signalosome, leading to the activation of Interferon (IFN) regulatory factor 3 (IRF3) and/or 7, Nuclear factor-κB (NF-κB), activator protein 1 (AP1) and signal transducer and activator of transcription (STAT)[94]. The activation of these factors leads to an increase in type I IFN genes transcription and inflammatory cytokines, promoting an antiviral environment[83].

IFNs are known to be important molecules in antiviral immunity. There are three families of IFNs: type I, type II, and type III. From these families, type I IFNs, that include IFN-α, IFN-β, IFN-ε, IFN-κ and IFN-ω, have been extensively studied for their antiviral role in infection[95]. It is reported that these molecules trigger apoptosis of infected cells, activate antiviral responses in infected and surrounding cells, activate effector cells and upregulate the expression of MHC class I on the surface of DCs[95]. In turn, these cellular events increase viral recognition and promote a T- helper 1 (Th1) response, leading to the secretion of IFN-γ (a type II interferon), Tumor Growth factor β (TGF-β), IL-2 and IL-10 that promote cytotoxic responses[95].

RLRs response to viral RNA is regulated through different mechanisms, preventing an exacerbated response to viral infections. Inhibitory proteins, such as NLRX1, PCBP2, Smurf2 and TRIM25, bind directly to MAVS or target it for degradation[93]. Furthermore, RIG-1 receptors are target for degradation or ubiquitination by regulatory proteins, also mediating the response[83].

1.3.3. C-type Lectin Receptors

C-type lectins are a family of more than a thousand proteins that contain one or more C-type lectin domain (CTLD)[96]. **Figure 7** illustrates the different types of C-type lectins that have been established according to their phylogeny and domain organization[96]. Secreted C-type lectins have different functions within the cell as they can act as growth factors, opsonins and antimicrobial proteins, while transmembrane C-type lectin receptors are involved in different signaling cascades and in the modulation of cellular, developmental, homeostatic and immunological responses[96].
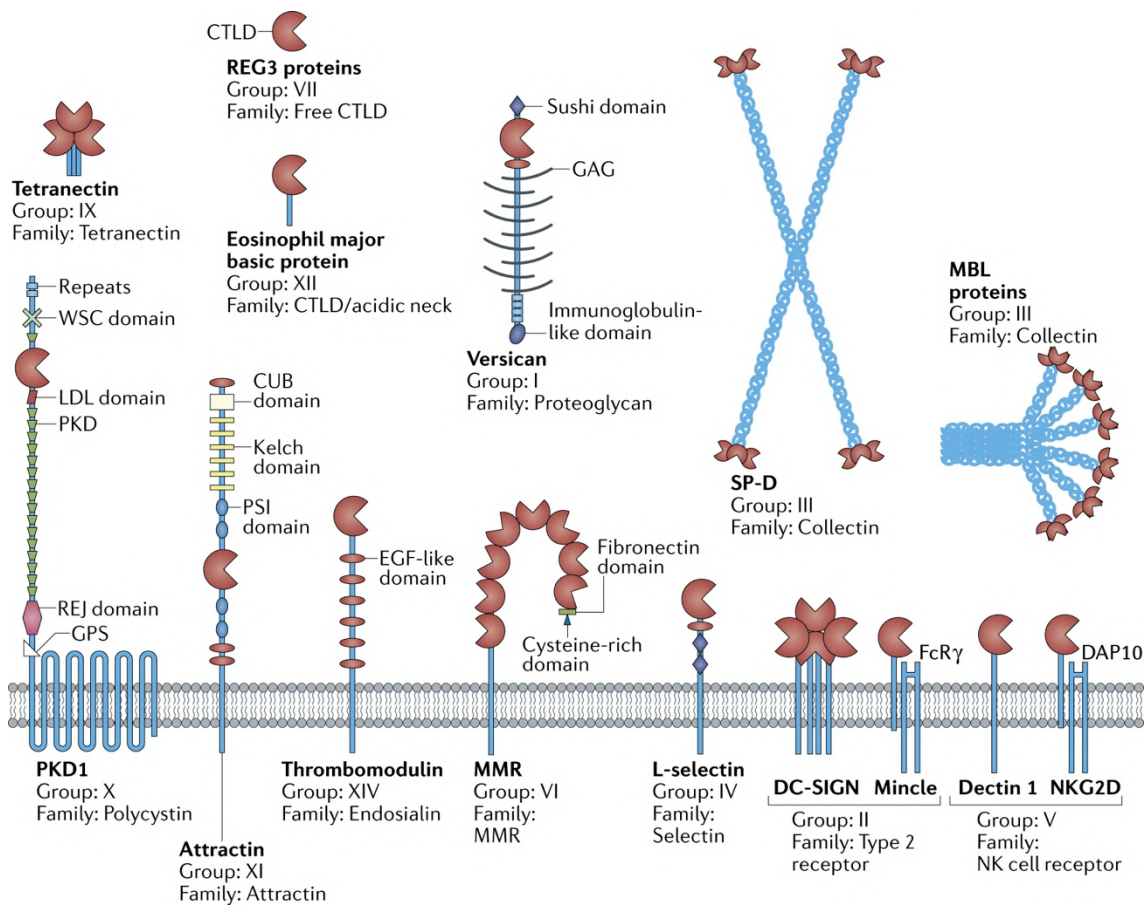
Figure 7. Transmembrane and soluble C-type lectins[96]. CUB, complement C1r/C1s; EGF, epidermal growth factor; FcRγ, Fc receptor γ-chain; GAG, glycosaminoglycan; GPS, G protein-coupled receptor proteolytic site; LDL, low-density lipoprotein; MBL, mannose-binding lectin; MMR, macrophage mannose receptor; PKD, polycystic kidney

disease; PSI, plexin–semaphorin–integrin; REJ, receptor for egg jelly; SP-D, surfactant protein D; WSC, cell wall integrity and stress response components.

As a type of PRR, C-type lectins are described as phagocytic receptors as they are able to recognize PAMPs and involve the pathogen in a cytoplasmic vesicle for direct digestion[82]. Namely, soluble C-type lectins such as collectins have been reported to have such function[96]. Additionally, membrane C-type lectins such as Dectin-1 can identify different fungi such as yeast, *Candida Albicans* and Aspergillus through binding with a carbohydrate, β-1,3-glucan, that activates a downstream signaling[82]. Innate immune signaling through these receptors has been linked to the development of Th1, Th17 and B cell responses which are crucial for systemic mucosal immunity during infections[96]. C-type lectins expressed on antigen presenting cells (APC) are able to attract other immune cells to the environment, such as neutrophils, by inducing the production of cytokines, which in turn contributes to bacterial clearance from the site[97].

Particularly, this PRRs are able to recognize glycan residues from both self and non-self-structures. On the CTLD there is a calcium-dependent carbohydrate recognition domain responsible for sensing this carbohydrates[97]. This function is important for bacterial recognition as the bacterial wall is extensively decorated with glycans[98]. While this is important for host defense through innate immunity, it is also known that bacteria exploit this recognition by C-type lectins for immune invasion, increasing bacterial load and overall virulence. Nevertheless, as illustrated in **Figure 8**, C-type lectins are expressed on different APCs and are able to recognize different important pathogens and initiate immune responses.
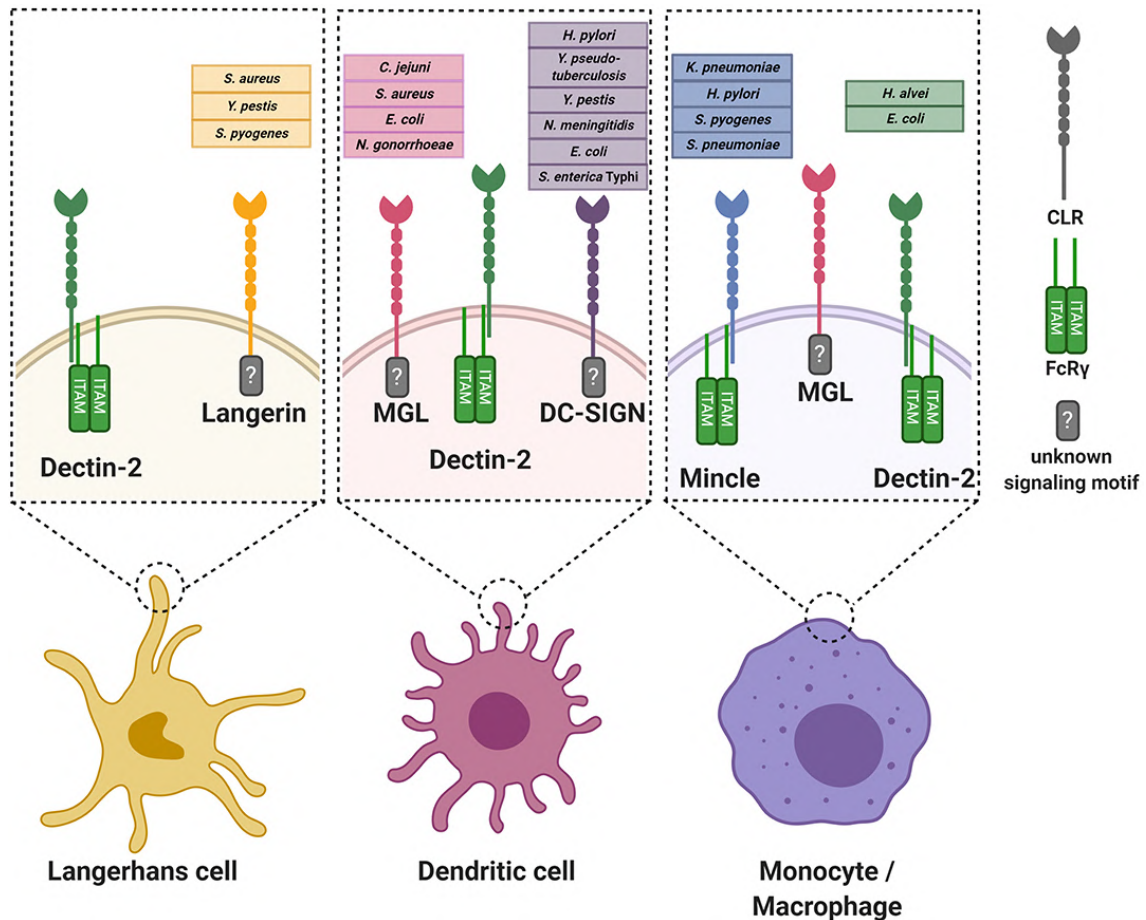
Figure 8. C-type lectin receptors on immune cells and recognized bacteria[98]. FcR*γ*, Fc receptor gamma chain

Particularly, DC-SIGN recognizes an important number of pathogens through interaction with Mannose α1-3, α1-4 fucosylated glycans and N-acetylglucosamine as it contains an amino acid motif that confers preference towards equatorial 3- and 4-hydroxyl groups[98]. Interestingly, DC-SIGN signaling converges with signaling from other PRRs, such as TLRs, in response to bacterial recognition[98].

1.3.4. Toll-like Receptors

TLRs were the first class of PRRs to be discovered and extensively studied. Indeed, in the 80s, studies in *Drosophila* led to the discovery of the NF-κB family of transcriptional factors and, subsequently, to the identification of the *Drosophila* toll, a receptor involved in anti-microbial activity[99]. Afterwards, TLR4 was identified as the human homolog and its innate immune roles began to be clarified throughout the decades[99]. These receptors are known to not only mediated immune responses, but also

regulate important aspects of homeostasis through regulation of tissue repair and regeneration[100]. So far, 10 TLR have been identified in humans[101].

Structurally, TLRs are type I transmembrane glycoproteins with three domains: an extracellular ectodomain, single-spanning transmembrane domain with a single helix configuration and a cytoplasmic TLR domain[100]. The extracellular ectodomain, or N-terminal ligand recognition domain, contains leucine rich repeats (LRRs) in a folded structure, while the cytosolic C-terminal domain has a Toll/IL-1R (TIR) homology[102]. TIR domains are part of different adaptor proteins involved in TLR signaling and are also found in plant proteins associated with resistance to pathogens, suggesting that this domain had an immune function before the divergence of plants and animals[103]. LRRs of the N-terminal domain of TLRs are typically 22-29 residues in length that adopt a loop structure due to hydrophobic and hydrophilic components that force the structure to acquire such shape, which resembles a horseshoe illustrated in **Figure 9**. Therefore, each LRR protein has a concave surface, a convex surface, an ascending lateral surface consisting of loops, and a descending lateral surface on the opposite side.[103]
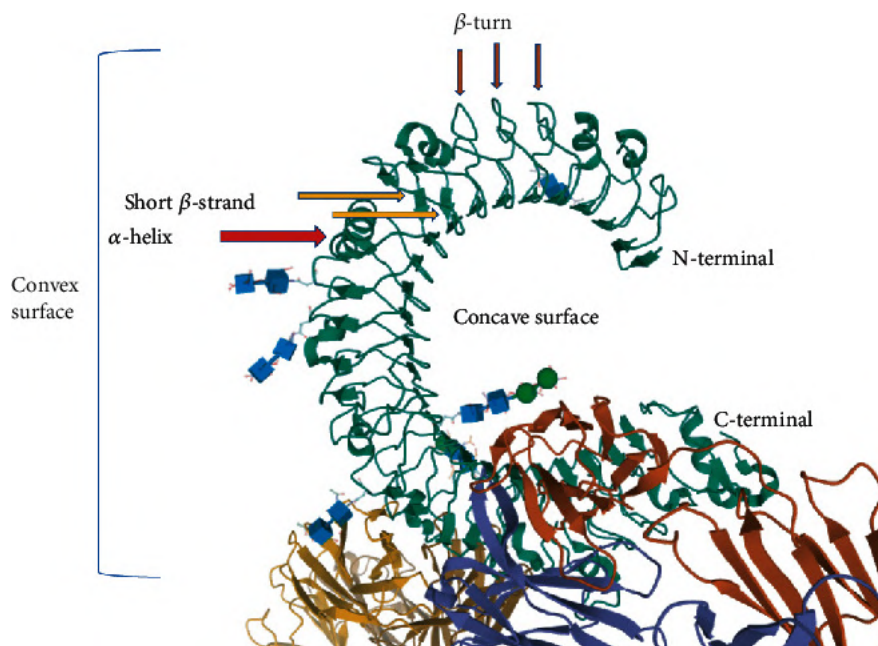
Figure 9. LRR of TLR3's ectodomain[102]

TLRs are synthesized in the endoplasmic reticulum (ER) and transported either to the plasma membrane, in the case of transmembrane TLRs, or to endosomal membranes, in the case of endosomal TLRs[104]. In the latter, trafficking from the ER to endosomal compartments requires the involvement of chaperon protein UNC93B1[105]. This

interaction is crucial for stability and ensures that activation of these receptors only occur in the desired location once the chaperon protein is released[106]. Moreover, UNC93B1 is further involved in regulating TLR7 activity by balancing the amount of TLR9 in detriment of TLR7[107].

TLRs bind to different PAMPs, according to their localization and binding pocket characteristics. Specifically, transmembrane TLRs such as TLR1, 2, 4, 5 and 6, recognize surface components of pathogens. On the other hand, endosomal TLRs, such as TLR3, 7, 8, 9 and 11-13 in mice, bind to nucleic acid or intracellular parasite components[108]. **Figure 10** illustrates TLRs localization and respective ligands. TLR2 recognizes lipoproteins from the surface of bacteria and forms heterodimers with either TLR1 or TLR6. TLR4 recognizes LPS and TLR5 interacts with flagellin of bacteria[101]. On the other hand, TLR3 interacts with dsRNA from virus and self RNA from damaged cells. TLR7 and 8 recognize single-stranded (ss) RNA while TLR9 recognizes ssDNA containing bacterial and viral unmethylated cytidine-phosphate guanosine (CpG) motifs[101]. It is hypothesized that TLR10 is involved in recognizing HIV-1's gp41 protein but this is not completely clarified[101].
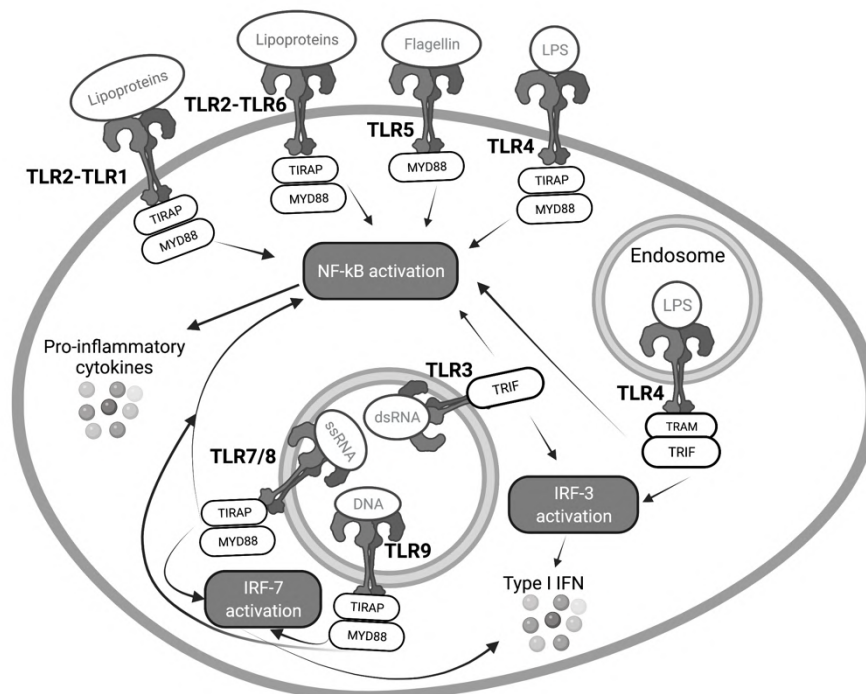
Figure 10. Schematic representation of TLRs localization, ligands and signaling

After ligand recognition, conformational changes occur and the TIR domain undergoes dimerization, forming either hetero- or homodimers[100]. These dimers interact with different TIR-containing adaptor proteins to start a downstream signaling cascade[100]. All TLRs, except for TLR3, bind to myeloid differentiation primary-response protein 88 (MyD88). On the other hand, TLR3 and endosomal TLR4, are able to bind to TIR domain-containing adaptor protein (TIRAP) inducing IFN- β (TRIF)[109]. Then, several kinases are activated, depending on the triggered receptor, leading to downstream signaling, activating c-Jun N-terminal kinase (JNK) and p38 mitogen-activated protein kinase (MAPK) and different transcription factors, such as NF-κB and IRFs[109].

1.3.5. TLR4: ligand recognition and signaling

TLR4 is one of the most studied TLRs and the first to be identified. It is also a particular case within the TLR family since it has dual-signaling. Besides the transmembrane activation and recruitment of MyD88, TLR4 can be internalized after dimerization, recruiting TRIF and stimulating intracellular pathways[110], as shown in **Figure 11**.
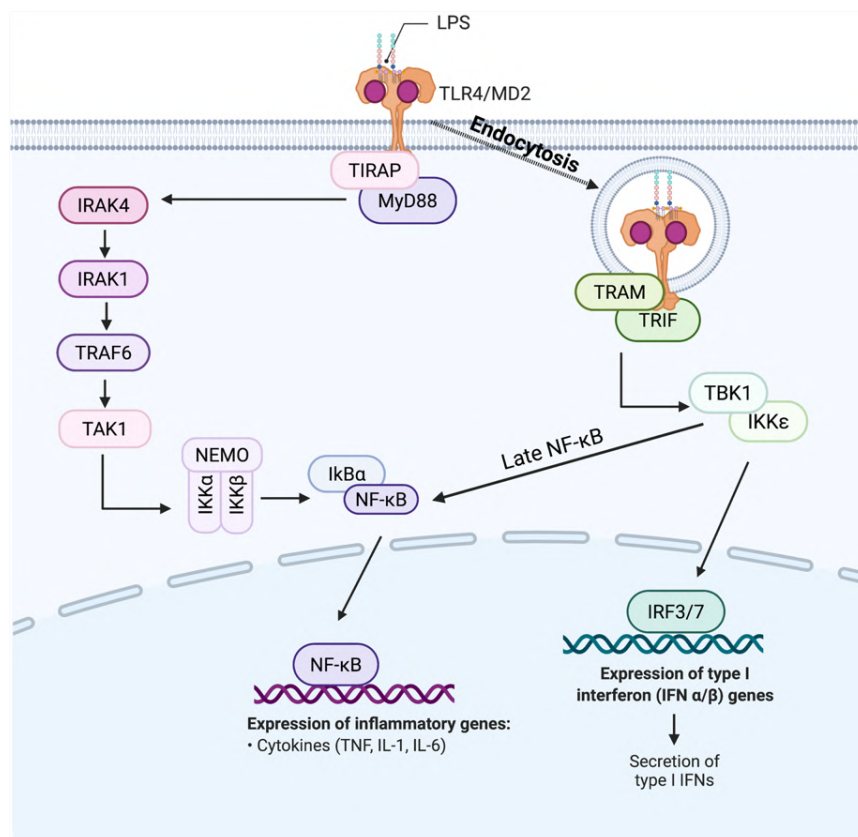
Figure 11. TLR4 dual signaling

TLR4 signaling in response to LPS, ultimately leads to an inflammatory cascade with the production of proinflammatory cytokines, such as TNF, IL-6 and IL-1β, as well as the production of type I IFN, such as IFN-β[111]. Additionally, TLR4 is also involved in the up-regulation of co-stimulatory molecules, as CD40, CD80 and CD86, and altered expression of chemokine receptors[101]. This shift in cellular immunity is critical for DC maturation, thus linking innate and adaptive immunity. Major histocompatibility complex (MHC) function is also controlled by TLR4 signaling, as activation of TLR4 leads to acidification and peptide loading onto MHC and controls redistribution of MHC-I and MHC-II on the surface of DC[104]. DC maturation and the release of cytokines are important events for T-cell differentiation and proliferation, which in turn is important for immune memory[101]. For example, CD8+ responses are promoted by TLR4 activation through the fusion of MHC-I endosomes with phagosomes, leading to the presentation of exogenous antigens[104]. **Figure 12** illustrates the impact of TLR4 on DC maturation and T cell differentiation.
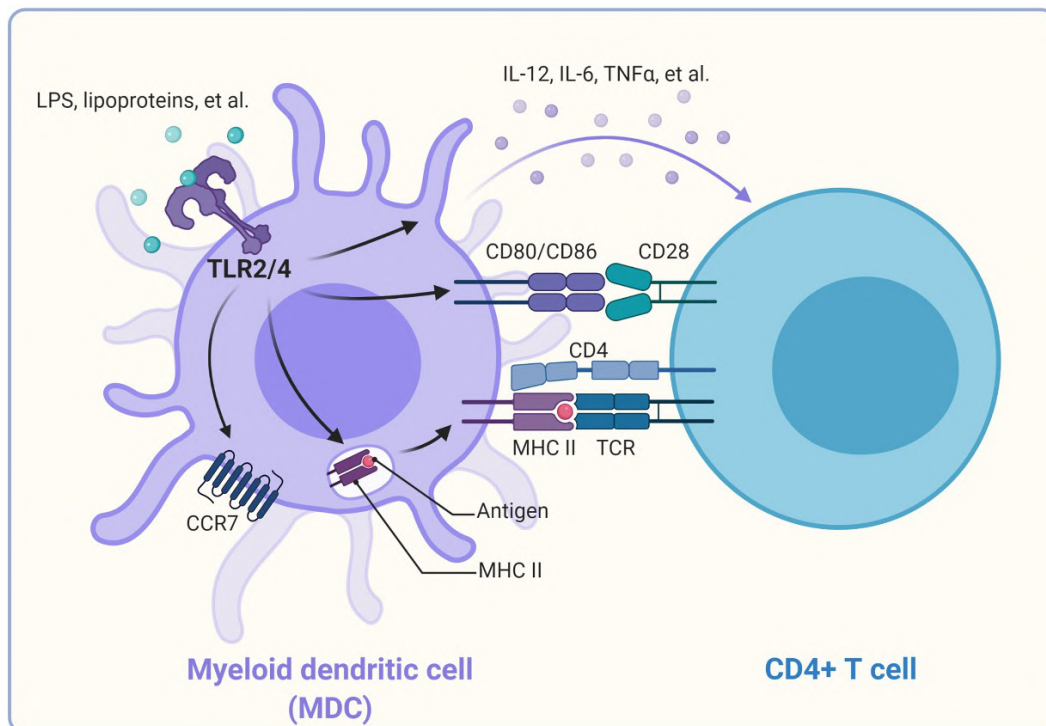
Figure 12. Promotion of CD4+ T cell activation by TLRs on DC[101]

The type of cytokines produced and released by the cell influences T cell response. For example, IL-12 and IL-18 production induces Th1 type responses, which are important for triggering cellular events against intracellular pathogens, leading to IFN-γ[112]. On the other hand, Th2 polarization, driven by IL-4 and other factors such as GATA3,

are important for helminth infection responses and they also play a key role in allergic diseases[112]. Th17 responses, on the other hand, are polarized by the production of IL-1, IL-6 and IL-23, together with TGFβ[104]. Th17 cells synthesize IL-17 and IL-22 which are produced in mucosal infection sites, revealing that they are important in triggering mucosal immunity against different pathogens[113].

TLR4 binds to LPS which is a complex glycolipid present in the Gram-negative cell wall. LPS can be divided into three different domains: a glycolipid portion called lipid A, a oligosaccharide core and a O-antigen glycan (**Figure 13**)[114]. Lipid A is responsible for membrane anchoring and it corresponds to the biologically active unit of LPS. Its structure consists of phosphorylated β(1,6)-linked-D-glucosamine disaccharide with associated lipid chains[115]. In fact, picomolar concentrations of lipid A are enough to activate TLR4 signaling[116]. Due to its amphiphilic character, LPS forms aggregates in a physiological aqueous environment[114].

LPS can be classified according to the appearance of the bacterial colonies that express it. Namely, smooth LPS (S-LPS) express complete LPS, while mutants lacking O-antigen form colonies with a rough appearance, thus with rough LPS (R-LPS)[114].
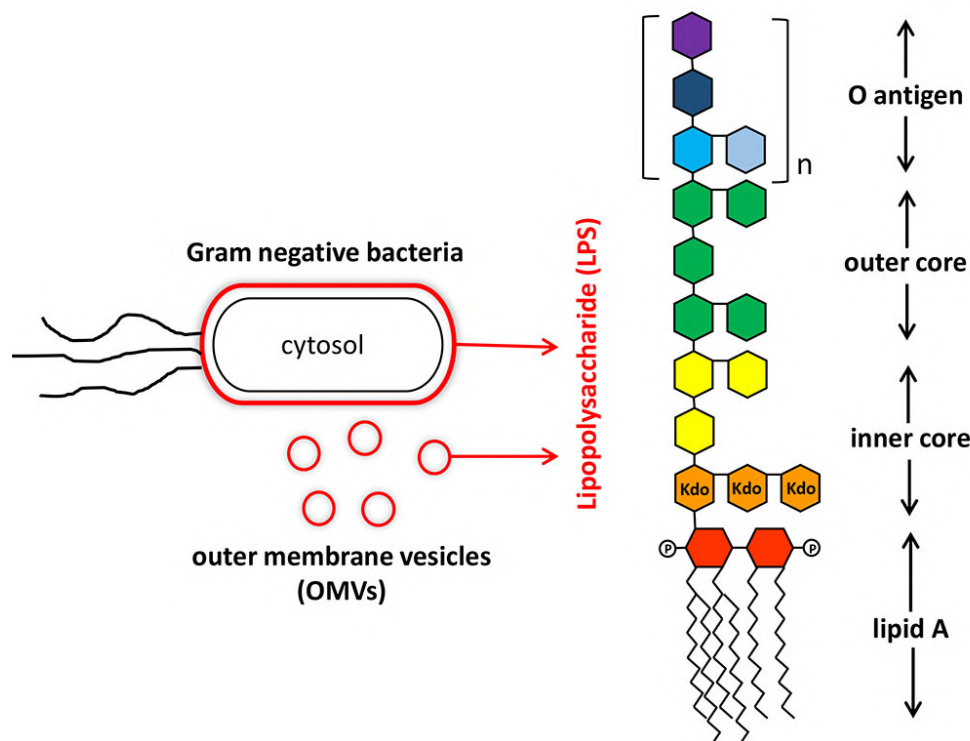
Figure 13. Simplified structure of LPS[117]

Binding to TLR4 occurs through mediation by two accessory proteins: LBP and CD14[118]. LBP is a glycoprotein with an elongated structure to facilitate transfer[119]. During infection, concentrations of this protein are elevated and, indeed, LBP enhance sensitivity to LPS in about 300 fold[120]. CD14 is a GPI-linked protein expressed in most TLR4 expressing cells[121] while it can also be found in a soluble form[104]. Interestingly, anchored CD14 is only necessary for MyD88 activation at low concentrations of LPS but, on the other hand, it is essential for endocytosis and TRIF activation[121]. This illustrates the importance of CD14 in transporting the receptor within the cell[121]. LBP interacts with either micelles of LPS or the bacterial membrane and facilitates the extraction of a single molecule of LPS by CD14, in a TLR4-dependent manner, onto myeloid differentiation protein 2 (MD2)[116]. One single LBP molecule is able to catalyze multiple LPS transfers[119].

MD2 interacts with the ectodomain of TLR4, forming heterodimers via ionic interactions[122]. This protein contains 160 amino acid residues and adopts a β-cup-folded structure composed of two antiparallel β-sheets with three and six β-strands that form a large hydrophobic pocket[122]. These characteristics are ideal to bind to five of the six hydrophobic acyl chains of LPS. Indeed, the sixth chain does not fit into the MD2 pocket but instead interacts with another TLR4 molecule[118]. In fact, decreasing the number of lipophilic chains results in decreased TLR4 agonistic activity[118]. LPS mediates the dimerization of two TLR4/MD2 heterodimers that occurs through hydrophobic and hydrophilic bonds between TLR4, LPS and MD2 (**Figure 14**)[118]. The phosphate groups of lipid A are also important for dimerization since they bind to a cluster of positively charged lysines and arginines from both TLR4 molecules and MD2[118]. Indeed, deletion of one of these groups results in decreased endotoxic activity and can lead to structural rearrangements that changes downstream signaling. For example, Monophosphoryl lipid A (MPLA), a TLR4 agonist derived from detoxification of *Salmonella minnesota* LPS, does not contain the 1-phosphate but only the 4-phosphate, and it is not able to induce MyD88 signaling but only TRIF signaling[123].
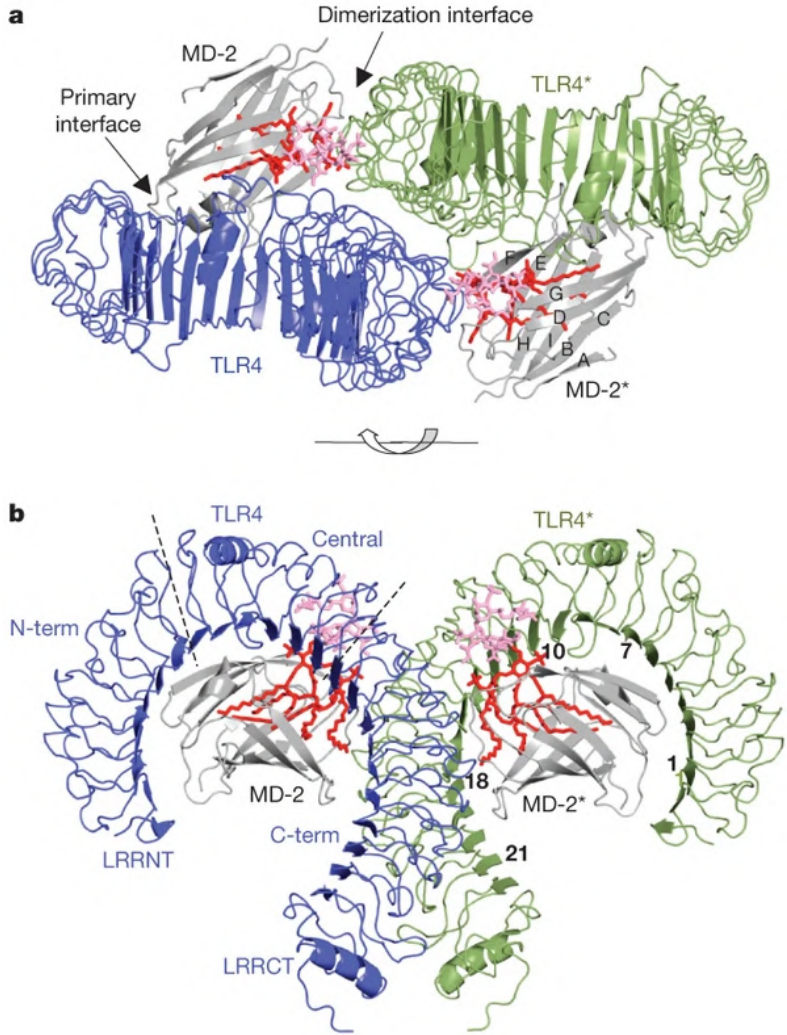
Figure 14. Top (a) and side (b) view of the structure of the TLR4-MD2-LPS complex[118]

The inner core of LPS usually consists of two to three 3-deoxy-d-manno-octulosonic acid (KDO) units linked to the distal glucosamine the lipid A, via a α-(2,6) linkage[124] (**Figure 15**).
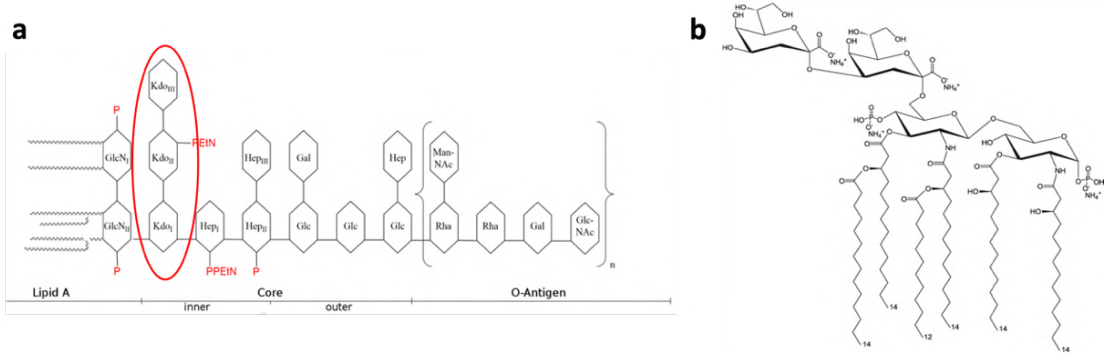
Figure 15. KDO localization in a schematic LPS molecule[114] **(a) and structure of KDO$_2$-Lipid A (b)**

These carbohydrates are reasonably conserved and KDO is important for lipid A activity and overall endotoxic activity of LPS[125]. However, due to bacterial heterogeneity between LPS of different species and pressure towards antibiotic resistance, these residues can be modified[126]. KDO has been shown to increase proinflammatory cytokine production, compared to lipid A alone in *Neisseria meningitids and E. coli strains*[127]. Indeed, although KDO only establishes interactions with TLR4 and not with MD2, which indicates that its presence is not essential to LPS activity, it establishes additional interactions with TLR4, contributing to binding affinity and overall activity[114]. Binding is improved due to interactions between TLR4's LRR and the negatively charged KDO residues and, also, due to conformational changes that allow for additional space for the LPS's acyl chains[114].

1.3.5.1. MyD88-dependent TLR4 signaling

MyD88 is a tripartite structure with an N-terminal, an intermediate and a C-terminal TIR domain that links TLR4/MD2 heterodimer to downstream kinases[128]. Once LPS triggers the dimerization of the TLR4/MD2 complex, there is recruitment of a receptor-proximal membrane protein, that contains a TIR domain, called TIRAP[104]. This protein is located near the plasma membrane but it can also be located in endosomal compartments where it mediates TLR9 signaling[107]. TIRAP recruitment stimulates the assembly of a supramolecular organizing center (SMOC), called the myddosome, that involves MyD88 and kinases from the IL-1 receptor associated kinase (IRAK) family[129] (**Figure 16**). IRAK family of kinases includes IRAK1 and 2 and IRAK4. IRAK4 is a serine-threonine kinase that is part of the myddosome[128]. The stoichiometry of the myddosome is not clear but it has been reported that it can be 7:4 and 8:4 MyD88 and IRAK4, although some crystallographic structures have been shown to have six MyD88, four IRAK4 and four IRAK1/2[130].
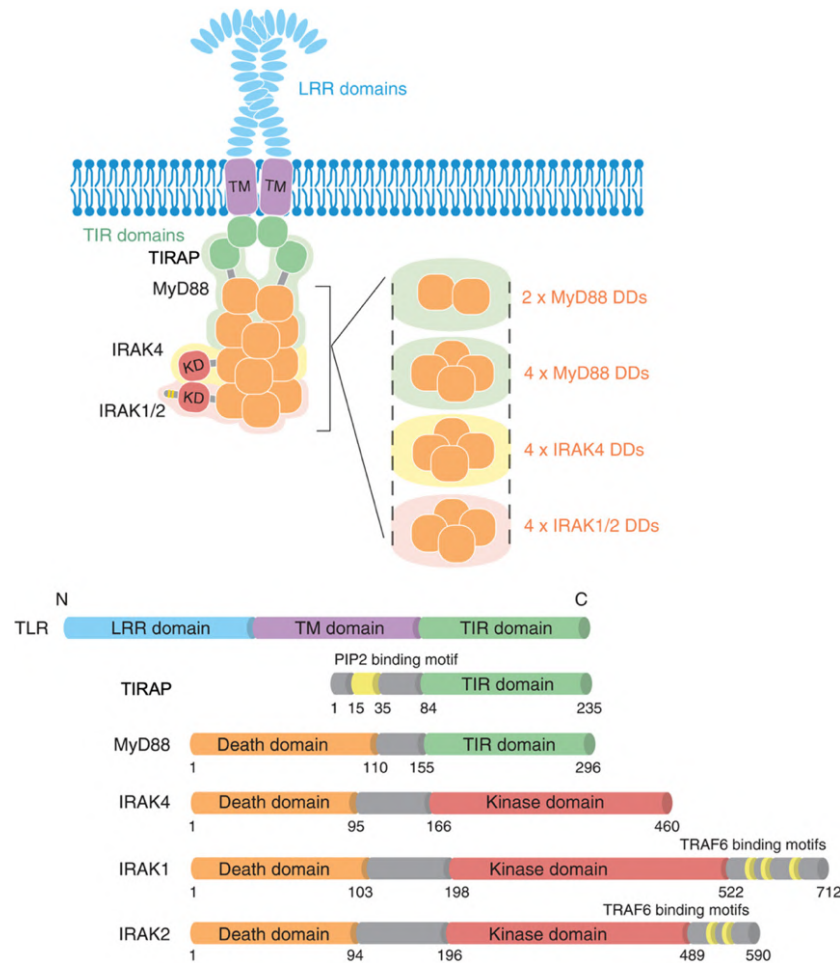
Figure 16. Schematic representation of the myddosome and structure of related proteins TLR, TIRAP, IRAK4, IRAK1 and IRAK2[128]

IRAK4 is activated by interacting with the kinase death domain of MyD88 that triggers its dimerization, trans-autophosphorylation and activation[131]. This activation leads to the phosphorylation of IRAK1 and IRAK2[128].

IRAK4 is essential for TLR4 signaling since its deficiency is linked to decreased MAPK and NF-κB inducible cytokines levels, in response to TLR4 agonists[131]. IRAK1 and 2, on the other hand, bind to TNF receptor-associated factor 6 (TRAF6) through their C-terminal[128]. This interaction is necessary for activation of downstream pathways such as the MAPK and NF-κB signaling[128]. Specifically, TRAF6 activates TAK1 and IKK through ubiquitination[132]. The latter is possible due to E3 ubiquitin ligase activity that catalyzes linked polyubiquitination between TRAF6 and its substrates[133].

MAPK members, such as ERK1/2, p38 and JNK are then activated through phosphorylation and mediate the activation and translocation of transcriptional factor AP-1[134]. AP-1 is actually a group of transcriptional factor consisted of four subfamilies: Jun,

that include c-Jun, JunB and JunD; Fos, c-Fos, FosB, Fra1 and Fra2; Maf, c-Maf, MafB, MAfA, Mafg/f/h and Nrl; and ATF-activating transcription factor (ATF2, LRF1/ATF3, BATF, JDP1 and JDP2[135]. TLR4-dependent activation of c-Jun leads to the formation of homo and heterodimers with other AP-1 members that then lead to the synthesis of TNF, IL-12 and IL-23[135]. Furthermore, it is also known that p38 activation in macrophages, induces transcription of AP-1 and expression of Il-12, IL-23, TNF, IL-6 and IL-1β[136]. **Figure 17** illustrates the TLR4-dependent activation of MAPK and translocation of AP-1.
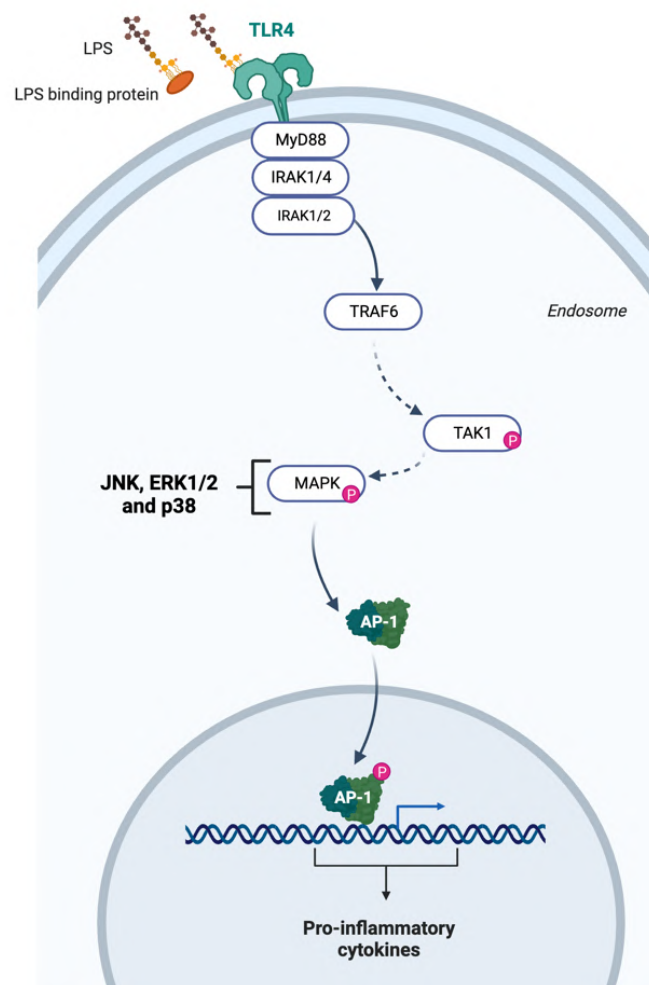
Figure 17. Simplified representation of TLR4-dependent MAPK signaling through MyD88

NF-κB is a crucial family of transcriptional factors involved in TLR4 activity and regulation. It is usually found in homo and heterodimers between the two subunits p50 and p65, although the p50 homodimer lacks the transactivation domain and thus is used as a regulator[137]. RelB, c-REL and p52 subunits were also identified[138]. Its main role

within the MyD88-dependent signaling pathway is to promote the expression of important proinflammatory cytokines such as TNF, IL-1β and IL-6[137]. Generally, NF-κB is important for the development and maintenance of the immune system, for the regulation of epithelial homeostasis and it also plays a role in cell cycle regulation, cell proliferation and cell death[139].

Activation of NF-κB through phosphorylation is controlled by the IKK complex (**Figure 18**). The latter is composed by NF-κB essential modulator (NEMO), also known as IKKγ and the catalytic subunits IKKα and IKKβ[140]. TAK1 forms a complex with IKK through K63 polyubiquitin chains and phosphorylates IKKβ. Additionally, linear ubiquitin dimers bind to IKKγ and also contribute to IKK activation[101]. In order to activate NF-κB, IKKβ phosphorylates the NF-κB inhibitor IκBα, leading to its ubiquitylation and proteasome mediated degradation[141]. After degradation, NF-κB is phosphorylated and translocated into the nucleus where it promotes transcription of proinflammatory cytokines after binding to specific DNA sequences named κB sites[141].
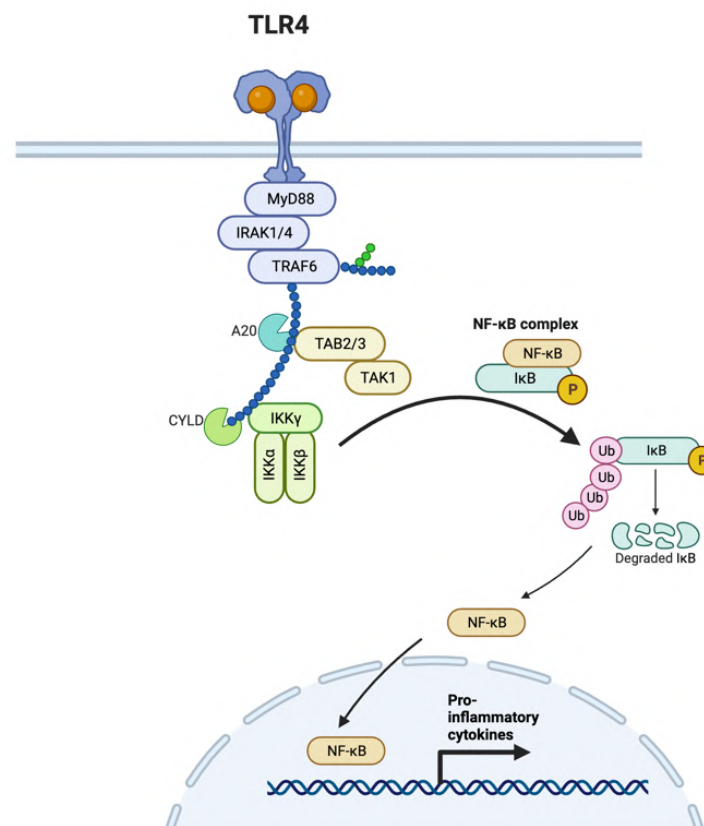
Figure 18. Simplified representation of TLR4-dependent NF-κB signaling through MyD88

1.3.5.2. TRIF-dependent TLR4 signaling

As mentioned above, TLR4 is unique among TLRs since it is able to induce two different intracellular pathways, using two different signaling adaptor proteins. Besides MyD88, TRIF is also able to bind to TLR4/MD2 to initiate a downstream cascade[142] (**Figure 19**). TRIF contains a N-terminal domain responsible for self-regulation, a TRAF6 binding motif, a TIR domain and a receptor-interacting protein homotypic interaction motif at the C-terminal[143].

This pathway begins with the internalization of the TLR4/MD2/LPS complex that is mediated by TRIF-related adaptor molecule (TRAM). Trafficking of the receptor occurs through the invagination of the plasma membrane and during this process MyD88 and TIRAP are released[110]. TRIF is able to interact with TRAM through their TIR domain forming a complex[143]. Afterwards, TRAM/TRIF recruits TRAF3 and TRAF6 that in turn recruit TBK1 and receptor-interacting serine threonine-protein kinase (RIPK), forming the triffosome[110]. This SMOC leads to the activation of IKKε and consequent phosphorylation and nuclear translocation of IRF-3, a transcriptional factor responsible for inducing the expression of Type I IFN[144]. It is also reported that TRAM/TRIF signaling enhances MyD88-dependent responses[129].
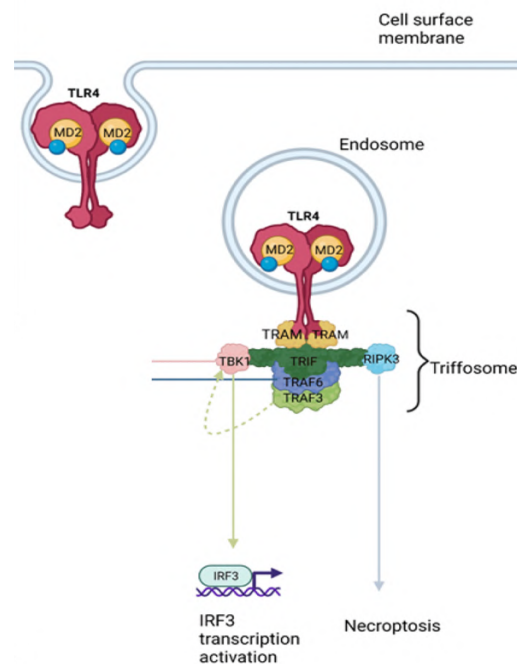
Figure 19. Schematic Representation of TRIF-dependent signaling[145]

TLR4 internalization is mandatory for TRIF-dependent signaling. This intracellular trafficking requires the intervention of CD14[121]. Furthermore, it was also clarified that this process is completely CD14 dependent but does not necessarily require the intervention of adaptor proteins such as MyD88, TRIF, TIRAP or TRAM[121]. Kinases Syk and PLC$_\gamma$2 are also important for the endocytosis of the receptor[110] (**Figure 20**).
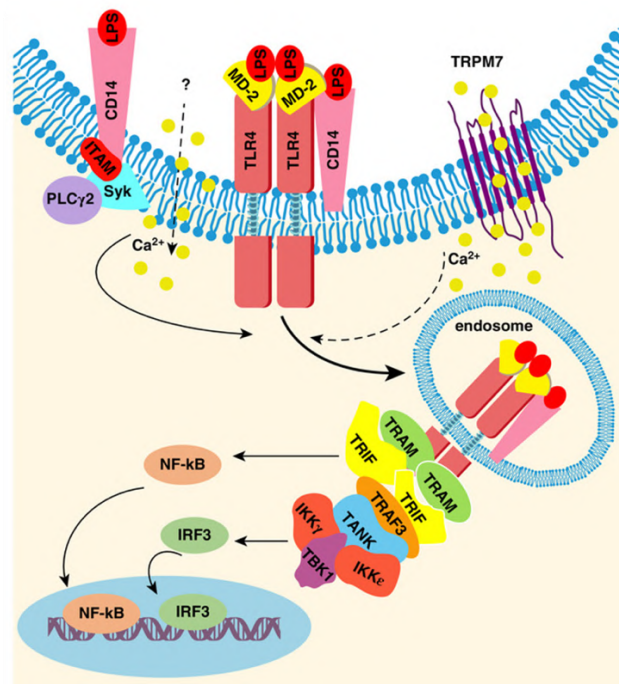
Figure 20. Schematic representation of CD14-dependent TLR4 trafficking to the endosome[110]

Regulation of this process is achieved through different regulators such as prostaglandin E$_2$[146] and glia-maturation factor -γ (GMF-γ)[147]. The former regulates TRIF signaling by activating the EP4 receptor which decreases TLR4 internalization via a negative feedback loop[146]. Instead, GMF-γ increases the internalization of TLR4, thus decreasing MyD88 signaling but increasing TRIF signaling and type I IFN responses[147]. Nevertheless, GMF-γ is also involved in terminating TRIF-dependent responses by trafficking the receptors from early endosomes to late endosomes[148]. Ultimately, response is terminated by lysosomal degradation of TLR4[149], although it is not clear whether there is a retrograde transport mechanism, involving GTPases RAB proteins, responsible for this[150]. This hypothesis is supported by the fact that acidification is required for internalization and activation of the pathway, suggesting that usual acidification to

promote ligand dissociation is not the degradation mechanism involved in endosomal TLR4 activity[149].

TRIF-dependent signaling induces Type I interferon responses through the phosphorylation and nuclear translocation of IRF-3[151]. The IRF family of transcriptional factors contain a DNA-binding domain that is common to all members and an IRF-associated domain that is unique for each IRF[152].

IRF-3 activation via TAK1 and IKKε seems to occur through the recruitment of scaffold proteins, such as NAP1, TBKBP1 and TANK, that bind to TBK1 forming complexes[152]. These complexes are then modified by TRAF3 which induces dimerization[152]. Afterwards, there is ubiquitination and recruitment of more complexes, ultimately leading to dimerization and phosphorylation of IRF3, which allows for its nuclear translocation[152]. This process is illustrated in **Figure 21**.
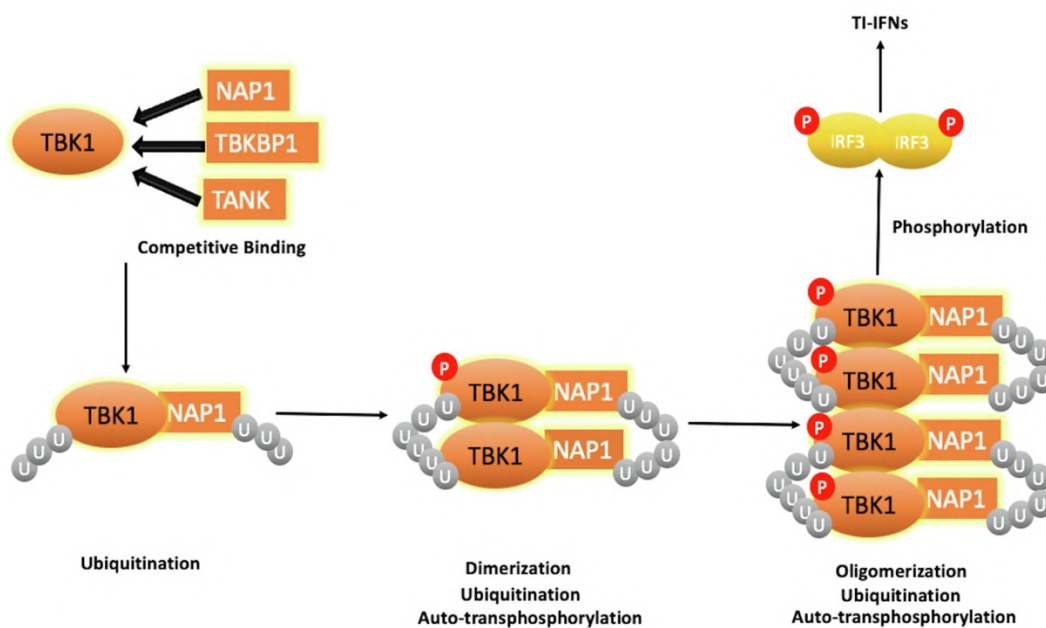
Figure 21. TBK1-dependent IRF3 phosphorylation[152]

Type I IFN signaling, triggered by IRF3, activates receptor-associated Janus kinase 1 (JAK1), tyrosine kinase 2 (TYK2) and STAT transcription factors that are responsible for inducing IFN-stimulated genes 3 (ISGF3)[154]. ISGF3 complex involves STAT1, STAT2 and IRF9 that induce the expression of proinflammatory chemokines and molecules responsible for antiviral responses[154]. This amplification of Type I interferon signaling is important not only for mediating innate immunity against pathogens but also to modulate

adaptive immune responses through the interaction between APCs and T-cell effector maturation and differentiation[155].

Interestingly, TRIF-dependent pathway is also able to induce late NF-κB activation[156]. This activation happens due to the recruitment of TRAF6 and RIP1 into the triffosome, that in turn activates TAK1 and the IKK complex to promote IκBα degradation and NF-κB phosphorylation[157] (**Figure 22**).
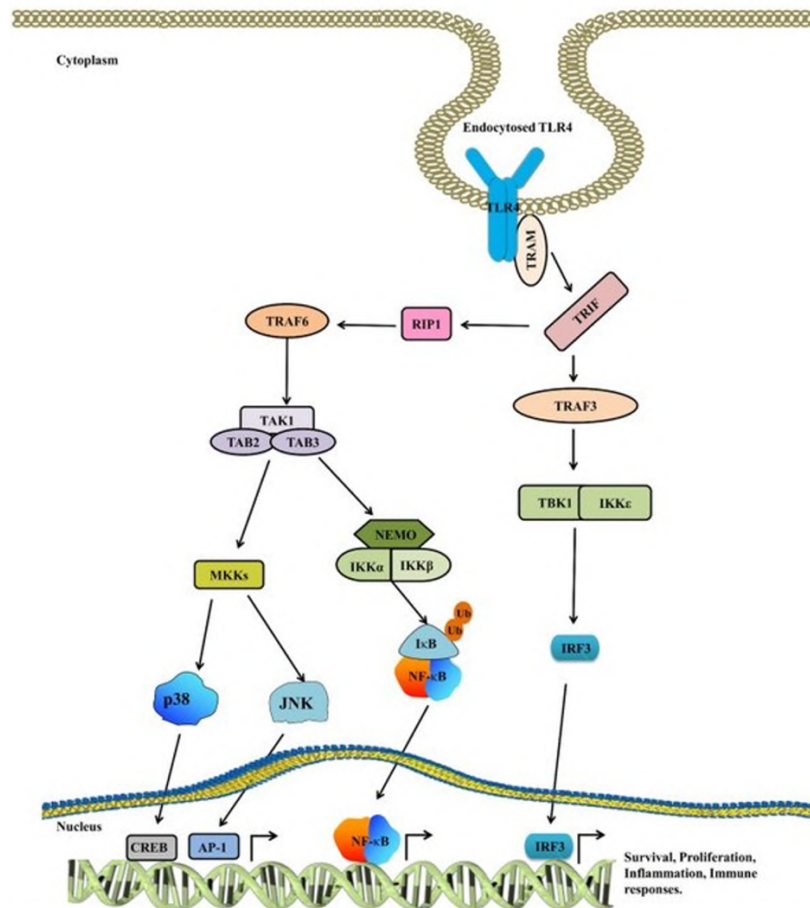
Figure 22. Late NF-κB activation promoted by TRIF-dependent signaling

1.4. Vaccine Adjuvants

Understanding innate immunity is essential for vaccine development. Particularly, using compounds to stimulate innate immune pathways and modulate them can be the key to potentiate an antigen response to a pathogen. In fact, adjuvants are chemical entities that can be added to a vaccine formulation in order to enhance the magnitude and durability of the immune response[158]. Adjuvants have been used for a long time, since the 1920s, with the introduction of alum that is included in vaccines against hepatitis B,

diphtheria, tetanus and pertussis[158]. Although safe to use, its mechanism of action is not clear and thus, it is not possible to tailor the immune response to particular pathogens and antigens[158]. Alum is usually present in the form of aluminum hydroxide or hydroxyphosphate and antigens are adsorbed to these molecules through electrostatic interactions and ligand exchange[159]. It is hypothesized that alum enhances antigen presentation by APCs and that it triggers the NLRP3 inflammasome[159]. Furthermore, alum, as well as other new adjuvant formulations, is thought to increase immunogenicity by promoting the depot effect, which is a term used to described the prolonged retention and sustained release of antigen and adjuvant in the injection site[160]. Over the last decades there has been an increased development and approval of vaccine adjuvants, as shown in **Figure 23.**
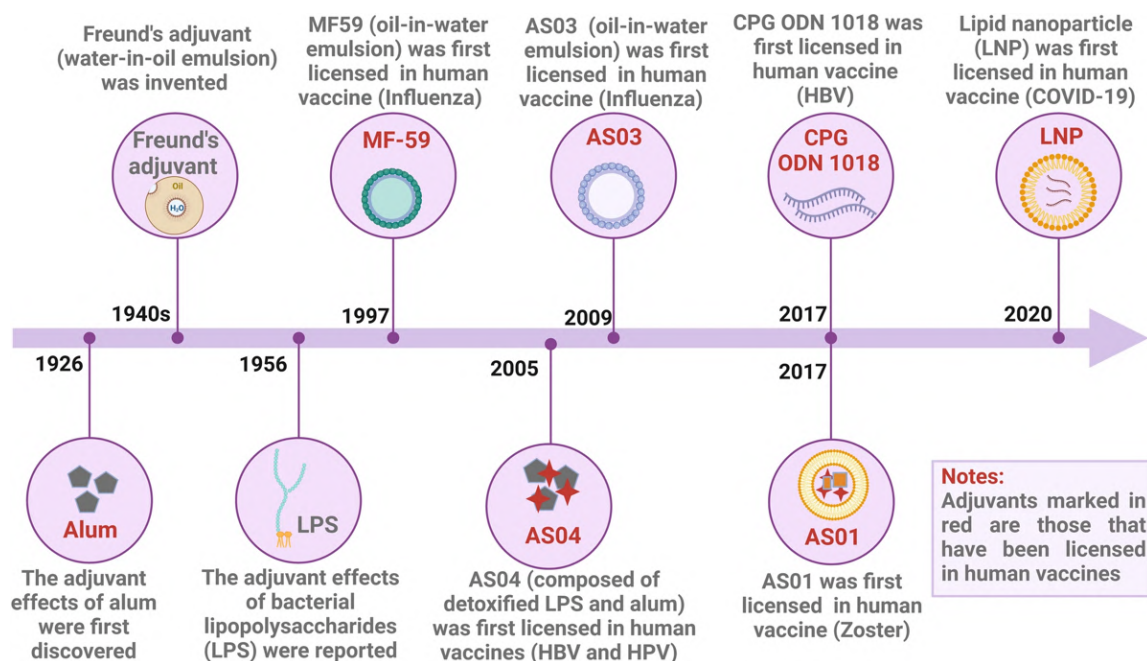
Figure 23. Timeline of adjuvant development[160]

Even though an adjuvant is used to improve the vaccine's activity, its introduction creates safety and compatibility concerns, which makes the understanding of its mechanism of action crucial[42]. An adjuvant should be economically viable, safe, well-tolerated, have good pharmaceutical features and durable shelf-life. There is a newly described condition associated with adjuvants named autoimmune/inflammatory syndrome induced by adjuvants or ASIA[159]. This syndrome describes symptoms associated with adjuvant responses in susceptible individuals and refers mainly to the production of autoantibodies leading to an autoimmune response. This is particularly

observed in formulations containing alum salts[159]. Once again, the need to develop new adjuvants with a clear mechanism of action is highlighted.

Since alum, new adjuvants with different mechanisms of action have been licensed and used in marketed products (**Figure 24**). Adjuvants can be classified either as immunostimulants or delivery systems. The former are molecules that are able to trigger PRRs, such as TLRs, C-type lectins and NOD-like receptors, promoting innate immunity and potentiating immune memory towards the pathogen[160]. Instead, delivery systems facilitate antigen presentation through improved bioavailability and targeted delivery[160]. Nevertheless, some antigen combinations combine the two properties by formulating immunostimulants into delivery systems.

Adjuvant systems (AS) are combinations of immunostimulants with delivery systems. In 2005, AS04, the first AS to be developed, was formulated into the human papilloma virus (HPV) vaccine and commercialized. This adjuvant contains a mixture of MPLA, a TLR4 agonist, adsorbed onto aluminum hydroxide and has been shown to increase antigen-specific T-cells and antibody responses through the production of TLR4-dependent cytokines[161]. Since then, other two AS with different composition were developed. AS03, an oil-in-water emulsion with squalene and α-tocopherol, has been used in H1N1 vaccines and its mechanism of action relies on the perturbation of lipid metabolism leading to monocyte activation[161]. MF59 is another oil-in-water squalene emulsion used in influenza vaccines[159]. On the other hand, AS01 contains a mixture of *Quillaja Saponaria* Molina: fraction 21 (QS-21), a saponin molecule, and MPLA on a liposome formulation. QS-21 is a mixture of two isomeric saponins and it is known to stimulate a Th1 cellular response as well as promote antigen-specific cytotoxic T lymphocytes[162]. Specifically, its mechanism of action is still unknown. It is hypothesized that it can bind to TLR2 and TLR4 and interact with C-type lectins, although its depot effect is also considered to be important for adjuvancy[162]. While it is used in this formulation, QS-21 is not used on its one due to difficulty in production, heterogeneity, instability and dose-limiting toxicity[162]. MPLA will be further discussed in the next section. Overall, AS01 synergically stimulates TLR4-dependent pathways and the NLRP3 inflammasome, leading to cytokine production and Th1 responses. It is currently used in a recombinant zoster vaccine and in a malaria vaccine[161]. It is important to note that, since these adjuvants are already approved and used with safety, they are being

studied in combination with novel antigens in new vaccine formulations, in particularly against AMR bacteria[65]. **Figure 24** shows marketed adjuvants and their proposed mechanism of action.
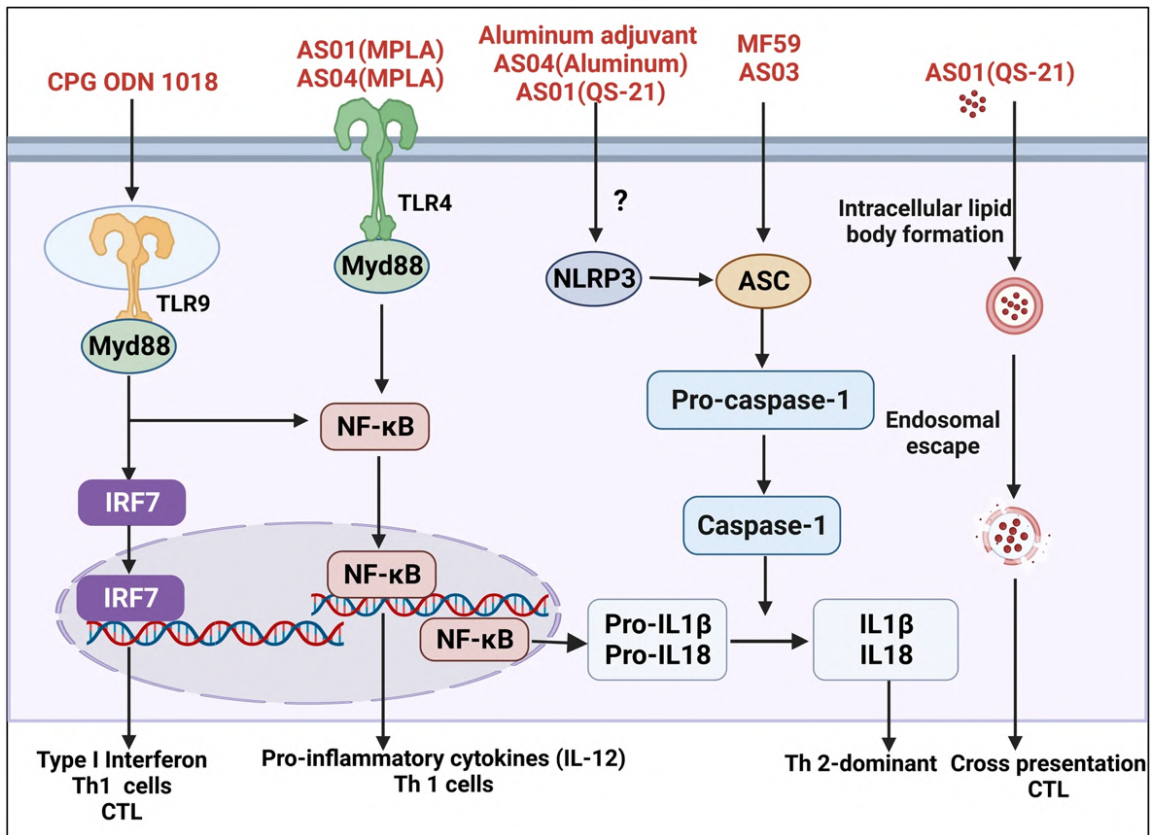
Figure 24. Marketed adjuvants and their proposed mechanism of action[160]

As mentioned before, TLRs agonists trigger a series of intracellular events that lead to the production of different innate immunity effectors and, subsequently, to adaptive immunity modulation. CpG-oligodeoxynucleotides (ODN) is a TLR9 stimulating adjuvant that consists of synthetic DNA molecules containing CpG motifs that are recognized by the receptor[163]. This adjuvant strongly induces Th1 responses and IFN-γ secretion through TLR9 MyD88 signaling. It also facilitates the expression of MHC, CD40 and CD86 on DCs. It is currently used in HEPLISAV-B recombinant hepatitis B vaccine[163]. In the pipeline there are other TLR-directed adjuvants that, even though are not commercialized, have been extensively studied. For example, Poly-IC is a synthetic dsRNA molecule with polyinosinic-polycytidylic acid that targets TLR3 and RIG-I-like receptors[164]. Some discouraging results led to the development of analogs of poly-IC, namely Poly-IC12U that exclusively activates TLR3. IC31 is a TLR9-taregting ODN based on poly-IC, that has also been linked to TLR3 agonism[164]. This compound contains

a single-stranded ODN with dimeric repeats of deoxy-Inosine/deoxy-cytosine combined with antimicrobial peptide KLKL$_5$KLK[164]. IC31 induces potent antigen-specific cytotoxic T cells and strong antibody responses and thus it has been incorporated in tuberculosis vaccines that are currently under development[164]. Imiquimod is a licensed nucleoside analog used for the treatment of warts keratosis and superficial basal cell carcinoma with TLR7 agonistic actvitity[164]. Binding to the receptor induces MyD88-dependent signaling and, consequently, to the expression of pro-inflammatory cytokines and type I IFN, such as IFN-α, TNF and IL-12[164]. It also stimulates a Th1 type response with the promotion of cytotoxic effectors[164]. Similarly, resiquimod is also being studied as a TLR7-targeting vaccine adjuvant. TLR4-targeting adjuvants, such as MPLA and glucopyranosyl lipid A (GLA), will be further discussed on section 1.4.1.

Other structures are also being exploited as possible targets for vaccine adjuvants. For example, activation of intracellular DNA sensing STING, a transmembrane protein, leads to activation of IRF3/7 signaling[165]. Its ligands, cyclic dinucleotides (CDNs), such as 2',3'-cyclic-GMP-AMP (cGAMP) leads to the transcription of different proinflammatory cytokines and type I IFN, particularly IFNβ[165]. As other nucleic acid sensing receptors, it has been shown that this is an important receptor for antiviral responses[158]. While targeting STING is appealing due to its immunostimulatory ability, a major challenge in developing new agonists is its intracellular delivery suggesting the need for new delivery systems[165]. **Figure 25** illustrates some of the above-mentioned adjuvants and their cellular targets.
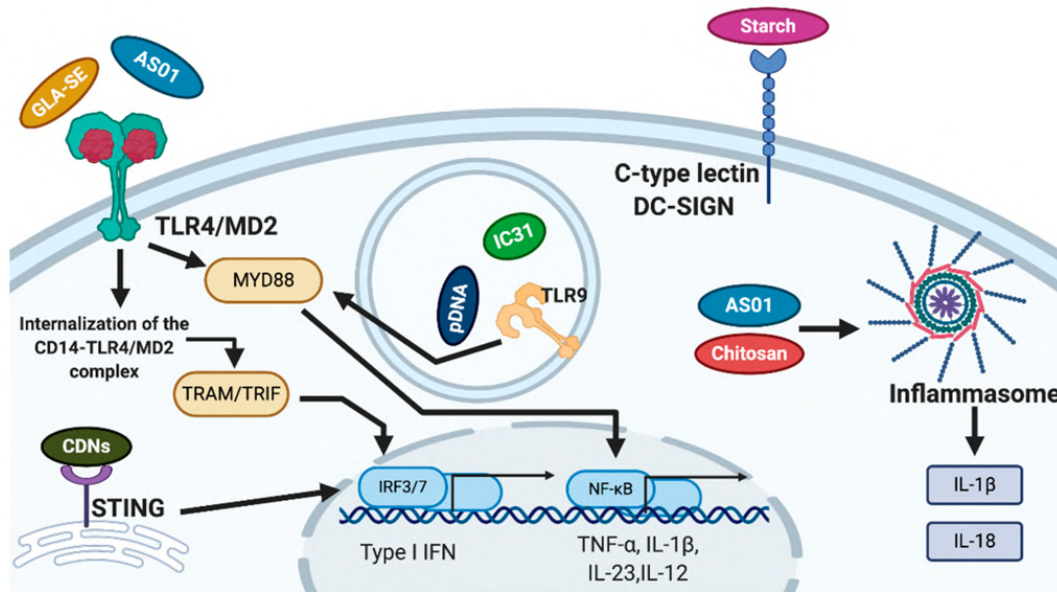
Figure 25. Examples of adjuvants and their proposed mechanism of action

Natural structures are also an important source of vaccine adjuvants due to their resemblance to natural ligands of PRRs. For example, zwitterionic polysaccharide adjuvants are carbohydrate structures isolated from bacteria[166] (**Figure 26**). It is thought that these structures are recognized by TLR2, inducing MyD88-dependent signaling leading to NF-κB activation and cytokine production, namely IL-12 and TNF[166].
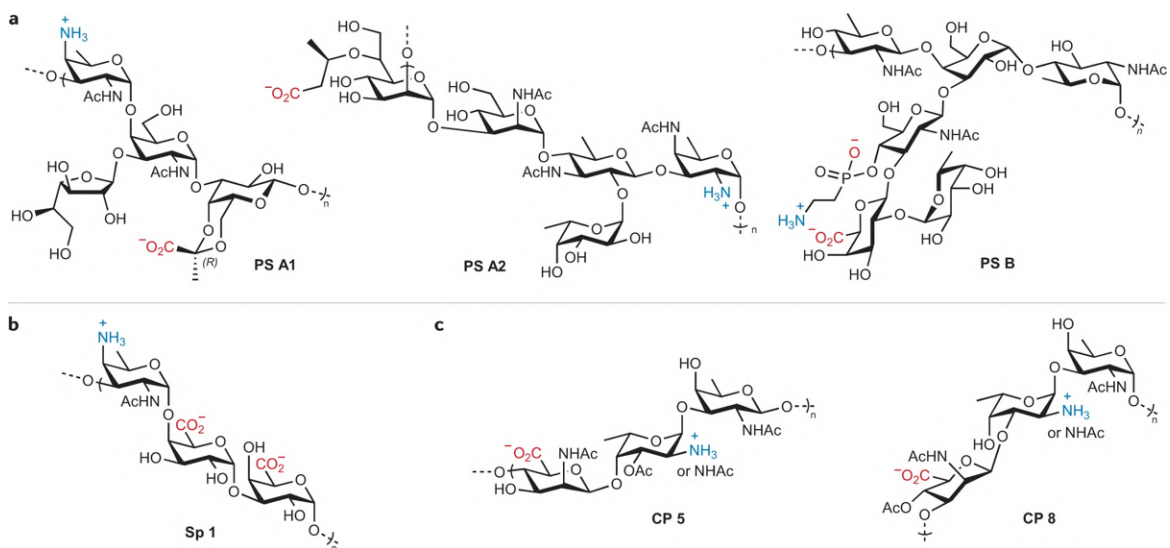
Figure 26. Structure of natural zwitterionic polysaccharides from *Bacteroides fragilis* (a), *Streptococcus pneumoniae (*b) and *Staphylococcus aureus* (c)[166]

Another example of a natural structure used as vaccine adjuvant is chitosan. Chitosan derives from poly β-1,4-*N*-acetyl-D-glucosamine or chitin, and it has demonstrated adjuvant activity by activating the NLRP3 inflammasome after charged-

based interactions or endocytosis that allow for its internalization[167]. Chitosan is particularly interesting for mucosal pathogens since it has been shown to promote Th1, Th17 and IgG2 responses[167]. Starch microparticles have been also studied as a possible adjuvant for BCG vaccines. These particles are recognized by APCs through C-type lectins and are able to induce CD4 and CD8 immune responses directly in the mucosa when administered intransally[168].

As mentioned above, liposomes and lipid nanoparticles belong to the delivery system category of vaccine adjuvants. Although they are already in use, for example as part of the AS01 adjuvant, this continues to be one of the most studied fields in adjuvant development. Liposomes possess several advantages namely biocompatibility, high loading capacity, encapsulation ability and flexibility towards modifications using surface modifiers[169]. Lipid-based carriers can have a contiguous bilayer, like a liposome, or assume micelle-like structure, like lipid nanoparticles that are used in mRNA vaccine platforms[169]. Lipid particles have themselves adjuvant activity since they are able to attract and activate DCs, macrophages and B cells. Nevertheless, their true advantage relies on combining multiple activities and controlling and targeting the release of the adjuvants and antigens[169]. For example, CAF01 is a cationic liposome able to induce Th1 responses on vaccinated mice, in a formulation against TB[170]. Furthermore, CAF01 was formulated with Poly-IC, enhancing the TLR3-dependent immunostimulatory properties of the adjuvant and controlling its release[171].

1.4.1. Vaccine Adjuvants targeting TLR4

LPS-triggered TLR4 signaling is one of the most studied innate immune responses since the discovery of TLR4. Indeed, it is known that TLR4 is able to produce a complex response through its dual signaling, leading to proinflammatory cytokine and type I interferon expression and, consequently, maturation of APCs and T-cell mediated response[172]. LPS itself, as well as its biologically active portion Lipid A, have been used as vaccine adjuvants in different formulations. Particularly, LPS has been studied as an intranasal adjuvant due to its ability to promote extensive Th1 and Th17 responses, making it able to modulate mucosal immunity. These responses are possible due to the stimulation of both MyD88 and TRIF-dependent pathways[173]. Furthermore, LPS has also been used as an adjuvant in allergy immunotherapy[174]. Nevertheless, it is known that LPS

has endotoxin activity and can lead to a exacerbated immune response and to a severe condition named cytokine storm[175].

Accordingly, over the years, efforts were made to detoxify LPS, while retaining TLR4 stimulating activity, in order to develop and effective but safe vaccine adjuvant. MPLA, a disaccharide glycolipid, was the first TLR4-targeted adjuvant to be approved and incorporated in marketed vaccines[176]. MPLA is a detoxified form of LPS from *Salmonella minnesota*, produced using mild acidic conditions leading to the cleavage of Lipid A and hydrolysis of the 1-phosphate group[177]. Interestingly, MPLA stimulates TLR4 in a TRIF-bias way, meaning that it poorly stimulates MyD88-dependent signaling, while it is able to induce TRIF-dependent signaling and corresponding Type I IFN responses and late NF-κB-associated responses[123]. Furthermore, it was also reported that MPLA is able to induce p38 MAPK signaling, which was associated with TNF and IL-10 production[178]. As previously mentioned, MPLA is a component of AS01 and AS04, and its approval has opened the door for the development of new TLR4-directed adjuvants[175].

GLA is a synthetic version of MPLA that showed similar ability to induce immune responses and act as a vaccine adjuvant[179]. Structurally, GLA, due to its synthetic nature, is homogeneous while MPLA, which is extracted from bacteria, shows some structure heterogenicity[180]. MPLA can have variable number of chains and carbons within the chains, while GLA has one structure. This data was confirmed by HPLC and Mass spectrometry[180]. Usually, GLA is formulated in aqueous suspensions, emulsions liposomes or with alum[160]. SLA is another MPLA analog with two shorter carbon chains, C12 instead of C14[181]. Alike GLA, SLA was also formulated in an oil-in-water emulsion to potentiate is immunostimulatory properties (SLA-SE). SLA-SE is able to induce Th1 responses and is able to promote antibody responses in mice, particularly IgG2[181]. Decreasing the lipid chains resulted in better binding energy of the ligand with the TLR4/MD2 receptor[182]. **Figure 27** represents the structure of MPLA, GLA and SLA, with the shorter chains from the latter highlighted in green.
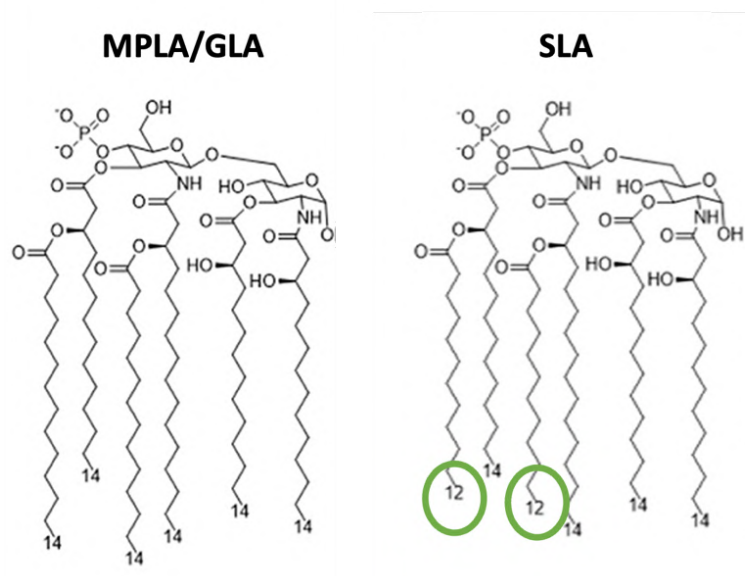
Figure 27. Structure of MPLA, GLA and SLA[183]

Other structures derived from LPS, based on MPLA and its method of extraction, were developed by engineering modifications of *Yersinia pestis* LPS using bacterial enzymatic combinatorial chemistry (BEEC) (**Figure 28**)[184]. This strategy removes or introduces exogenous enzymes and uses temperature changes in order to modify lipid A's biosynthetic pathway, yielding different structures shown in **Figure 28**[184]. After initial screenings, compounds **a** and **f** showed similar results to GLA. The same strategy was used to further develop another Yersinia Pestis modified lipid A adjuvant BECC438. The latter was formulated with a protective antigen against the same bacteria. *In vitro* results showed comparable results to GLA, while *in vivo* assessment revealed a higher ability to stimulate specific IgG[185]. Later, the same technique yielded another adjuvant, BECC470, that has been shown to have promising adjuvant activity in an influenza model[186].

There are other examples of Lipid A mimetics that are being studied as possible vaccine adjuvants. Namely, structures derived from the LPS of commensal bacteria, such as *Alcaligenes faecalis,* have been developed[187]. In fact, this species is responsible for non-harmful activation of the immune system through TLR4 signaling. Thus, Lipid A from *A. faecalis,* which is actually a mixture of three different structures with different number of acyl chains, six, five and four, was investigated. The hexa-acylated structure

was found to be active and demonstrated adjuvant activity when formulated in a intranasal vaccine candidate[187].
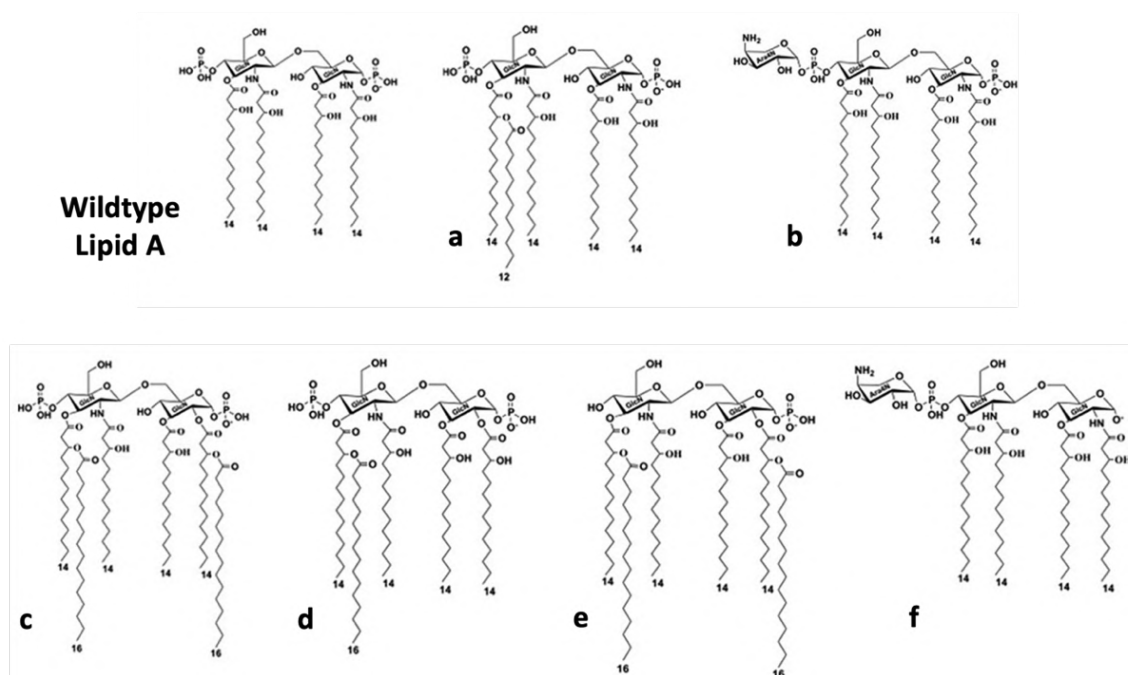
Figure 28. Examples of BEEC generated structures using *Yersinia pestis* non virulent strains[184]

While glycolipid structures were extensively studied due to their resemblance with the natural ligand LPS, there are other compounds being developed as TLR4-agonists that have chemically diverse structures. Namely, E6020, a hexa-acylates structure, has been shown to trigger TLR4 and induce an immune response comparable to MPLA[188] (**Figure 29a**). Another scaffold is pyrimido[5,4-*b*]indoles. These compounds, even though they possess a completely different structure, showed TLR4-stimulating activity[189] (**Figure 29b**). These small molecules are able to bind both to the TLR4 and to the MD2 through electrostatic interactions and hydrogen bonds, triggering NF-κB signaling[189].

Overall, it is clear that there is an interest in continuing to develop new TLR4 agonists, considering the promising results of different scaffolds, glycolipid and non-glycolipid.
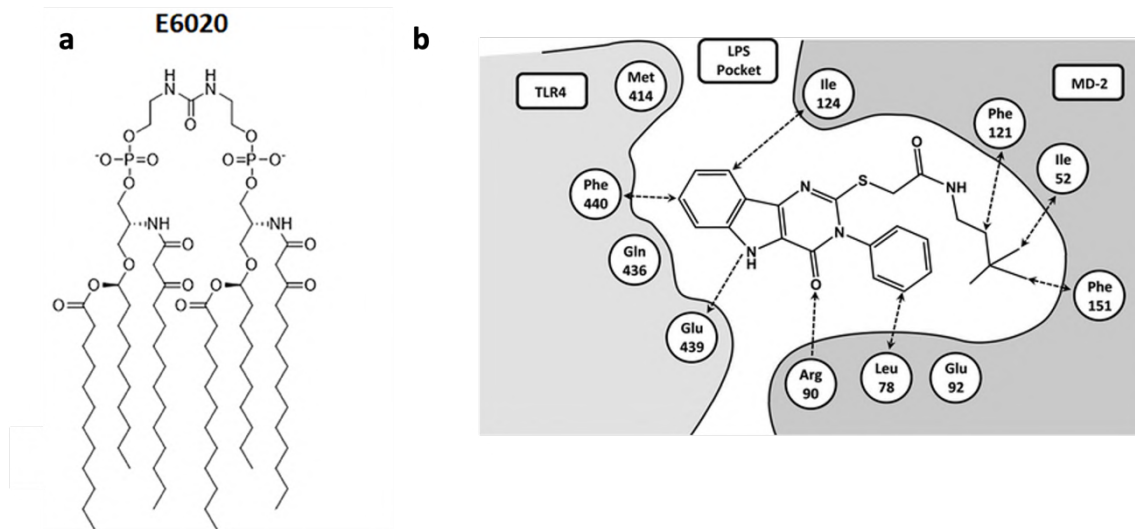
Figure 29. Structure of E6020 (a) and general structure of pyrimido[5,4-*b*]indoles and binding to TLR4/MD2 (b)

2. Aim of the Work

MDR microorganisms are a current burden for global health, leading to significant morbidity and mortality[190]. Particularly, ESKAPE pathogens show multiple mechanisms of resistance, associated with an intrinsic virulence, causing an increase in nosocomial infections especially in immunocompromised patients[191]. With the consistent failure of antibiotics and new emergent resistances, vaccines against these bacteria are a promising strategy to fight AMR. While the discovery of new antigens can be supported by new technologies, such as proteomics and transcriptomics, there is a need to discover new adjuvants in order to potentiate the outcome of new vaccine candidates[192].

The development of new adjuvants was delayed due to a poor understanding of their mechanism of action. Discovery of PRRs, particularly of TLRs, has changed the paradigm and has led to the development of new molecules with the ability to stimulate the innate immune system and modulate acquired immunity[193]. MPLA was the first approved TLR4 agonist and has paved the way for new molecules. Despite their clinical success, the semi-synthesis of MPLA and the synthesis of its synthetic analog GLA are long and complex. Thus, the development of new TLR4-directed adjuvants with shorter synthesis but with comparable or higher immunostimulatory properties and safety is pertinent for vaccine development.

Our group has previously developed new TLR4-directed agonists, named FP compounds, based on a glucosamine scaffold[194]. These compounds were developed considering the lipid X structure, the precursor of lipid A, and other TLR4 agonists such as ONO4007 and SDZ MRL 953 (**Figure 30**). While Lipid X demonstrated antagonistic activity, its structure has served as model for the development of new analogs, both antagonists and agonists, by variating the number of lipophilic chains and substituents[195]. Indeed, ONO4007 and SDZ MRL 953 are lipid X analogs with agonist activity. The former was developed by a Japanese pharmaceutical company and it contains a triacylated sulphonated backbone[196]. While showing promising anticancer activity due to its TNF production in tumor cells, development was halted due to delivery issues[197]. On the other hand, SDZ MRL 953 was developed as simplified synthetic analog of *Salmonella abortus equi*'s Lipid A[198]. It has been found that this compound is able to enhance host defense against pathogens[197] and it has also been studied as anticancer immunotherapy[199].
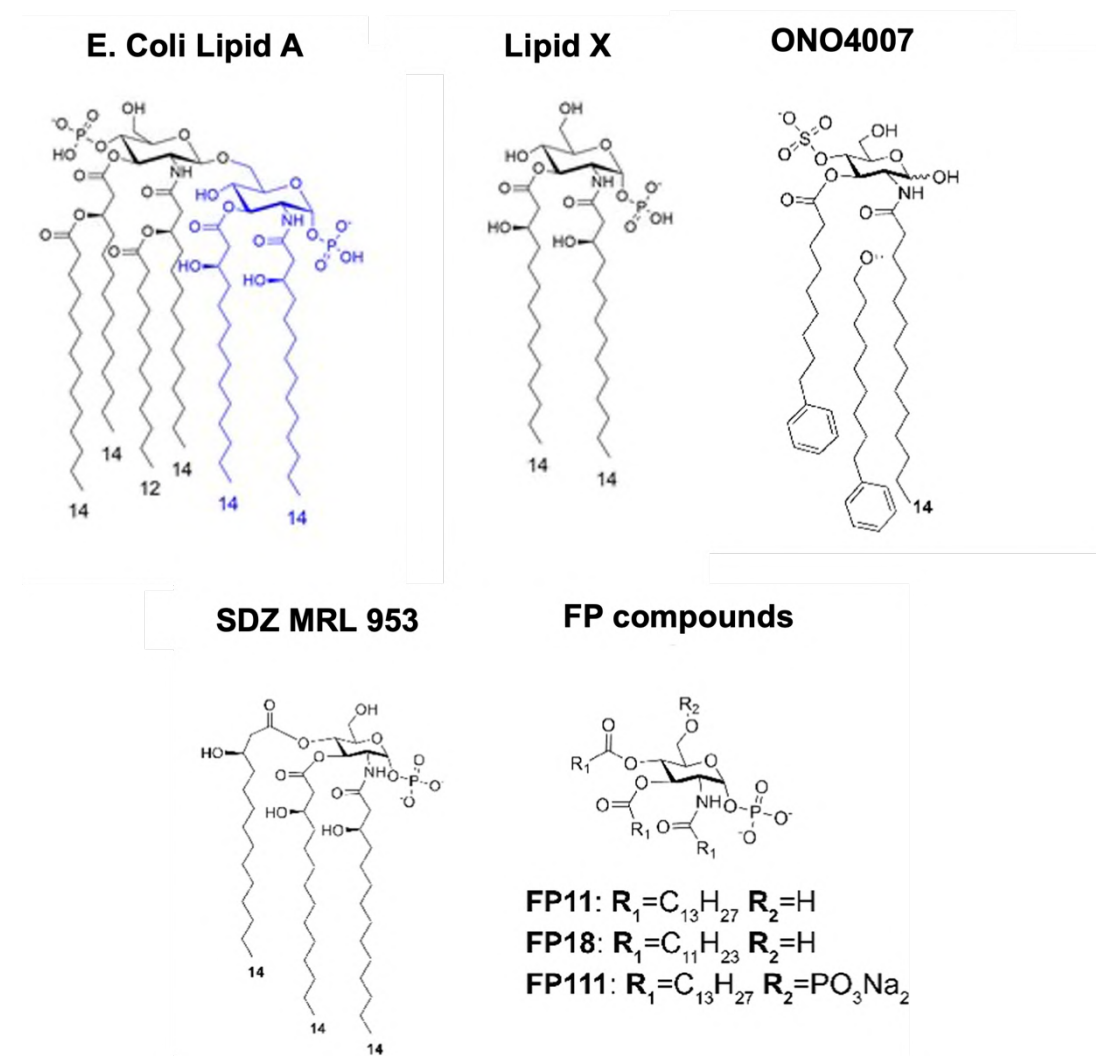
Figure 30. Structures of Lipid A, Lipid X and TLR4 synthetic agonists ONO4007, SDZ MRL 953 and FP compounds

FP11 and FP18 showed TLR4-directed activity, although FP18 demonstrated higher activity when compared to FP11 and comparable activity to MPLA. As MPLA, FP18 showed a bias towards the TRIF pathway, while it was also able to stimulate MyD88 pathway and the NLRP3 inflammasome.

While FP18 showed promising activity, the phosphate in the anomeric position causes chemical instability when functionalization of position C6 was attempted. Accordingly, there was a need to develop new structures in order to increase activity by increasing similarity to LPS and, consequently, the interaction with the TLR4/MD2 receptor.

Therefore, the aim of this work was to design and synthesize new glycolipid TLR4-directed adjuvants and clarify their mechanism of action using different cell-biology

techniques. New TLR4 agonists have been synthesized based on lipid X and its TLR4-stimulating analogs. Their biological characterization was carried out using a human macrophage-like cell line (THP-1 X-Blue derived macrophages) and by employing ELISA and western blot techniques to measure cytokine production and protein expression. High throughput imaging techniques were also used to follow intracellular targets using fluorescence labelling. Additionally, a novel FTIR screening method for proinflammatory compounds was developed using LPS and applied to the project in order to identify new proinflammatory TLR4-stimulating molecules. **Figure 31** illustrates the overall workflow of this PhD project.
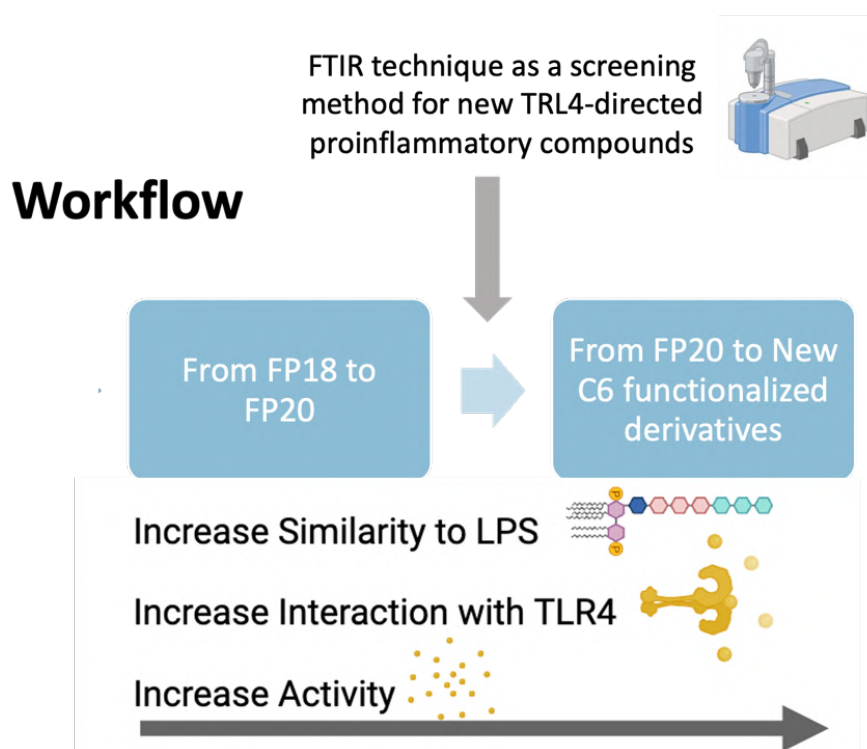
Figure 31. Schematic representation of the PhD project

3. Materials and Methods

3.1. General

All reagents and solvents were purchased from commercial sources and used without further purifications unless stated otherwise. Reactions were carried out under a nitrogen atmosphere unless otherwise noted and were monitored by thin-layer chromatography (TLC) performed over Silica Gel 60 F254 plates (Merck). Flash chromatography purifications were performed on silica gel 60 (40–63 μm) from commercial sources. ^{1}H and ^{13}C NMR spectra of compounds were recorded with a Bruker Advance 400 with TopSpin software, or with an NMR Varian 400 with Vnmrj software. Chemical shifts are reported in parts per million (ppm) relative to the residual solvent; coupling constants are expressed in Hz. The multiplicity in the ^{13}C spectra was deduced by attached proton test (APT) pulse sequence; peaks were assigned with the help of 2D-COSY and 2D-HSQC experiments. Exact masses were recorded with Agilent 6500 Series Q-TOF LC/MS System. Purity of final compounds was >95% as assessed by quantitative NMR analysis.

3.2. Synthesis of FP20 and derivatives
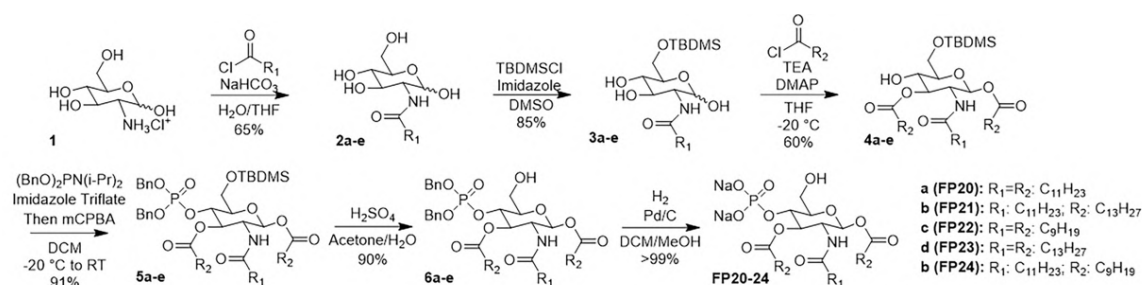
Compounds 2a–e

2-Dodecanamido-2-deoxy-α,β-d-glucopyranose

Glucosamine hydrochloride **1** (10 g, 46.5 mmol, 1 eq.) and NaHCO$_3$ (10.54 g, 126 mmol, 2.7 eq.) were dissolved in water (120 mL). Then, previously dissolved acyl chloride (11.20 g, 51.2 mmol, 1.1 eq.) in THF (120 mL) was added dropwise to the solution at 0 °C. Reaction was stirred for 5 h at RT; a white precipitate was formed in the

reaction flask. Solution was filtered and a white solid was obtained, which was washed with 4 °C water. The solid was resuspended in 75 mL of 0.5 HCl for c.a 30 min and then filtered again and washed with THF. Excess water in the solid was then co-evaporated with toluene under reduced pressure, to obtain the desired products **2a–e** as a white powder in 65% yield (11.10 g) as an anomeric mixture. Compounds were used without further purification.

Compounds 3a–e

2-Dodecanamido-2-deoxy-6-O-tert-butyldimethylsilyl-α,β-d-glucopyranose

To a solution of **2a–e** (3 g, 8.3 mmol, 1 eq.) and imidazole (850 mg, 12.4 mmol, 1.5 eq.) in dimethyl sulfoxide (166 mL, 0.05 M), a solution of TBDMSCl (1.4 g, 9.1 mmol, 1.1 eq.) in DCM (15 mL) was added dropwise under an inert atmosphere in an ice bath. Subsequently, the solution was allowed to return at room temperature and stirred overnight. The reaction, monitored by TLC (DCM/MeOH 9:1), was then stopped and the solution concentrated under reduced pressure. Then, it was diluted with AcOEt and washed three times with NH_4Cl. The organic phase thus obtained was dried with Na_2SO_4, and the solvent was removed by rotavapor. The crude product thus obtained (3.65 g) was resuspended in EtPet at 0 °C for 30 min. Then, the suspension was filtered under vacuum and the desired compound was recovered as a white solid. After filtration, 3.51 g of compounds **3a–e** were obtained, in 85% yield.

Compounds 4a–e

1,3-Di-O-dodecanoyl-2-dodecanamido-2-deoxy-6-O-tert-butyldimethylsilyl-β-d-glucopyranose

Compounds **3a–e** (2.0 g, 4.2 mmol, 1 eq.) were dissolved in anhydrous THF (84 mL, 0.05 M) under an Ar atmosphere. TEA (2.4 mL, 17.2 mmol, 4.1 eq.) and acyl chloride (2.2 mL, 9.2 mmol, 2.2 eq.) were added dropwise to the solution at −20 °C, and then also 4-dimethylaminopyridine (26 mg, 0.2 mmol, 0.05 eq.) was added. The reaction was slowly allowed to return to 0 °C and stirred over 2 h and then controlled by TLC (EtPet/AcOEt 6:4). Subsequently, the solution was diluted in AcOEt and washed with 1 M HCl. The organic phase thus obtained was dried with Na_2SO_4, and the solvent was removed by a rotavapor. The crude product thus obtained (4 g) was purified using Biotage

Isolera LS System (Tol/AcOEt 99:1 to 88:12 over 10 CV). After purification, 2.12 g of compounds **4a–e** was obtained, in 60% yield.

Compounds 5a–e

1,3-Di-O-dodecanoyl-2-dodecanamido-2-deoxy-4-O-(dibenzyl)phospho-6-O-tert-butyldimethylsilyl-β-d-glucopyranose

Compounds **4a–e** (2.12 g, 2.4 mmol, 1 eq.) and imidazole triflate (1.4 g, 5.4 mmol, 2.25 eq.) were dissolved in DCM (121 mL, 0.02 M) under an inert atmosphere. Dibenzyl *N,N*-diisopropylphosphoramidite (1.83 g, 5.3 mmol, 2.2 eq) was added to the solution at 0 °C. The reaction was monitored by TLC (EtPet/acetone 9:1); after 30 min, substrate depletion was detected. Solution was then cooled at −20 °C, and a solution of *meta*-chloroperbenzoic acid (1.66 g, 9.7 mmol, 4 eq.) in 17 mL of DCM was added dropwise. After 30 min, the reaction was allowed to return to RT and left stirring overnight.

After TLC analysis, the reaction was quenched with 15 mL of a saturated $NaHCO_3$ solution and concentrated by a rotavapor. The mixture was then diluted in AcOEt and washed three times with a saturated $NaHCO_3$ solution and three times with a 1 M HCl solution. The organic phase was recovered and dried with Na_2SO_4, and the solvent was removed by rotavapor.

The crude product thus obtained was purified by flash column chromatography (EtPet/acetone 9:1). 2.41 g of pure compounds **5a–e** was obtained as a yellow oil in a 91% yield.

Compounds 6a–e

1,3-Di-O-dodecanoyl-2-dodecanamido-2-deoxy-4-O-(dibenzyl)phospho-β-d-glucopyranose

Compounds **5a–e** (2.41 g, 2.4 mmol, 1 eq.) were dissolved in acetone (48 mL, 0.05 M), and 480 μL (1% v/v) of a 5% v/v solution of H_2SO_4 in H_2O was added at RT. The solution was left stirring for 8 h and monitored by TLC (EtPet/acetone 8:2). After reaction completion, the solution was diluted in AcOEt and washed three times with a saturated $NaHCO_3$ solution. The organic phase thus obtained was dried with Na_2SO_4, and the solvent was removed by rotavapor. The crude product thus obtained was purified by flash

column chromatography (EtPet/acetone 85:15). After purification (2.1 g), compounds **6a–e** were obtained as a white solid in a 90% yield.

Compounds FP20–24

1,3-Di-O-dodecanoyl-2-dodecanamido-2-deoxy-4-O-phospho-β-d-glucopyranose

Compounds **6a–e** (50 mg, 0.05 mmol, 1 eq.) were dissolved in a mixture of DCM (2.5 mL) and MeOH (2.5 mL) and put under an Ar atmosphere. The Pd/C catalyst (10 mg, 20% m/m) was then added to the solution. Gases were then removed from the reaction environment, which was subsequently put under a H_2 atmosphere. The solution was allowed to stir for 2 h, and then H_2 was removed, and reaction monitored by TLC (EtPet/acetone 8:2).

TEA (100 μL, 2.5% v/v) was then added to the reaction, which was stirred for 15 min. The solution was subsequently filtered on syringe filters PALL 4549 T Acrodisc 25 mm with a GF/0.45 μm Nylon to remove the Pd/C catalyst, and solvents were evaporated by a rotavapor. The crude product was resuspended in a DCM/MeOH solution, and IRA 120 H^+ was added. After 30 min of stirring, IRA 120 H^+ was filtered, solvents were removed by a rotavapor, the crude was resuspended in DCM/MeOH, and IRA 120 Na^+ was added. After 30 min stirring, IRA 120 Na^+ was filtered and solvents were removed by a rotavapor.

The crude product was purified through reverse chromatography employing a C4-functionalized column (PUREZZA-Sphera Plus Standard Flash Cartridge C4─25 μm, size 25 g) in the Biotage Isolera LS System (gradient: H_2O/THF 70:30 to 15:85 over 10 CV with 1% of an aqueous solution of Et_3NHCO_3 at pH 7.4). 45 mg of **FP20–24** was obtained as a white powder in a quantitative yield.

3.3. Cryo-EM sample preparation and acquisition

Prior to vitrification, FP20 was dissolved in 100 mM phosphate buffer (pH 7.4) solution with 16% of DMSO to a final concentration of 0.65 mg/mL. 4 μL of the sample were then applied onto a 200-mesh Quantifoil R 2/2 copper grid and vitrified using a LEICA EM GP2 plunge freezer (Leica). 2D images were collected using a JEOL JEM-2200 transmission electron microscope (JEOL Japan) operating at 200 kV in cryo-

conditions and equipped with a K2 Summit direct detection camera (GATAN). Different magnifications were tested ranging from 2000× to 30,000×. The images collected at high magnification (30,000×) resulted into a 0.13 nm pixel size at the specimen.

3.4. Cell Cultures

THP-1-XBlue™ cells (InvivoGen) were cultured in RPMI 1640 medium, 2 mM L-glutamine, 10% heat-inactivated fetal bovine serum, 100 U/ml-100 μg/ml Penicillin-Streptomycin. Cells were maintained in a humidified 37°C, 5% CO_2 incubator. Cells were subcultured every two days. Exponentially growing cells were adjusted to 0.5-0.7 × 10^6/mL according to the routine procedure. RAW-Blue™, HEK-Blue™-hTLR4 and HEK-Blue™-hTLR2 cells (InvivoGen) were maintained in DMEM, 2 mM L-glutamine, 10% heat-inactivated fetal bovine serum, 100 U/ml-100 μg/ml Penicillin- Streptomycin and subcultured at 80% confluence. To maintain selection pressure, 100 μg/mL of Zeocin™ and HEK-Blue™ Selection (InvivoGen) were added to the growth medium of THP1-XBlue™, RAW-Blue™ and HEK-Blue™ cells, respectively, every other passage. Media and supplements were purchased from Euroclone unless otherwise stated. For experimental procedures, HEK-Blue™ cells and RAW-Blue™ cells were plated at a density of 0.4 × 10^4 cells/well while THP-1 X-Blue™ were seeded at a density of 0.4 × 10^6 cells/mL and plated using 180 μL/well (96-well-plate), 1 mL/well (24-well-plate) 1.5 mL/well (12 well-plate), and 3 mL/well (6 well-plate).

3.5. THP-1 derived macrophages differentiation from THP-1-XBlue™

THP-1-derived macrophages (TDM) were generated from THP-1-XBlue™ monocytic cells (0.4 × 10^6 cells/ml) by exposure to 100 ng/mL of phorbol 12-myristate-13-acetate (PMA) (InvivoGen). Aliquots (180 μl/well) of the cell suspensions were seeded into a 96-well plate before culture at 37°C, 5% CO_2. Following 72 h of differentiation, medium was removed and replaced with fresh medium, in absence of PMA, prior to further treatments. Monocyte-to-macrophage differentiation was assessed by optical microscopy inspection. Macrophage-like cells adhered to the support and displayed a flattened and elongated morphology compared to floating round-shaped monocytes.

3.6.   Cell Viability Assay (MTT)

Cells were treated with increasing concentrations of the tested compound. After 16-18 h, cell supernatants were removed and cell viability was assessed by MTT assay, according to the described method[200]. This colorimetric assay relies on the reduction 3-(4,5- dimethylthiazol-2-yl)-2,5-diphenyltetrazolium bromide (MTT) (Sigma-Aldrich) to measure cellular metabolic activity as an indicator of cell viability. Viable cells contain NAD(P)H-dependent oxidoreductase enzymes which reduce the MTT reagent to formazan, an insoluble crystalline product with a deep purple color. After 4 h incubation with the MTT solution at 37 °C, formazan crystals are then dissolved using a solubilizing solution and absorbance is measured at 570 nm using a plate- reader. 100% cell viability was attributed to the non-treated wells and cell viability of the treated wells was calculated in respect to it.

3.7.   Detection of AP-1 and NF-κB activation (SEAP assay)

THP-1-XBlue[TM] cells were specifically designed for monitoring the AP-1/NF-κB signal transduction pathway. THP-1-XBlue[TM] were derived from the human THP-1 monocyte cell line by stable integration of an AP-1/NF-κB-inducible secreted embryonic alkaline phosphatase (SEAP) reporter construct. THP-1-XBlue[TM] cells are highly responsive to TLR4 agonists that trigger the NF-κB pathway. HEK-Blue[TM] hTLR4 cells and HEK-Blue[TM] hTLR2 were obtained by transfection of the human TLR4 or human TLR2 receptor, respectively, and an inducible SEAP reporter gene into HEK293 cells. HEK-Blue[TM] hTLR4 cells were also co-transfected with MD-2 and CD14 co- receptor genes, RAW-Blue[TM] cells are derived from the murine RAW 264.7 macrophages with chromosomal integration of a SEAP reporter construct inducible by AP-1/NF-κB. In general, cell supernatants were collected after 16-18 h. Monitoring of NF-κB activation by determining the activity of SEAP in the cell culture supernatant, was assessed with QUANTI-Blue[TM] (InvivoGen) reagent according to the manufacturer's instruction. Briefly, 50 μL of the supernatants of SEAP-expressing cells were incubated with 180 μL of QUANTI- Blue[TM] substrate in a 96-well plate for $0.5 - 4$ h at 37 °C, then optical density (OD) was measured at 630 nm. Positive controls were S-LPS from *Salmonella minnesota* (Innaxon) and MPLA from *Salmonella minnesota* (Innaxon). 100% SEAP expression was

attributed to the positive control S-LPS and SEAP expression of treated wells was calculated in respect to it.

3.8.   Enzyme-linked Immunosorbent Assay (ELISA)

Pro-inflammatory cytokines released in the medium by human macrophage-like cells were measured by ELISA assays. Generally, TDM were treated for 6 or 18h, depending on the experiment. At defined time points of incubation, cell culture supernatants were collected and stored at −20 °C. Samples were analyzed in at least duplicate of three independent experiments. The concentrations of IL- 1β, IL-6 and TNF were detected using commercial ELISA kits according to manufacturer's instructions (DuoSet® ELISA Development Systems, R&D Systems). Briefly, 100 µl of standards and samples were added in respective wells of 96-well NUNC™ antibody coated plate and incubate for 2 h. After incubation and washing steps, detection antibodies were added for 2 h followed by same washing steps, followed by a 20 min incubation with Streptavidin-HRP. Then substrate solution was added in each well followed by addition of stop solution. The optical density of each well was determined using a microplate reader set to 450 nm (wavelength correction: 570 nm). The concentration of cytokines was calculated using a standard curve calculated using the standards.

3.9.   FTIR cell stimulation and Treatment

THP-1 X-Blue™ monocytes were seeded in 100 mm cell culture dishes (Corning), 5×10^6 cells per dish in 10 mL of medium and differentiated to TDM by exposure to 100 ng/mL PMA (InvivoGen) for 72 h. Following differentiation, the PMA containing medium was removed and replaced by PMA-free fresh medium immediately prior to treatment. Then, TDM were stimulated with 100 ng/mL of Escherichia coli 055:B5 LPS (Sigma-Aldrich) or the tested compound throughout different exposure periods: 15 min, 3 h and 24 h. After exposure to treatment, dishes were placed on ice and the medium removed. Cells were then washed with PBS (Euroclone), scraped using a cell scraper and collected into centrifuge tubes. After centrifugation at 4 °C for 10 min at approximately 125× g, PBS was discarded and cell pellets were resuspended in physiological solution (NaCl 0.9%) for further centrifugation at 4 °C, 5 min at 125× g. This washing step was repeated 3 times to ensure no medium contamination. Afterwards live cells were resuspended in 10 µL of physiological solution immediately prior to FTIR measurements.

3.10. Immunofluorescence Analysis

TDM (2×10^4 cells/well) were seeded into PhenoPlate 96-well, black, optically clear flat-bottom, poly-d-lysine-coated microplates (PerkinElmer Inc), where they were exposed to PMA. After differentiation, cell culture media were replaced with either fresh RPMI (NT) or RPMI containing 100 ng/mL of *E. coli* 055:B5 LPS or the tested compound. At the end of the time course treatment (0–4 h), cells were fixed with paraformaldehyde 4% (Sigma-Aldrich) and permeabilized with 0.5% Triton X-100 (Sigma-Aldrich) solution or fixed and permeabilized with ice-cold 100% methanol (according to the antibody's manufacturer's instructions). Then, blocking was performed using 1× PBS/5% BSA/0.3% Triton X-100. Subsequently, cells were labeled with NF-κB p65 XP Rabbit mAb (1:400; #8242, Cell Signaling Technology, Inc.) or Phospho-IRF-3 (Ser386) XP Rabbit mAb (1:400; #E7J8G, Cell Signaling Technology, Inc.). Cells were then tagged with PhenoVue Fluor 568 conjugated anti-rabbit secondary antibody (#2GXRB568C1, PerkinElmer Inc.) to allow target visualization. Nuclei were counter-labeled with PhenoVue Hoechst 33342 Nuclear Stain (#CP71, PerkinElmer Inc.). Images were acquired using the Operetta CLS High-Content Analysis System and analyzed by using the Harmony 4.5 software (PerkinElmer Inc.).

3.11. Protein Extraction and Western Blot Analysis

TDM were plated into 12-well plates at a density of 0.4×10^6 cells/well. Cells were treated for 0 - 4 h with the tested compound or the positive control S-LPS. For protein extraction, cells were washed with 1 mL of PBS and then lysate adding 80 μL of RIPA Buffer (#9806, Cell Signalling Technology, Inc.), containing a protein inhibitor cocktail mixture (SIGMAFAST Protease Inhibitor Cocktail Tablet, S8820, Sigma-Aldrich) and a phosphatase inhibitor cocktail mixture (Phosphatase Inhibitor Cocktail (100X) #5870, Cell Signalling Technology, Inc.), and incubated for 30 min on ice. Then, the whole cell lysates were collected and centrifuged for membrane removal. Protein concentration was measured by spectrophotometric analysis using the Pierce™ BCA Protein Assay Kit (#23227, Thermo Scientific™) according to manufacturer instructions. Cell lysates were resuspended in the Laemmli buffer and denatured for 5 min at 100 ºC. Cell extracts were separated using 10% Mini-Protean TGX Stain-Free Gels reagent kit (Bio-Rad Laboratories) and transferred to nitrocellulose membranes using Trans-Blot Turbo

Transfer System (Bio-Rad Laboratories). Antibodies against anti-phospho-p38 MAPK (Thr180/Tyr182) (CST # D3F9 diluted 1:1000), anti-IκBα (L35A5) Mouse mAb (CST #4814 diluted 1:1000), anti-phospho NF-κB (Ser536) (93H1) Rabbit mAb (CST #3033 diluted 1:1000), anti-phospho-IRF-3 (1:500 dilution/E7J8G, Cell Signalling Technology, Inc.), anti-phospho-STAT1 (1:1000 dilution/#9167, Cell Signalling Technology, Inc.) and anti-β-actin (13E5) rabbit mAb (CST #4970 diluted 1:1000). were diluted in 0.1% TBS-Tween 20 (TBS-T) buffer containing 5% BSA and applied to membranes, followed by overnight incubation at 4°C. The next day, membranes were washed three times with TBS-Tween for 5 min and incubated for 1 h with anti-Rabbit IgG and HRP-linked secondary antibody (Cell Signaling #7074, diluted 1:2000) or anti-Mouse IgG and HRP-linked secondary antibody (Cell Signaling #7076, diluted 1:2000). The antigen–antibody complexes were then detected using ECL Star Enhanced Chemiluminescent Substrate (#EMP001005, Euroclone) or LiteAblot Turbo Extra- Sensitive Chemiluminescent Substrate (#EMP012001, Euroclone). Quantitative densitometry of bands was carried out through ChemiDoc system (Bio-Rad Laboratories), and the quantification of the signal was performed by ImageJ.

3.12. Statistical Analysis

Data related to biological assays were analyzed using GraphPad Prism software (ver.9.0.2 and 10.0.2, GraphPad Software Inc.) and the results were shown as means ± standard error of the mean (SEM). Data obtained in three or more independent experiments were compared by one-way analysis of variance (ANOVA) followed by post hoc Dunnett's test. Differences between samples were considered statistically significant when $p < 0.05$. Two groups of data were compared using Student's t-test (statistically different when, $p < 0.05$).

4. Results and Discussion

This section will be dedicated to the discussion of experimental results obtained throughout the PhD. It is organized into five chapters that follow the workflow described in section 2. The first chapter focuses to the synthesis and development of FP20 using a multidisciplinary approach. *In vitro* and *in vivo* data will be presented as well as computational data and Cryo-EM results that, all together, allow for a complete characterization of this series of new TLR4-directing vaccine adjuvants.

The second chapter is dedicated to the design and development of new glycosylated derivatives of FP20. This section will focus on the challenges of glycosylating position C6 of the glycolipid and how they were overcome to achieve a new library of disaccharide compounds. Preliminary *in vitro* and *in vivo* characterization of these compounds will be also reported.

The third chapter continues to be focused on C6 functionalized FP20 derivatives. In this section FP20Hmp, a molecule containing a dihydroxyl-propionic acid derivative in position C6, will be described. This molecule was characterized both *in vivo* and *in vitro* and its mechanism of action was clarified. Furthermore, FP20Hmp was formulated with PpiC, a *E. faecium* antigen, to form a vaccine candidate. This formulation was tested using a rabbit model and the production of protective antibodies was evaluated.

Finally, chapter four will describe a new FTIR approach for screening of proinflammatory TLR4-targeting compounds. This analysis provides an untargeted approach to identify the most significant spectral components affected by the treatment. LPS markers were identified, and the results are reported.

CHAPTER I

New glucosamine-based TLR4 agonists :

The FP20 series

Adapted from: Alessio Romerio*, Nicole Gotri*, **Ana Rita Franco***, Valentina Artusa, Mohammed Monsoor Shaik, Samuel T. Pasco, Unai Atxabal et al. "New Glucosamine-Based TLR4 Agonists: Design, Synthesis, Mechanism of Action, and In Vivo Activity as Vaccine Adjuvants." Journal of Medicinal Chemistry 66, no. 4 (2023): 3010-3029. https://doi.org/10.1021/acs.jmedchem.2c01998

*co-authors

Author contribution: Contributed to the design of the study. Performed experimental work at the exception of the dynamic light scattering analysis, Cryo-EM acquisition, molecular docking studies and *in vivo* analysis. Participated in the development of the Cryo-EM method. Contributed to the writing of most of the manuscript.

4.1. Background

Vaccination is one of the most successful public health achievements ever carried out and continues to have a large impact in preventing the spread of infectious diseases worldwide[201,202]. The most recent example of vaccines' success was the Covid-19 pandemic and the impact of vaccination in the decrease of disease burden worldwide[203].

Subunit vaccines contain specific purified pathogen antigens and show an improved safety profile compared with whole-pathogen vaccines, by eliminating the risk of incomplete inactivation[45,204,205]. They are also often less immunogenic and require combination with adjuvants to enhance, accelerate and prolong antigen-specific immune responses by triggering and modulating both the innate and adaptive immunity.[206,207].

Adjuvants also allow the decrease in antigen dose, reduce booster immunizations, generate more rapid and durable immune responses, and increase the effectiveness of vaccines in poor responders. TLR4 agonist MPLA is a detoxified *S. minnesota* R595 lipid A analogue obtained through hydrolysis of the C1-phosphate and (R)-3-hydroxytetradecanoyl groups[208]. The lack of the C1 phosphate group allows it to maintain its immunostimulanting properties while eliminating toxicity. Its activity, as well as that of its synthetic analogue GLA, is based on TLR4 stimulation that results in promotion of Th1 biased immune response[179,180,206]. Despite its good activity and widespread use, MPLA synthesis is challenging (>25 steps, including stereoselective reactions)[209].

Due to the reduced chemical variety of approved adjuvants and the lack of clarification of their mechanism of action, there is still a pressing need for novel, potent and less toxic adjuvants, and new formulations for use in subunit vaccines. The accumulating knowledge in PRRs, as it is the case of TLR4, has led to the development of new adjuvants that target these receptors in immune cells.[158]

Recently, it has been demonstrated that many clinical approved adjuvants, including alum and combinatorial vaccine adjuvants AS01 and AS04 promote immunogenicity also through inflammasome-mediated signalling, activating the NLRP3 inflammasome which leads to the activation of caspase-1, resulting in cleavage of pro-IL-1β and pro-IL-18 and secretion of their mature forms[167]. Importantly, the IL-1 family cytokines are important

for T cell activation and memory cell formation which is crucial for the achievement of immune protection[210].

We recently reported the activity as vaccine adjuvants of two structurally simplified MPLA analogues, the FP11 and FP18 molecules (**Figure 32**), whose chemical structure is composed by the glucosamine monosaccharide bearing three fatty acid chains and one phosphate group in C1[194].
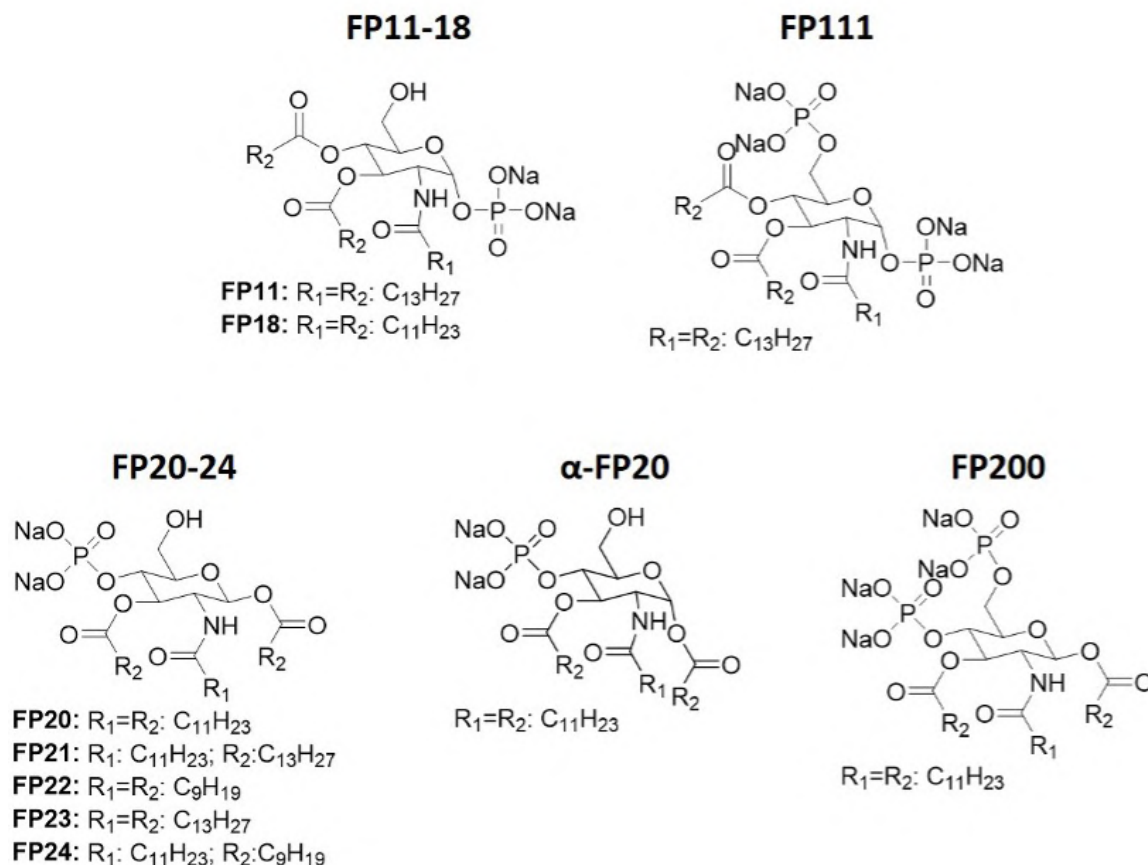
Figure 32. Structures of TLR4 agonists FP11 and 18 and new derivatives FP20-24, α-FP20 and FP200

Despite their simplified monosaccharide structures when compared to disaccharide lipid A and MPLA, the FP molecules, in particular FP18, strongly activate both MyD88- and TRAM/TRIF-dependent pathways, leading respectively to production of TNF, IL-6 and IFN-β. FP18 also activates the NLRP3 inflammasome thus inducing IL-1β maturation and release. Moreover, OVA immunisation experiments showed that FP18 has adjuvant activity similar to MPL[194]. The presence of an anomeric phosphate, that is a good leaving group, causes chemical instability of FP18-type compounds. We then designed a new series of triacylated glucosamine derivatives in which the C1 phosphate is moved to C4 position.

4.2. Experimental Design

Compounds FP20-24 present variable chain lengths, with the anomeric acyl chain always in the beta-configuration. To better assess the structure-activity relationship (SAR), we also designed and synthesised a compound with anomeric acyl chain in the alfa configuration (α-FP20) and a molecule with both C4 and C6 positions phosphorylated (FP200). Cryo-EM and dynamic light scattering techniques were used to study the aggregation properties of FP20.

Molecular Docking simulations were performed to understand how chain length, chain configuration and number of phosphates would alter the ability of FP20 derivatives to bind to TLR4/MD2 receptor. In parallel, cell studies were performed in TDM to further understand the SAR of this library of compounds. Mechanism of action studies were then performed on FP20 to clarify how this TLR4-agonist works and the type of response that it triggers. Considering the results obtained *in vitro*, FP20 was then formulated with OVA and injected into mice in a two immunization approach, to further understand its possibility to be developed as a new vaccine adjuvant.

4.3. Results and Discussion

4.3.1. Chemical Synthesis

Compounds FP20-24 were obtained by means of a six-steps synthesis (**Figure 33 a**). Commercially available glucosamine hydrochloride was acylated on the amino group in position C2-with different acyl chlorides, obtaining compounds **2**, which were regioselectivity protected in C6 position as *tert*-butyldimethylsylyl (TBDMS) ethers, obtaining compounds **3**. The acylation of compounds **3** by reaction with acyl chlorides in the presence of triethylamine (TEA) and *N,N*-dimethylaminopyridine (DMAP) in THF, at low temperature, afforded compounds **8** with anomeric lipid chains in the beta configuration. The regio- and stereoselectivity observed is due to the combination of steric effects (TBDMS in C6 hindering position C4), electronic effects (increased nucleophilicity of beta-anomer) and solvent effects (the dipolar moment of the solvent THF partially suppress the alpha effect). Compounds **4a-e** are then phosphorylated on C4 position through the phosphite insertion strategy using dibenzyl *N,N*-diisopropylphosphoramidite, giving compounds **5a-e** that were desylylated in diluted

acids and then debenzylated by catalytic hydrogenation thus obtaining the final compounds FP 20-24. The overall yield was about 30% for all compounds.
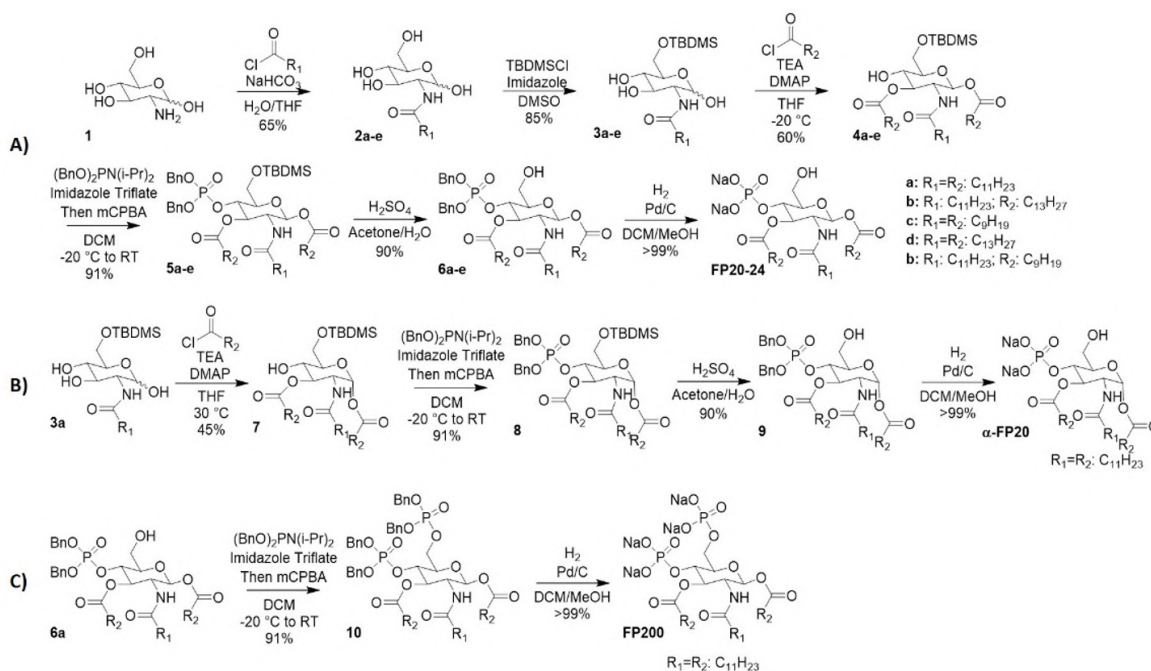
Figure 33. (A) Synthetic pathway to compounds FP20-24, (B) to compound α-FP20, which can be obtained starting from intermediate 3a, and (C) to compounds FP200-203, which can be obtained starting from intermediate 10a.

This synthetic pathway is shorter than the previously published one for FP11 and FP18 compounds[194], as well as more cost effective because it only requires 3 purification steps instead of the 7 required for FP18. Furthermore, FP20 synthesis also requires 3 less steps than FP18 and avoids the large use of toxic solvents (e.g., pyridine, DMF) used in the previous synthesis. By means of the same strategy, and changing the conditions (temperature, concentration, and amount of catalyst) of acylation of compound **3a**, α-FP20 was obtained. (**Figure 33 b**). Compound FP200 was obtained by phosphorylating compound **6a**, then deprotecting compound **10** by catalytic hydrogenation, yielding product 14 with a 26% overall yield (**Figure 33 c**).

4.3.2. Cryogenic Electron Microscopy (Cryo-EM) and Dynamic Light Scattering (DLS)

The aggregation behaviour in solution of lipid A, lipid X and their synthetic analogues strongly influences the potency of TLR4 agonists, so that it has been stated that aggregates are the biologically active units of endotoxin[211]. It is therefore important to know the aggregation properties in aqueous environment of this new family of

compounds. In previous studies carried out with monosaccharide glycolipids derived from lipid X, such as in the case of FP7 glycolipid[212], a critical micelle concentration (CMC) of 9 μM was found. Compound FP15, bearing two succinate esters instead of phosphates in C1 and C4 positions, formed spherical and homogeneous small unilamellar vesicles (SUVs)[213]. The different disposition of fatty acids and phosphate groups in the FP20-series compared to FP11, affected the aggregation properties. A CMC value lower than 5 μM was found for FP20, since the formation of large aggregates could be observed even at such low concentrations. Simultaneously, DLS data indicated a CMC value between 1,87-3,75 μM, much lower than any other synthetic glycolipid and even lower than the parent lipid X (**Figure 34**). Furthermore, DLS allowed the calculation of the hydrodynamic diameter of FP20 particles. Particles with a diameter of about 100 nm could be identified in solution when a concentration between 15 μM and 3.75 μM was used.
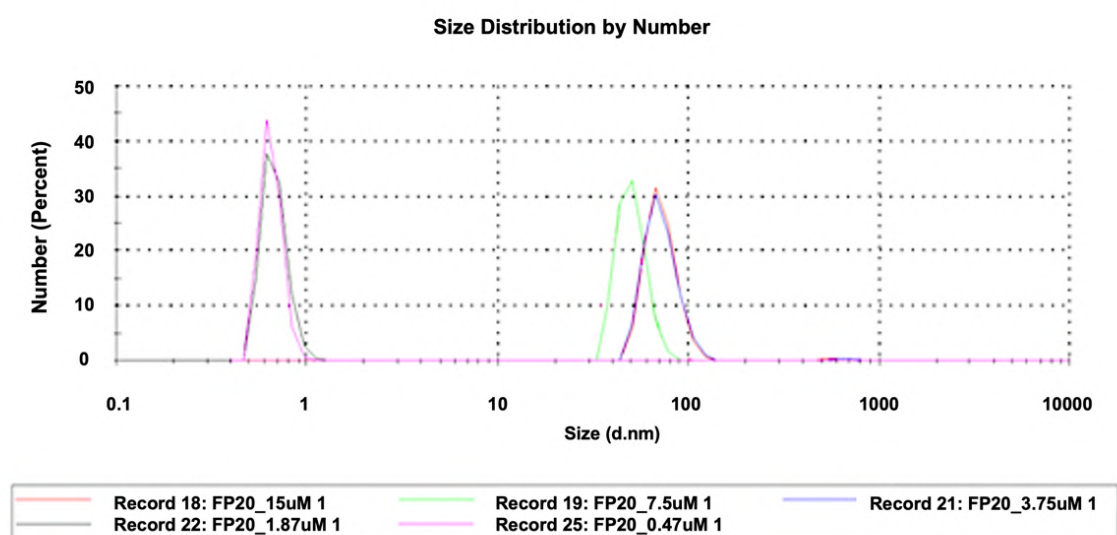
Figure 34. Detection of the hydrodynamic diameter of FP20 at different conditions in solution using DLS

FP20 was selected as a model compound for transmission cryo-electron microscopy studies (**Figure 35**). Collected 2D images using glycolipid concentrations of 0.8 and 1.0 mM respectively, showed few supramolecular structures. Some of these structures organized as large unilamellar vesicles (LUV) with a diameter ranging from about 130 to 400 nm, and some with polygonal shape (**Figure 35 A-B**). Others were assembling in cylindrical vesicles with different lengths and in bilayer sheets (**Figure 35 B-C**). When lower concentrations of the glycolipid FP20 were used in DLS experiments, no large aggregates could be detected. The combined cryo-EM and DLS results might indicate

that at lower concentrations the FP20 leans towards the formation SUVs, but when the concentration is increased then higher order aggregates, such as LUV and/or cylindrical vesicles start forming simultaneously.
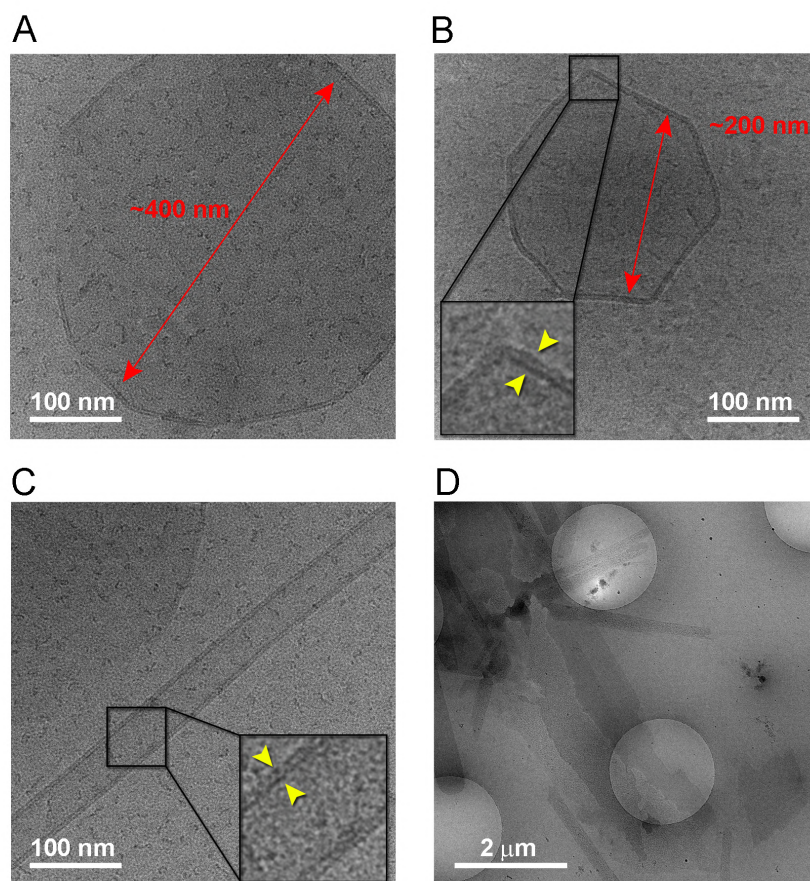
Figure 35. Cryo-EM images of FP20 supramolecular structures formed at a concentration of 0.65 mg/mL. (A) LUV; (B) polygonal LUV; (C) cylindrical vesicle and LUV; (D) low magnification view of large assemblies presents on the TEM grid.

4.3.3. TLR4 selectivity studies in HEK-Blue™ hTLR4 and HEK-Blue™ hTLR2

The selectivity of compounds FP20-24 towards human TLR4 was investigated using specific HEK reporter cell lines. HEK-Blue™ hTLR4 and HEK-Blue™ hTLR2 are cell lines designed to study the activation of human TLR4 and TLR2 receptors, respectively, by monitoring the activation of transcription factors NF-κB and AP-1. Stimulation with TLR4 (HEK-Blue hTLR4) or TLR2 ligands (HEK-Blue hTLR2) activates NF-κB and AP- 1, inducing the production and release of the SEAP in the extracellular environment. SEAP release can then be measured using a colorimetric assay, QUANTI-Blue™ which relies on the ability of SEAP to process its substrate generating

a chromogenic product whose wavelength of maximum absorbance is 630 nm. HEK-Blue™ hTLR4 (**Figure 36 A**) and HEK-Blue™ hTLR2 (**Figure 36 B**) were treated with increasing concentrations of FP20-24 (0,1-25 μM) and incubated for 18h. S-LPS from *S. minnesota* and MPLA were used as positive controls for TLR4 activation while Pam$_2$CSK$_4$ was used as a positive control for the TLR2-mediated response. As shown in **Figure 36**, all compounds showed selective activity towards TLR4 and no activity on TLR2.
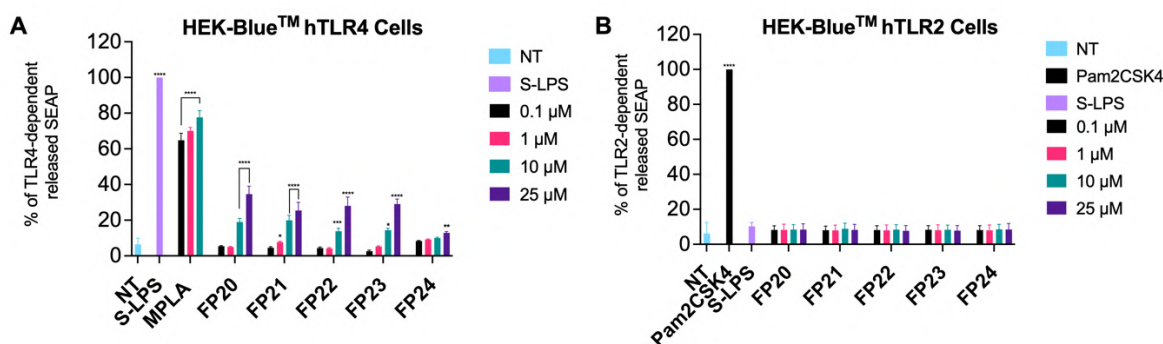
Figure 36. Selectivity of FP compounds towards TLR4. HEK-Blue™ hTLR4 cells (A) and HEK-Blue™ TLR2 (B) were treated with the shown concentrations of FP20-24, MPLA (1 μg/mL), LPS (100 ng/mL) and Pam2CSK4 (1 ng/mL) and incubated for 16-18 hours. The 100% stimulation has been assigned to the positive control LPS (A) or Pam2CSK4 (B) Data are expressed as mean ± SEM of at least three independent experiments. (Treated Vs Non-treated: *P<0.05; **P<0.01; ***P<0.001; ****P<0.0001).

4.3.4. Activity on THP-1 derived macrophages (TDM)

To assess the biological activity of FP compounds, an initial screening was performed using TDM. Human THP-1 X-Blue™ monocytes were differentiated into macrophages by exposure to PMA (100 ng/mL). THP1-Blue™ were derived from the human THP-1 monocyte cell line by stable integration of an NF-κB/AP-1-inducible SEAP reporter construct. The analysis of levels of NF-κB/AP-1-induced SEAP in the cell culture supernatant, which correlates with the activation of the NF-κB/AP-1 pathway, was performed using QUANTI-Blue™ solution, a SEAP detection reagent.

Cells were treated with increasing concentrations of FP20-24 (0,1-25 μM) and incubated for 18h. S-LPS from *S. minnesota* and MPLA were used as positive controls. Results show that most compounds significantly induce SEAP release in human myeloid cell line in a dose-dependent manner (**Figure 37**). Compound FP23, with C$_{14}$ fatty acid (FA) chains, is the only glycolipid whose activity is not statistically significant in macrophage-like human cells. On the contrary, FP22, with C$_{10}$ FA, shows an increased NF-κB/AP-1 activation when compared to FP20.

To further investigate the SAR of this series of compounds in human cells, α-FP20 and FP200 were tested in TDM using the same assay as the previously mentioned derivatives. As shown in **Figure 37 B**, α-FP20 with alpha-anomeric FA chain, shows no significant activity. This fact points out the importance of the anomeric configuration of the lipid chain in C1, that could affect the physico-chemical properties of FP aggregates in the extracellular aqueous medium and have a direct impact in their detection by innate immune system[214,215].
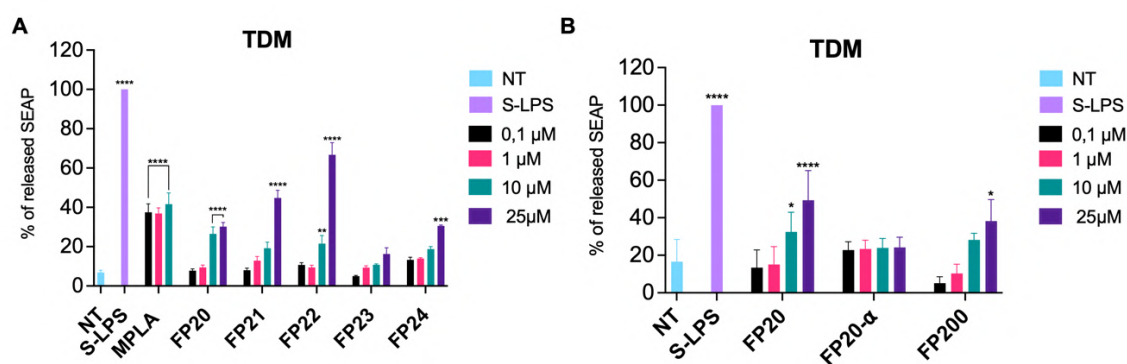
Figure 37. Activity of FP compounds in macrophage-like cells. TDM cells were treated with the shown concentrations of FP20, FP21, FP22, FP23 and FP24 (A) or FP20, α-FP20 and FP200 (B) and incubated for 16-18 hours. MPLA (1μg/μL) and S-LPS (100 ng/mL) were used as controls. The 100% stimulation has been assigned to the positive control. Data are expressed as mean ± SEM of at least three independent experiments. (Treated Vs Non-treated: *P<0.05; **P<0.01; ***P<0.001; ****P<0.0001).

We performed molecular dynamics (MD) simulations to reveal the influence of the anomeric configuration on the packing of α-FP20 and FP20 (with β-anomeric configuration) glycolipids at the atomic level. Starting from a random mixture of either α-FP20 or FP20 molecules in water (see **Appendix I** for computational methods), the two systems were observed to self-organize into a bilayer. The calculated bilayer area was greater for FP20 compared to α-FP20, indicating that the lipid chains are less packed in the case of the β-anomer FP20. In each monolayer, FP20 molecules were regrouped in assemblies Interestingly, in the α-FP20 molecules, the carbonyl group of the acyl chain at the anomeric carbon was always pointing in the same direction in all the molecules that formed the same arrangement. Thus, this position of the carbonyl group could contribute to the ordering of the bilayer, driven by entropic factors, suggesting that the α-FP20 compound induces a more ordered phase in the FP20 assemblies, which favours more compact lipid packing, and could difficult the transfer of the α-FP20 along the TLR4

extracellular cascade, in agreement with the experimental lack of activity observed for this compound.

FP200, a derivative with two phosphates was also tested. We previously reported that compound FP111, the di-phosphorylated analogue of FP11, was inactive as TLR4 agonist[194]. In contrast with this observation[194], FP200 retains activity as TLR4 agonist (**Figure 37 B**). This indicates that the position of the phosphate groups on the glucosamine scaffold is important for activity.

4.3.5. Computational studies of the TLR4 binding of FP20, FP22, and FP24

Compounds FP20, FP22, and FP24 were selected as representative compounds to study computationally and to provide insights at the atomic level of their binding to TLR4. The 3D structure of human (TLR4/MD-2)$_2$ heterodimer in the agonist conformation was firstly used (PDB ID 3FXI)[118] to carry out molecular docking calculations, followed by molecular dynamics (MD) calculations of selected (TLR4/MD-2/ligand)$_2$ complexes.

Preliminary docking calculations performed with AutoDock Vina,[216] predicted plausible binding modes for all the explored ligands. Most docked poses could be classified into three main binding types (type-A, B and C) (**Figure 38**). The binding poses inserted the FA chains into the hydrophobic pocket of MD-2 interacting with many hydrophobic and aromatic residues, and with the saccharide moiety positioned at the MD-2 rim, either establishing polar interactions with residues from the MD-2 entrance (type-A and B binding modes, rotated 180° between them, see Supporting Information) or shifted upward towards the partner TLR4 (designated TLR4*) allowing the formation of polar interactions with TLR4* residues at the dimerization interface (type-C binding mode) (**Figure 38**).

These predicted poses were used as starting geometries for redocking calculations with AutoDock 4[217]. Similarly to Vina, AutoDock 4 also predicted poses belonging to the types A, B, and C binding modes. Nevertheless, not all the binding types (A, B and C) were predicted for the three FP ligands in the redocking calculations; type-A was predicted for FP20 and FP22, type B for all the ligands, and type-C only for FP24.
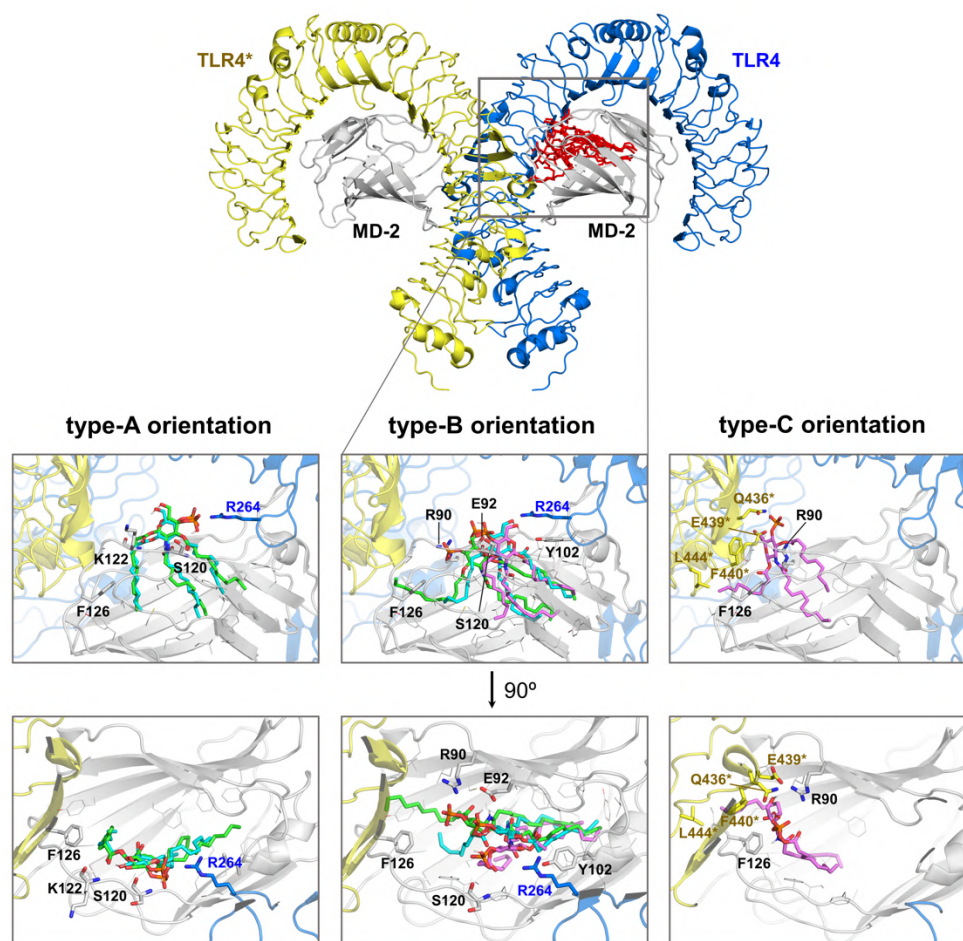
Figure 38. Compounds FP20, FP22, and FP24 docked into the (TLR4/MD-2)2 complex. Top: 3D structure of human (TLR4/MD-2)2 dimer (yellow, dark blue and grey cartoon) used for docking calculations to assess the binding of FP20, FP22 and FP24 (all in red sticks). Below: Docked poses corresponding to type-A, B, and C orientations; best AutoDock 4 predicted binding modes for ligands FP20 (green), FP22 (blue), and FP24 (magenta) are shown in sticks. For each binding mode the front view (top) and the 90° rotated view (below) are depicted, as well as details of the interactions with residues of TLR4 (blue sticks), MD-2 (grey sticks), and TLR4* (yellow sticks). Type-A and B poses differ by 180º rotation along the lipid chains axis: binding orientation type-A places the phosphate group pointing towards residue Arg264 of TLR4, whereas binding orientation type-B orients the phosphate pointing towards the partner TLR4.

Regarding the positioning of the FA chains, two different behaviours were observed for all the ligands. Independently of the binding mode (type-A, B, or C), in most cases, the three FA chains were placed inside the MD-2 pocket. However, some poses placed one FA chain (either C1 or C3 chain) into the MD-2 channel delimited by Phe126[118] and the other FA chains inside the MD-2 cavity. Overall, the docking predictions point to a different behaviour for FP24 in comparison to FP20 and FP22.

The stability of the best predicted binding modes was confirmed by MD simulations (200 ns). The root-mean-square deviation (RMSD) was monitored along the simulation time and confirmed the stability of the (TLR4/MD-2/ligand)2 complexes. The orientation of the FP molecules along the simulation was assessed, observing that the FP compounds

did not undergo orientation flip, pointing to the ability of these ligands to interact with TLR4 in different orientations. Remarkably, FP24 type-C binding mode turned into type-A. During MD simulations, most interactions were maintained for FP20 and FP22 binding poses and, additionally, new interactions with the key TLR4 residues Lys341 and Lys362[118] were formed. Conversely, for FP24 complexes, the important interactions with either TLR4 Lys341 or Lys362 were not observed at the end of the simulations. Regarding the FA chains, the acyl chain initially placed at the MD-2 channel migrated into the MD-2 pocket in all cases. (Despite this common observation, a different behaviour was detected for FP24 acyl chains compared with FP20 and FP22: whereas FP20 and FP22 FA chains were inserted linearly into the MD-2 pocket, the FP24 FA chains were often bent, especially, the FA chain C2, the longest one. Interestingly, FP20 and FP22 retained the Phe126 agonist conformation in both MD-2 chains of the (TLR4/MD-2/ligand)$_2$ complex only in the type-B binding mode, whereas FP24 only in type-A (type-C at the beginning of the simulations).

As observed from the docking calculations and the MD simulations, FP24 behaves differently than FP20 and FP22, in agreement with the fact that FP24 is less active in stimulating TLR4. Although FP24 was reaching similar regions of the MD-2 pocket as FP20, the sugar moiety was not able to establish interactions that are key in TLR4 agonist recognition. Since the shape of the LPS lipid A component may be a key determinant for the TLR4 activation,[218] we wondered about the shape of these three FP analogues, finding that the active compounds FP20 and FP22 adopted a cylindrical shape, whereas the less-active FP24 displayed an inverted-cone shape impeding potential polar interactions that occur for FP20 and FP22 saccharide moieties. Altogether, our computational studies suggest that there is an optimal shape and length for the FA chains for an appropriate TLR4 agonist binding, in addition to the presence of a single phosphate group and its positioning at the pyranose ring.

4.3.6. Pro-inflammatory cytokine profile in human macrophages

Lead compounds FP20, 21 and 22 were tested both on TDM and primary human macrophages in order to evaluate their adjuvant activity. First, the release of pro-inflammatory cytokines after treatment with the synthetic glycolipids, in the same human macrophage-like model mentioned above. S-LPS from *S. minnesota* served as positive

control as it induces the release of TNF, IL-β and IL-6 upon binding to TLR4 and activation of the MyD88 pathway and the inflammasome.

FP20, 21 and 22 induced a significant TNF release in TDM only when used at the highest concentration (25 μM) and in reduced amounts compared to S-LPS (**Figure 39 A**). In contrast, a remarkable, dose-dependent release of IL-1β was observed upon FP20 and FP21 treatment. FP20 was able to induce a level of IL-1β comparable to the S-LPS at the highest tested concentration (25 μM) (**Figure 39 B**). The three tested glycolipids were not able to induce IL-6 secretion in TDM. As shown in **Figure 40**, MTT assays were performed to assess cytotoxicity in TDM, and the results revealed that the compounds are did not affected cell viability.
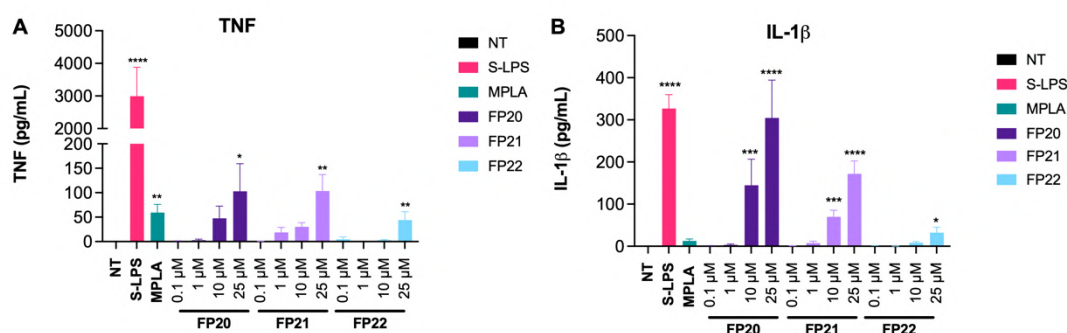
Figure 39. FP compounds pro-inflammatory cytokine release in TDM. TDM cells were treated with increasing concentrations of FP20, 21 and 22 (0.1-25 μM) and LPS (100 ng/mL). TNF (A) and IL-1β (B) levels were evaluated by ELISA after 6 hours of incubation. Data are expressed as mean ± SEM of at least three independent experiments. (Treated Vs Non- treated: *P<0.05; **P<0.01; ***P<0.001; ****P<0.0001).

Figure 40. Cell Viability of TDM treated with FP20-24 compounds. TDM cells were treated with the shown concentrations of FP20, FP21, FP22, FP23 and FP24 and incubated for 16-18 hours. The 100% cell viability has been assigned to the non-treated wells. Data are expressed as mean ± SEM of at least three independent experiments. (Treated Vs Non-treated: *P<0.05; **P<0.01; ***P<0.001; ****P<0.0001).

To evaluate pro-inflammatory cytokine production in primary cells, peripheral blood mononuclear cells (PBMCs) were isolated from whole blood of healthy donors and treated with 10 μM and 25 μM of FP20-22. After 6 hours of incubation, cytokine release

was measured *via* ELISA. Results show the ability of these molecules to induce a dose-dependent TNF and IL-1β production (**Figure 41**). The release of IL-6 from stimulated PBMCs was highly variable among donors even in the case of S-LPS and MPLA stimulation (see error bars); consequently, it was not possible to appreciate a statistically significant correlation between the different treatments and the production of this cytokine (**Figure 41 C**). In addition, since we do not observe any IL-6 production in TDM, we can assume that the IL-6 release observed in PBMCs might result from the contribution of mononuclear cells different from macrophages (e.g., monocytes and lymphocytes) which can contribute to the observed variability. MTT assays were performed to assess cytotoxicity in PBMCs. None of the compounds affected cell viability even at higher concentrations (0,1-25 μM), as shown in **Figure 42**.
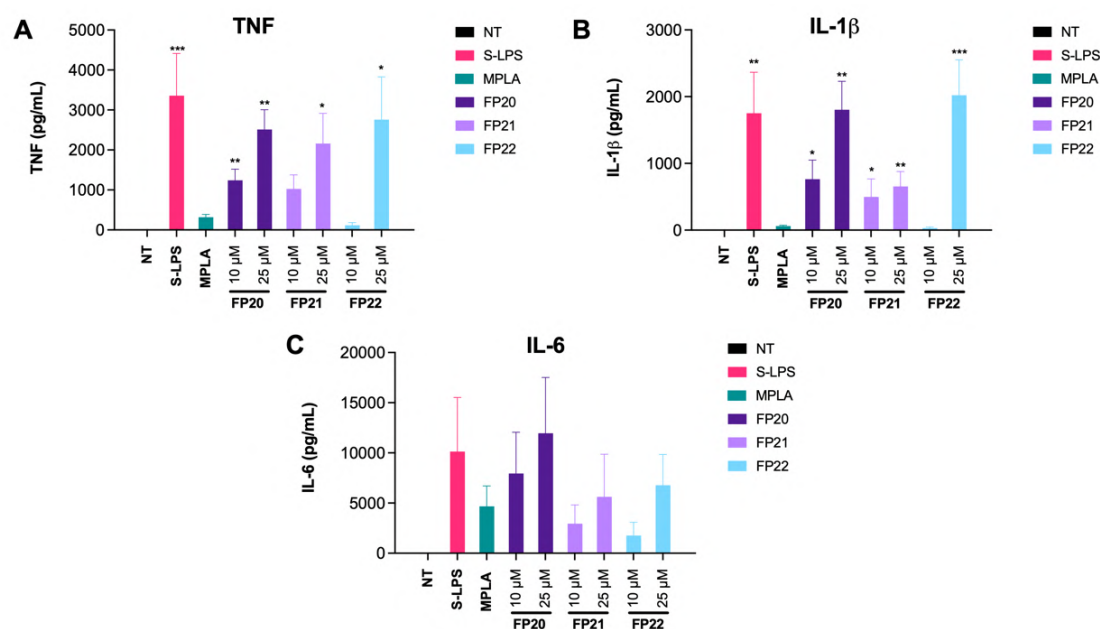
Figure 41. Cytokine release induction by FP molecules in PBMCs. PBMCs were treated with two selected active concentrations of FP20, 21 and 22 (10 and 25μM) and LPS (100 ng/mL). TNF (A), IL-1β (B) and IL-6 (C) levels were evaluated by ELISA after 6 hours of incubation. Data are expressed as mean ± SEM of at least three independent experiments. (Treated vs Non-treated: *P<0.05; **P<0.01; ***P<0.001; ****P<0.0001).
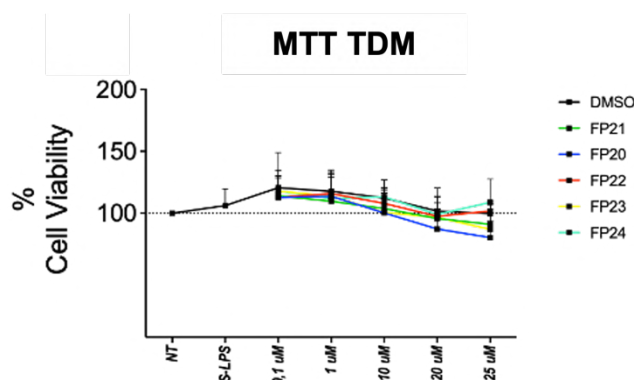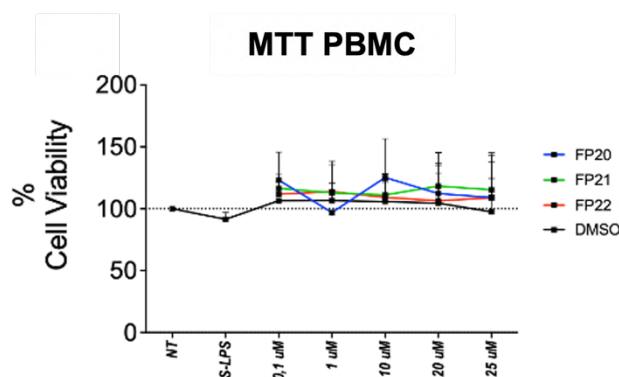
Figure 42. Cell viability of PBMC treated with FP20-22 compounds.

4.3.7. FP20 mechanism of action studies in TDM

The mechanism of action of FP20 was investigated in TDM, a simple and reliable cell line model to study macrophage activity in inflammation[219]. Since we observed a modest but significative release of TNF when compared with S-LPS, we wanted to elucidate the effect of FP20 on the MyD88-dependent NF-κB pathway. We did not detect any p-p65 by immunodetection. To confirm this data, we employed immunofluorescence analysis using the Operetta® CLS High Content Analysis System. The results showed no p65 translocation into the nucleus upon treatment with FP20 between 0 to 4 hours, while treatment with S-LPS triggered p65 translocation with a peak at 1.5 h (**Figure 43**).
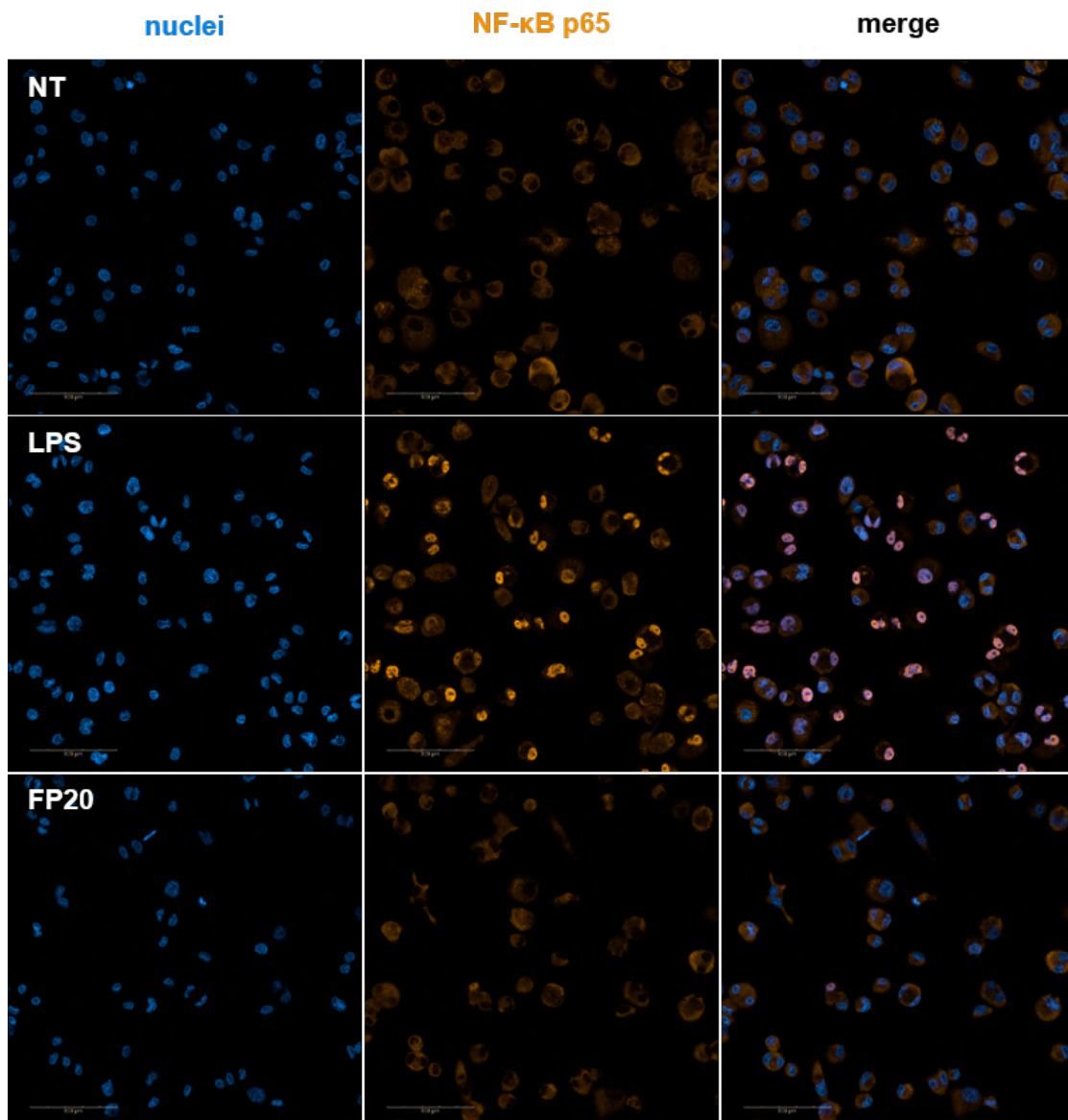
Figure 43. Immunofluorescence analysis of NF-κB translocation. Phospho- NF-κB localization in TDM after LPS stimulation and FP20 25 μM treatment at t=1.5h.

Following the same strategy, we studied the involvement of the TRIF/IRF3 axis in the FP-induced intracellular signalling. IRF-3 phosphorylation was assessed using Western blotting and also using the Operetta® CLS High Content Analysis System. As in the case of the p-NF-κB p65 subunit, p-IRF-3 was not detected by immunoblotting (data not shown) and these data were confirmed by immunofluorescence analysis. As shown in **Figure 44**, the positive control, S-LPS, was able to induce p-IRF-3 nuclear translocation at 2h, when p-IRF-3 translocation reached its peak, (**Figure 44**) and 4 hours (**Figure 45**), while FP20 did not induce any phosphorylation and therefore no nuclear translocation as in the case of non-treated samples.
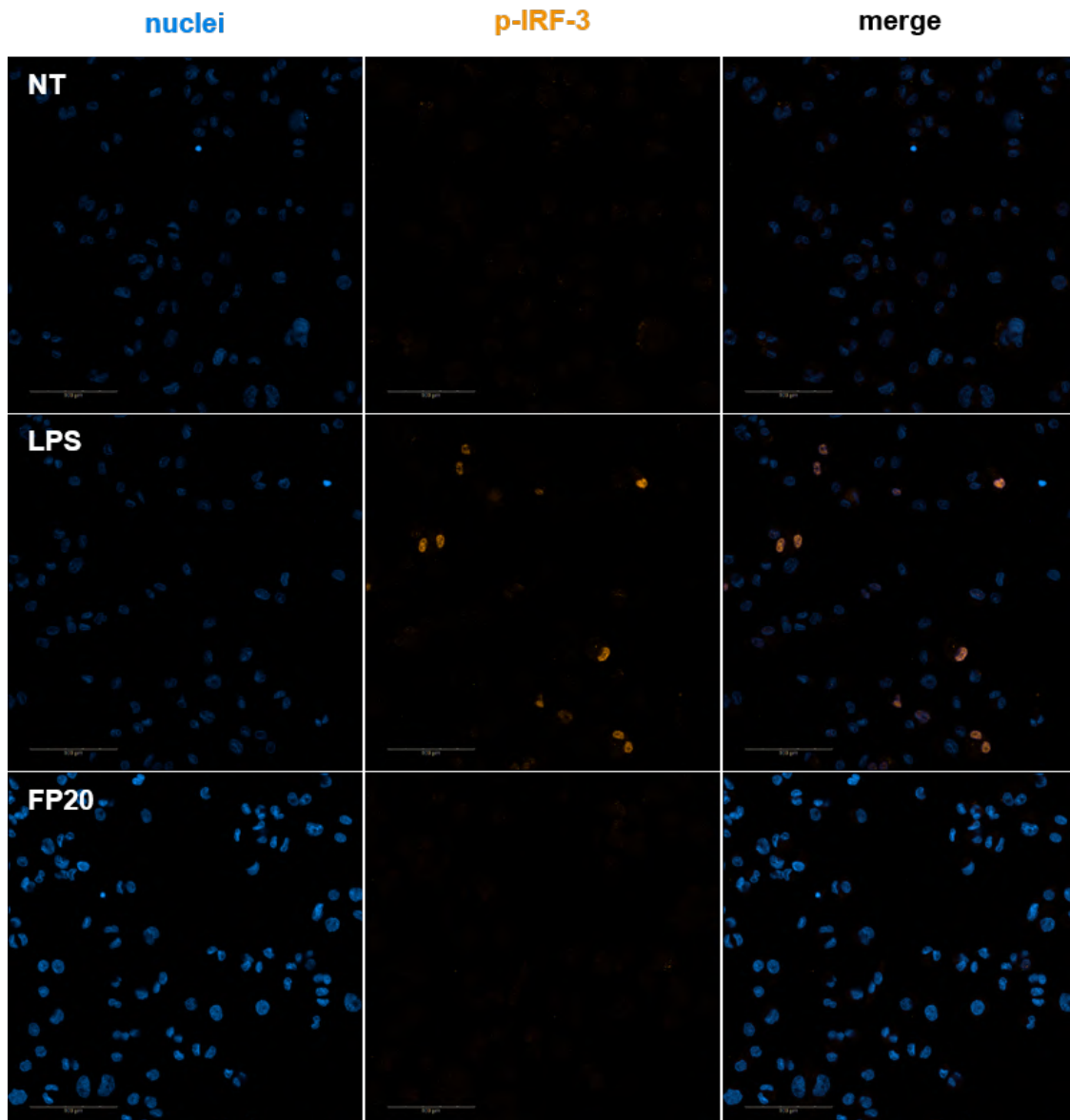
Figure 44.Immunofluorescence analysis of p-IRF-3 nuclear translocation at 2 hours. phospho-IRF-3 localization in TDM after LPS stimulation and FP20 25 µM treatment at t=2 h.
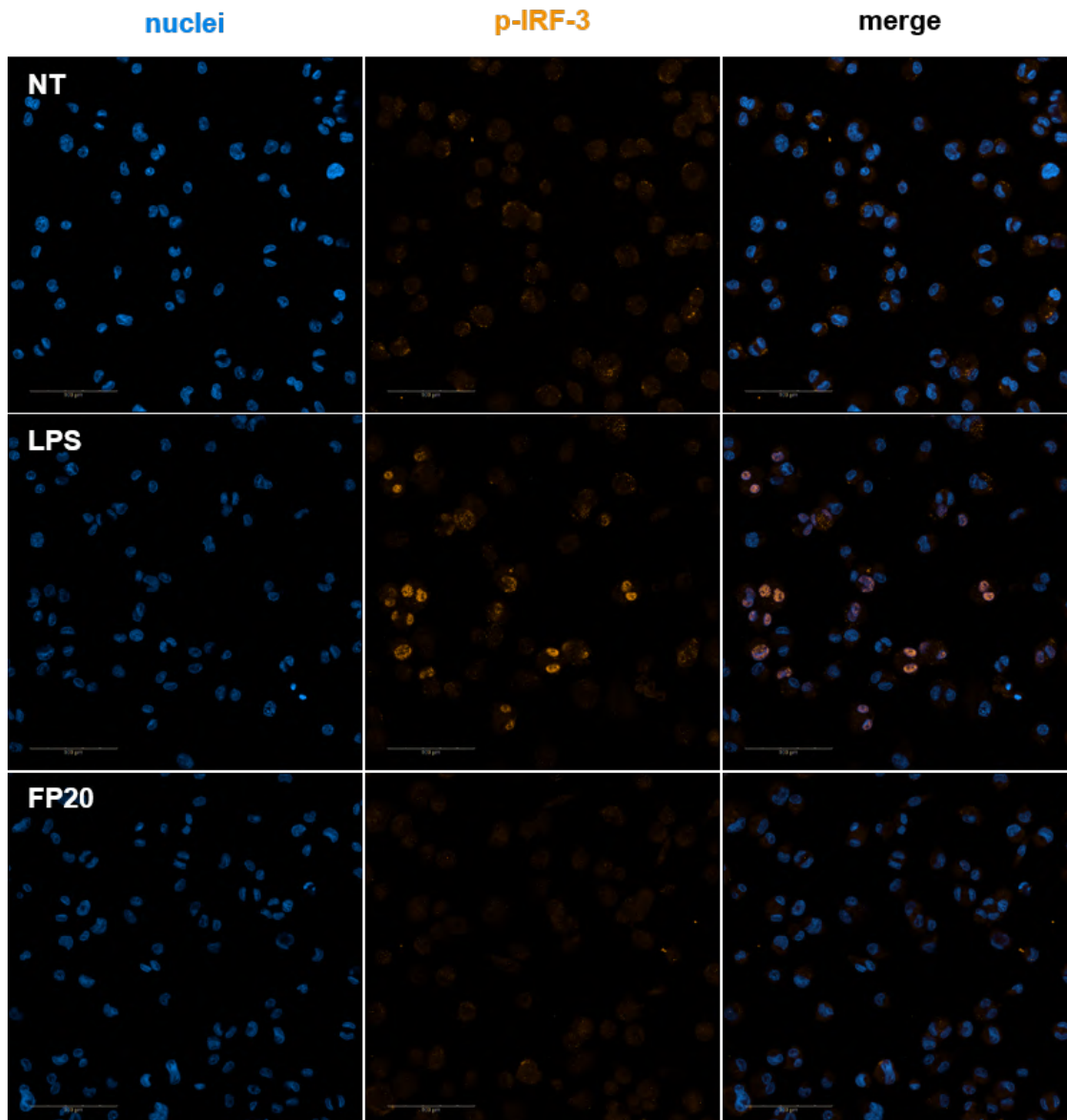
Figure 45. Immunofluorescence analysis of p-IRF-3 nuclear translocation at 4 hours. phospho-IRF-3 localization in THP-1-derived macrophages (TDM) after LPS stimulation and FP20 25 μM treatment at t=4 h.

Considering the lack of activation and nuclear translocation of the NF-κB p-65 subunit and of IRF-3, we decided to investigate p38 MAPK since it is known to play an important role in TLR4-mediated inflammatory response after the activation of the receptor and the assembly of myddosome[220,221]. It is reported that activation of MAPK cascades (p38 and JNK) leads to the phosphorylation of AP-1 components and consequently to their nuclei translocation[104]. AP-1-induced transcription is associated with the production of proinflammatory cytokines[222] and p38 activation has been linked with the induction of TNF in cells treated with TLR4 agonist MPLA[178]. Western blot analysis showed that FP20 was able to induce a significant activation of p-p38 MAPK at

1.5h, 2h and 2.5h (**Figure 46 A**). This can explain both the production of TNF in the absence of active p-p65 in FP20-treated TDM and the FP20-induced SEAP release, which can be ascribable to AP-1 activation.

Nevertheless, looking into the cytokine profile of FP20, it is clear that the levels of IL-1β are comparable to S-LPS, which indicates that its release is significant for activity and may greatly contribute to explain FP20 activity. It is known that p38 also plays a role in regulating pro-IL-1β transcription[223], while, activation of the NLRP3 inflammasome and its downstream cascade is essential to the cleavage of pro-IL-1β and the release of mature IL-1β[224] trough membrane permeabilization[225]. Considering the above-mentioned results, we set out to investigate whether the NLRP3 inflammasome was involved in FP20 activity. First, we measured the amount of IL-1β released at 6 hours after S-LPS or FP20 treatment (**Figure 46 B**). Then, we pre-treated TDM with increasing concentrations of MCC950 (0.01—10 μM), a known NLRP3 inhibitor, prior to 6 hours of S-LPS or FP20 in order to observe its impact on IL-1β release. We observed a dose-dependent inhibition that in the case of FP20 resulted in a decrease of IL-1β in the range of 50% with the highest dose of MCC950. (**Figure 46 C**). This result confirms the involvement that NLRP3 inflammasome in the FP20-induced production and release of IL-1β. This mechanism of action is particularly interesting in the case of vaccine adjuvant development, since inflammasome-mediated immunogenicity is necessary to mount a proper immune response[167].
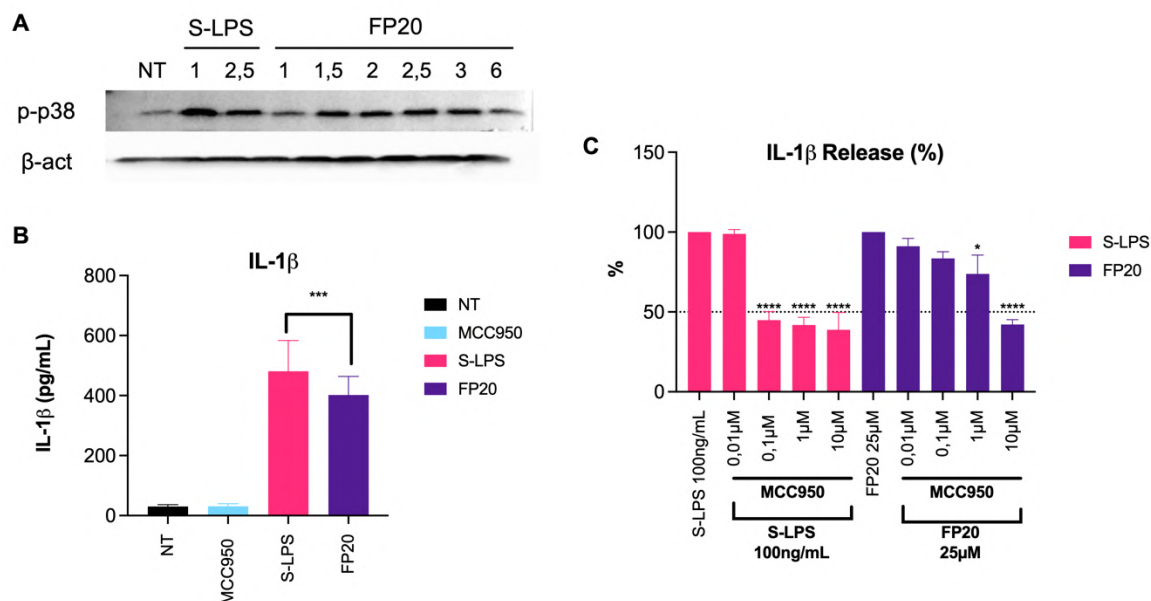
Figure 46. Study of p38 activation (A) and NLRP3 inflammasome activation (B) and (C). (A) TDM cells were treated with 25μM of FP20 or 100 ng/mL of S-LPS from 0 to 6 hours. p-p38 MAPK was detected by western blot in cell lysates. (B) TDM cells were treated with 25μM of FP20 or 100 ng/mL of S-LPS for 6 hours. IL-1β levels in supernatant were detected by ELISA. Data are expressed as mean ± SEM of at least three independent experiments. (Treated Vs Non- treated: *P<0.05; **P<0.01; ***P<0.001; ****P<0.0001). (C) TDM cells were pre-treated with NLRP3 inhibitor MCC950 for 1 hour followed by treatment with 25μM of FP20 or 100 ng/mL of S-LPS for 6 hours. The effect of MCC950 on IL-1β release was measured in supernatants using ELISA and expressed as percentage. Data are expressed as mean ± SEM of at least three independent experiments. (Treated Vs Non- treated: *P<0.05; **P<0.01; ***P<0.001; ****P<0.0001)

4.3.8. Activity in murine cells and in vivo immunization experiments

Prior to *in vivo* immunization, FP20 was tested using the RAW-Blue™ cell line. This murine cell line is derived from the murine RAW 264.7 macrophage-like cells with chromosomal integration of a SEAP reporter construct inducible by NF-κB and AP-1. As shown in **Figure 47**, FP20 displays a higher activity in the murine cell line, when compared to human cells. In fact, the compound is active at the lowest concentration tested (0.1 μM) in RAW-Blue™ cells whilst in TDM cells the activity is only significant from a 100-fold higher concentration (10 μM). This species-specific activity has been observed in the case of similar TLR4 antagonists [226] and it is related to differences in the structure and binding sites in the human and murine TLR4/MD-2 receptor complex[227–229]. Overall, these data confirm that FP20 is active in a murine cell line and thus it is worth it to test its efficacy and safety *in vivo*.
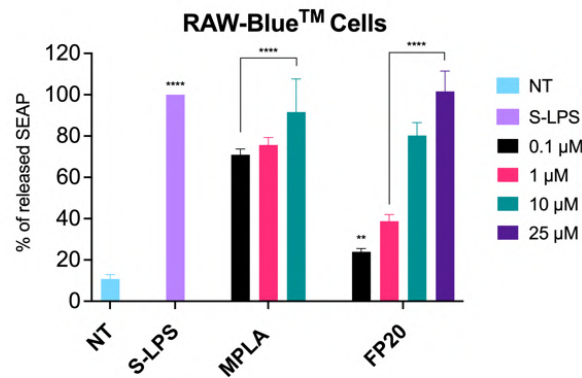
Figure 47. Activity of FP20 in murine macrophages. RAW-BlueTM cells were treated with the shown concentrations of FP20 and incubated for 16-18 hours. MPLA (1µg/mL) and LPS (100 ng/mL) were used as controls. The 100% stimulation has been assigned to the positive control LPS. Data are expressed as mean ± SEM of at least three independent experiments. (Treated Vs Non-treated: *P<0.05; **P<0.01; ***P<0.001; ****P<0.0001).

In order to evaluate the adjuvant efficacy of FP20 *in vivo*, C57BL/6 mice were immunized with 10ug of the model antigen chicken ovalbumin (OVA), formulated with or without 10ug of MPLA, the previously developed agonist FP18, and FP20. MPLA and FP18 were used as controls. After 21 days, the total anti-OVA IgG response was evaluated. Following the priming immunisation, FP18 performed as well as the MPLA control, while FP20 produced significantly higher titters than the OVA control (**Figure 48 A**). Mice then received a boost immunisation on day 22, and final antibody responses, including IgG subtyping, were evaluated on day 42. Although not statistically significant, FP18 generated slightly higher total IgG titters than MPLA, while FP20 titters were significantly higher than OVA but lower than MPLA (**Figure 48 B**).
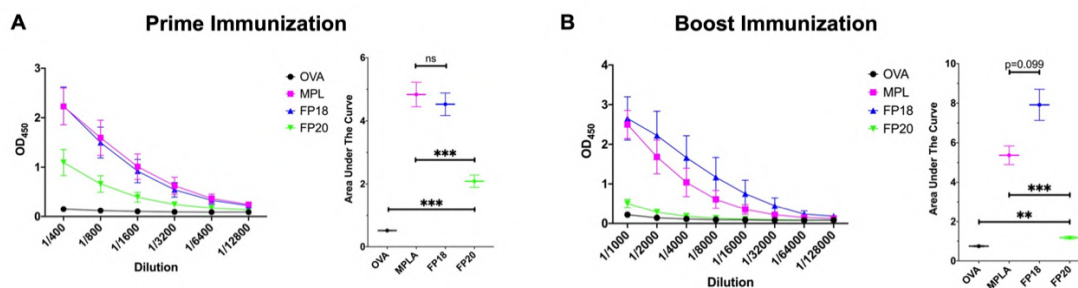
Figure 48. Results from *in vivo* studies using an OVA model after prime (A) and boost (B) immunizations. C57BL/6 mice were immunized with OVA formulated with or without MPLA, FP18, and FP20 as adjuvants (A) Total antibody response to prime OVA immunization 21 days post immunization. (B) Total antibody response to boost immunization 42 days post immunization. Values represent mean ± SEM. Brown-Forsythe and Welch one-way ANOVA tests (with an alpha of 0.05) were utilized to compare the areas under each curve. *, p<0.05; **, p<0.01; ***, p<0.001.

MPLA IgG1 titters did not differ significantly from FP18 and were significantly higher than the FP20 group (**Figure 49 A**). IgG2b titters of MPLA and FP18 were not significantly different, and there was no difference between FP20 and the OVA control

group (**Figure 49 B**). MPLA produced significantly higher IgG2c titters than FP20, while FP18 did not differ from the OVA control group (**Figure 49 C**). FP18 and FP20 did not significantly differ to OVA in IgG3 production (**Figure 49 D**). Taken together, these data show that FP20, while being less active than FP18, retains adjuvant activity. As shown in **Figure 50**, overall liver transaminases data indicate that both FP18 and FP20 are non-toxic in this immunization scheme.
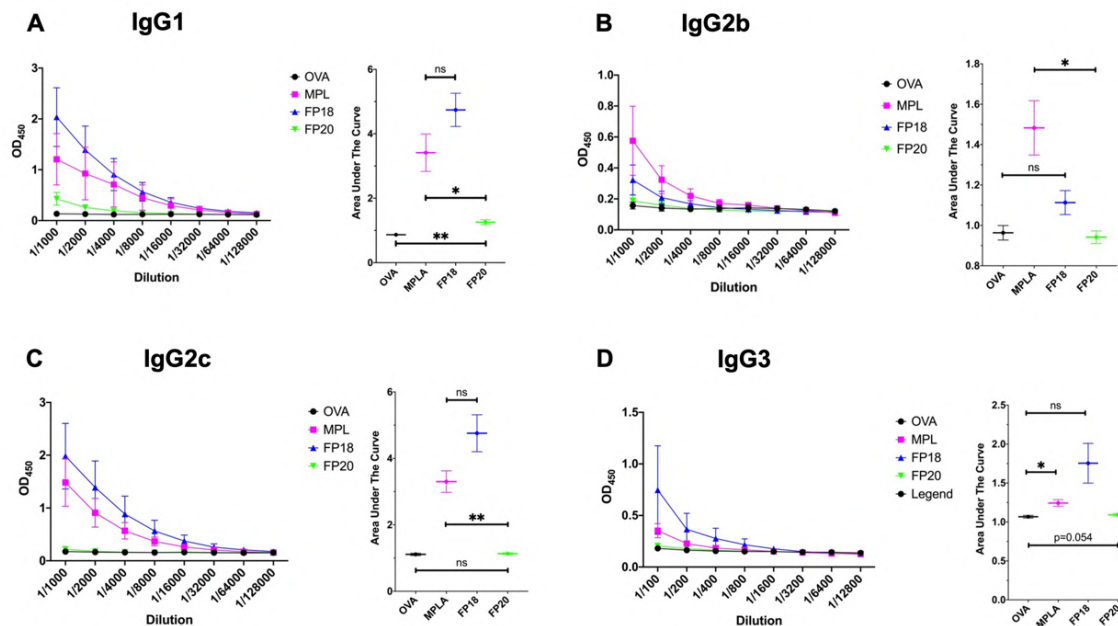
Figure 49. IgG profile responses to boost OVA immunization 42 days post immunization. (A) IgG1 (B) IgG2b (C) IgG2c (D) IgG3. Values represent mean ± SEM. Brown-Forsythe and Welch one-way ANOVA tests (with an alpha of 0.05) were utilized to compare the areas under each curve. *, $p<0.05$; **, $p<0.01$; ***, $p<0.001$.

Figure 50. Liver transaminases of C57BL/6 mice immunized with FP18 and FP20. FP20 (A) Aspartate transaminase (AST) and (B) Alanine transaminase (ALT) relative to the OVA control group in mice serum 0-, 21- and 42-days post-immunization.

CHAPTER II

New glycosylated derivatives of FP20 :

Increasing the similarity to LPS by

mimicking the oligosaccharide core

Author Contribution: Participated in the design of the study. Performed the *in vitro* characterization and analyzed the results. Wrote the biological portion of the manuscript.

4.4. Background

LPS is a fundamental component of bacterial outer membrane formed by a large, polysaccharide moiety and a smaller lipophilic moiety[230,231]. The lipophilic moiety is the immunogenic portion, which binds to TLR4 co-receptor MD2. Nonetheless, the hydrophilic core oligosaccharide of LPS plays an important role by directly interacting with TLR4 (**Figure 51**). This interaction, mainly mediated by the first monosaccharide bound to lipid A (Kdo I), is crucial to increase the binding affinity between LPS and TLR4[114,118,232]. The oligosaccharide core portion of LPS plays an important role in LPS-TLR4/MD-2 interaction. Therefore, mimicking the oligosaccharide core by adding a carbohydrate moiety to FPs could increase its affinity for the receptor and its biological activity. This approach can solve another underlying issue of FPs: their inherent hydrophobicity. By adding a carbohydrate, the pharmacokinetic profile may improve.
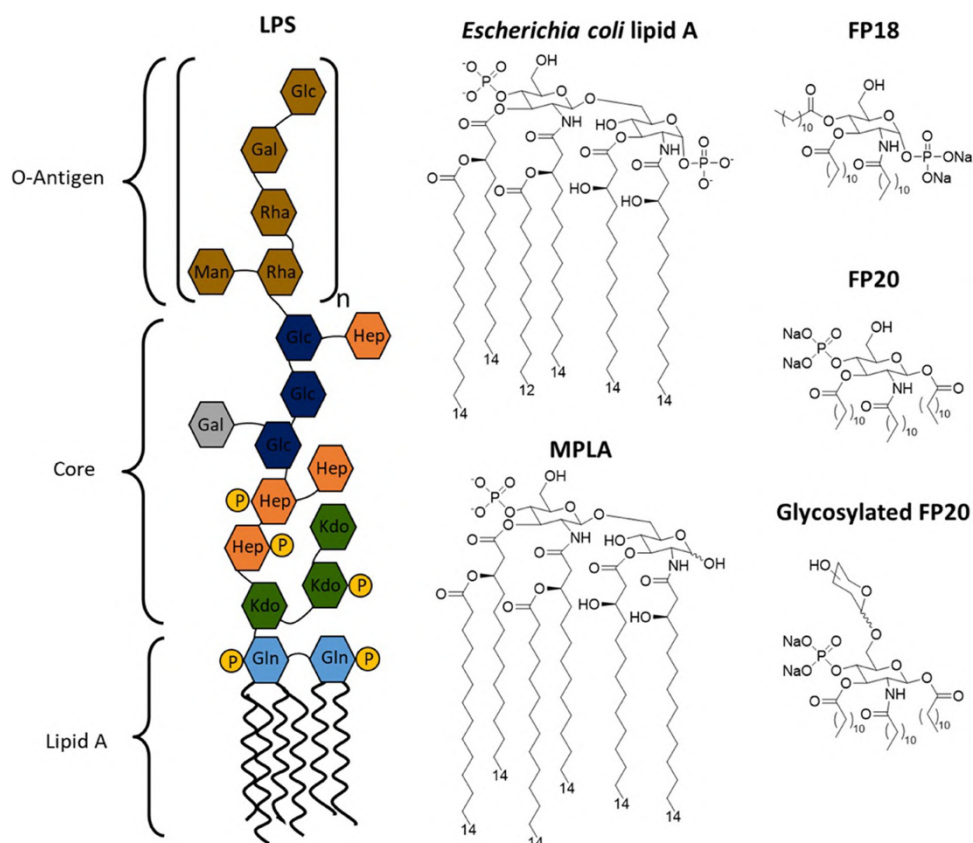
Figure 51. Structure of KDO, lipid A, MPLA and new synthetic derivatives FP18, FP20 and Glycosylated FP20

Chemical synthesis of glycans can be achieved via glycosylation reaction where a glycosyl donor reacts with a glycosyl acceptor. These reactions are performed with the

assistance of a promoter that helps the departure of a leaving group on the donor[233] followed by a nucleophilic substitution with the glycosyl acceptor. Chemical glycosylations remain challenging: outcomes vary depending on protecting groups[234], solvents, leaving groups and promoter systems[235,236].

4.5. Experimental Design

This study focused on the optimization of the glycosylation of FP20, leading to a new series of derivatives functionalized on the C-6 free hydroxyl group with different monosaccharides (**Figure 52**). Owing to the presence of ester bonds and phosphates, mild conditions were required for glycosylation, and a recently developed cooperatively-catalyzed Koenigs-Knorr reaction was employed, as well as a novel, acid free, regenerative protocol[237–240].

The obtained compounds were tested in cells expressing hTLR4 and hTLR2 receptors in order to evaluate whether they had maintained selectivity and activity. Further characterization in macrophage-like human cells is ongoing.
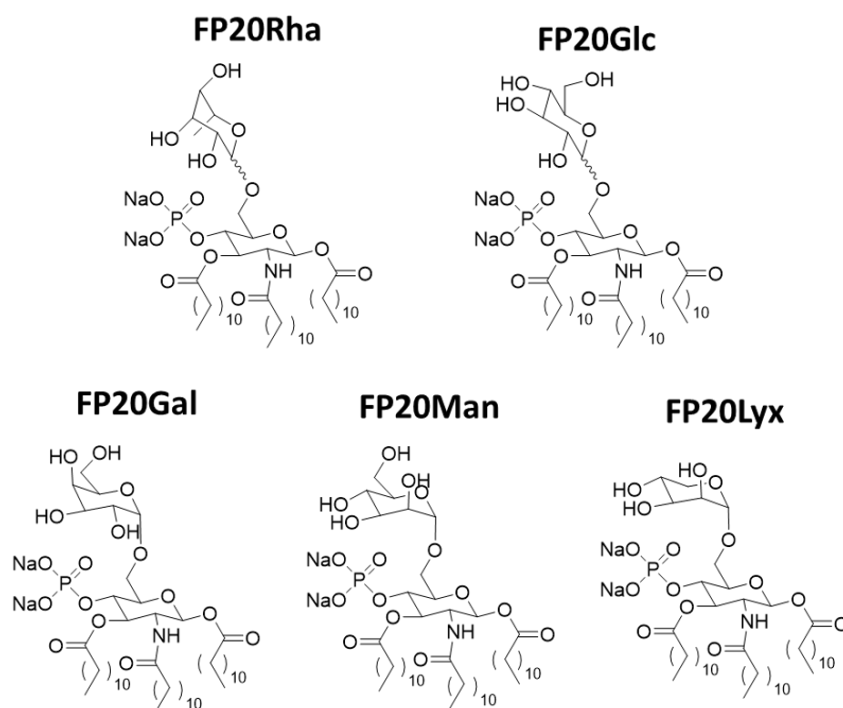
Figure 52. New TLR4-targetting FP20 glycosylated derivatives

4.6. Results and Discussion

4.6.1. Chemical Synthesis

FP20 has been glycosylated at C-6 with five different monosaccharides: glucose (Glc), galactose (Gal), mannose The glycosylation was planned after the desilylation step of the reported synthesis for FP20[241] (**Figure 53**), to minimize the reactions involved using compound **6** as glycosyl acceptor. We initially decided to use fully benzylated donors, as they are normally very reactive and can be readily deprotected in the final hydrogenation[242,243].
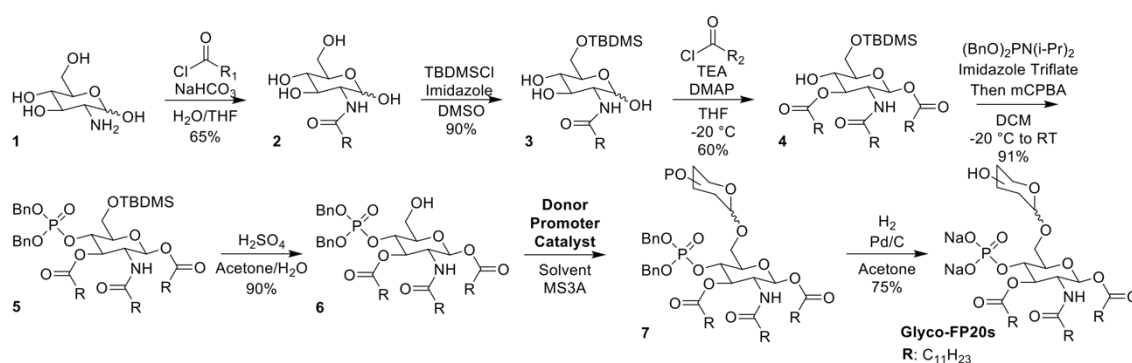
Figure 53. Synthesis of Glycosylated FP20

We elected to use L-rhamnose as model glycosyl donor, as it is known to be specifically recognized by a protein involved in TLR4 pathway, CD14. CD14 presents the ligand to TLR4 and it is pivotal for initiating the TRIF/IRF3 pathway, a determinant contributor to MPLA's mechanism of action: engaging it could improve FPs' activity as adjuvants[244]. However, glycosylation of compound **6** proved to be challenging, due to the lability of the lipid chain on position C1. Indeed, several common reaction conditions were tried (**Table 2**, entries 1-5), but the lipid chain on the anomeric position always acted as a leaving group, resulting in substrate degradation.

Table 2. Conditions used in early screening of glycosylation methods.

Donors	Entry	Donor (Eq)	Solvent (M)	Promoter (Eq)	Catalyst (Eq)	Temperature (°C)	Yield (%)
a	**1**	a (3)	DCM (0.05)	N/A	TMSOTf (0.5)	0	N/D
	2	a (3)	DCM (0.05)	N/A	TMSOTf (0.5)	-20	N/D
	3	a (3)	DCM (0.05)	N/A	TMSOTf (0.5)	-78	N/D
	4	b (2)	DCM (0.05)	N/A	$FeCl_3$ (0.1)	-20	N/D
	5	b (2)	DCM (0.05)	N/A	$FeCl_3$ (0.1)	-60	N/D
b	**6**	b (1.25)	Tol (0.05)	Ag_2O (1)	TfOH (0.2)	0	20
	7	b (1.25)	Tol (0.05)	Ag_2O (1.5)	TfOH (0.3)	0	35
	8	b (1.25)	Tol (0.1)	Ag_2O (2.5)	TfOH (0.4)	0	60
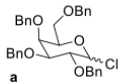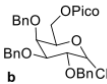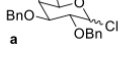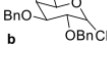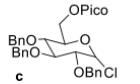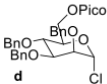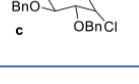
Since the conditions used were too harsh on the substrate, we needed a milder protocol to avoid FA cleavage. Consequently, we investigated if a new method developed by Demchenko and co-workers, comprising a cooperatively-catalyzed Koenigs-Knorr glycosylation reaction, would be suitable. According to these conditions, a small amount of a strong acid additive allows to achieve short reaction times[237].

Applying this protocol, we obtained the desired compound (FP20Rha), with a lower than desired yield (20%). Encouraged by this result, we made a small screening of reaction conditions (Table 2, entries 6-8), raising the yield to 60%. When the same conditions were applied to other donors, a dramatic decrease in yield was observed. This result was rationalized by a greater steric hindrance of Glc, Gal, and Man donors compared to Rha. This is further supported by the fact that glycosylations with Lyx, a pentose sugar, gave similar yields to those of Rha.

Further conditions were screened by varying the amount of acid and silver salt employed in the reaction or the protecting groups on the glycosyl donor (a picoloyl ester was introduced at C-6, because partially acylated glycosyl donors have shown unusually high reactivity under these conditions)[237,245]. However, only small improvement in the reaction outcome has been observed (30-45% yield).

Shadrick et al. recently described $Bi(OTf)_3$ as a milder and more efficient alternative to silver salts, also doubling as the acid catalyst[238,240]. After a brief optimization using this protocol, yields between 84-94% were obtained with several picoloylated glycosyl donors (**Table 3**).

Table 3.Conditions using bismuth triflate as a promoter.
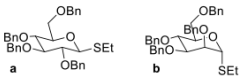
Donors		Entry	Donor (Eq)	Solvent (M)	Promoter (Eq)	Time (h)	Yield (%)
a	b	1	a (1.2)	DCM (0.05)	$Bi(OTf)_3$ (0.35)	72	45
		2	b (1.2)	DCM (0.05)	$Bi(OTf)_3$ (0.35)	72	46
		3	b (1.5)	DCM (0.05)	$Bi(OTf)_3$ (0.50)	20	60
		4	b (2.0)	DCM (0.05)	$Bi(OTf)_3$ (0.75)	18	84
c	d	5	c (2.0)	DCM (0.05)	Bi(OTf)3 (0.75)	16	84
		6	d (1.25)	DCM (0.05)	$Bi(OTf)_3$ (0.75)	18	94
		7	b (1.25)	DCM (0.05)	$Bi(OTf)_3$ (0.90)	18	80

When $Bi(OTf)_3$ amount was increased beyond 0.75 Eq., a decrease in yield was observed, rationalized by occurrence of disruptive interactions between the metal and acceptor's amide, as $Bi(OTf_3)$ is known to catalyze reactions involving nitrogen and

oxygen[246,247]. This hypothesis was confirmed when fully benzylated donors were used instead of the ones with a picoloyl ester in C-6 and the yield markedly dropped.

Therefore, while robust and high yielding, this protocol can only be applied to our molecules when a C-6 picoloylated donor is used, which requires additional manipulation to arrive to the final product. Hence, fully benzylated donors were again tested with a different glycosylation protocol developed by Demchenko and co-workers, involving regenerative glycosylation with thioglycoside donors[239]. Using this method, we achieved efficient glycosylation. The respective disaccharides were obtained in high yields (84-91%) and short reaction time (0.75 - 4 h, **Table 4**).

Table 4. Conditions used for FP20 glycosylation applying a regenerative glycosylation protocol.

Donors	Entry	Donor (Eq)	Solvent (M)	Promoter (Eq)	Catalyst (Eq)	Time (h)	Yield (%)
	1	a (1.2)	DCM (0.05)	NIS (1.2)	HOFox (0.05)	72	84
	2	a (2.0)	DCM (0.05)	NIS (2.0)	HOFox (0.05)	72	84
	3	b (2.0)	DCM (0.05)	NIS (2.0)	HOFox (0.05)	20	90
	4	c (2.0)	DCM (0.05)	NIS (2.0)	HOFox (0.05)	18	91
	5	d (2.0)	DCM (0.05)	NIS (2.0)	HOFox (0.05)	16	86

Once we managed to consistently achieve glycosylation with different donors, we prepared five derivatives (Glc, Gal, Man, Rha, Lyx; **Figure 52**) of FP20 and deprotected them through hydrogenation on Pd/C. FP20Rha and FP20Glc have been obtained as an inseparable mixture of α and β anomers, while FP20Man, FP20Lyx and FP20Gal have been obtained as pure α anomers that mimic the α-anomeric configuration of lipid A-linked Kdo in LPS (**Figure 51**). However, as will be discussed below, no significant difference in TLR4 selectivity has been observed between the mixtures and the pure diastereomer, suggesting that the nature of the intermonomeric glycosidic linkage it is not a crucial factor for biological activity.

4.6.2. Selectivity towards hTLR4

The selectivity of new glycosylated FP20 molecules towards hTLR4 was tested using HEK-Blue cells. These cells were co-transfected with either the hTLR4 or hTLR2 receptors genes along with the SEAP reporter gene. When the receptors are stimulated with respective ligands, NF-κB and AP-1 transcription is activated through the

intracellular pathway leading to the release of SEAP that can be quantified using a colorimetric assay.

HEK-Blue hTLR4 and h-TLR2 were treated with increasing concentrations of FP20Glc, FP20Gal, FP20Man, FP20Lyx, and FP20Rha (0.1-25 μM) and incubated for 18h. Smooth LPS from *Salmonella minnesota* and MPLA were used as positive controls for hTLR4 activation while PAM2CSK4 was used as a positive control for hTLR2 activation.

As shown in **Figure 54**, no activity for hTLR2 was observed, indicating that these derivatives are selective hTLR4 agonists. Furthermore, no significant difference in selectivity emerged between FP20Man, FP20Lyx, and FP20Gal (purely α configured), and the other two compounds: this is an indication that the configuration of the glycosidic bond might not be a contributing factor for TLR4 ligand recognition and activation. Also, it suggests that both configurations are active, otherwise we would observe a decrease in activity of FP20Glc and FP20Rha (mixtures) when compared with FP20Man, FP20Lyx, and FP20Gal (purely α configured). No significant differences between the derivatives were observed, suggesting that the nature of the monosaccharide does not influence selectivity and activity in this cell model.
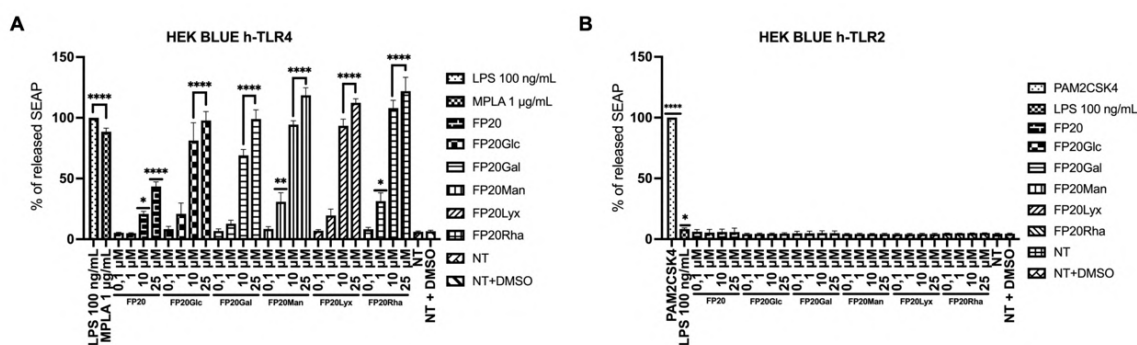
Figure 54. Selectivity of glycosylated FP20s towards hTLR4. HEK-Blue hTLR4 cells (A) and HEK-Blue TLR2 (B) were treated with the shown concentrations of FP20Glc, FP20Gal, FP20Man, FP20Lyx and FP20Rha, MPLA (1μg/mL), LPS (100 ng/mL), and Pam2CSK4 (1 ng/mL) and incubated for 16–18 h. The 100% stimulation has been assigned to the positive control LPS (A) or Pam2CSK4 (B). Data are expressed as mean ± SEM of at least three independent experiments (treated vs non-treated: *P < 0.05; **P < 0.01; ***P < 0.001; ****P < 0.0001).

Noteworthy, the TLR4 activation ability in this cell line at the concentration of 10 μM is very similar to MPLA (1μg/mL) for all glycosylated compounds and higher than parent compound FP20. Furthermore, at 25 μM the compounds show a higher activity than MPLA (1μg/mL) and S-LPS (100ng/mL). This data suggests that the introduction of

a monosaccharide moiety strongly potentiates the interaction with the TLR4/MD-2 receptor complex.

4.6.3. Activity of FP20Glyco in TDM

Further characterization was performed using TDM cells on compounds Fp20Rha, FP20Lyx and FP20Man. The ability of these compounds to activate TDM cells was evaluated using a SEAP assay (**Figure 55**). Although at a concentration of 1µM FP20Rha seems to be more active than the other derivatives, at 10µM activity is quite similar. However, it is very clear the dramatic increase in activity when compared to the parent compound FP20. Furthermore, FP20Glyco activate TDM cells at the same magnitude as the positive control S-LPS, at a concentration of 10µM. MTT assay results demonstrated that the FP20glyco compounds are not toxic in a TDM cell model, in the tested concentrations.
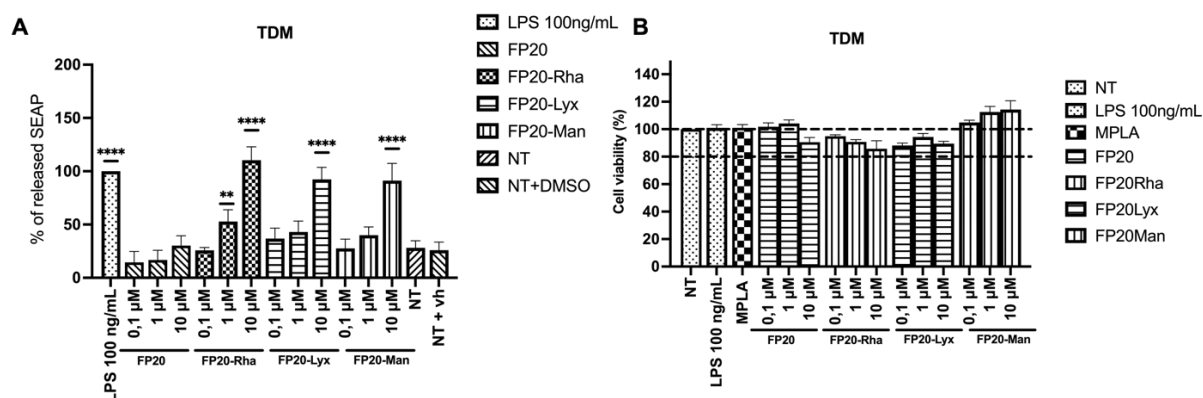
Figure 55. Activity of FP20Glyco compounds in TDM (A) and cell viability (B) TDM were treated with the shown concentrations of FP20 and FP20Glyco compounds and incubated for 16–18 h. S-LPS (100 ng/mL) was used as control. (A) The 100% stimulation has been assigned to the positive control. (B) 100% cell viability has been assigned to non-treated wells. Data are expressed as mean ± SEM of at least three independent experiments (treated vs non-treated: *P < 0.05; **P < 0.01; ***P < 0.001; ****P < 0.0001).

Cytokine expression was evaluated for three of the synthesized compounds – FP20Rha, FP20Lyx and FP20Man (**Figure 56**). Overall, there was no significative differences were observed between the compounds, although FP20Rha seems to produce more IL-1β and IL-6. Mechanistic studies following intracellular factors using western blot and immunofluorescence are needed to clarify if changing the monosaccharide on C6 affects interaction with the receptor.
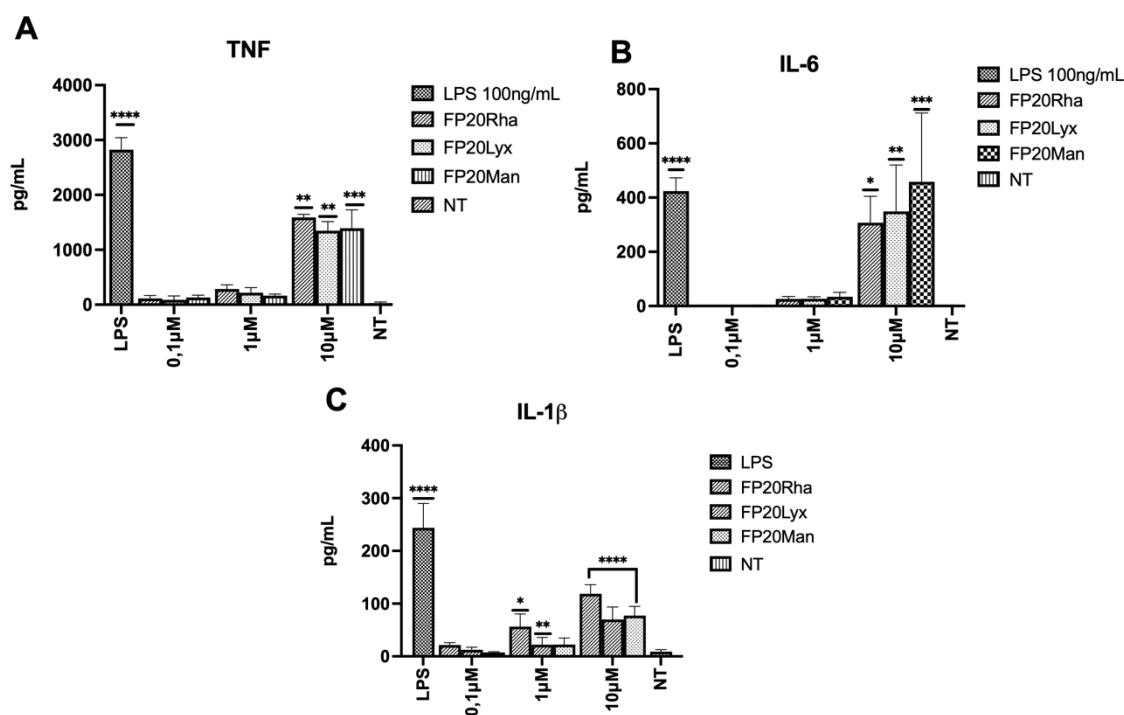
Figure 56. Cytokine profile of Glyco FP20s. TDM cells were treated with increasing concentrations of FP20Rha, FP20Man and FP20Lyx and (0.1–10 μM), S-LPS (100 ng/mL) and MPLA (1 μg/mL). TNF (A), IL-6 (B) and IL-1β (C) levels were evaluated by ELISA after 16-18 h of incubation. Data are expressed as mean ± SEM of at least three independent experiments (treated vs non-treated: $*P < 0.05$; $**P < 0.01$; $***P < 0.001$; $****P < 0.0001$).

4.6.4. FP20Rha *in vitro* preliminary characterization in TDM (data not published)

Since all three tested compounds – FP20Rha, FP20Man and FP20Lyx – showed similar ability to activate TDM and a similar cytokine profile. FP20Rha was chosen to be further investigated. We decided to compare the cytokine profile of FP20, FP20Rha and LPS at different time points, 3, 6 and 18h (**Figure 57**). Although data is not shown in this thesis, these time points were chosen to validate results obtained by employing a new FTIR-based method develop to screen proinflammatory compounds, that will be discussed in CHAPTER IV.
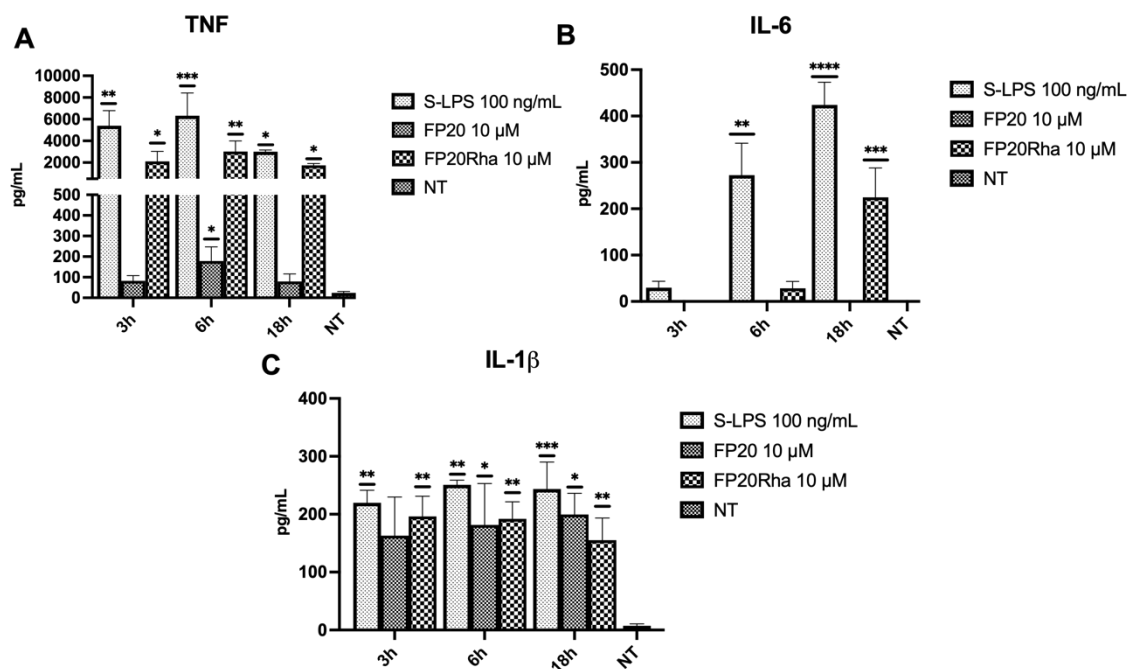
Figure 57. Cytokine profile of LPS, FP20 AND FP20Rha at 3, 6 and 18 h. TDM were treated with LPS (100ng/mL) , FP20 and FP20Rha (10μM) for 3, 6 or 18h. TNF (A), IL-6 (B) and IL-1β (C) levels were evaluated by ELISA. Data are expressed as mean ± SEM of at least three independent experiments (treated vs non-treated: *P < 0.05; **P < 0.01; ***P < 0.001; ****P < 0.0001).

Results show that FP20Rha has a distinct profile compared to FP20, suggesting that it might interact differently with the TLR4/MD2 receptor and possibility activate different signaling cascades. Interestingly, IL-1β levels are similar to LPS and to FP20, suggesting that there might be a NLRP3 contribution. Indeed, preliminary data using MCC950, a NLRP3 inhibitor was used as a pre-treatment in cells treated with FP20Rha and IL-1β levels decreased dramatically, compared to group treated with 10 μM of compound (**Figure 58**). Nevertheless, this data has to be validated with further experiments.
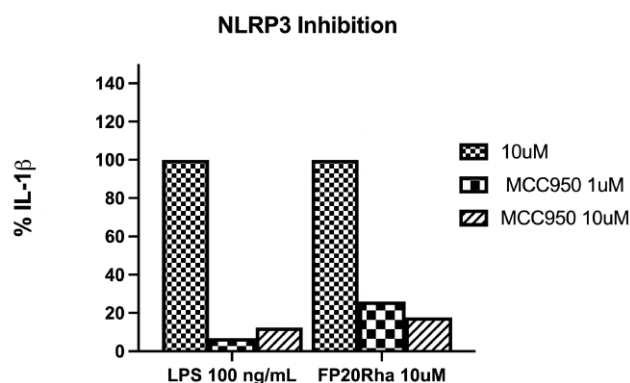
Figure 58. Preliminary data on NLRP3 activation by FP20Rha. Control TDM were treated with 100 ng/mL of LPS or 10μM of FP20Rha and the values were normalized as 100% IL-1β release. Tested TDM were pre-treated wither with 1μM or 10μM of MCC950 for 1 hour, followed by treatment with 100 ng/mL LPS or 10μM of FP20Rha for 6 hours. Supernatant was collected and IL-1β levels were assessed by ELISA.

Preliminary assessment of MyD88 and TRIF-dependent activation was performed using immunofluorescence experiments. NF-κB and p-IRF3 nuclear translocation were assessed by treating TDM with either the positive control LPS or FP20Rha for different time points (0 to 4 hours). Images were acquired and analyzed using the Harmony software from the Operetta CLS. A threshold for nuclear translocation was defined and number of positive nuclei were evaluated as a percentage of nuclei in respect to the total number. Results indicate that there is likely activation of both pathways. NF-κB translocation is evident while p-IRF3 translocation seems to be mild compared to LPS. Nevertheless, when compared to the NT cells there seems to be a slight activation that needs to be confirmed using other methods (**Figure 59**).
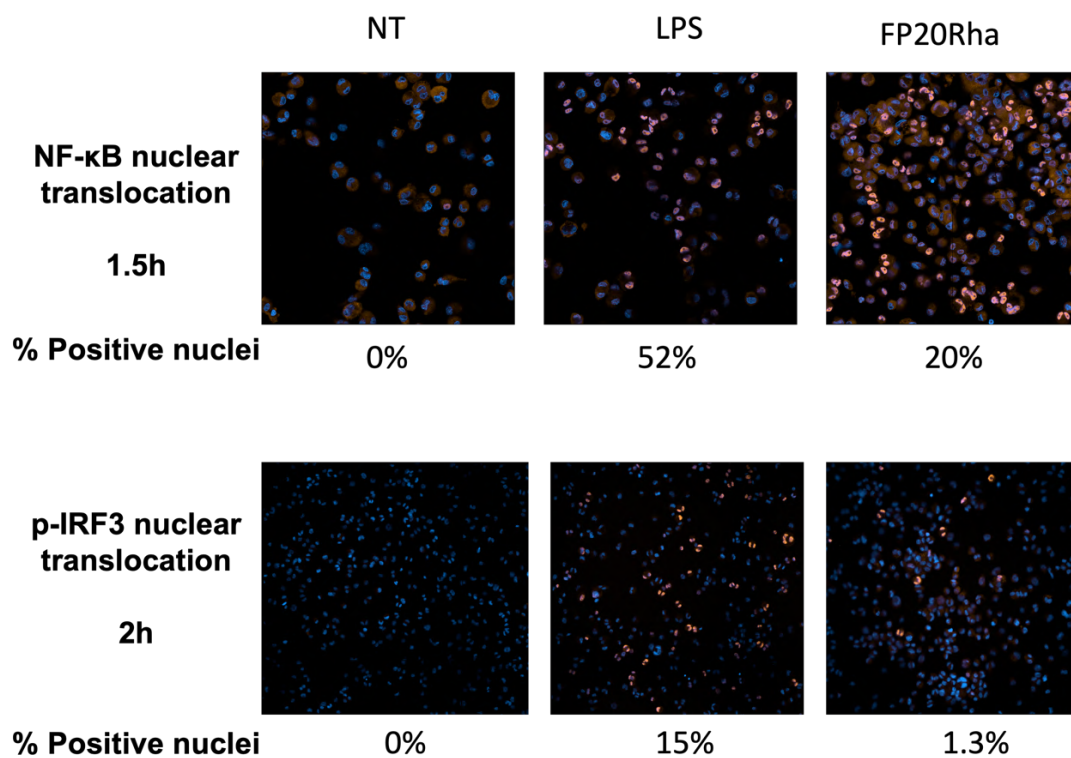
Figure 59. Immunofluorescence analysis of NF-κB nuclear translocation at 1.5h and p-IRF3 nuclear translocation at 2h.

CHAPTER III

New C6 functionalized FP20 derivative: a novel vaccine adjuvant for an *Enterococcus faecium* vaccine

Author Contribution: Designed the study. Performed the experimental work presented except for the synthesis, *in vivo* experiments, and whole-cell ELISA. Wrote the experimental and discussion sections of the manuscript.

4.7. Background

As it was mentioned above, while MPLA is safe and efficient, its synthesis is complex and expensive. With the aim to simplify the molecular structure of MPLA and reduce synthetic steps, we developed new synthetic TLR4 agonists, based on a monosaccharide structure instead of disaccharide core of MPLA. FP18 showed strong TLR4 agonistic activity both *in vitro* and *in vivo*, with the ability to initiate similarly to MPLA, the MyD88 and the TRAM/TRIF pathway, as well as inflammasome activation. However, FP18 has an anomeric phosphate on position C1 which made it impossible to further functionalize its structure in an attempt to increase activity[194]. With that in mind, we developed the FP20 variant[241], mentioned in CHAPTER I. The C1 phosphate was moved to the C4 position while retaining activity. FP20 also showed TLR4 agonistic activity *in vitro* and *in vivo*[241]. Nevertheless, the increased stability of the phosphate group allowed for further functionalization, particularly in position C6.

As mentioned in the previous chapter, glycosylating position C6 can improve activity by mimicking the KDO portion of natural occurring LPS. Nonetheless, as it was demonstrated by the results of CHAPTER II, glycosylation is a difficult chemical process that can lead to low yields and requires time for optimization. While the introduction of a monosaccharide was thought to be the ideal functionalization, the addition of another moiety in position C6 could also improve the interaction between the compound and the hTLR4 receptor.

Enterococcus faecium is part of the commensal microbiota in the gastrointestinal tract, having a key role in physiological pH regulation and immune system stimulation[248–250]. However, when the microbiota balance is affected, bacteria from the genus enterococcus can cause pathogenesis[251]. While *E. faecium* can be found in the environment and be responsible for community-acquired infections[252], it is also known as a nosocomial pathogen. Enterococci are the third cause of nosocomial bacteremia[253]. *E. faecium* also ranked fourth in the worldwide most common nosocomial isolated pathogens[254]. It can present in many types of healthcare-associated infections, such as bloodstream infections, surgical site infections, catheter-associated urinary tract infections, etc[255].

E. faecium is recognized as part of the ESKAPE pathogen group (*E. faecium, Staphylococcus aureus, Klebsiella pneumoniae, Acinetobacter baumannii, Pseudomonas aeruginosa*, and *Enterobacter spp)*. These bacteria are defined as capable of "escaping" the biocidal effect of antibiotics. They were also clustered thanks to their prevalence in the clinical setting, where vulnerable individuals gather, making their multiple antibiotic resistance a great concern[256]. Vancomycin-resistant *E. faecium* (VRE) is classified within the high priority pathogen lost from WHO.[258] Indeed, these gram-positive pathogens possess a versatile genome that allows for further resistance acquisition, meaning that an effective vaccine is urgently needed[259].

Numerous attempts to create a formulation against *E. faecium* have unfortunately never led to the commercialization of an effective vaccine[260]. However, several antigens have been investigated, including PpiC, a peptidyl-prolyl cis-trans isomerase protein (PPIase)[58,59,261,262]. This enzyme is a surface-exposed foldase, involved in several essential cellular activities such as penicillin-binding protein folding and trafficking[263]. It has also been characterized as a potential virulence factor due to its involvement in resistance to high NaCl concentration and ampicillin[264,265]. Also, PPIases are ubiquitous and known to have a role in the pathogenicity of several other bacteria, such as *Helicobacter pylori* and *Listeria monocytogenes*[266,267]. All those characteristics led us to believe that a formulation containing a TLR4-activating adjuvant and PpiC could be effective against *E. faecium*.

4.8.   Experimental Design

FP20 was functionalized using 2,2-Bis(hydroxymethyl) propionic acid (HMP), yielding FP20Hmp **(Figure 60)**, a novel FP20 C6-functionalized derivative. The propionic acid-derived hydrophilic group was introduced via acylation. We considered acylation a valid approach to achieve functionalization since its chemistry allows for good atom economy and simple reactions. Furthermore, the carboxylic group formed in this reaction is present in several natural and synthetic commercialized molecules, making it an interesting group to add to a potential new drug. This functional group was chosen in the attempt to improve physico-chemical properties by increasing hydrophilicity due to the hydroxyl groups. Indeed, while the lipophilic lipid A is the immunogenic portion of

LPS, the hydrophilic moiety also plays an important role in ligand recognition, as it binds directly to TLR4[241].
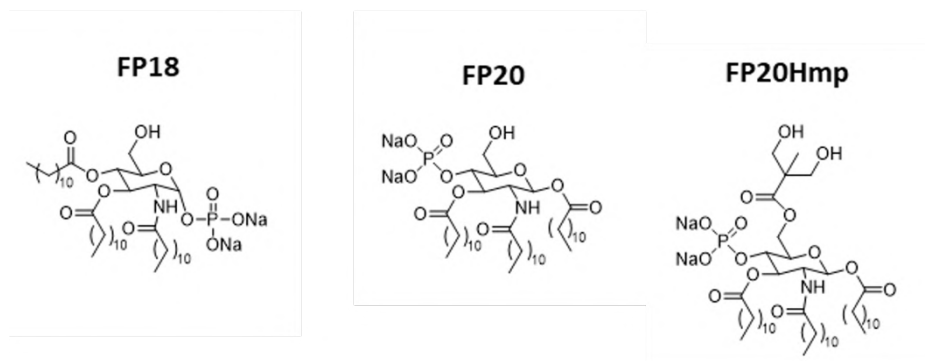
Figure 60. FP20Hmp, its parent compound FP20 and previous generation FP derivative FP18

Characterization of this new derivative was achieved in a TDM model by applying different techniques such as SEAP assay, ELISA, and Western Blot. Immunofluorescence experiments were also performed to track intracellular transcriptional factors, in order to clarify FP20Hmp's mechanism of action. *In vivo* mice studies were performed using an OVA vaccination model to understand the ability of FP20Hmp to induce the production of OVA-specific IgG. We then investigated the *in vivo* activity of FP20Hmp when formulated with model and enterococcal antigen PpiC, to assess the possibility of incorporating this adjuvant in a novel vaccine candidate against this pathogen. To achieve this, rabbits were immunized with PpiC and with or without MPLA or FP20Hmp**.** Sera was then collected and the ability of FP20Hmp to enhance PpiC specific antibodies was evaluated.

4.9.   Results and Discussion

4.9.1. Chemical Synthesis

FP20Hmp was synthesized from compound **6,** which was obtained by means of a previously described synthesis[266,267] followed by a C6 functionalization (**Figure 61**). Briefly, glucosamine hydrochloride was acylated with lauroyl chloride, followed by protection of C6 as TBDMS ethers and acylation of positions C1 and C3 with lauroyl chloride in the presence of TEA and DMAP in THF, at low temperature. Position C4 of compound **4** was then phosphorylated employing a phosphite insertion strategy using N,N-diisopropylphosphoramidite, followed by desylation on sulfuric acid, yielding compound **6**. Compound **6** was then functionalized with **7**, a benzylidene derivative of

2,2-Bis(hydroxymethyl) propionic acid obtained through a previously reported eprotocol[268,269]: this protection strategy was chosen in order to facilitate deprotection of the final compound in just one step by hydrogenation. Initially, functionalization was attempted through compound **7** chlorination and reaction with **6** in presence of triethylamine and *N,N*-dimethylaminopyridine DMAP, but this approach gave low yields (25-30%). Therefore, a direct acylation using the free acid in the presence of 1-Ethyl-3-(3-dimethylaminopropyl)carbodiimide EDC and DMAP was followed, which gave a 60% yield.
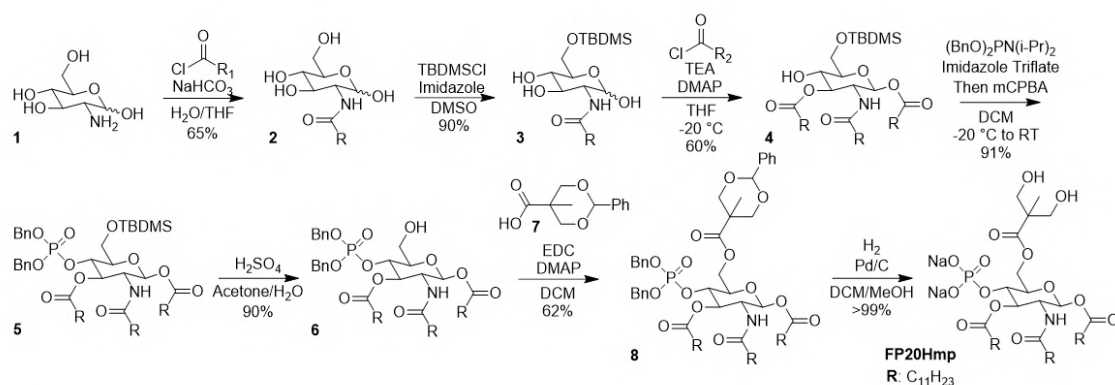
Figure 61. Synthesis of FP20Hmp

4.9.2. FP20Hmp stimulates hTLR4 and not hTLR2 in HEK cells

To evaluate the ability of FP20Hmp to selectively activate TLR4, we used HEK-Blue hTLR4 and hTLR2 reporter cells. Cells were treated with increasing concentrations of FP20Hmp ($0.1 - 25$ µM). S-LPS and MPLA derived from *Salmonella minnesota* were used as a positive control for TLR4 activation in HEK-Blue hTLR4 cells, while PAM$_2$CSK$_4$, a known TLR2 agonist, was used as a positive control of the TLR2-mediated response in HEK-Blue hTLR2 cells. Results (**Figure 62**) show that FP20Hmp is able to selectively stimulate TLR4 receptor in a dose-dependent way (A), while being inactive on the TLR2 receptor (B).
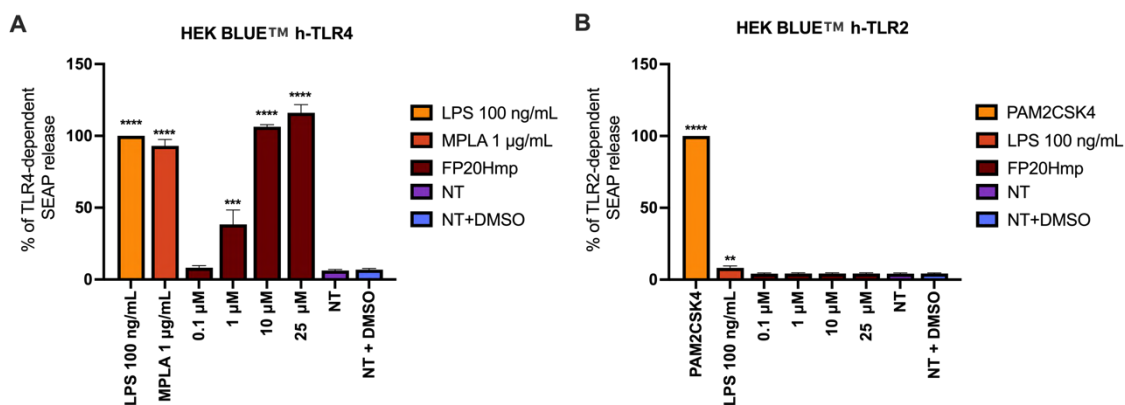
Figure 62. Selectivity of FP20Hmp towards hTLR4. HEK-Blue™ hTLR4 cells (A) and HEK-Blue™ hTLR2 (B) were treated with the shown concentrations of FP20Hmp, MPLA (1 μg/mL), S-LPS (100 ng/mL) and PAM2CSK4 (1 ng/mL) and incubated for 16-18 hours. The 100% stimulation has been assigned to the positive control S-LPS (A) or Pam2CSK4 (B). Data are expressed as mean ± SEM of at least three independent experiments. (treated vs non-treated: *P<0.05; **P<0.01; ***P<0.001; ****P<0.0001).

4.9.3. FP20Hmp activity in THP-1-derived Macrophages

To assess the immunostimulanting activity of **FP20Hmp,** macrophage-cell like cells, derived from PMA stimulated THP-1 monocytic human leukemia cell line, were used. This approach has been described as a validated model to study either monocyte or macrophage function, namely immune responses and signaling pathways[241]. Particularly, we chose to employ the THP-1 X-Blue cell line as these cells are highly responsive to PRR agonists, including TLR4, and allow the monitoring of pathway activation by stable integration of an NF-κB/AP-1-inducible SEAP reporter construct. As in the case of HEK-Blue cells mentioned above, when treated with a compound able to induce NF-κB/AP-1-dependent transcription THP-1 X-Blue cells release SEAP in the medium.

To this end, after differentiation TDM were treated with increasing concentrations of FP20 and FP20Hmp (0.1 – 10 μM). S-LPS and MPLA were used as positive controls. As shown in **Figure 63 A**, FP20Hmp showed increased potency compared to MPLA and its parent compound, FP20. Additionally, it is possible to observe that at the highest tested concentration – 10 μM, FP20Hmp is only about 25% less active than the positive control S-LPS. These findings demonstrate that, in comparison to FP20, the introduction of a hydrophilic group in position C6 results in a significant increase in activity. Furthermore, FP20Hmp show no *in vitro* toxicity in this cell model, as shown in **Figure 63 B**.
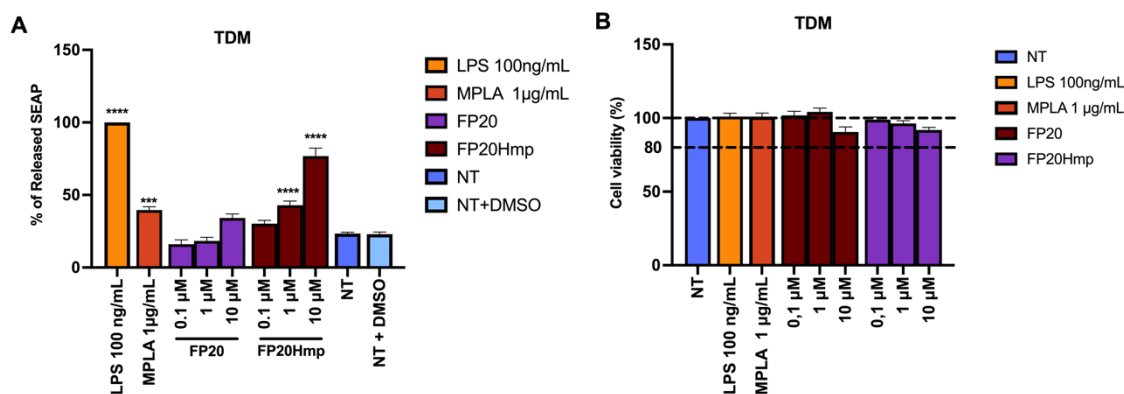
Figure 63. Activity of FP20 in TDM (A) and cell viability in TDM (B). TDM were treated with the shown concentrations of FP20 and FP20Hmp and incubated for 16–18 h. MPLA (1 µg/mL) and S-LPS (100 ng/mL) were used as controls. (A) The 100% stimulation has been assigned to the positive control. (B) 100% cell viability has been assigned to non-treated wells. Data are expressed as mean ± SEM of at least three independent experiments (treated vs non-treated: *P < 0.05; **P < 0.01; ***P < 0.001; ****P < 0.0001).

To further characterize its immunostimulatory activity, FP20Hmp proinflammatory cytokine profile was determined by measuring the release of TNF, IL-6 and IL-1β. Increasing concentrations of the compound were tested and compared with S-LPS, MPLA and FP20. As displayed in **Figure 64**, FP20Hmp is able to induce a dose-dependent release of all the three studied cytokines that reach significant amounts at the highest dose - 10 µM. It is worth noting that, FP20 does not induce IL-6 production as previously reported[241], while FP20Hmp is able to induce the release of this cytokine. Also, FP20Hmp-induced TNF release is considerably higher compared to the FP20 one. Being both NF-κB/AP-1-dependent cytokines, these findings parallel the marked increase of SEAP detected in previous experiments (**Figure 63**). This indicates that the new derivative might have a different mechanism of action than FP20, showing that the introduction of a new functional group in C6 position can indeed lead to changes in activity. On the contrary, when comparing IL-1β release induced by FP20 and FP20Hmp, the latter is lower. NLRP3-dependent inflammasome activation seems to be crucial for the activity of FP20[224] as the activation of this multiprotein complex results in cleavage of pro-IL-1β and release of mature IL-1β. This can explain why the parent compound, despite showing a lower activity in terms of NF-κB/AP-1-driven transcription (**Figure 63**), shows higher levels of this cytokine[104].
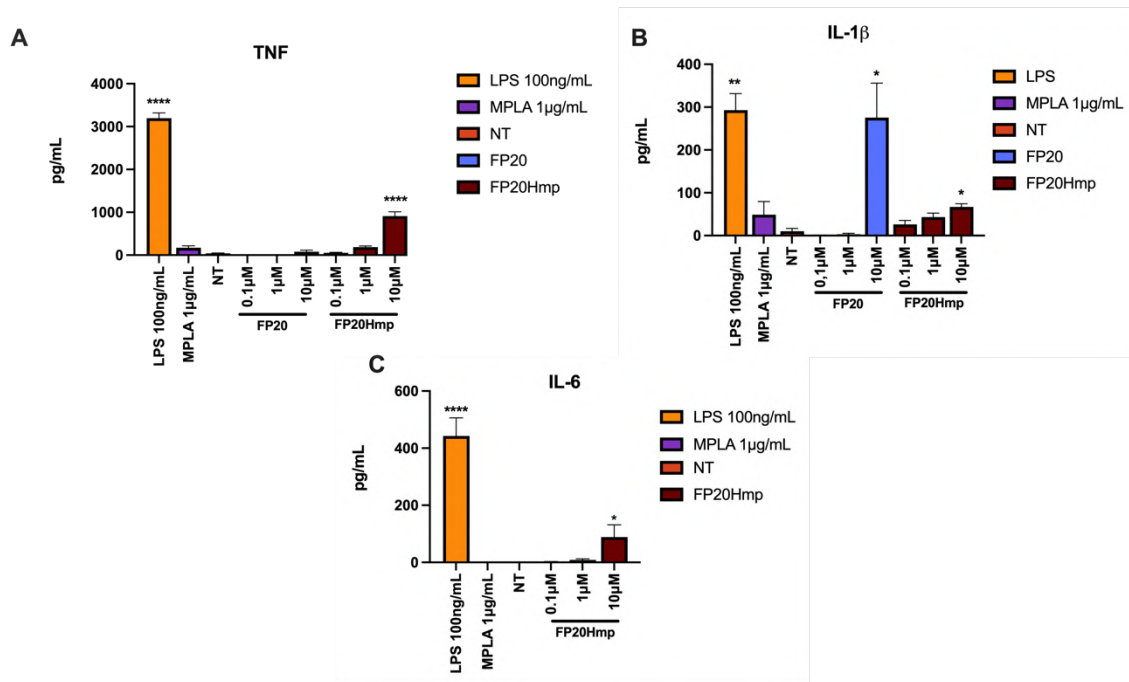
Figure 64. FP20Hmp proinflammatory cytokine release in TDM. TDM cells were treated with increasing concentrations of FP20 and FP20Hmp (0.1–10 μM), S-LPS (100 ng/mL) and MPLA (1 μg/mL). TNF (A), IL-1β (B) and IL-6 (C) levels were evaluated by ELISA after 16-18 h of incubation. Data are expressed as mean ± SEM of at least three independent experiments (treated vs non-treated: *P < 0.05; **P < 0.01; ***P < 0.001; ****P < 0.0001).

Given the results obtained we decided to further investigate the molecular events that occur within the NF-κB-dependent signal transduction cascade. As previously mentioned, the activation of TLR4 by its natural ligand LPS triggers the initiation of the MyD88-dependent intracellular signaling[104]. As a consequence of Myddosome activation there is degradation of IκBα with subsequent NF-κB (p65 subunit) phosphorylation and nuclear translocation[194]. Accordingly, in order to investigate whether FP20Hmp was able to trigger this TLR4-mediated pathway, the kinetics of IκBα degradation and p65 phosphorylation was investigated by Western-blot analysis. In a previous work, it was determined that S-LPS induce IκBα degradation within the first 30 min of treatment, which lead to a peak of p65 phosphorylation at around 90 min after stimulation[268]. The kinetics of IκBα degradation and p65 phosphorylation for FP20Hmp is slightly shifted in respect to S-LPS (**Figure 65**). Indeed, a more rapid IκBα degradation (15 min) and a delayed p65 phosphorylation starting at 120 min and being sustained even after 240 min is observed, in contrast with the sharper 90-120 min peak described for S-LPS.
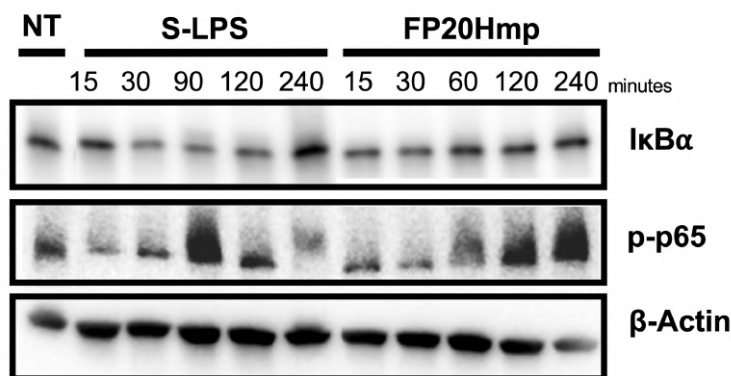
Figure 65. Western Blot analysis of MyD88-dependent pathway activation. TDM were treated with S-LPS (100 ng/mL), FP20Hmp (10 μM) or left untreated (NT) and collected after the indicated time. The levels of IκBα, phospho-p65 and actin were detected by immunoblotting.

To further confirm the ability of FP20Hmp to signal through the MyD88/NF-κB pathway, we performed time course (0 to 4 h) immunofluorescence experiments, with the aim of monitoring NF-κB (p65 subunit) nuclear translocation. In these experiments, LPS from *Escherichia coli* was used as a positive control while FP20 was used for comparative purposes. Acquisition of the images was carried out on an Operetta CLS™ High-Content Analysis System. Image analysis of the different time points showed that the peak of p65 nuclear translocation for LPS occurred at around 90 minutes, while for FP20Hmp we observed a delayed peak at 120 minutes (**Figure 66** and **Figure 67**). Additionally, FP20Hmp was able to induce p65 nuclear translocation in about 19% of cells compared to the positive control LPS (t = 120 min). Matching Western blot and imaging data, we can state that FP20Hmp stimulation results in a rapid IκBα degradation (from 15 min on), that in turn enables NF-κB phosphorylation (**Figure 65**) and its consequent nuclear translocation (**Figure 67)**, being both events recorded after 120 min. Thus, FP20Hmp activity is characterized by a different kinetics and potency compared to S-LPS. It is known, through the implementation of mathematical models, that the amount of NF-κB translocation and its kinetics depends on the strength of activation of the receptor, as well as other signaling factors[270]. This happens most probably due to different binding with the receptor. Furthermore, it has been reported that LPS response is more homogenous amongst macrophages, while responses to other stimuli lead to different cell-to-cell NF-κB dynamics even within the same population[241]. The latter can help to explain why the response of our new compound has a more prolonged kinetics compared to LPS.

Interestingly, this data, compared to the parent compound FP20, shows that the C6-functionalized FP20Hmp appears to have a different mechanism of action. FP20 does not seem to stimulate the activation of the MyD88 pathway, namely NF-κB transcription or nuclear translocation[143]. On the other hand, as the data in **Figure 66** and **Figure 67** illustrates, FP20Hmp is able to induce MyD88-dependent p65 nuclear translocation.

TLR4 activation by LPS is also able to initiate the internalization of the receptor and activation of a second signaling cascade, the TRAM/TRIF-dependent pathway, that results in IRF3 phosphorylation and nuclear translocation, ultimately leading to IFN-β production[269]. We found no evidence of TRAM/TRIF pathway activation neither in Western blot analysis, by investigating the presence of p-IRF3 and p-STAT1, nor in immunofluorescence analysis by detecting p-IRF3 nuclear translocation. Additionally, no IFN-β production was observed. Altogether, the data on TDM shows that FP20Hmp is an active TLR4 agonist able to induce the MyD88 pathway but not the TRAM/TRIF pathway. This observation helps to explain why the cytokine profile between S-LPS and FP20Hmp is different. It its reported that MyD88 activation is important for early NF-κB responses and subsequent cytokine production, while TRIF is required for more sustained responses which leads to higher levels of pro-inflammatory modulators, such as TNF[271]. LPS is known for its highly inflammatory response that can lead, in some cases, to cytokine storm and sepsis[272]. In the context of vaccine adjuvant development, we aim for a modulating and immunostimulanting scenario without associated toxicity, which can be decreased by lowering the probability of an exacerbated inflammatory response.
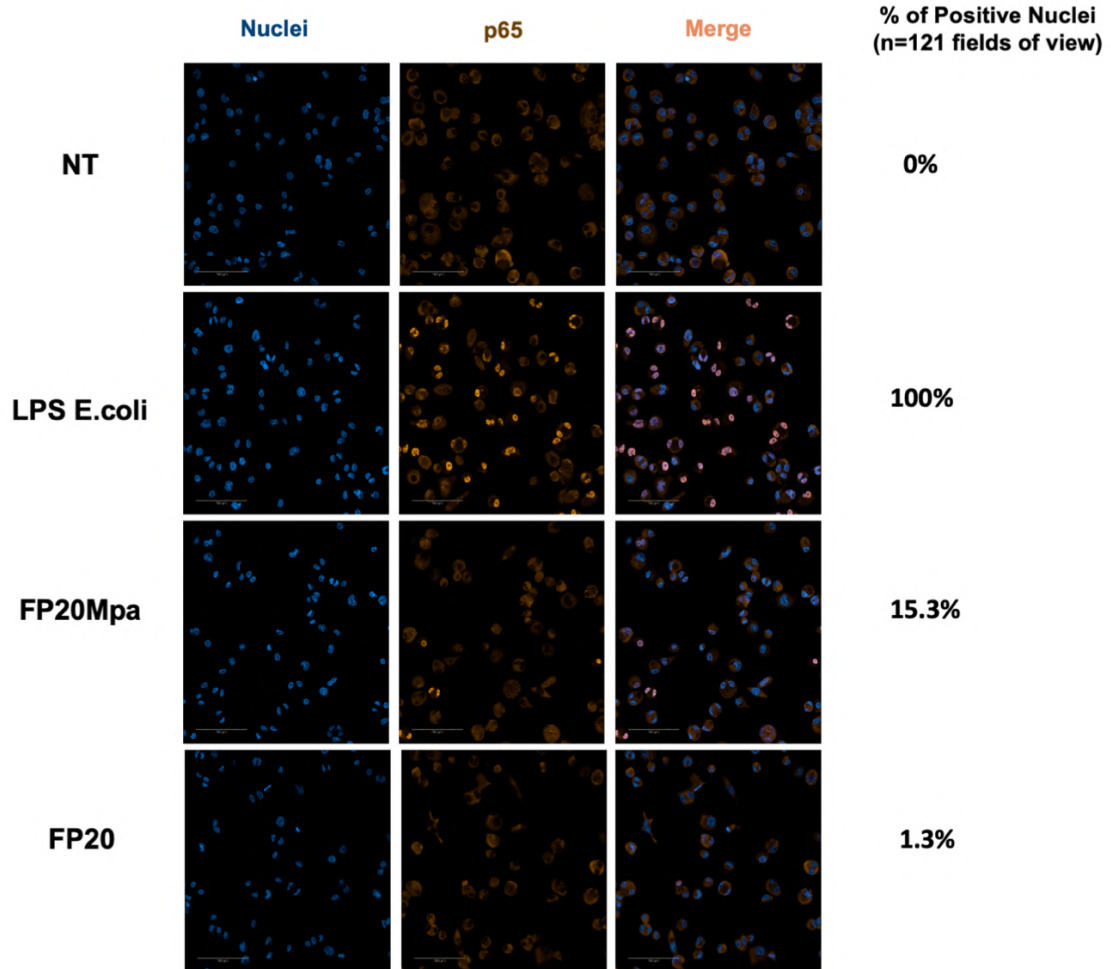
Figure 66. Immunofluorescence analysis of NF-κB (p65 subunit) nuclear translocation, 90 minutes after treatment with LPS (100ng/mL) or FP20Hmp (10μM)
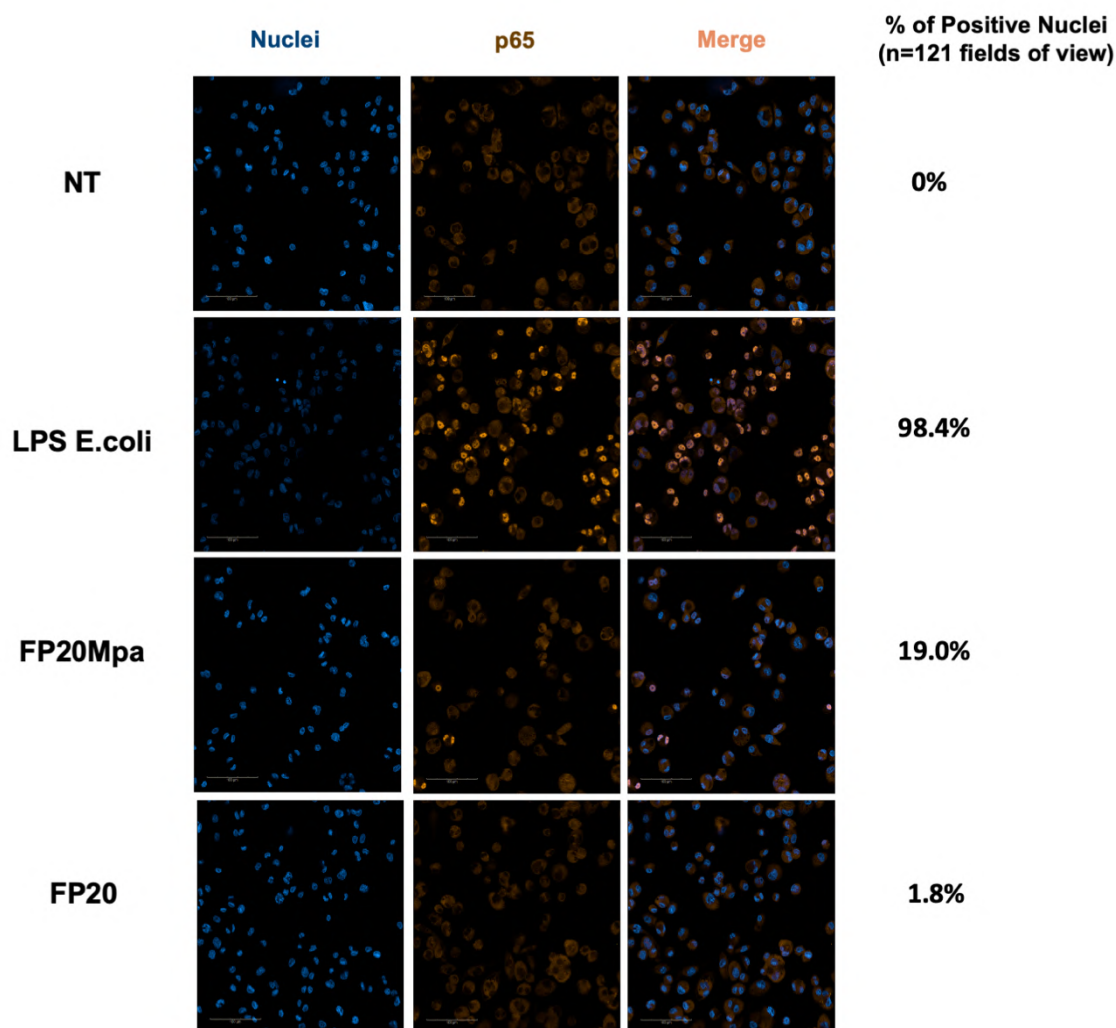
Figure 67. Immunofluorescence analysis of NF-κB (p65 subunit) nuclear translocation, 2 hours after treatment with LPS (100ng/mL) or FP20Hmp (10μM)

4.9.4. Adjuvant Activity of FP20Hmp in mice

To assess the adjuvant efficacy of FP20Hmp *in vivo,* C57BL/6 mice were immunized at day 0 and day 21 with 10μg of the model OVA formulated either with or without 10μg of adjuvant (MPLA or FP20Hmp). Pre-boost antibody responses on day 21 and final antibody responses on day 42 were evaluated and are shown in **Figure 68**. Total IgG data shows that FP20Hmp is able to induce significant levels of IgG compared to the OVA control similarly to MPLA, after two immunizations. *In vivo* toxicity was evaluated by monitoring weight changes as well as liver transaminases levels (ALT and AST) and no significant toxicity was detected (**Figure 69**).
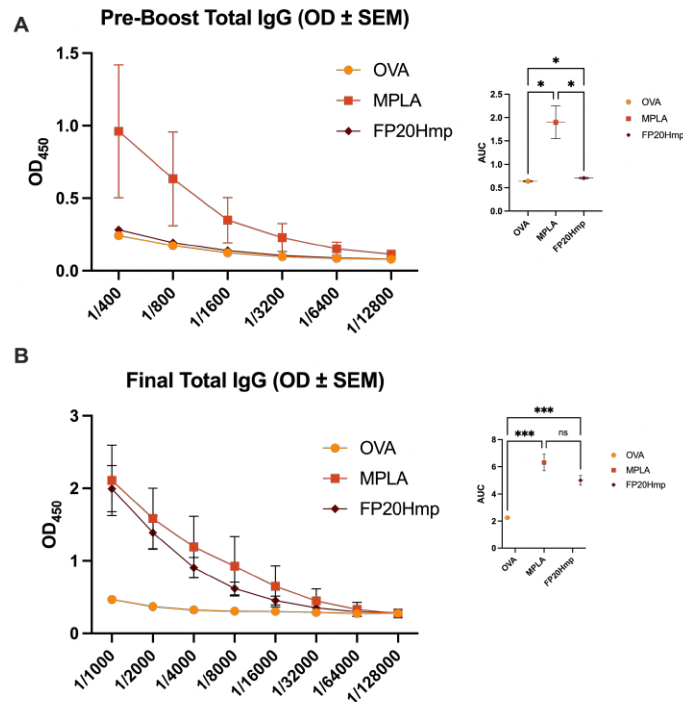
Figure 68. Total anti-OVA IgG after one (A) and boost immunization (B). C57BL/6 mice were immunized with OVA formulated with or without MPLA and FP20Hmp as adjuvants. (A) Total antibody response to prime OVA immunization 21 days post immunization. (B) Total antibody response to boost immunization 42 days post immunization. Values represent mean ± SEM. Brown–Forsythe and Welch one-way ANOVA tests (with an alpha of 0.05) were utilized to compare the areas under each curve. *p < 0.05; **p < 0.01; ***p < 0.001.
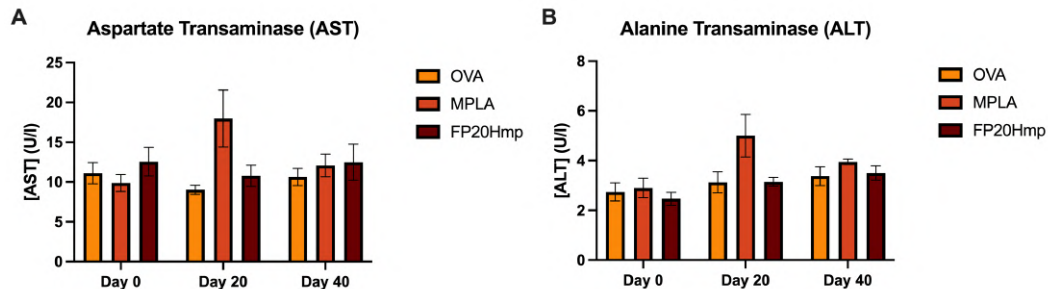
Figure 69. Liver transaminases of C57BL/6 mice immunized with MPLA and FP20Hmp

Looking at IgG subtyping in **Figure 70**, it is possible to observe that MPLA and FP20Hmp show similar profiles for IgG2c and IgG3. On the other hand, IgG1 profiles are slightly different and FP20Rha does not induce OVA-specific IgG2b, while MPLA does. Both MPLA and FP20Hmp induce significatively IgG1, which has been associated with a Th2 response[273]. Furthermore, both MPLA and FP20Hmp significatively induce IgG2c, which has been associated with Th1 responses[274]. Interestingly, MPLA is able to significatively induce IgG2b while FP20Hmp is not. This subtype of IgG has also been described as part of Th1 responses and MPLA results are consistent with previous literature[275].
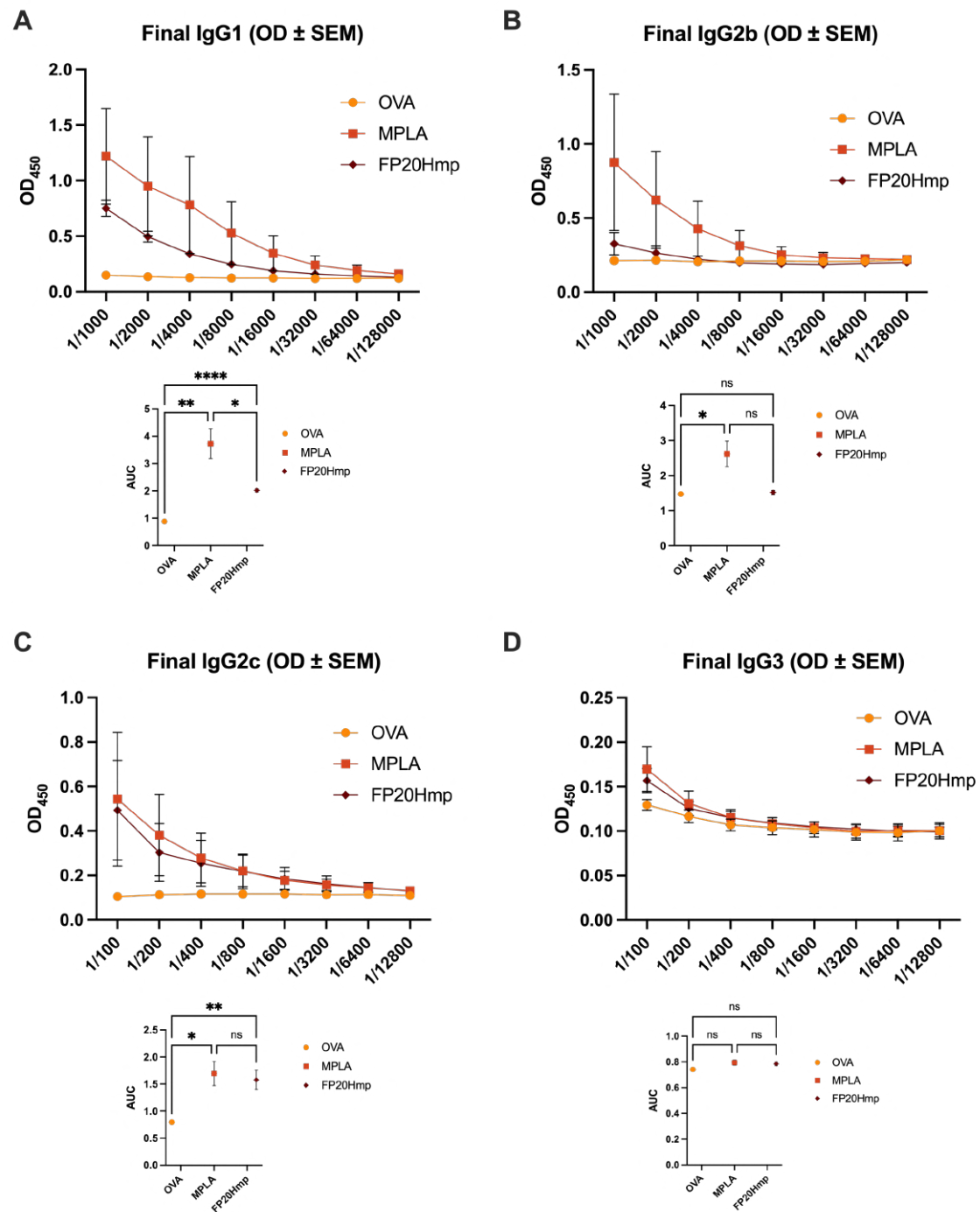
Figure 70. IgG profile in response to boost OVA immunization, formulated with or without MPLA and FP20Hmp, 42 days post immunization. (A) IgG1, (B) IgG2b, (C) IgG2c, and (D) IgG3. Values represent mean ± SEM. Brown–Forsythe and Welch one-way ANOVA tests (with an alpha of 0.05) were utilized to compare the areas under each curve. *p < 0.05; **p < 0.01; ***p < 0.001.

4.9.5. Adjuvant activity of FP20Hmp in a formulation with *E. faecium* antigen PpiC

Four groups of rabbits were immunized with either FP20Hmp, the recombinantly produced PpiC, PpiC and MPLA or PpiC and FP20Hmp. The rabbit sera collected were

evaluated by ELISA for PpiC-specific antibodies (**Figure 71**). Rabbits immunized only with FP20Hmp did not produce antibodies, as expected. The sera from the three other groups of rabbits contained antibodies capable of binding specifically to PpiC. while every group of rabbits immunized with either PpiC, PpiC and MPLA or PpiC and FP20Hmp showed a significant increase in their terminal bleeds (TBs) while compared with the associated pre-immunization serum (PI). Sera collected from rabbits immunized with PpiC and an adjuvant, whether it was MPLA or FP20Hmp, presented with significantly higher PpiC-specific antibodies than the group immunized with the antigen alone. Although higher titters were found, there was no statistical difference between the quantity of antibodies binding specifically to PpiC when comparing TB-PpiC+MPLA to TB-PpiC+FP20Hmp. The data presented shows that FP20Hmp could trigger the production of antibodies binding to the *E. faecium* antigen PpiC in similar quantities as the difficult-to-produce and already commercialized adjuvant MPLA.
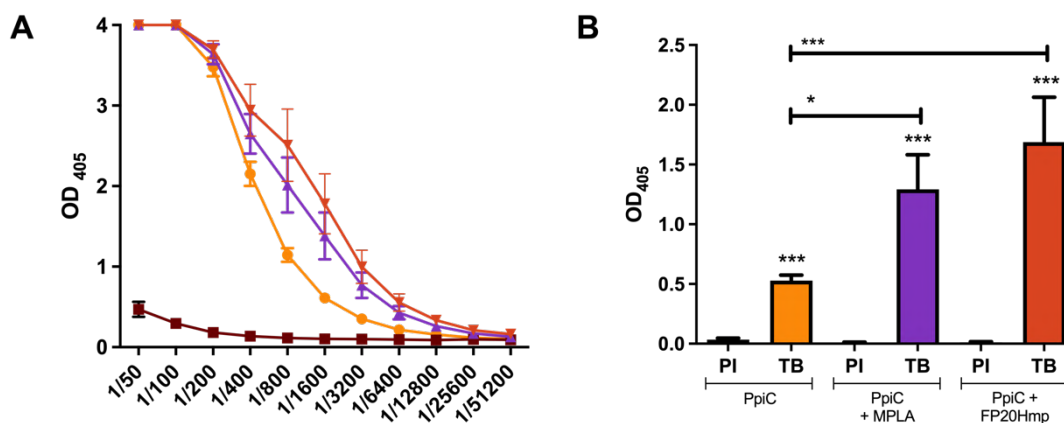
Figure 71. Immunoreactivity towards PpiC. (A) Total anti-PpiC IgG determined by ELISA, rabbits immunized with FP20Hmp (brown), PpiC (yellow), PpiC and MPLA (purple) and PpiC and FP20HMP (red). (B) Absorbances of pre-immune (PI) and terminal bleeds (TB), diluted at 1:1600, for the rabbits immunized with PpiC (purple), PpiC and MPLA (orange) and PpiC and FP20HMP (blue). The values for PIs and TBs were statistically compared using an unpaired two-tailed T-test with a 95% confidence interval. Statistical differences were also assessed between TBs of the different conditions with the same statistical test. Bars and whiskers represent mean values ± standard error of the mean (SEM). *$P \leq 0.05$, *** $P \leq 0,001$.

To verify that the IgG produced were able to bind the bacteria, we performed a Whole-bacterial-cell ELISA by coating Nunc-Immuno MaxiSorp 96-well plates with a previously fixed *E. faecium* 11236/1 and adding the PIs and TBs diluted at 1:50. The difference of absorbances at 405nm (ΔAbs_{405nm}) was calculated and plotted in **Figure 72**. While the immunization with PpiC coupled with MPLA did increase the quantity of *E. faecium* 11236/1-binding antibodies, the difference was not statistically significant when compared to the ΔAbs_{405nm} obtained in rabbits immunized with the antigen alone.

However, the increase of antibodies binding to the bacterium by immunization with PpiC and FP20Hmp was significantly higher when compared to the group immunized with PpiC alone.
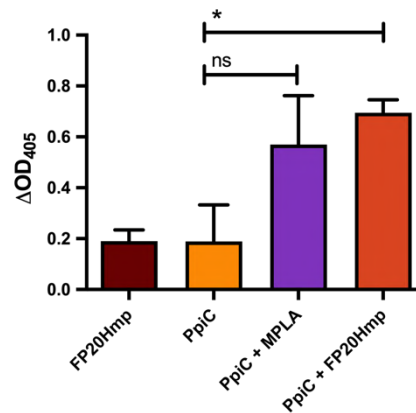
Figure 72.Immunoreactivity towards *E. faecium* 11236/1 determined by Whole-bacterial-cell ELISA. The difference of absorbances at 405nm (ΔAbs405nm) was calculated by subtracting the absorbance obtained after incubation of PI at 1:50 to the absorbance obtained with TB at the same dilution. Rabbit sera tested were collected before or after immunization with FP20Hmp (brown), PpiC (yellow), PpiC and MPLA (purple) and PpiC and FP20Hmp (red). Statistical differences were also assessed between TBs of the different conditions with the same statistical test. Bars and whiskers represent mean values ± standard error of the mean (SEM). NS, not significant (P > 0.05), *P ≤ 0.05.

CHAPTER IV

New screening method for TLR4-targeting proinflammatory compounds using FTIR: A global inflammation signature

Adapted from: Diletta Ami, **Ana Rita Franco**, Valentina Artusa, Paolo Mereghetti, Francesco Peri, and Antonino Natalello. "A global picture of molecular changes associated to LPS treatment in THP-1 derived human macrophages by Fourier transform infrared microspectroscopy." International Journal of Molecular Sciences 23, no. 21 (2022): 13447. https://doi.org/10.3390/ijms232113447

Author Contribution: Contributed to the study design. Performed cell treatments. Contributed to the writing of the manuscript.

4.10. Background

Fourier Transform Infrared (FTIR) microspectroscopy is a vibrational spectroscopic technique used in different fields. This technique studies the interaction between matter and infrared (IR) radiation[276]. The infrared region of the electromagnetic spectra is composed of waves with a wavelength between 0.8 to 100 μm and its typically divided into near-, mid- and far-IR. When a molecule is exposed to radiation, its bonds will absorb the IR radiation that has the same frequency of vibration. This allows for the identification of different bonds in different regions of the spectra. **Figure 73** represents the different regions of the mid-IR spectra.
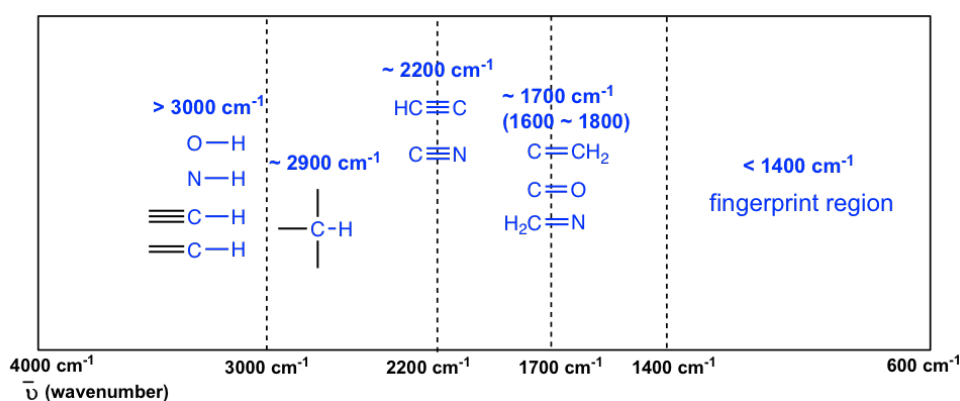
Figure 73. Representative spectrum in the mid-IR region.

By coupling an infrared microscope to a FTIR spectrometer it is possible to collect IR spectra from samples with an area as little as 20 x 20 microns[277]. The unique spectra and posterior analysis enables the identification of molecular conformations, bonding types, functional groups and intermolecular interactions[276]. FTIR peaks are usually narrow and can be related to a particular chemical bond or functional group[278]. More importantly, FTIR is a reproducible and non-destructive technique, with minimal samples required[278]. Sample preparation is a key aspect of FTIR measurements. In order to study changes occurring in cells or tissue, it is very important to standardize sample preparation to ensure that significant spectral components are due to the process of interest and not to changes in the processing[277]. While samples need to be dried before being measured, it was proven by Raman spectroscopy, a similar technique whose results are not altered by water, that drying the samples did not affect their IR spectra.[277]

When applied to whole cells, FITR puts into evidence the global composition of a sample and provides a global picture of what is contained within the cell, such as lipids,

proteins, nucleic acids, among others[279]. For example, when applied to cancer cells it was demonstrated that cells that went through the same metabolic changes would have similar FTIR spectra[279]. However, the information contained within the spectra is quite complex and, in order to attribute meaning to the findings, it needs to be examined using a multivariate analysis approach[280]. This becomes even more important when studying time-sensitive processes, namely cell differentiation and maturation. This type of analysis creates a statistical model between the spectra and the cellular response. By establishing a basal spectra, it is possible to understand which spectral components underwent significative change[280]. Nevertheless, before starting a multivariate analysis, enhancement of the IR spectra can be performed to clarify absorption bands using a second derivative analysis[277]. One of the multivariate analysis that can be employed is partial least-squares discriminant analysis (PLS-DA)[281]. Briefly, this analysis applies a partial least-square algorithm. It determines the threshold of discrimination and separates classes[282]. In short, it is the combination of the second derivative with the PLS-DA analysis that allows for a clear identification of the spectral components that are significative for each studied cellular process.

As it was discussed in the introduction section, innate immune inflammatory process are complex cellular events that might include different receptors and cellular mediators. Furthermore, there is a constant flow of newly synthesized cytokines, chemokines and other mediators[283]. Accordingly, it is fitted that this is one of the processes in which FTIR can be applied to further understand this event. It is possible to find several works that apply FTIR to the study of anti-inflammatory drugs, showing its value to the drug development field[284–288]. A recent work has also used this technique as a diagnosis tool of inflammatory fibrous hyperplasia, to distinguish between pathologic and non-pathological tissue samples[289]. Nevertheless, the application of this technique in understanding inflammation triggered by LPS is lacking.

LPS bind to the TLR4/MD2 complex and promotes the activation of different inflammatory mediators through a downstream cascade that leads to gene transcription. Particularly, LPS stimulate NF-κB and IRF3 dependent transcription as well as activation of NLRP3 inflammasome. In turn, these events lead to the production of different inflammatory mediators, such as pro and anti-inflammatory cytokines, Type I interferon and pyroptosis[290]. All of these processes lead to significant changes in the cell

composition in terms of biomolecules, as well as number of protein-protein interactions.[289]

In particular, macrophages are susceptible cells to LPS-mediated inflammation. While these cells also express PRRs and therefore are able to start signaling cascades, they also undergo polarization into M1 proinflammatory phenotype, in response to LPS[291]. This type of macrophages characteristically produces TNF, IL-6, IL-12, IL-23 and reactive oxygen species such as NO[292]. This change comes with a metabolic reprograming with enhancement of glycolysis processes and fatty acid synthesis, a process called Warburg effect[292]. The latter leads to an increased uptake of glucose, amino acids and fatty acids, which are processes that require cellular energy and lipid metabolism involvement[293].

Thus, LPS signaling leads to several changes in biomolecules within the cells, as well as interactions between them. For example, the assembly of SMOCs, like the myddosome and triffosome, require a number of protein-protein interactions[294]. Understanding the timing of such alterations, as well as the molecular entities involved, could bring better understanding to LPS-dependent changes via TLR4-activation in macrophages. Therefore, applying FTIR measurements combined with PLS-DA analysis can be of great advantage to the field. Furthermore, creating a global picture of TLR4-dependent inflammation could lead to the development of a screening method for anti- and proinflammatory compounds.

4.11. Experimental Design

The biochemical modifications occurring in TDM cells exposed to LPS were investigated by FTIR microspectroscopy. In particular, we employed PLS-DA to compare FTIR data obtained from intact TDM treated with LPS at different time points over the course of 24 hours, with data obtained from non-treated TDM. Cells were seeded and differentiated. After differentiation cells were treated during a time course with collection at t= 15 minutes, 3 hours, and 24 hours. After washing, intact cells were measured using FTIR. **Figure 74** illustrates the experimental design.
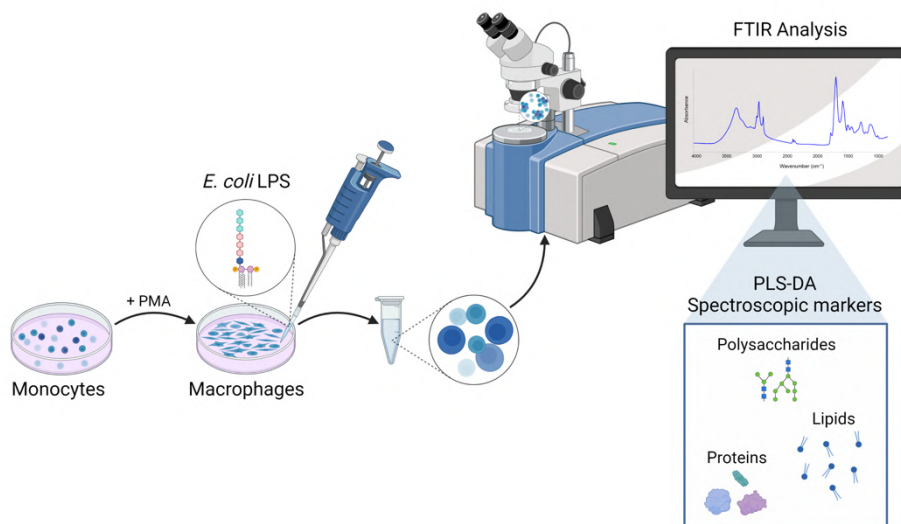
Figure 74. Experimental design

This multivariate analysis, indeed, allowed not only the evaluation of the statistical significance of the observed spectral differences, but also the identification of the spectral components responsible for the discrimination between treated and untreated cells, taking also into account the period of LPS exposure. The analysis has been performed on the second derivative spectra that have been calculated to better resolve the overlapped components in the absorption bands, necessary for the identification of peak positions and their assignment to the vibrational modes of the different molecules[295–297].

4.12. Results and Discussion

4.12.1. Euclidean distance values of PLS-DA of TDM treated with LPS

Figure 75 shows the Euclidean distance values of the PLS-DA projections of TDM cells treated with LPS and zero-time untreated cells (0 h), considering both the different spectral ranges and the period of incubation with LPS. The two-ways repeated-

measurement ANOVA analysis indicates that the distances between treated and untreated TDM cells were significant for all the spectral regions and times considered.
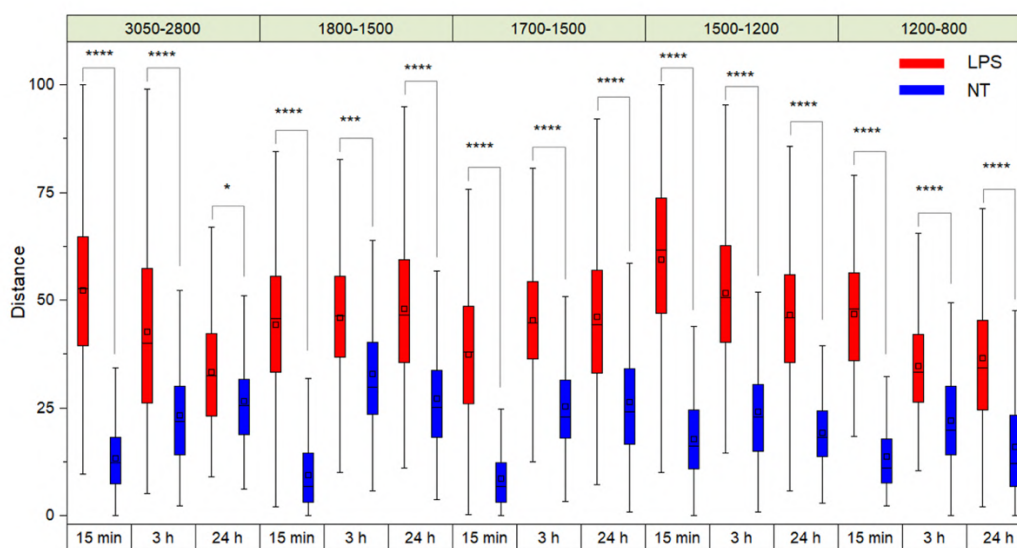
Figure 75. Elucidation distance values of the PLS-DA projections of TDM cells treated with LPS and non-treated cells (NT). The black horizontal line within the box is the median, the square within the box is the mean, the box ends show the first (Q1) and third (Q3) quartiles, the lower whisker is computed as the maximum value between the absolute minimum and Q1 – 1.5 × IQR, and the upper whisker is the minimum between the absolute maximum and Q3 + 1.5 × IQR. Here, IQR is the interquartile range computed as Q3–Q1. Stars indicate the statistical significance evaluated by a two-ways repeated-measurement ANOVA analysis.

4.12.2. FTIR analysis of protein secondary structure modifications in TDM cells exposed to LPS

Figure 76 reports the second derivative analysis of the Amide I band, in the 1700−1600 cm−1 range, due to the C=O stretching vibration of the peptide bond, which provides information on the secondary structures of the whole cell proteins.[298,299] Untreated cells second derivative spectrum (0 h) was characterised by a component at ~1655 cm^{-1}, which arises from α-helix and random coil structures and a component at ~1639 cm^{-1}, which can be assigned to β-sheets[298,299]. After 15 minutes of LPS treatment, a downshift of the β-sheet band (to ~1637 cm^{-1}) was detected (**Figure 76**), accompanied by the appearance of a shoulder at lower wavenumbers that can be assigned to intermolecular β-sheets, typical of protein aggregates and/or protein-protein interactions[297,300,301]. Then, starting from 3 h of treatment with LPS, and up to the end of our observation (24 h), an intensity increase of the α-helix / random coil band at ~1655 cm^{-1} was found, together with the disappearance of the shoulder at ~1628 cm^{-1} (Figure 76). Moreover, in particular in the 24 h LPS-treated spectrum, an intensity decrease of the

1638 cm^{-1} band was also detected (**Figure 76**). Notably, 15 minutes after LPS administration, PLS-DA identified the spectral component at ~1628 cm^{-1}, typical of protein aggregates and/or protein-protein interactions, as the most relevant for the discrimination (overall weight 100%).

The increase of the α-helix band intensity (**Figure 76**) that we observed in the 3 h (overall weight 100 %) and 24 h (overall weight 100 %) spectra, accompanied by a further downshift of the β-sheet band, might be diagnostic of LPS-induced expression of proteins with both α-helix and β-sheet structures.
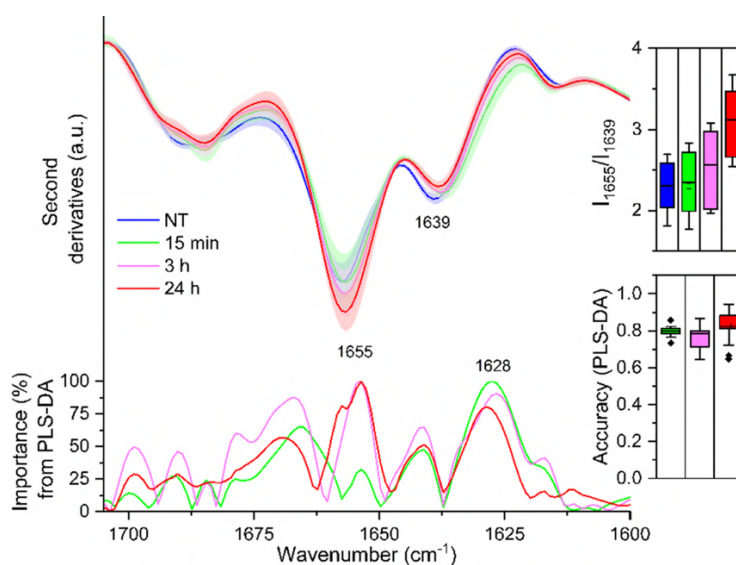
Figure 76. Mean second derivative spectra in the Amide I band of TDM at t=0, 15 min, 3h an 24h of LPS treatment. Standard deviation has also been displayed as a shadowed area. In the inset, the intensity ratio between the 1655 cm-1 and the 1639 cm-1 peaks, taken from the second derivatives, is illustrated. Below, the wavenumber importance for PLS-DA discrimination performed in the 1700-1600 cm-1 spectral range is shown. The PLS-DA discrimination accuracy has been also reported.

Overall, our findings indicate that LPS stimulation induces significant global changes in the protein content and likely also in the protein-protein interactions that in the IR spectra can be detected as changes in the whole cell protein secondary structures.

These results are in agreement with Meijer et al.[302] proteomic analysis that showed that LPS stimulation leads to significant up-regulation of a cluster of pro-inflammatory proteins, including the pro-inflammatory proteins macrophage migration inhibitory factor (MIF) and TNF, and various pro-inflammatory chemokines. The increased ex-pression of several chemokines points to an important role of LPS-stimulated macrophages in recruiting other immune cells to sites of inflammation. Another upregulated functional cluster consists of proteins involved in actin cytoskeleton organisation, migration,

chemotaxis and phagocytosis, as well as in transduction of LPS-induced TLR4 signalling and MHC-II mediated antigen presentation[302]. Proteoglycans (PGs) - glycosylated proteins, which have covalently attached glycosaminoglycans (GAGs) - are also known to be produced as extracellular and cell surface proteoglycans in response to LPS stimulation[303]. Moreover, Dhungana et al.[304] report a stimulus-induced statistically significant global increase in the number of distinct proteins in rafts in LPS-stimulated RAW macrophages. Authors described an LPS-induced dynamic exchange of proteasome subunits in macrophage triggered by LPS, which is thought to be "targeted" to lipid rafts in host cells in part through its interactions with raft-resident proteins (i.e. CD14). Specifically, they suggest that during LPS exposure a substantial number of new (i.e. basally raft-excluded) proteins are recruited to rafts in a time-dependent manner. Our observations about protein-protein interactions could pair with their data that collectively provide evidence for the localization of proteasome subunits to rafts, their reorganisation within rafts following LPS exposure, and an associated functional change in proteasomal activity specific to rafts that occurs during LPS signalling[304].

Interestingly, the appearance of the 1628 cm^{-1} shoulder might be associated with the interaction of LPS with the TLR4/MD-2 complex situated on the plasma membrane to initiate the MyD88-dependent signalling. Protein-protein interactions are essential for TLR4 signalling, especially for the formation of the necessary SMOCs, the myddosome and the triffosome[297,303,304].

4.12.3. FTIR analysis of lipid modifications in TDM cells upon exposure to LPS: insights from the 1500-1200 cm^{-1} and 3050-2800 cm^{-1} spectral ranges

The infrared absorption of TDM cells in the 1500−1200 cm^{-1} spectral range is mainly due to the absorption of methyl and methylene groups from different biomolecules, including lipid hydrocarbon chains and head groups[299,305,306]. Moreover, the absorption of phosphate groups mainly from nucleic acids and lipids also occurs in this spectral range[299,305–307]. Notably, comparing the NT (0 h) sample with LPS-treated cells spectra, PLS-DA identified as relevant – at each time point – only the component at ~1467 cm^{-1} (**Figure 77 a**), mainly ascribable to the overlapping absorption of CH2 and CH3 groups from lipid hydrocarbon chains[299,305,306]. The intensity of this component,

higher in the NT (0 h) cells, decreases rapidly at 15 minutes, and then increases again up to 24 h.

To investigate more in detail the effects of LPS on THP-1 derived macrophage lipids, FTIR analysis has been extended to the 3050–2800 cm^{-1} spectral range, dominated by the absorption of lipid hydrocarbon chains. As shown in **Figure 77 b**, the spectrum of untreated cells (0 h) was characterized by four main absorption bands: ~2921 cm^{-1} and 2852 cm^{-1}, due to the antisymmetric and symmetric stretching of CH2; the ~2959 cm^{-1} and 2872 cm^{-1}, due to the asymmetric and symmetric stretching of CH3[299,305,306].

The CH2 bands decreased in intensity at 15 minutes of LPS treatment, and then increased again at 3 h, up to 24 h. In **Figure 77 a**, the ratio between the intensity of the CH2 and CH3 bands[308,309] is shown. The increase of this ratio, which is significant at 24 h post LPS treatment, is ascribable to the formation of longer hydrocarbon chains, in agreement with the spectral profile variation of the ~1467 cm^{-1} band, discussed above (**Figure 77 a**). In addition, this result is also supported by the spectral changes displayed by the C=O band at ~ 1742 cm^{-1}, whose intensity, compared to that of untreated cells (0 h), decreased at 15 minutes and then increased again up to 24 h This absorption is mainly associated with the stretching vibration of lipid ester groups[305].

As it will be further discussed in the next section these results indicate that LPS stimulation induced a modification of the physicochemical properties of cell lipids. Interestingly, recent discoveries point to a complex metabolic network during macrophage activation, in particular regarding macrophage immunometabolism from the perspective of the metabolism of lipids (reviewed by Batista-Gonzalez et al.[310]). In particular, it has been reported that the cell membrane lipid constituents, including glycerophospholipids and sphingolipids, are essential in modulating the pathogen recognition, and alterations in these molecules have been reported in LPS stimulated cells[293,311]. Among these, it has been speculated that some sphingolipid species can specifically regulate the early pro-inflammatory or late pro-resolution phases of TLR4 activation[312]. Furthermore, phospholipids play a crucial role in cell-mediated inflammatory responses, including LPS-induced inflammation, since they are important signaling molecules involved in the regulation of cytokine production and because they provide precursors for the synthesis of potent lipid mediators[313]. Recent experimental evidence suggests that LPS-stimulated macrophages increase their fatty acid synthesis to

store increased amounts of triacylglycerols and cholesterol esters in lipid droplets.[314] This induction of fatty acid synthesis is indispensable for effector functions such as T cell priming[315], inflammasome activation[316] and pro-inflammatory cytokine production[314,315].
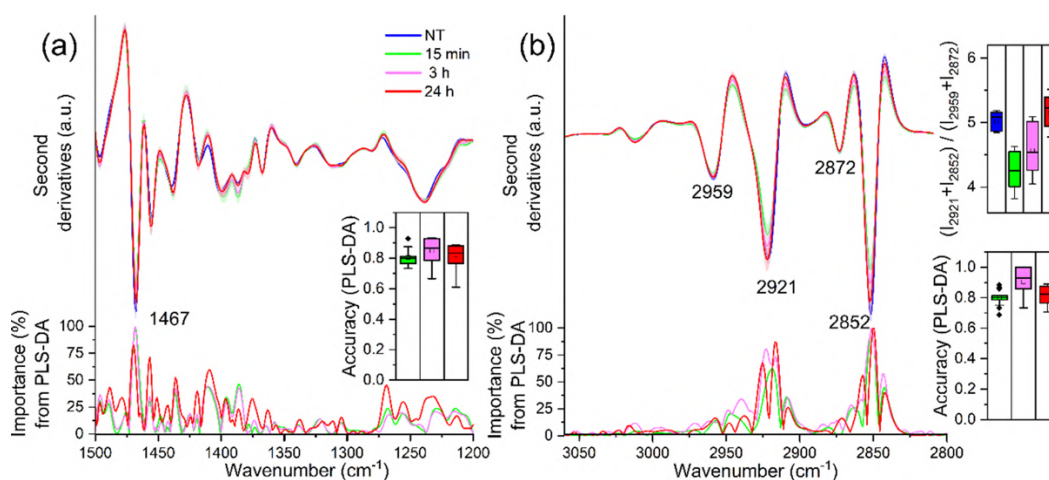
Figure 77. Mean second derivative spectra in the 1500-1200 cm⁻¹ (a) and 3050-2800 cm⁻¹ (B) ranges of TDM cells at t=0, 15 min, 3h and 24h of treatment with LPS. Standard deviation has also been displayed as a shadowed area. Below, the wavenumber im-portance for PLS-DA discrimination performed in the selected spectral range is shown for each panel. In the insets, the PLS-DA discrimination accuracy (panels a and b) and the intensity ratio among the CH2 and the CH3 peaks (panel b) are reported.

4.12.4. FTIR analysis of TDM exposed to LPS: analysis of the fingerprint region

The 1200-800 cm⁻¹ spectral range, the so-called fingerprint, is a very crowded and highly overlapped region of the spectrum, being dominated by the absorption of complex carbohydrate modes, isolated and/or associated or bound to other molecules, with important contributions also from lipids and nucleic acids. For this reason, the band assignment in this spectral range is not easy and, sometimes, not unequivocal. Overall, as we will describe in the following lines, the spectral components pulled out by PLS-DA are mostly ascribable to saccharides (including also GAGs), and lipids, in particular phospholipids and sphingomyelin.

Giving a look at the loading plot relative to 15 minutes and 3 h of LPS treatment, PLS-DA brought out only one component carrying the higher spectral variance between treated and untreated cells: the ~1172 cm⁻¹ (overall weight ~100) (**Figure 78**), which decreased in intensity at 15 minutes upon LPS incubation, and then increased again up to 3 h (**Figure 78**). As mentioned above, the assignment of this band is not immediate due to the overlapping contributions of different components. Considering its intensity

variation, which is synchronous with that of other bands assigned to lipid moieties, we tentatively assign it mainly to the CO-O-C stretching vibrations of phospholipids.[299,305] Moreover, it has been also associated with the (C-OH) and (C-C) stretching and (C–O–H) bending of carbohydrates[317,318] and with the SO4 and C-O-S stretching of GAGs, such as heparin and heparan sulphate[319,320]. GAGs are highly heterogeneous linear macromolecules made up of a repeating disaccharide unit, with a variable number of sulphates. They are not only typical extracellular matrix components but are also present in the cell membrane and as intracellular granules[321]. Considering that GAGs associated with PGs are known to play a crucial role in immune defense, being also involved in cytokine and chemokine regulation[322], we cannot also exclude a contribution of these complex molecules to the ~1172 cm^{-1} absorption.

Noteworthy, PLS-DA relative to 24 h of treatment (**Figure 78**) depicts a more complex scenario. The analysis, indeed, disclosed different components responsible for the classification: in addition to the ~ 1172 cm^{-1} band (overall weight ~75%), displaying again a lower intensity compared to NT cells but similar to that of LPS-3 h, PLS-DA identified two more components that occurred at higher intensities in the 24 h treated cells compared to untreated cells (0 h): at ~1022 cm^{-1} and ~968 cm^{-1} (both with an overall weight ~75%). The first band is ascribable mainly to the symmetric stretching of (C-O) ring vibrations of polysaccharides[317,318], being also typical of glycosylated proteins[323] and lipids[324]. The ~ 1022 cm^{-1} band falls in a spectral range associated also with the vibrations of GAG pyranose ring structures[319]. Then, considering again the simultaneous variation in intensity of other absorption bands associated to lipids, we assign the component at ~ 968 cm-1 mainly to the antisymmetric stretching of the N(CH3)$_3$ group[305], which is characteristic not only of phosphatidylcholine but also of the sphingolipid sphingomyelin. In particular, sphingolipids do not just form the building blocks of eukaryotic cell membranes, but also, they play a significant role in regulating cell functions. In this regard, Olona et al. reported that LPS induces the biosynthesis of sphingolipids that promote TLR4 signaling in macrophages[312].

Furthermore, PLS-DA identified two other significant components, which displayed a higher intensity in untreated cells (0 h) compared to 24 h: the component around 1104 cm^{-1} (overall weight ~75%) and that at ~ 1082-1073 cm^{-1} (overall weight ~100%). The assignment of these bands is particularly difficult, because in this spectral

window the absorption of phosphates, mainly from nucleic acids and lipids[305,307], is dominant as well as that of polysaccharides[325]. Indeed, these absorptions are also associated with different vibrational modes from polysaccharide rings, including the ones from GAGs, such as hyaluronic acid[319,326]. Notably, the ~ 1082-1073 cm^{-1} band is also assigned to the symmetric phosphate (PO2-) stretching mode typical, for instance, of phospholipids and sphingomyelin[305].

Even if its overall weight is lower than 75% (~73%), we should also mention the ~ 834 cm-1 component, detected in untreated cells (0 h), and downshifted to ~824 cm-1 in 24 h treated cells, where it is also more resolved, which might reflect structural differences in the glycosidic linkages of polysaccharides, being assigned mainly to C1-H ring vibrations[318,327]. Moreover, this absorption has been also assigned to the C-O-S vibration from GAGs[328,329].
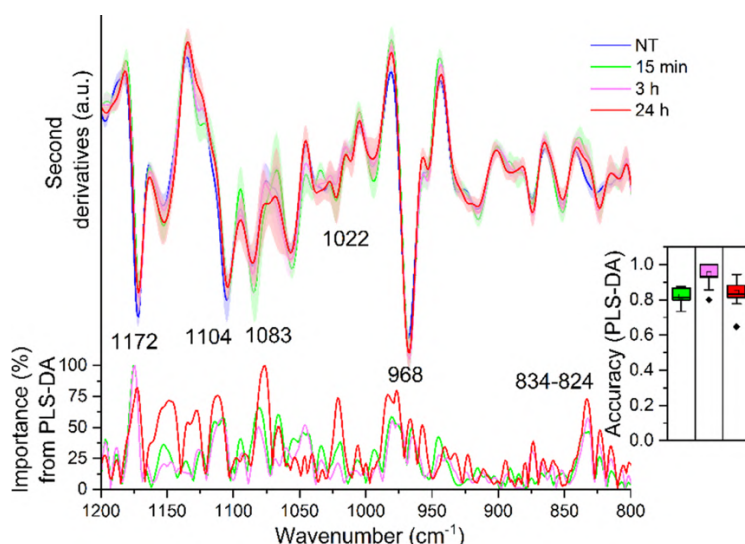
Figure 78. Mean second derivative spectra in the 1200-800 cm^{-1} range of TDM at t=0, 15 min, 3h and 24h after treatment with LPS. Standard deviation has also been displayed as a shadowed area. Below, the wavenumber im-portance for PLS-DA discrimination performed in the 1200-800 cm-1 spectral range is shown. The PLS-DA discrimination accuracy has been also reported in the inset.

Overall, the fingerprint analysis on one hand supports the importance of the physicochemical variations of lipids triggered by LPS, as discussed above; on the other, it sheds lights on a possible involvement of glycan modifications that could impact on the cell mechanical properties which in turn may contribute to higher phagocytosis activity.[330] In addition, the observed changes, upon LPS stimulation, in sulfated sugars could be associated with the biosynthesis of sulfated glycosphingolipids or GAGs that are known to be endogenous ligands for the TLR4/MD-2 complex.[331]

5. Conclusion and outlooks

The pipeline for new and safe vaccines to target AMR is slow and affected by the lack of effective vaccine adjuvants. Nevertheless, vaccines are the most attractive strategy since they can reduce disease burden caused by resistant bacteria and overall antibiotic consumption[330]. The development of small molecules able to modulate and enhance the immune system's response to antigens is crucial. TLR4 agonists have shown the ability to initiate potent proinflammatory responses after the activation of intracellular pathways, namely MyD88 and TRAM/TRIF pathway[332]. Some studies have also shown that some TLR4 activating molecules, such as MPLA, are able to increase resistance to infection through immune cell modulation and increased bacterial clearance[333–335]. Thus, TLR4-direct adjuvants are important molecules to include in novel antimicrobial vaccine formulations. Previously developed compound FP18, showed proinflammatory activity *in vitro* and *in vivo*[226]. However, its structural features made it difficult to functionalize the molecule to improve its interaction with the receptor, activity, and solubility.

Monosaccharide FP20, a novel structure with a phosphate group in position C4 instead of C1 and three FA chains in C1, 2 and 3, was developed, along with a small library of derivatives. The change of phosphate position from C1 to C4 should ensure an increased chemical stability of FP20 compared to FP18 which in turn would allow for further functionalization of free C6 hydroxyl.

Compounds FP20-24 were tested *in vitro* in TDM cells and using MD techniques, to study the effect of the FA chain length in the activity as TLR4 agonists. Results show that three C_{12} chains (FP20) or C_{10} chains (FP22) are better ligands for TLR4/MD-2 in MD simulations and have higher biological activity on TDM. This observation parallels what we described in the case of TLR4 antagonists with a similar structure (Compounds FP7, 10, 12 and 16)[194]. In MD simulations, it was observed that FP24, with one C_{12} and two C_{10} FA chains has an inverted-cone shape which decreased its polar interactions with the target receptor. Through MD simulations it was also observed that the α-anomer of FP20 (α-FP20) presents a different packing of the lipophilic chains, which decreases the interaction with TLR4/MD-2, and upstream with the PBP and CD14 proteins, in respect

to its β analogue. This data was validated through lack of activity in α-FP20 treated TDM cells. In the same cell line, FP200, with two phosphates, shows lower activity which is consistent with the MD data that shows that one phosphate and an anomeric-β FA chain are optimal for receptor interaction. **Figure 79** summaries the findings described in this paragraph.
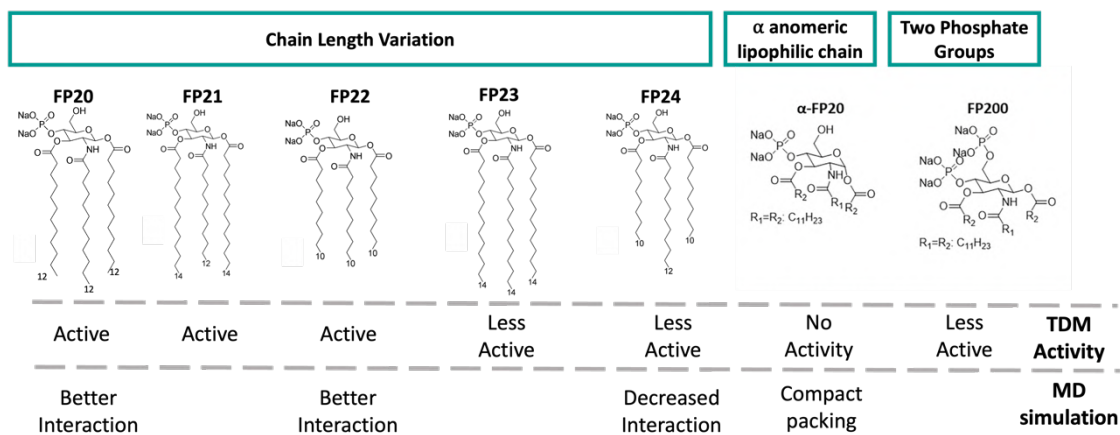
Figure 79. FP20 series overall SAR findings using *in vitro* characterization in TDM and MD simulations

FP20-22 were further characterised and their cytokine profile both in PBMCs and in TDM revealed a significant production of TNF and IL-1β. FP20 did not induce NF-κB (p65 subunit) nor p-IRF-3 nuclear translocation in immunofluorescence experiments. As these transcriptional factors were not detected in Western blot analysis, we did analyse another important protein in TLR4 signalling, the p38 MAPK. p38 activation was detected using Western blot, suggesting that it has a role in the downstream transcriptions leading to the synthesis of pro-inflammatory cytokines. Remarkably, IL-1β production in TDM treated with FP20 was comparable with the one of the positive control S-LPS which suggested an important contribution of NLRP3 inflammasome to the proinflammatory activity of this type of molecules, also reflecting what observed in the case of FP18[192]. A reduction in IL-1β production in TDM treated with FP20 after a pre-treatment with NLRP3 inhibitor MCC950 was observed, indicating a role of this protein complex in the mechanism of action of FP20. NLRP3 inflammasome activation has been previously described as a mechanism of action of other adjuvants[334] and in particular it has been associated with the approved and widely used adjuvants MF59 and Alum[336].

While having a straightforward short synthesis, FP20s are less active than the commercially available MPLA and have limited water solubility. Functionalizing the free C-6 hydroxyl of FP20 increases its activity, which might be related to an improved

interaction with the receptor and possible improvement in physico-chemical properties, namely solubility but also to a stronger interaction with the TLR4/MD2 dimer and thus improved pharmacodynamics.

Based on the knowledge of natural and synthetic agonist's interaction with TLR4/MD2 dimer in the activated conformation, glycosylation of position C6 is a logical approach, due to the possibility of mimicking the first sugar of the LPS core, named KDO I[337]. However, achieving such modification is challenging due to the possibility of substrate degradation due to the liability of the phosphate and ester bonds in the glycosylation reaction. Considering this difficulty, other substitutions of position C6 can be attempted with the same goal of optimizing activity but with simpler reactions. Considering this, two different types of FP20 derivatives were developed – FP20Glyco series and FP20Hmp. FP20Glyco is a small library of disaccharide compounds obtained from the glycosylation of FP20. On the other hand, FP20Hmp was obtained through the acylation of FP20 with a hydroxylated acid.

The new glycosylated FP20 derivatives showed selectivity towards the hTLR4 receptor in HEK-Blue hTLR4 reporter cells with high activity, regardless of the anomeric configuration of the sugars or the sugar moiety itself. Promising activity was observed in TDM cells, with released SEAP levels comparable to the positive control S-LPS. The dramatic increase in activity of glycosylated FP20 compared to parent molecule suggests a specific role of the added glycosyl moiety in the interaction with the receptor, as it was intended. Further characterization in TDM revealed that these compounds are able to induce proinflammatory cytokines, namely TNF, IL-6 and IL-1β. Contrarily to its parent compound FP20, FP20Rha is likely to activate MyD88 and TRIF-dependent signaling. It is also probable that FP20Rha activates NLRP3 inflammasome, although further testing is required. Considering all the data, the introduction of a sugar moiety in position C6 seems to have driven the activity of FP20 derivates towards a more potent and complex response, similarly to lipid A, without apparent toxicity in the tested concentrations. Further characterization and *in vivo* studies are needed to confirm FP20Rha and the other GlycoFP20 as viable new TLR4-targeting adjuvants.

FP20Hmp retained TLR4 selectivity as the previous generation molecule FP20. As with the GlycoFP20 series, *in vitro* characterization in TDM showed a marked increase in activity compared to FP20, with the 10 µM concentration showing twice as much SEAP

release than the parent compound. This increase in activity is accompanied by a different mechanism of action. While FP20 was able to induce p38 activation and NLRP3-dependent inflammasome activation but no MyD88 induction[336], FP20Hmp, showed the ability to induce this pathway. This is illustrated by significant proinflammatory cytokine production, namely TNF, IL-6 and IL-1β, IκBα degradation and NF-κB phosphorylation and nuclear translocation. Interestingly, and contrarily to FP20Rha, no TRAM/TRIF activation was detected. *In vivo* OVA vaccination experiments showed levels of anti-OVA IgG comparable to MPLA and no toxicity, meaning that FP20Hmp has immunostimulatory ability when formulated with an antigen and administered to mice. Considering the promising results from mice immunization, the ability of FP20Hmp to stimulate the production of antibodies against an enterococcal antigen was evaluated and compared to MPLA, by means of a rabbit immunization study with subsequent serum analysis. Interestingly, the formulation containing FP20Hmp and PpiC induced higher levels of antibodies against the *E. faecium* antigen than the formulation with MPLA and PpiC. Altogether, this data shows that FP20Hmp is a promising and safe adjuvant to be used in novel antibacterial vaccine formulations.

Looking at the data from all synthesized derivatives, it seems that a different position of the phosphate group, as in the case of FP20 and FP18, and different functionalization, as it is the case of FP20Rha and FP20Hmp compared to FP20, can lead to different TLR4-dependent mechanisms of action, most probably based on the different interaction with the TLR4/MD2 receptor (**Figure 80**). Changing the phosphate from position C1 (FP18) to C4 (FP20) resulted in a slight decrease in activity and lack of MyD88 and TRIF stimulation. Nevertheless, functionalizing C6 restored the ability of triggering these pathways and resulted in a dramatic increase in activity. Thus, confirming that the phosphate group can indeed be located in position C4 as long as other interactions are improved. **Figure 80** summarizes the chemical modifications made to FP compounds over the last series and their reflection on the mechanism of action. It is worth noting that while FP20Rha activates the same signaling pathways as FP18, its activity is higher.
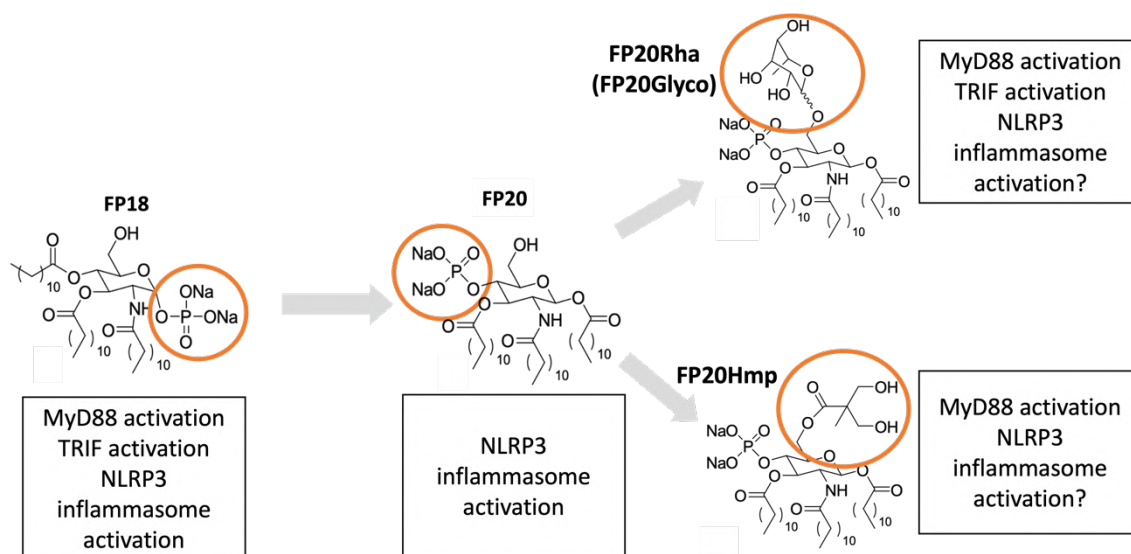
Figure 80. Chemical modifications on FP compounds over the series and respective mechanism of action

Future research is needed to understand the implications of the physico-chemical properties of these molecules. Stability and solubility studies in aqueous solvents are important to evaluate if the molecules have favorable drug-like properties. Other formulations, such as the mentioned liposomes and emulsions, can also be considered as a vehicle for these glycolipids that might, with its adjuvancy properties, produce synergic effects.

It would be of interest to continue to better characterize these molecules and incorporate them into formulations with pathogen-specific antigens. As it was mentioned throughout this document, the type of response matters when it comes to modulating adaptive immunity[338]. Therefore, evaluating *in vitro* and *in vivo* responses to these adjuvants together with a pathogen-directed antigen or mixture of antigens can be the decisive answer to the question of whether or not these molecules should advance to clinical phase of development.

While not every synthesized compound will make the pipeline and be formulated into new vaccine formulations, developing new TLR4 agonists is important to improve SAR data for the development of future molecules and to further understand the immunological events that happen within the cell. Furthermore, understanding the responses triggered by its natural ligand, LPS, are fundamental to develop new compounds.

LPS induces a series of complex events within the cells leading to a potent TLR4-dependent proinflammatory response that, despite a large number of studies, are not completely understood. Using FTIR, followed by PLS-DA analysis, to obtain a snapshot of the molecular events sparked by LPS stimulation in macrophage-like cells, the most significative biomolecules involved in this complex process can be identified. This in turn can then lead to a targeted deeper investigation on different biomarkers, saving resources and time. Furthermore, FTIR analysis of intact macrophage cells has the advantage of being a non-destructive, non-time consuming and label-free method to measure the main molecular changes occurring in cells.

The main findings, obtained through a global picture of LPS-dependent inflammation in TDM, are represented by the identification of different classes of molecules that stand out as the most affected. We observed changes in cell protein secondary structures, significant intensity variation of a few bands ascribable to lipid moieties and change in sulfated sugars that could be associated with the biosynthesis of sulfated glycosphingolipids and/or GAGs.

Looking at what is known of the inflammatory process, time dependent changes in protein content and interactions can be attributed to cellular events related to pathway activation, namely MyD88, TRIF and inflammasome-mediated signaling[339]. Differences in bands related to lipids confirms their importance as markers of inflammatory response[312,313]. It is known that a metabolic reprogramming occurs upon LPS stimulus and macrophage polarization and that this can have an effect on lipid content within the cell[340]. For example, oxidative stress derived from lipid peroxidation, driven by proinflammatory stimuli, has long been identified as a biomarker of inflammation[341]. Regarding changes in glycosphingolipid sulphates, it has been shown that these are endogenous ligands for the TLR4/MD-2 complex[331]. Moreover, GAGs play a crucial role in the recruitment and control of a wide range of innate/cellular immune system regulatory proteins[322,342].

Ultimately, this new approach of using FTIR and PLS-DA analysis to study the cellular events associated with LPS stimulation, can also be important for drug development. Having established a global picture of LPS-triggered TLR4-dependent inflammation, the same technique can be applied to new TLR4 agonists to evaluate if the molecule can induce the same changes or not. This method potentiates the use of this

technique as a new screening method for TLR4-directed proinflammatory compounds to be used in different contexts but particularly as vaccine adjuvants. Future research is needed to consolidate this screening method in the expectation of transfer it to pharmaceutical development.

Overall, the work developed during this PhD project contributed to vaccine adjuvant development and to the understanding of TLR4-dependent inflammation. Different molecules were developed, and their mechanism of action clarified. Application of different techniques from different fields, such as FTIR, contributed to a better characterization of the compounds and the events associated with them. This PhD body of work consolidates a medicinal chemistry approach, focusing on applying a multidisciplinary strategy to develop innovative compounds to be incorporated into novel vaccine formulations, while tackling a bottleneck in vaccine development.

6.List of Publications

- **Ana Rita Franco**, Valentina Artusa, and Francesco Peri. "Use of Fluorescent Chemical Probes in the Study of Toll-like Receptors (TLRs) Trafficking." In Toll-Like Receptors: Methods and Protocols, pp. 57-74. New York, NY: Springer US, 2023. https://doi.org/10.1007/978-1-0716-3366-3_3

- Alessio Romerio, **Ana Rita Franco**, Melanie Shadrick, Mohammed Monsoor Shaik, Valentina Artusa, Alice Italia, Federico Lami, Alexei V. Demchenko, and Francesco Peri. "Overcoming Challenges in Chemical Glycosylation to Achieve Innovative Vaccine Adjuvants Possessing Enhanced TLR4 Activity." ACS omega (2023). https://doi.org/10.1021/acsomega.3c05363

- Alessio Romerio*, Nicole Gotri*, **Ana Rita Franco***, Valentina Artusa, Mohammed Monsoor Shaik, Samuel T. Pasco, Unai Atxabal et al. "New Glucosamine-Based TLR4 Agonists: Design, Synthesis, Mechanism of Action, and In Vivo Activity as Vaccine Adjuvants." Journal of Medicinal Chemistry 66, no. 4 (2023): 3010-3029. https://doi.org/10.1021/acs.jmedchem.2c01998

  *Co-authors

- Diletta Ami, **Ana Rita Franco**, Valentina Artusa, Paolo Mereghetti, Francesco Peri, and Antonino Natalello. "A global picture of molecular changes associated to LPS treatment in THP-1 derived human macrophages by Fourier transform infrared microspectroscopy." International Journal of Molecular Sciences 23, no. 21 (2022): 13447. https://doi.org/10.3390/ijms232113447

- **Ana Rita Franco**, and Francesco Peri. "Developing new anti-tuberculosis vaccines: focus on adjuvants." Cells 10, no. 1 (2021): 78. https://doi.org/10.3390/cells10010078

7.References

1.   *WHO strategic priorities on antimicrobial resistance: preserving antimicrobials for today and tomorrow*. (World Health Organization, 2021).

2.   O'Neill, J. Tackling drug-resistant infections globally: final report and recommendations. *Government of the United Kingdom* (2016).

3.   Antimicrobial Resistance Collaborators. Global burden of bacterial antimicrobial resistance in 2019: a systematic analysis. *Lancet* **399**, 629–655 (2022).

4.   Mulani, M. S., Kamble, E. E., Kumkar, S. N., Tawre, M. S. & Pardesi, K. R. Emerging Strategies to Combat ESKAPE Pathogens in the Era of Antimicrobial Resistance: A Review. *Front. Microbiol.* **10**, 539 (2019).

5.   Gygli, S. M. *et al.* Publisher Correction: Prisons as ecological drivers of fitness-compensated multidrug-resistant Mycobacterium tuberculosis. *Nat. Med.* **27**, 1308 (2021).

6.   Lan, Z. *et al.* Drug-associated adverse events in the treatment of multidrug-resistant tuberculosis: an individual patient data meta-analysis. *Lancet Respir Med* **8**, 383–394 (2020).

7.   Health Organization, W. WHO global lists of high burden countries for tuberculosis (TB), TB/HIV and multidrug/rifampicin-resistant TB (MDR/RR. https://apps.who.int/iris/bitstream/handle/10665/341980/9789240029439-eng.pdf (2021).

8.   Prestinaci, F., Pezzotti, P. & Pantosti, A. Antimicrobial resistance: a global multifaceted phenomenon. *Pathog. Glob. Health* **109**, 309–318 (2015).

9.   Costello, A. & Peterson, S. S. Birth in a time of antibiotic-resistant bacteria. *World Health Organization Commentary* (2016).

10.   Akram, F., Imtiaz, M. & Haq, I. U. Emergent crisis of antibiotic resistance: A silent pandemic threat to 21st century. *Microb. Pathog.* **174**, 105923 (2023).

11.   De Oliveira, D. M. P. *et al.* Antimicrobial Resistance in ESKAPE Pathogens. *Clin. Microbiol. Rev.* **33**, (2020).

12.   Smith, W. P. J., Wucher, B. R., Nadell, C. D. & Foster, K. R. Bacterial defences: mechanisms, evolution and antimicrobial resistance. *Nat. Rev. Microbiol.* **21**, 519–534 (2023).

13.   Zhang, Z. *et al.* Assessment of global health risk of antibiotic resistance genes. *Nat. Commun.* **13**, 1553 (2022).

14.   Reygaert, W. C. An overview of the antimicrobial resistance mechanisms of bacteria. *AIMS Microbiol* **4**, 482–501 (2018).

15.   Blair, J. M. A., Webber, M. A., Baylay, A. J., Ogbolu, D. O. & Piddock, L. J. V. Molecular mechanisms of antibiotic resistance. *Nat. Rev. Microbiol.* **13**, 42–51 (2015).

16.   Darby, E. M. *et al.* Molecular mechanisms of antibiotic resistance revisited. *Nat. Rev. Microbiol.* **21**, 280–295 (2023).

17.   Uddin, T. M. *et al.* Antibiotic resistance in microbes: History, mechanisms, therapeutic strategies and future prospects. *J. Infect. Public Health* **14**, 1750–1766 (2021).

18.   Ventola, C. L. The antibiotic resistance crisis: part 1: causes and threats. *P T* **40**, 277–283 (2015).

19.   Larsson, D. G. J. & Flach, C.-F. Antibiotic resistance in the environment. *Nat. Rev. Microbiol.* **20**, 257–269 (2022).

20.   Health Organization, W. 2019 antibacterial agents in clinical development. https://apps.who.int/iris/bitstream/handle/10665/330420/9789240000193-eng.pdf (2019).

21.   Beyer, P. & Paulin, S. Priority pathogens and the antibiotic pipeline: an update. *Bull. World Health Organ.* **98**, 151 (2020).

22.   Butler, M. S., Henderson, I. R., Capon, R. J. & Blaskovich, M. A. T. Antibiotics in the clinical pipeline as of December 2022. *J. Antibiot.* **76**, 431–473 (2023).

23.   Mullard, A. Pull incentives for antibiotics get push from the UK. *Nat. Rev. Drug Discov.* **21**, 406 (2022).

24.   Glover, R. E., Singer, A. C., Roberts, A. P. & Kirchhelle, C. The antibiotic subscription model: fostering innovation or repackaging old drugs? *Lancet Microbe* **4**, e2–e3 (2023).

25.   Zhang, Y., Saint Fleur, A. & Feng, H. The development of live biotherapeutics against Clostridioides difficile infection towards reconstituting gut microbiota. *Gut Microbes* **14**, 2052698 (2022).

26.   Lagadinou, M. *et al.* Antimicrobial Properties on Non-Antibiotic Drugs in the Era of Increased Bacterial Resistance. *Antibiotics* **9**, 107 (2020).

27.   Durães, F. *et al.* Antimicrobial Activity of a Library of Thioxanthones and Their Potential as Efflux Pump Inhibitors. *Pharmaceuticals* **14**, (2021).

28.   Durães, F. *et al.* Marine-derived fungi as a source of potential antimicrobial adjuvants. (2021).

29.   Gray, D. A. & Wenzel, M. Multitarget Approaches against Multiresistant Superbugs. *ACS Infect Dis* **6**, 1346–1365 (2020).

30.   Pereira, D. *et al.* New Chalcone–Triazole Hybrids with Promising Antimicrobial Activity in Multidrug Resistance Strains. *Int. J. Mol. Sci.* **23**, 14291 (2022).

31.   Majumder, M. A. A. *et al.* Antimicrobial Stewardship: Fighting Antimicrobial Resistance and Protecting Global Public Health. *Infect. Drug Resist.* **13**, 4713–4738 (2020).

32.   Rosini, R., Nicchi, S., Pizza, M. & Rappuoli, R. Vaccines Against Antimicrobial Resistance. *Front. Immunol.* **11**, 1578 (2020).

33.   Frost, I. *et al.* The role of bacterial vaccines in the fight against antimicrobial resistance: an analysis of the preclinical and clinical development pipeline. *Lancet Microbe* **4**, e113–e125 (2023).

34.   Atkins, K. E. *et al.* Use of mathematical modelling to assess the impact of vaccines on antibiotic resistance. *Lancet Infect. Dis.* **18**, e204–e213 (2018).

35.   Gabutti, G. Available evidence and potential for vaccines for reduction in antibiotic prescriptions. *Hum. Vaccin. Immunother.* **18**, 2151291 (2022).

36.   Jansen, K. U., Knirsch, C. & Anderson, A. S. The role of vaccines in preventing bacterial antimicrobial resistance. *Nat. Med.* **24**, 10–19 (2018).

37.   García-Quintanilla, M., Pulido, M. R., Carretero-Ledesma, M. & McConnell, M. J. Vaccines for Antibiotic-Resistant Bacteria: Possibility or Pipe Dream? *Trends Pharmacol. Sci.* **37**, 143–152 (2016).

38.   Tom, J. K. *et al.* Applications of Immunomodulatory Immune Synergies to Adjuvant Discovery and Vaccine Development. *Trends Biotechnol.* **37**, 373–388 (2019).

39.   Clift, C. & Salisbury, D. M. Enhancing the role of vaccines in combatting antimicrobial resistance. *Vaccine* **35**, 6591–6593 (2017).

40.   Henriques-Normark, B. & Normark, S. Bacterial vaccines and antibiotic resistance. *Ups. J. Med. Sci.* **119**, 205–208 (2014).

41.   Klugman, K. P. & Black, S. Impact of existing vaccines in reducing antibiotic resistance: Primary and secondary effects. *Proc. Natl. Acad. Sci. U. S. A.* **115**, 12896–12901 (2018).

42.   Khalid, K. & Poh, C. L. The Promising Potential of Reverse Vaccinology-Based Next-Generation Vaccine Development over Conventional Vaccines against Antibiotic-Resistant Bacteria. *Vaccines (Basel)* **11**, (2023).

43.   Gupta, S. & Pellett, S. Recent developments in vaccine design: From live vaccines to recombinant toxin vaccines. *Toxins (Basel)* **15**, (2023).

44.   Rumata, N. R. *et al.* Progress and Challenges in Antimicrobial Resistance and Bacterial Vaccines. *Biointerface Research in Applied Chemistry* **13**, (2023).

45.   Vetter, V., Denizer, G., Friedland, L. R., Krishnan, J. & Shapiro, M. Understanding modern-day vaccines: what you need to know. *Ann. Med.* **50**, 110–120 (2018).

46.   Roldão, A., Mellado, M. C. M., Castilho, L. R., Carrondo, M. J. T. & Alves, P. M. Virus-like particles in vaccine development. *Expert Rev. Vaccines* **9**, 1149–1176 (2010).

47.   Pardi, N., Hogan, M. J., Porter, F. W. & Weissman, D. mRNA vaccines - a new era in vaccinology. *Nat. Rev. Drug Discov.* **17**, 261–279 (2018).

48.   Ye, Z. *et al.* The mRNA Vaccine Revolution: COVID-19 Has Launched the Future of Vaccinology. *ACS Nano* **17**, 15231–15253 (2023).

49.   Chen, S. *et al.* Nanotechnology-based mRNA vaccines. *Nature Reviews Methods Primers* **3**, 1–19 (2023).

50.   Barbier, A. J., Jiang, A. Y., Zhang, P., Wooster, R. & Anderson, D. G. The clinical progress of mRNA vaccines and immunotherapies. *Nat. Biotechnol.* **40**, 840–854 (2022).

51.   Ye, J. & Chen, X. Current Promising Strategies against Antibiotic-Resistant Bacterial Infections. *Antibiotics (Basel)* **12**, (2022).

52.   Atkins, K. E. & Flasche, S. Vaccination to reduce antimicrobial resistance. *Lancet Glob Health* **6**, e252 (2018).

53.   Borba, R. C. N., Vidal, V. M. & Moreira, L. O. The re-emergency and persistence of vaccine preventable diseases. *An. Acad. Bras. Cienc.* **87**, 1311–1322 (2015).

54.   Troiano, G. & Nardi, A. Vaccine hesitancy in the era of COVID-19. *Public Health* **194**, 245–251 (2021).

55.   Ismail, S. *et al.* Pan-vaccinomics approach towards a universal vaccine candidate against WHO priority pathogens to address growing global antibiotic resistance. *Comput. Biol. Med.* **136**, 104705 (2021).

56.   Kalfopoulou, E. & Huebner, J. Advances and Prospects in Vaccine Development against Enterococci. *Cells* **9**, (2020).

57.   Kodali, S. *et al.* A Vaccine Approach for the Prevention of Infections by Multidrug-resistant Enterococcus faecium. *J. Biol. Chem.* **290**, 19512–19526 (2015).

58.   Kropec, A. *et al.* Identification of SagA as a novel vaccine target for the prevention of Enterococcus faecium infections. *Microbiology* **157**, 3429–3434 (2011).

59.   Romero-Saavedra, F. *et al.* Identification of peptidoglycan-associated proteins as vaccine candidates for enterococcal infections. *PLoS One* **9**, e111880 (2014).

60.   Fatoba, A. J. *et al.* Immunoinformatics design of multiepitope vaccine against Enterococcus faecium infection. *Int. J. Pept. Res. Ther.* **27**, 2183–2198 (2021).

61.   Scully, I. L. *et al.* Performance of a Four-Antigen Staphylococcus aureus Vaccine in Preclinical Models of Invasive S. aureus Disease. *Microorganisms* **9**, (2021).

62.   Clegg, J. *et al.* Staphylococcus aureus Vaccine Research and Development: The Past, Present and Future, Including Novel Therapeutic Strategies. *Front. Immunol.* **12**, 705360 (2021).

63.   Jahantigh, H. R. *et al.* The Candidate Antigens to Achieving an Effective Vaccine against Staphylococcus aureus. *Vaccines (Basel)* **10**, (2022).

64.   Choi, M., Tennant, S. M., Simon, R. & Cross, A. S. Progress towards the development of Klebsiella vaccines. *Expert Rev. Vaccines* **18**, 681–691 (2019).

65.   Costanzo, V. & Roviello, G. N. The Potential Role of Vaccines in Preventing Antimicrobial Resistance (AMR): An Update and Future Perspectives. *Vaccines (Basel)* **11**, (2023).

66.   Ma, C. & McClean, S. Mapping Global Prevalence of Acinetobacter baumannii and Recent Vaccine Development to Tackle It. *Vaccines (Basel)* **9**, (2021).

67.   Gellings, P. S., Wilkins, A. A. & Morici, L. A. Recent Advances in the Pursuit of an Effective Acinetobacter baumannii Vaccine. *Pathogens* **9**, (2020).

68.   Sainz-Mejías, M., Jurado-Martín, I. & McClean, S. Understanding Pseudomonas aeruginosa–Host Interactions: The Ongoing Quest for an Efficacious Vaccine. *Cells* (2020).

69.   Dey, J., Mahapatra, S. R., Patnaik, S. & Lata, S. Molecular Characterization and Designing of a Novel Multiepitope Vaccine Construct Against Pseudomonas aeruginosa. *International Journal of* (2022).

70.   Killough, M., Rodgers, A. M. & Ingram, R. J. Pseudomonas aeruginosa: Recent Advances in Vaccine Development. *Vaccines* **10**, 1100 (2022).

71.   Fereshteh, S. *et al.* Defeating a superbug: A breakthrough in vaccine design against multidrug-resistant Pseudomonas aeruginosa using reverse vaccinology. *PLoS One* **18**, e0289609 (2023).

72.   Plotkin, S. A. & Plotkin, S. L. The development of vaccines: how the past led to the future. *Nat. Rev. Microbiol.* **9**, 889–893 (2011).

73.   Diamond, M. S. & Kanneganti, T.-D. Innate immunity: the first line of defense against SARS-CoV-2. *Nat. Immunol.* **23**, 165–176 (2022).

74.   Arango Duque, G. & Descoteaux, A. Macrophage cytokines: involvement in immunity and infectious diseases. *Front. Immunol.* **5**, 491 (2014).

75.   Bashir, S., Sharma, Y., Elahi, A. & Khan, F. Macrophage polarization: the link between inflammation and related diseases. *Inflamm. Res.* **65**, 1–11 (2016).

76.   Juhas, U., Ryba-Stanisławowska, M., Szargiej, P. & Myśliwska, J. Different pathways of macrophage activation and polarization. *Postepy Hig. Med. Dosw.* **69**, 496–502 (2015).

77.   Murray, P. J. Macrophage Polarization. *Annu. Rev. Physiol.* **79**, 541–566 (2017).

78.   Shapouri-Moghaddam, A. *et al.* Macrophage plasticity, polarization, and function in health and disease. *J. Cell. Physiol.* **233**, 6425–6440 (2018).

79.   Rathinam, V. A. K., Zhao, Y. & Shao, F. Innate immunity to intracellular LPS. *Nat. Immunol.* **20**, 527–533 (2019).

80.   Kaur, B. P. & Secord, E. Innate Immunity. *Pediatr. Clin. North Am.* **66**, 905–911 (2019).

81.   Turvey, S. E. & Broide, D. H. Innate immunity. *J. Allergy Clin. Immunol.* **125**, S24-32 (2010).

82.   Li, D. & Wu, M. Pattern recognition receptors in health and diseases. *Signal Transduct Target Ther* **6**, 291 (2021).

83.   Wicherska-Pawłowska, K., Wróbel, T. & Rybka, J. Toll-like receptors (TLRs), NOD-like receptors (NLRs), and RIG-I-like receptors (RLRs) in innate immunity. TLRs, NLRs, and RLRs ligands as immunotherapeutic agents for hematopoietic diseases. *Int. J. Mol. Sci.* **22**, 13397 (2021).

84.   Yang, X., Lin, G., Han, Z. & Chai, J. Structural Biology of NOD-Like Receptors. *Adv. Exp. Med. Biol.* **1172**, 119–141 (2019).

85.   Platnich, J. M. & Muruve, D. A. NOD-like receptors and inflammasomes: A review of their canonical and non-canonical signaling pathways. *Arch. Biochem. Biophys.* **670**, 4–14 (2019).

86.   Dinarello, C. A. Overview of the IL-1 family in innate inflammation and acquired immunity. *Immunol. Rev.* **281**, 8–27 (2018).

87.   He, W.-T. *et al.* Gasdermin D is an executor of pyroptosis and required for interleukin-1β secretion. *Cell Res.* **25**, 1285–1298 (2015).

88.   Downs, K. P., Nguyen, H., Dorfleutner, A. & Stehlik, C. An overview of the non-canonical inflammasome. *Mol. Aspects Med.* **76**, 100924 (2020).

89.   Chauhan, D., Vande Walle, L. & Lamkanfi, M. Therapeutic modulation of inflammasome pathways. *Immunol. Rev.* **297**, 123–138 (2020).

90.   Wright, S. S., Vasudevan, S. O. & Rathinam, V. A. Mechanisms and Consequences of Noncanonical Inflammasome-Mediated Pyroptosis. *J. Mol. Biol.* **434**, 167245 (2022).

91.   Wang, B., Tian, Y. & Yin, Q. AIM2 Inflammasome Assembly and Signaling. *Adv. Exp. Med. Biol.* **1172**, 143–155 (2019).

92.   Fan, X. & Jin, T. Structures of RIG-I-Like Receptors and Insights into Viral RNA Sensing. *Adv. Exp. Med. Biol.* **1172**, 157–188 (2019).

93.   Dutta, S., Das, N. & Mukherjee, P. Picking up a Fight: Fine Tuning Mitochondrial Innate Immune Defenses Against RNA Viruses. *Front. Microbiol.* **11**, 1990 (2020).

94.   Xu, S., Jin, T. & Weng, J. Endothelial Cells as a Key Cell Type for Innate Immunity: A Focused Review on RIG-I Signaling Pathway. *Front. Immunol.* **13**, 951614 (2022).

95.   Raftery, N. & Stevenson, N. J. Advances in anti-viral immune defence: revealing the importance of the IFN JAK/STAT pathway. *Cell. Mol. Life Sci.* **74**, 2525–2535 (2017).

96.   Brown, G. D., Willment, J. A. & Whitehead, L. C-type lectins in immunity and homeostasis. *Nat. Rev. Immunol.* **18**, 374–389 (2018).

97.   Mayer, S., Raulf, M.-K. & Lepenies, B. C-type lectins: their network and roles in pathogen recognition and immunity. *Histochem. Cell Biol.* **147**, 223–237 (2017).

98.   Mnich, M. E., van Dalen, R. & van Sorge, N. M. C-Type Lectin Receptors in Host Defense Against Bacterial Pathogens. *Front. Cell. Infect. Microbiol.* **10**, 309 (2020).

99.   O'Neill, L. A. J., Golenbock, D. & Bowie, A. G. The history of Toll-like receptors - redefining innate immunity. *Nat. Rev. Immunol.* **13**, 453–460 (2013).

100.   Mokhtari, Y. *et al.* Toll-like receptors (TLRs): An old family of immune receptors with a new face in cancer pathogenesis. *J. Cell. Mol. Med.* **25**, 639–651 (2021).

101.   Duan, T., Du, Y., Xing, C., Wang, H. Y. & Wang, R.-F. Toll-Like Receptor Signaling and Its Role in Cell-Mediated Immunity. *Front. Immunol.* **13**, 812774 (2022).

102.   Behzadi, P., García-Perdomo, H. A. & Karpiński, T. M. Toll-Like Receptors: General Molecular and Structural Biology. *Journal of Immunology Research* **2021**, 9914854 (2021).

103.   Botos, I., Segal, D. M. & Davies, D. R. The structural biology of Toll-like receptors. *Structure* **19**, 447–459 (2011).

104.   Fitzgerald, K. A. & Kagan, J. C. Toll-like Receptors and the Control of Immunity. *Cell* **180**, 1044–1066 (2020).

105.   Lind, N. A., Rael, V. E., Pestal, K., Liu, B. & Barton, G. M. Regulation of the nucleic acid-sensing Toll-like receptors. *Nat. Rev. Immunol.* (2021) doi:10.1038/s41577-021-00577-0.

106.   Majer, O. *et al.* Release from UNC93B1 reinforces the coHmprtmentalized activation of select TLRs. *Nature* **575**, 371–374 (2019).

107.   Kawasaki, T. & Kawai, T. Toll-Like Receptor Signaling Pathways. *Front. Immunol.* **5**, (2014).

108.   Tan, Y. & Kagan, J. C. Microbe-inducible trafficking pathways that control Toll-like receptor signaling. *Traffic* **18**, 6–17 (2017).

109.   Dolasia, K., Bisht, M. K., Pradhan, G., Udgata, A. & Mukhopadhyay, S. TLRs/NLRs: Shaping the landscape of host immunity. *Int. Rev. Immunol.* **37**, 3–19 (2018).

110.   Marongiu, L., Gornati, L., Artuso, I., Zanoni, I. & Granucci, F. Below the surface: The inner lives of TLR4 and TLR9. *J. Leukoc. Biol.* **106**, 147–160 (2019).

111.   Molteni, M., Gemma, S. & Rossetti, C. The Role of Toll-Like Receptor 4 in Infectious and Noninfectious Inflammation. *Mediators Inflamm.* **2016**, 6978936 (2016).

112.   Butcher, M. J. & Zhu, J. Recent advances in understanding the Th1/Th2 effector choice. *Fac Rev* **10**, 30 (2021).

113.   Kolls, J. K. & Khader, S. A. The role of Th17 cytokines in primary mucosal immunity. *Cytokine Growth Factor Rev.* **21**, 443–448 (2010).

114.   Cochet, F. & Peri, F. The Role of Carbohydrates in the Lipopolysaccharide (LPS)/Toll-Like Receptor 4 (TLR4) Signalling. *Int. J. Mol. Sci.* **18**, (2017).

115.   Tsukamoto, H., Fukudome, K., Takao, S., Tsuneyoshi, N. & Kimoto, M. Lipopolysaccharide-binding protein-mediated Toll-like receptor 4 dimerization enables rapid signal transduction against lipopolysaccharide stimulation on membrane-associated CD14-expressing cells. *Int. Immunol.* **22**, 271–280 (2010).

116.   Gioannini, T. L. *et al.* Isolation of an endotoxin–MD-2 complex that produces Toll-like receptor 4-dependent cell activation at picomolar concentrations. *Proceedings of the National Academy of Sciences* **101**, 4186–4191 (2004).

117.   Lin, T.-L. *et al.* Like Cures Like: Pharmacological Activity of Anti-Inflammatory Lipopolysaccharides From Gut Microbiome. *Front. Pharmacol.* **11**, 554 (2020).

118.   Park, B. S. *et al.* The structural basis of lipopolysaccharide recognition by the TLR4–MD-2 complex. *Nature* **458**, 1191–1195 (2009).

119.   Ryu, J.-K. *et al.* Reconstruction of LPS Transfer Cascade Reveals Structural Determinants within LBP, CD14, and TLR4-MD2 for Efficient LPS Recognition and Transfer. *Immunity* **46**, 38–50 (2017).

120. Fitzgerald, K. A., Rowe, D. C. & Golenbock, D. T. Endotoxin recognition and signal transduction by the TLR4/MD2-complex. *Microbes Infect.* **6**, 1361–1367 (2004).

121. Zanoni, I. *et al.* CD14 Controls the LPS-Induced Endocytosis of Toll-like Receptor 4. *Cell* **147**, 868–880 (2011).

122. Chen, L., Fu, W., Zheng, L., Wang, Y. & Liang, G. Recent progress in the discovery of myeloid differentiation 2 (MD2) modulators for inflammatory diseases. *Drug Discov. Today* **23**, 1187–1202 (2018).

123. Mata-Haro, V. *et al.* The vaccine adjuvant monophosphoryl lipid A as a TRIF-biased agonist of TLR4. *Science* **316**, 1628–1632 (2007).

124. Huang, J. X. *et al.* Molecular Characterization of Lipopolysaccharide Binding to Human α-1-Acid Glycoprotein. *J. Lipids* **2012**, 475153 (2012).

125. Klein, G. & Raina, S. Regulated Assembly of LPS, Its Structural Alterations and Cellular Response to LPS Defects. *Int. J. Mol. Sci.* **20**, (2019).

126. Valvano, M. A. Remodelling of the Gram-negative bacterial Kdo2-lipid A and its functional implications. *Microbiology* **168**, (2022).

127. Mazgaeen, L. & Gurung, P. Recent Advances in Lipopolysaccharide Recognition Systems. *Int. J. Mol. Sci.* **21**, (2020).

128. Balka, K. R. & De Nardo, D. Understanding early TLR signaling through the Myddosome. *J. Leukoc. Biol.* **105**, 339–351 (2019).

129. Tan, Y. & Kagan, J. C. Innate Immune Signaling Organelles Display Natural and Programmable Signaling Flexibility. *Cell* **177**, 384-398.e11 (2019).

130. Bryant, C. E., Symmons, M. & Gay, N. J. Toll-like receptor signalling through macromolecular protein complexes. *Mol. Immunol.* **63**, 162–165 (2015).

131. Yadav, H. & Shirumalla, R. K. Emerging trends in IRAK-4 kinase research. *Mol. Biol. Rep.* **50**, 7825–7837 (2023).

132. Walsh, M. C., Lee, J. & Choi, Y. Tumor necrosis factor receptor- associated factor 6 (TRAF6) regulation of development, function, and homeostasis of the immune system. *Immunol. Rev.* **266**, 72–92 (2015).

133. Dhillon, B., Aleithan, F., Abdul-Sater, Z. & Abdul-Sater, A. A. The Evolving Role of TRAFs in Mediating Inflammatory Responses. *Front. Immunol.* **10**, 104 (2019).

134. Peroval, M. Y., Boyd, A. C., Young, J. R. & Smith, A. L. A critical role for MAPK signalling pathways in the transcriptional regulation of toll like receptors. *PLoS One* **8**, e51243 (2013).

135. Atsaves, V., Leventaki, V., Rassidakis, G. Z. & Claret, F. X. AP-1 Transcription Factors as Regulators of Immune Responses in Cancer. *Cancers* **11**, (2019).

136. Rajpoot, S. *et al.* TIRAP in the Mechanism of Inflammation. *Front. Immunol.* **12**, 697588 (2021).

137. Vidya, M. K. *et al.* Toll-like receptors: Significance, ligands, signaling pathways, and functions in mammals. *Int. Rev. Immunol.* **37**, 20–36 (2018).

138. Dorrington, M. G. & Fraser, I. D. C. NF-κB Signaling in Macrophages: Dynamics, Crosstalk, and Signal Integration. *Front. Immunol.* **10**, 705 (2019).

139. Christian, F., Smith, E. L. & Carmody, R. J. The Regulation of NF-κB Subunits by Phosphorylation. *Cells* **5**, 12 (2016).

140. Clark, K., Nanda, S. & Cohen, P. Molecular control of the NEMO family of ubiquitin-binding proteins. *Nat. Rev. Mol. Cell Biol.* **14**, 673–685 (2013).

141. Mulero, M. C., Huxford, T. & Ghosh, G. NF-κB, IκB, and IKK: Integral Components of Immune System Signaling. *Adv. Exp. Med. Biol.* **1172**, 207–226 (2019).

142. Kieser, K. J. & Kagan, J. C. Multi-receptor detection of individual bacterial products by the innate immune system. *Nat. Rev. Immunol.* **17**, 376–390 (2017).

143. Ullah, M. O., Sweet, M. J., Mansell, A., Kellie, S. & Kobe, B. TRIF-dependent TLR signaling, its functions in host defense and inflammation, and its potential as a therapeutic target. *J. Leukoc. Biol.* **100**, 27–45 (2016).

144. Colonna, M. TLR pathways and IFN-regulatory factors: to each its own. *Eur. J. Immunol.* **37**, 306–309 (2007).

145. Papadakos, S. P. *et al.* The Role of TLR4 in the Immunotherapy of Hepatocellular Carcinoma: Can We Teach an Old Dog New Tricks? *Cancers* **15**, (2023).

146.   Perkins, D. J. *et al.* Autocrine–paracrine prostaglandin E2 signaling restricts TLR4 internalization and TRIF signaling. *Nat. Immunol.* **19**, 1309–1318 (2018).

147.   Aerbajinai, W., Lee, K., Chin, K. & Rodgers, G. P. Glia Maturation Factor-γ Negatively Modulates TLR4 Signaling by Facilitating TLR4 Endocytic Trafficking in Macrophages. *J. Immunol.* **190**, 6093 (2013).

148.   Bruscia, E. M. *et al.* Abnormal Trafficking and Degradation of TLR4 Underlie the Elevated Inflammatory Response in Cystic Fibrosis. *J. Immunol.* **186**, 6990 (2011).

149.   Murase, M. *et al.* Intravesicular Acidification Regulates Lipopolysaccharide Inflammation and Tolerance through TLR4 Trafficking. *J. Immunol.* **200**, 2798 (2018).

150.   Ciesielska, A., Matyjek, M. & Kwiatkowska, K. TLR4 and CD14 trafficking and its influence on LPS-induced pro-inflammatory signaling. *Cell. Mol. Life Sci.* **78**, 1233–1261 (2021).

151.   Lannoy, V., Côté-Biron, A., Asselin, C. & Rivard, N. TIRAP, TRAM, and Toll-Like Receptors: The Untold Story. *Mediators Inflamm.* **2023**, 2899271 (2023).

152.   Al Hamrashdi, M. & Brady, G. Regulation of IRF3 activation in human antiviral signaling pathways. *Biochem. Pharmacol.* **200**, 115026 (2022).

153.   Schwanke, H., Stempel, M. & Brinkmann, M. M. Of Keeping and Tipping the Balance: Host Regulation and Viral Modulation of IRF3-Dependent IFNB1 Expression. *Viruses* **12**, (2020).

154.   Ivashkiv, L. B. & Donlin, L. T. Regulation of type I interferon responses. *Nat. Rev. Immunol.* **14**, 36–49 (2014).

155.   Guinn, Z., Lampe, A. T., Brown, D. M. & Petro, T. M. Significant role for IRF3 in both T cell and APC effector functions during T cell responses. *Cell. Immunol.* **310**, 141–149 (2016).

156.   Ding, J. & Liu, Q. Toll-like receptor 4: A promising therapeutic target for pneumonia caused by Gram-negative bacteria. *J. Cell. Mol. Med.* **23**, 5868–5875 (2019).

157.   Liu, T., Zhang, L., Joo, D. & Sun, S.-C. NF-κB signaling in inflammation. *Signal Transduct. Target. Ther.* **2**, 17023 (2017).

158.   Pulendran, B., S Arunachalam, P. & O'Hagan, D. T. Emerging concepts in the science of vaccine adjuvants. *Nat. Rev. Drug Discov.* **20**, 454–475 (2021).

159.   Facciolà, A., Visalli, G., Laganà, A. & Di Pietro, A. An Overview of Vaccine Adjuvants: Current Evidence and Future Perspectives. *Vaccines (Basel)* **10**, (2022).

160.   Zhao, T. *et al.* Vaccine adjuvants: mechanisms and platforms. *Signal Transduct. Target. Ther.* **8**, 283 (2023).

161.   Laupèze, B., Hervé, C., Di Pasquale, A. & Tavares Da Silva, F. Adjuvant Systems for vaccines: 13 years of post-licensure experience in diverse populations have progressed the way adjuvanted vaccine safety is investigated and understood. *Vaccine* **37**, 5670–5680 (2019).

162.   Wang, P. Natural and Synthetic Saponins as Vaccine Adjuvants. *Vaccines (Basel)* **9**, (2021).

163.   Shi, S. *et al.* Vaccine adjuvants: Understanding the structure and mechanism of adjuvanticity. *Vaccine* **37**, 3167–3178 (2019).

164.   Luchner, M., Reinke, S. & Milicic, A. TLR Agonists as Vaccine Adjuvants Targeting Cancer and Infectious Diseases. *Pharmaceutics* **13**, (2021).

165.   O'Hagan, D. T., Lodaya, R. N. & Lofano, G. The continued advance of vaccine adjuvants – 'we can work it out.' *Seminars in Immunology* vol. 50 101426 Preprint at https://doi.org/10.1016/j.smim.2020.101426 (2020).

166.   Pifferi, C., Fuentes, R. & Fernández-Tejada, A. Natural and synthetic carbohydrate-based vaccine adjuvants and their mechanisms of action. *Nature Reviews Chemistry* **5**, 197–216 (2021).

167.   Reinke, S., Thakur, A., Gartlan, C., Bezbradica, J. S. & Milicic, A. Inflammasome-Mediated Immunogenicity of Clinical and Experimental Vaccine Adjuvants. *Vaccines (Basel)* **8**, (2020).

168.   Moreno-Mendieta, S. *et al.* Raw starch microparticles have immunostimulant activity in mice vaccinated with BCG and challenged with Mycobacterium tuberculosis. *Vaccine* **35**, 5123–5130 (2017).

169.   Chatzikleanthous, D., O'Hagan, D. T. & Adamo, R. Lipid-Based Nanoparticles for Delivery of Vaccine Adjuvants and Antigens: Toward Multicomponent Vaccines. *Mol. Pharm.* **18**, 2867–2888 (2021).

170.   van Dissel, J. T. *et al.* A novel liposomal adjuvant system, CAF01, promotes long-lived Mycobacterium tuberculosis-specific T-cell responses in human. *Vaccine* **32**, 7098–7107 (2014).

171.   Hansen, J. *et al.* CAF05: cationic liposomes that incorporate synthetic cord factor and poly(I:C) induce CTL immunity and reduce tumor burden in mice. *Cancer Immunol. Immunother.* **61**, 893–903 (2012).

172.   Kumar, S., Sunagar, R. & Gosselin, E. Bacterial Protein Toll-Like-Receptor Agonists: A Novel Perspective on Vaccine Adjuvants. *Front. Immunol.* **10**, 1144 (2019).

173.   Caucheteux, S. M., Hu-Li, J., Mohammed, R. N., Ager, A. & Paul, W. E. Cytokine regulation of lung Th17 response to airway immunization using LPS adjuvant. *Mucosal Immunol.* **10**, 361–372 (2017).

174.   Kirtland, M. E., Tsitoura, D. C., Durham, S. R. & Shamji, M. H. Toll-Like Receptor Agonists as Adjuvants for Allergen Immunotherapy. *Front. Immunol.* **11**, 599083 (2020).

175.   Kumar, V. Toll-like receptors in sepsis-associated cytokine storm and their endogenous negative regulators as future immunomodulatory targets. *Int. Immunopharmacol.* **89**, 107087 (2020).

176.   Reed, S. G., Hsu, F.-C., Carter, D. & Orr, M. T. The science of vaccine adjuvants: advances in TLR4 ligand adjuvants. *Curr. Opin. Immunol.* **41**, 85–90 (2016).

177.   Casella, C. R. & Mitchell, T. C. Putting endotoxin to work for us: monophosphoryl lipid A as a safe and effective vaccine adjuvant. *Cell. Mol. Life Sci.* **65**, 3231–3240 (2008).

178.   Cekic, C. *et al.* Selective activation of the p38 MAPK pathway by synthetic monophosphoryl lipid A. *J. Biol. Chem.* **284**, 31982–31991 (2009).

179.   Arias, M. A. *et al.* Glucopyranosyl Lipid Adjuvant (GLA), a Synthetic TLR4 agonist, promotes potent systemic and mucosal responses to intranasal immunization with HIVgp140. *PLoS One* **7**, e41144 (2012).

180.   Coler, R. N. *et al.* Development and characterization of synthetic glucopyranosyl lipid adjuvant system as a vaccine adjuvant. *PLoS One* **6**, e16333 (2011).

181.   Liang, H. *et al.* The TLR4 agonist adjuvant SLA-SE promotes functional mucosal antibodies against a parenterally delivered ETEC vaccine. *NPJ Vaccines* **4**, 19 (2019).

182.   Carter, D. *et al.* A structure-function approach to optimizing TLR4 ligands for human vaccines. *Clin. Transl. Immunology* **5**, e108 (2016).

183.   Romerio, A. & Peri, F. Increasing the Chemical Variety of Small-Molecule-Based TLR4 Modulators: An Overview. *Front. Immunol.* **11**, 1210 (2020).

184.   Gregg, K. A. *et al.* Rationally Designed TLR4 Ligands for Vaccine Adjuvant Discovery. *MBio* **8**, (2017).

185.   Gregg, K. A. *et al.* A lipid A-based TLR4 mimetic effectively adjuvants a Yersinia pestis rF-V1 subunit vaccine in a murine challenge model. *Vaccine* **36**, 4023–4031 (2018).

186.   Haupt, R. E. *et al.* Novel TLR4 adjuvant elicits protection against homologous and heterologous Influenza A infection. *Vaccine* **39**, 5205–5213 (2021).

187.   Shimoyama, A. & Fukase, K. Lipid A-Mediated Bacterial–Host Chemical Ecology: Synthetic Research of Bacterial Lipid As and Their Development as Adjuvants. *Molecules* **26**, 6294 (2021).

188.   Gopalakrishnan, A. *et al.* E6020, a TLR4 Agonist Adjuvant, Enhances Both Antibody Titers and Isotype Switching in Response to Immunization with Hapten-Protein Antigens and Is Diminished in Mice with TLR4 Signaling Insufficiency. *The Journal of Immunology* **209**, 1950–1959 (2022).

189.   Chan, M. *et al.* Identification of substituted pyrimido[5,4-b]indoles as selective Toll-like receptor 4 ligands. *J. Med. Chem.* **56**, 4206–4223 (2013).

190.	Ikhimiukor, O. O., Odih, E. E., Donado-Godoy, P. & Okeke, I. N. A bottom-up view of antimicrobial resistance transmission in developing countries. *Nat Microbiol* **7**, 757–765 (2022).

191.	Jadimurthy, R., Mayegowda, S. B., Nayak, S. C., Mohan, C. D. & Rangappa, K. S. Escaping mechanisms of ESKAPE pathogens from antibiotics and their targeting by natural compounds. *Biotechnol Rep (Amst)* **34**, e00728 (2022).

192.	Bastola, R. *et al.* Vaccine adjuvants: smart components to boost the immune system. *Arch. Pharm. Res.* **40**, 1238–1248 (2017).

193.	Kaur, A., Baldwin, J., Brar, D., Salunke, D. B. & Petrovsky, N. Toll-like receptor (TLR) agonists as a driving force behind next-generation vaccine adjuvants and cancer therapeutics. *Curr. Opin. Chem. Biol.* **70**, 102172 (2022).

194.	Facchini, F. A. *et al.* Synthetic glycolipids as molecular vaccine adjuvants: Mechanism of action in human cells and in vivo activity. *J. Med. Chem.* **64**, 12261–12272 (2021).

195.	Calabrese, V., Cighetti, R. & Peri, F. Molecular simplification of lipid A structure: TLR4-modulating cationic and anionic amphiphiles. *Mol. Immunol.* **63**, 153–161 (2015).

196.	Ireton, G. C. & Reed, S. G. Adjuvants containing natural and synthetic Toll-like receptor 4 ligands. *Expert Rev. Vaccines* **12**, 793–807 (2013).

197.	Marzabadi, C. H. & Franck, R. W. Small-molecule carbohydrate-based immunostimulants. *Chemistry* **23**, 1728–1742 (2017).

198.	Lam, C. *et al.* SDZ MRL 953, a novel immunostimulatory monosaccharidic lipid A analog with an improved therapeutic window in experimental sepsis. *Antimicrob. Agents Chemother.* **35**, 500–505 (1991).

199.	Reisser, D., Pance, A. & Jeannin, J.-F. Mechanisms of the antitumoral effect of lipid A. *Bioessays* **24**, 284–289 (2002).

200.	Mosmann, T. Rapid colorimetric assay for cellular growth and survival: application to proliferation and cytotoxicity assays. *J. Immunol. Methods* **65**, 55–63 (1983).

201. Kayser, V. & Ramzan, I. Vaccines and vaccination: history and emerging issues. *Hum. Vaccin. Immunother.* **17**, 5255–5268 (2021).

202. Stewart, A. J. & Devlin, P. M. The history of the smallpox vaccine. *J. Infect.* **52**, 329–334 (2006).

203. Zheng, C. *et al.* Real-world effectiveness of COVID-19 vaccines: a literature review and meta-analysis. *Int. J. Infect. Dis.* **114**, 252–260 (2022).

204. Shah, R. R., Hassett, K. J. & Brito, L. A. Overview of Vaccine Adjuvants: Introduction, History, and Current Status. *Methods Mol. Biol.* **1494**, 1–13 (2017).

205. Delany, I., Rappuoli, R. & De Gregorio, E. Vaccines for the 21st century. *EMBO Mol. Med.* **6**, 708–720 (2014).

206. Reed, S. G., Orr, M. T. & Fox, C. B. Key roles of adjuvants in modern vaccines. *Nat. Med.* **19**, 1597–1608 (2013).

207. Jones, L. H. Recent advances in the molecular design of synthetic vaccines. *Nat. Chem.* **7**, 952–960 (2015).

208. Qureshi, N., Mascagni, P., Ribi, E. & Takayama, K. Monophosphoryl lipid A obtained from lipopolysaccharides of Salmonella minnesota R595. Purification of the dimethyl derivative by high performance liquid chromatography and complete structural determination. *Journal of Biological Chemistry* vol. 260 5271–5278 Preprint at https://doi.org/10.1016/s0021-9258(18)89017-2 (1985).

209. Reed, S. G. & Carter, D. Synthetic glucopyranosyl lipid adjuvants. *US Patent* (2014).

210. Evavold, C. L. & Kagan, J. C. How Inflammasomes Inform Adaptive Immunity. *J. Mol. Biol.* **430**, 217–237 (2018).

211. Mueller, M. *et al.* Aggregates are the biologically active units of endotoxin. *J. Biol. Chem.* **279**, 26307–26313 (2004).

212. Cighetti, R. *et al.* Modulation of CD14 and TLR4·MD-2 Activities by a Synthetic Lipid A Mimetic. *ChemBioChem* vol. 15 250–258 Preprint at https://doi.org/10.1002/cbic.201300588 (2014).

213.   Cochet, F. *et al.* Novel carboxylate-based glycolipids: TLR4 antagonism, MD-2 binding and self-assembly properties. *Sci. Rep.* **9**, 919 (2019).

214.   Brade, L. *et al.* The immunogenicity and antigenicity of lipid A are influenced by its physicochemical state and environment. *Infect. Immun.* **55**, 2636–2644 (1987).

215.   Brandenburg, K. & Wiese, A. Endotoxins: Relationships between Structure, Function, and Activity. *Curr. Top. Med. Chem.* **4**, 1127–1146 (2004).

216.   Trott, O. & Olson, A. J. AutoDock Vina: improving the speed and accuracy of docking with a new scoring function, efficient optimization, and multithreading. *J. Comput. Chem.* **31**, 455–461 (2010).

217.   Morris, G. M. *et al.* AutoDock4 and AutoDockTools4: Automated docking with selective receptor flexibility. *J. Comput. Chem.* **30**, 2785–2791 (2009).

218.   Seydel, U. *et al.* The generalized endotoxic principle. *Eur. J. Immunol.* **33**, 1586–1592 (2003).

219.   Chanput, W., Mes, J. J. & Wichers, H. J. THP-1 cell line: an in vitro cell model for immune modulation approach. *Int. Immunopharmacol.* **23**, 37–45 (2014).

220.   Risco, A. *et al.* p38γ and p38δ kinases regulate the Toll-like receptor 4 (TLR4)-induced cytokine production by controlling ERK1/2 protein kinase pathway activation. *Proc. Natl. Acad. Sci. U. S. A.* **109**, 11200–11205 (2012).

221.   Medvedev, A. E. *et al.* Role of TLR4 tyrosine phosphorylation in signal transduction and endotoxin tolerance. *J. Biol. Chem.* **282**, 16042–16053 (2007).

222.   Jenei-Lanzl, Z., Meurer, A. & Zaucke, F. Interleukin-1β signaling in osteoarthritis - chondrocytes in focus. *Cell. Signal.* **53**, 212–223 (2019).

223.   Baldassare, J. J., Bi, Y. & Bellone, C. J. The role of p38 mitogen-activated protein kinase in IL-1β transcription. *The Journal of Immunology* (1999).

224.   Kelley, N., Jeltema, D., Duan, Y. & He, Y. The NLRP3 Inflammasome: An Overview of Mechanisms of Activation and Regulation. *Int. J. Mol. Sci.* **20**, (2019).

225.   Martín-Sánchez, F. *et al.* Inflammasome-dependent IL-1β release depends upon membrane permeabilisation. *Cell Death Differ.* **23**, 1219–1231 (2016).

226.   Facchini, F. A. *et al.* Structure–Activity Relationship in Monosaccharide-Based Toll-Like Receptor 4 (TLR4) Antagonists. *J. Med. Chem.* **61**, 2895–2909 (2018).

227.   Ohto, U., Fukase, K., Miyake, K. & Shimizu, T. Structural basis of species-specific endotoxin sensing by innate immune receptor TLR4/MD-2. *Proc. Natl. Acad. Sci. U. S. A.* **109**, 7421–7426 (2012).

228.   Matsuura, M., Kiso, M. & Hasegawa, A. Activity of monosaccharide lipid A analogues in human monocytic cells as agonists or antagonists of bacterial lipopolysaccharide. *Infect. Immun.* **67**, 6286–6292 (1999).

229.   Sestito, S. E. *et al.* Amphiphilic Guanidinocalixarenes Inhibit Lipopolysaccharide (LPS)- and Lectin-Stimulated Toll-like Receptor 4 (TLR4) Signaling. *J. Med. Chem.* **60**, 4882–4892 (2017).

230.   Alexander, C. & Rietschel, E. T. Bacterial lipopolysaccharides and innate immunity. *Endotoxin Research* (2001).

231.   Molinaro, A. *et al.* Chemistry of lipid A: at the heart of innate immunity. *Chemistry* **21**, 500–519 (2015).

232.   Kim, H. M. *et al.* Crystal structure of the TLR4-MD-2 complex with bound endotoxin antagonist Eritoran. *Cell* **130**, 906–917 (2007).

233.   Demchenko, A. V. *Handbook of Chemical Glycosylation: Advances in Stereoselectivity and Therapeutic Relevance*. (John Wiley & Sons, 2008).

234.   Volbeda, A. G., van der Marel, G. A. & Codée, J. D. C. Protecting group strategies in carbohydrate chemistry. *Protecting Groups* 1–27 Preprint at https://doi.org/10.1002/9783527697014.ch1 (2019).

235.   Bochkov, A. F. & Zaikov, G. E. *Chemistry of the O-Glycosidic Bond: Formation and Cleavage*. (Elsevier, 2016).

236.   Christensen, H. M., Oscarson, S. & Jensen, H. H. Common side reactions of the glycosyl donor in chemical glycosylation. *Carbohydr. Res.* **408**, 51–95 (2015).

237.   Geringer, S. A., Singh, Y., Hoard, D. J. & Demchenko, A. V. A highly efficient glycosidation of glycosyl chlorides by using cooperative silver(I) oxide-triflic acid catalysis. *Chemistry* **26**, 8053–8063 (2020).

238. Shadrick, M., Stine, K. J. & Demchenko, A. V. Expanding the scope of stereoselective α-galactosylation using glycosyl chlorides. *Bioorg. Med. Chem.* **73**, 117031 (2022).

239. Escopy, S., Singh, Y., Stine, K. J. & Demchenko, A. V. A streamlined regenerative glycosylation reaction: Direct, acid-free activation of thioglycosides. *Chemistry* **27**, 354–361 (2021).

240. Steber, H. B., Singh, Y. & Demchenko, A. V. Iii) Triflate as a Novel and Efficient Activator for Glycosyl Halides. *Org. Biomol. Chem* **2021**, 3220–3233.

241. Romerio, A. *et al.* New Glucosamine-Based TLR4 Agonists: Design, Synthesis, Mechanism of Action, and In Vivo Activity as Vaccine Adjuvants. *J. Med. Chem.* **66**, 3010–3029 (2023).

242. Kulkarni, S. S., Wang, C. C. & Sabbavarapu, N. M. "One-pot" protection, glycosylation, and protection–glycosylation strategies of carbohydrates. *J. Mol. Catal. A: Chem.* (2018).

243. Fraser-Reid, B., Wu, Z., Udodong, U. E. & Ottosson, H. Armed/disarmed effects in glycosyl donors: rationalization and sidetracking. *J. Org. Chem.* **55**, 6068–6070 (1990).

244. Oliva, C., Turnbough, C. L., Jr & Kearney, J. F. CD14-Mac-1 interactions in Bacillus anthracis spore internalization by macrophages. *Proc. Natl. Acad. Sci. U. S. A.* **106**, 13957–13962 (2009).

245. Singh, Y. & Demchenko, A. V. Koenigs-Knorr glycosylation reaction catalyzed by trimethylsilyl trifluoromethanesulfonate. *Chemistry* **25**, 1461–1465 (2019).

246. Cai, X.-H., Guo, H. & Xie, B. Direct Passerini Reaction of Aldehydes, Isocyanides, and Aliphatic Alcohols Catalyzed by Bismuth (III) Triflate. *Int. J. Chem.* **3**, (2011).

247. Guérinot, A., Reymond, S. & Cossy, J. Ritter reaction: Recent catalytic developments. *European J. Org. Chem.* **2012**, 19–28 (2012).

248. Krawczyk, B., Wityk, P., Gałęcka, M. & Michalik, M. The Many Faces of Enterococcus spp.—Commensal, Probiotic and Opportunistic Pathogen. *Microorganisms* **9**, 1900 (2021).

249.   Gilmore, M. S., Clewell, D. B., Ike, Y. & Shankar, N. *Enterococci: From Commensals to Leading Causes of Drug Resistant Infection*. (Massachusetts Eye and Ear Infirmary, 2014).

250.   Wan, L. Y. M., Chen, Z. J., Shah, N. P. & El-Nezami, H. Modulation of Intestinal Epithelial Defense Responses by Probiotic Bacteria. *Crit. Rev. Food Sci. Nutr.* **56**, 2628–2641 (2016).

251.   Megran, D. W. Enterococcal endocarditis. *Clin. Infect. Dis.* **15**, 63–71 (1992).

252.   Denissen, J. *et al.* Prevalence of ESKAPE pathogens in the environment: Antibiotic resistance status, community-acquired infection and risk to human health. *Int. J. Hyg. Environ. Health* **244**, 114006 (2022).

253.   Wisplinghoff, H. *et al.* Nosocomial bloodstream infections in US hospitals: analysis of 24,179 cases from a prospective nationwide surveillance study. *Clin. Infect. Dis.* **39**, 309–317 (2004).

254.   Werner, G. *et al.* Emergence and spread of vancomycin resistance among enterococci in Europe. *Euro Surveill.* **13**, (2008).

255.   Weiner, L. M. *et al.* Antimicrobial-resistant pathogens associated with healthcare-associated infections: summary of data reported to the National Healthcare Safety Network at the Centers for Disease Control and Prevention, 2011--2014. *Infect. Control Hosp. Epidemiol.* **37**, 1288–1301 (2016).

256.   Rice, L. B. Federal funding for the study of antimicrobial resistance in nosocomial pathogens: no ESKAPE. *The Journal of infectious diseases* vol. 197 1079–1081 (2008).

257.   Antimicrobial resistance: a global threat | UNEP - UN Environment Programme.   https://www.unep.org/explore-topics/chemicals-waste/what-we-do/emerging-issues/antimicrobial-resistance-global-threat.

258.   Tacconelli, E. *et al.* Discovery, research, and development of new antibiotics: the WHO priority list of antibiotic-resistant bacteria and tuberculosis. *Lancet Infect. Dis.* **18**, 318–327 (2018).

259. García-Solache Mónica & Rice Louis B. The Enterococcus: a Model of Adaptability to Its Environment. *Clin. Microbiol. Rev.* **32**, 10.1128/cmr.00058-18 (2019).

260. Health Organization, W. Bacterial vaccines in clinical and preclinical development 2021: an overview and analysis. https://apps.who.int/iris/bitstream/handle/10665/359172/9789240052451-eng.pdf?sequence=1 (2022).

261. Romero-Saavedra, F. *et al.* Characterization of Two Metal Binding Lipoproteins as Vaccine Candidates for Enterococcal Infections. *PLoS One* **10**, e0136625 (2015).

262. Laverde, D. *et al.* Targeting Type IV Secretion System Proteins to Combat Multidrug-Resistant Gram-positive Pathogens. *J. Infect. Dis.* **215**, 1836–1845 (2017).

263. Hyyryläinen, H.-L. *et al.* Penicillin-binding protein folding is dependent on the PrsA peptidyl-prolyl cis-trans isomerase in Bacillus subtilis. *Mol. Microbiol.* **77**, 108–127 (2010).

264. Galat, A. Peptidylprolyl cis/trans isomerases (immunophilins): biological diversity--targets--functions. *Curr. Top. Med. Chem.* **3**, 1315–1347 (2003).

265. Kouri, E. D. *et al.* Molecular and biochemical characterization of the parvulin-type PPIases in Lotus japonicus. *Plant Physiol.* **150**, 1160–1173 (2009).

266. Jakob, R. P. *et al.* Dimeric Structure of the Bacterial Extracellular Foldase PrsA. *J. Biol. Chem.* **290**, 3278–3292 (2015).

267. Cahoon, L. A. & Freitag, N. E. Listeria monocytogenes virulence factor secretion: don't leave the cell without a chaperone. *Front. Cell. Infect. Microbiol.* **4**, 13 (2014).

268. Hao, X. *et al.* Dendrimers as scaffolds for multifunctional reversible addition-fragmentation chain transfer agents: Syntheses and polymerization. *J. Polym. Sci. A Polym. Chem.* **42**, 5877–5890 (2004).

269. Ihre, H., Padilla De Jesús, O. L. & Fréchet, J. M. Fast and convenient divergent synthesis of aliphatic ester dendrimers by anhydride coupling. *J. Am. Chem. Soc.* **123**, 5908–5917 (2001).

270.   Bagaev, A. V. *et al.* Elevated pre-activation basal level of nuclear NF-κB in native macrophages accelerates LPS-induced translocation of cytosolic NF-κB into the cell nucleus. *Sci. Rep.* **9**, 4563 (2019).

271.   Cheng, Z., Taylor, B., Ourthiague, D. R. & Hoffmann, A. Distinct single-cell signaling characteristics are conferred by the MyD88 and TRIF pathways during TLR4 activation. *Sci. Signal.* **8**, ra69 (2015).

272.   Moriyama, K. & Nishida, O. Targeting Cytokines, Pathogen-Associated Molecular Patterns, and Damage-Associated Molecular Patterns in Sepsis via Blood Purification. *Int. J. Mol. Sci.* **22**, (2021).

273.   Patil, H. P. *et al.* Evaluation of monophosphoryl lipid A as adjuvant for pulmonary delivered influenza vaccine. *J. Control. Release* **174**, 51–62 (2014).

274.   Jain, S. *et al.* The parasite-derived rOv-ASP-1 is an effective antigen-sparing CD4+ T cell-dependent adjuvant for the trivalent inactivated influenza vaccine, and functions in the absence of MyD88 pathway. *Vaccine* **36**, 3650–3665 (2018).

275.   Chen, C. *et al.* Monophosphoryl-Lipid A (MPLA) is an Efficacious Adjuvant for Inactivated Rabies Vaccines. *Viruses* **11**, (2019).

276.   Fadlelmoula, A., Pinho, D., Carvalho, V. H., Catarino, S. O. & Minas, G. Fourier Transform Infrared (FTIR) Spectroscopy to Analyse Human Blood over the Last 20 Years: A Review towards Lab-on-a-Chip Devices. *Micromachines (Basel)* **13**, (2022).

277.   Ami, D., Mereghetti, P. & Doglia, S. M. Multivariate analysis for Fourier transform infrared spectra of complex biological systems and processes. *Multivariate analysis in* (2013).

278.   Movasaghi, Z., Rehman, S. & ur Rehman, D. I. Fourier Transform Infrared (FTIR) Spectroscopy of Biological Tissues. *Appl. Spectrosc. Rev.* **43**, 134–179 (2008).

279.   Derenne, A., Vandersleyen, O. & Goormaghtigh, E. Lipid quantification method using FTIR spectroscopy applied on cancer cell extracts. *Biochim. Biophys. Acta* **1841**, 1200–1209 (2014).

280.   Ami, D., Mereghetti, P. & Natalello, A. Contribution of Infrared Spectroscopy to the Understanding of Amyloid Protein Aggregation in Complex Systems. *Front Mol Biosci* **9**, 822852 (2022).

281. Fakayode, S. O. *et al.* Molecular (Raman, NIR, and FTIR) spectroscopy and multivariate analysis in consumable products analysis1. *Appl. Spectrosc. Rev.* **55**, 647–723 (2020).

282. Walkowiak, A., Ledziński, Ł., Zapadka, M. & Kupcewicz, B. Detection of adulterants in dietary supplements with Ginkgo biloba extract by attenuated total reflectance Fourier transform infrared spectroscopy and multivariate methods PLS-DA and PCA. *Spectrochim. Acta A Mol. Biomol. Spectrosc.* **208**, 222–228 (2019).

283. Newton, K. & Dixit, V. M. Signaling in innate immunity and inflammation. *Cold Spring Harb. Perspect. Biol.* **4**, (2012).

284. Hassib, S. T., Hassan, G. S., El-Zaher, A. A., Fouad, M. A. & Taha, E. A. Quantitative analysis of anti-inflammatory drugs using FTIR-ATR spectrometry. *Spectrochim. Acta A Mol. Biomol. Spectrosc.* **186**, 59–65 (2017).

285. Nikzad-Langerodi, R. *et al.* Assessment of anti-inflammatory properties of extracts from Honeysuckle (Lonicera sp. L., Caprifoliaceae) by ATR-FTIR spectroscopy. *Talanta* **175**, 264–272 (2017).

286. Osei Akoto, C. *et al.* Anthelminthic, anti-inflammatory, antioxidant, and antimicrobial activities and FTIR analyses of Vernonia camporum stem-bark. *J. Chem.* **2021**, 1–15 (2021).

287. Wiens, R. *et al.* Synchrotron FTIR microspectroscopic analysis of the effects of anti-inflammatory therapeutics on wound healing in laminectomized rats. *Anal. Bioanal. Chem.* **387**, 1679–1689 (2007).

288. Paemanee, A. *et al.* Mass spectrometry and synchrotron-FTIR microspectroscopy reveal the anti-inflammatory activity of Bua Bok extracts. *Phytochem. Anal.* **33**, 1086–1098 (2022).

289. Rodrigues, L. M. *et al.* Evaluation of inflammatory processes by FTIR spectroscopy. *J. Med. Eng. Technol.* **42**, 228–235 (2018).

290. Płóciennikowska, A., Hromada-Judycka, A., Borzęcka, K. & Kwiatkowska, K. Co-operation of TLR4 and raft proteins in LPS-induced pro-inflammatory signaling. *Cell. Mol. Life Sci.* **72**, 557–581 (2015).

291.   Orecchioni, M., Ghosheh, Y., Pramod, A. B. & Ley, K. Macrophage Polarization: Different Gene Signatures in M1(LPS+) vs. Classically and M2(LPS–) vs. Alternatively Activated Macrophages. *Front. Immunol.* **10**, (2019).

292.   Marrocco, A. & Ortiz, L. A. Role of metabolic reprogramming in pro-inflammatory cytokine secretion from LPS or silica-activated macrophages. *Front. Immunol.* **13**, 936167 (2022).

293.   Zhang, C. *et al.* Quantitative profiling of glycerophospholipids during mouse and human macrophage differentiation using targeted mass spectrometry. *Sci. Rep.* **7**, (2017).

294.   Kagan, J. C., Magupalli, V. G. & Wu, H. SMOCs: supramolecular organizing centres that control innate immunity. *Nat. Rev. Immunol.* **14**, 821–826 (2014).

295.   Baker, M. J. *et al.* Using Fourier transform IR spectroscopy to analyze biological materials. *Nat. Protoc.* **9**, 1771–1791 (2014).

296.   Morais, C. L. M., Lima, K. M. G., Singh, M. & Martin, F. L. Tutorial: multivariate classification for vibrational spectroscopy in biological samples. *Nat. Protoc.* **15**, 2143–2162 (2020).

297.   Ami, D., Mereghetti, P. & Maria, S. Multivariate analysis for Fourier transform infrared spectra of complex biological systems and processes. in *Multivariate Analysis in Management, Engineering and the Sciences* (InTech, 2013).

298.   Barth, A. Infrared spectroscopy of proteins. *Biochim. Biophys. Acta* **1767**, 1073–1101 (2007).

299.   Tamm, L. K. & Tatulian, S. A. Infrared spectroscopy of proteins and peptides in lipid bilayers. *Q. Rev. Biophys.* **30**, 365–429 (1997).

300.   Seshadri, S., Khurana, R. & Fink, A. L. Fourier transform infrared spectroscopy in analysis of protein deposits. *Methods Enzymol.* **309**, 559–576 (1999).

301.   Natalello, A., Doglia, S. M., Carey, J. & Grandori, R. Role of flavin mononucleotide in the thermostability and oligomerization of Escherichia coli stress-defense protein WrbA. *Biochemistry* **46**, 543–553 (2007).

302.   Meijer, K. *et al.* Quantitative proteomics analyses of activation states of human THP-1 macrophages. *J. Proteomics* **128**, 164–172 (2015).

303.   Kolseth, I. B. M. *et al.* Serglycin is part of the secretory repertoire of LPS-activated monocytes. *Immun. Inflamm. Dis.* **3**, 23–31 (2015).

304.   Dhungana, S., Merrick, B. A., Tomer, K. B. & Fessler, M. B. Quantitative proteomics analysis of macrophage rafts reveals coHmprtmentalized activation of the proteasome and of proteasome-mediated ERK activation in response to lipopolysaccharide. *Mol. Cell. Proteomics* **8**, 201–213 (2009).

305.   Casal, H. L. & Mantsch, H. H. Polymorphic phase behaviour of phospholipid membranes studied by infrared spectroscopy. *Biochim. Biophys. Acta* **779**, 381–401 (1984).

306.   Lewis, R. N. A. H. & McElhaney, R. N. Fourier transform infrared spectroscopy in the study of lipid phase transitions in model and biological membranes: practical considerations. *Methods Mol. Biol.* **400**, 207–226 (2007).

307.   Banyay, M., Sarkar, M. & Gräslund, A. A library of IR bands of nucleic acids in solution. *Biophys. Chem.* **104**, 477–488 (2003).

308.   Dučić, T., Stamenković, S., Lai, B., Andjus, P. & Lučić, V. Multimodal synchrotron radiation microscopy of intact astrocytes from the hSOD1 G93A rat model of amyotrophic lateral sclerosis. *Anal. Chem.* **91**, 1460–1471 (2019).

309.   Ami, D. *et al.* Tear-based vibrational spectroscopy applied to amyotrophic lateral sclerosis. *Anal. Chem.* **93**, 16995–17002 (2021).

310.   Batista-Gonzalez, A., Vidal, R., Criollo, A. & Carreño, L. J. New insights on the role of lipid metabolism in the metabolic reprogramming of macrophages. *Front. Immunol.* **10**, 2993 (2019).

311.   Lee, J. W. *et al.* UPLC-QqQ/MS-based lipidomics approach to characterize lipid alterations in inflammatory macrophages. *J. Proteome Res.* **16**, 1460–1469 (2017).

312.   Olona, A. *et al.* Sphingolipid metabolism during Toll-like receptor 4 (TLR4)-mediated macrophage activation. *Br. J. Pharmacol.* **178**, 4575–4587 (2021).

313.   Conde, T. A. *et al.* Differential modulation of the phospholipidome of proinflammatory human macrophages by the flavonoids quercetin, naringin and naringenin. *Molecules* **25**, 3460 (2020).

314.   Castoldi, A. *et al.* Triacylglycerol synthesis enhances macrophage inflammatory function. *Nat. Commun.* **11**, (2020).

315.   Everts, B. *et al.* TLR-driven early glycolytic reprogramming via the kinases TBK1-IKKε supports the anabolic demands of dendritic cell activation. *Nat. Immunol.* **15**, 323–332 (2014).

316.   Moon, J.-S. *et al.* UCP2-induced fatty acid synthase promotes NLRP3 inflammasome activation during sepsis. *J. Clin. Invest.* **125**, 665–680 (2015).

317.   Gazi, E. *et al.* Biomolecular profiling of metastatic prostate cancer cells in bone marrow tissue using FTIR microspectroscopy: a pilot study. *Anal. Bioanal. Chem.* **387**, 1621–1631 (2007).

318.   Kacuráková, M. FT-IR study of plant cell wall model compounds: pectic polysaccharides and hemicelluloses. *Carbohydr. Polym.* **43**, 195–203 (2000).

319.   Brézillon, S. *et al.* Glycosaminoglycan profiling in different cell types using infrared spectroscopy and imaging. *Anal. Bioanal. Chem.* **406**, 5795–5803 (2014).

320.   *nfrared Microspectroscopy and Imaging Analysis of Inflammatory and Non-Inflammatory Breast Cancer Cells and Their GAG Secretome.*

321.   Makatsori, E. *et al.* Synthesis and distribution of glycosaminoglycans in human leukemic B- and T-cells and monocytes studied using specific enzymic treatments and high-performance liquid chromatography. *Biomed. Chromatogr.* **15**, 413–417 (2001).

322.   Taylor, K. R. & Gallo, R. L. Glycosaminoglycans and their proteoglycans: host-associated molecular patterns for initiation and modulation of inflammation. *FASEB J.* **20**, 9–22 (2006).

323.   Derenne, A., Derfoufi, K.-M., Cowper, B., Delporte, C. & Goormaghtigh, E. FTIR spectroscopy as an analytical tool to compare glycosylation in therapeutic monoclonal antibodies. *Anal. Chim. Acta* **1112**, 62–71 (2020).

324.   Kirschbaum, C. *et al.* Unravelling the structural complexity of glycolipids with cryogenic infrared spectroscopy. *Nat. Commun.* **12**, 1201 (2021).

325.   Kačuráková, M. & Mathlouthi, M. FTIR and laser-Raman spectra of oligosaccharides in water: characterization of the glycosidic bond. *Carbohydr. Res.* **284**, 145–157 (1996).

326.   Pan, N. C., Pereira, H. C. B., da Silva, M. de L. C., Vasconcelos, A. F. D. & Celligoi, M. A. P. C. Improvement production of hyaluronic acid by streptococcus zooepidemicus in sugarcane molasses. *Appl. Biochem. Biotechnol.* **182**, 276–293 (2017).

327.   Synytsya, A. Fourier transform Raman and infrared spectroscopy of pectins. *Carbohydr. Polym.* **54**, 97–106 (2003).

328.   Foster, A. B., Martlew, E. F., Stacey, M., Taylor, P. J. M. & Webber, J. M. 236. Amino-sugars and related compounds. Part VIII. Some properties of 2-deoxy-2-sulphoamino-D-glucose, heparin, and related substances. *J. Chem. Soc.* 1204 (1961).

329.   Parker, F. *Applications of Infrared Spectroscopy in biochemistry, biology, and medicine*. (Springer, 2012).

330.   Zhao, Y., Mahajan, G., Kothapalli, C. R. & Sun, X.-L. Sialylation status and mechanical properties of THP-1 macrophages upon LPS stimulation. *Biochem. Biophys. Res. Commun.* **518**, 573–578 (2019).

331.   Su, L. *et al.* Sulfatides are endogenous ligands for the TLR4–MD-2 complex. *Proc. Natl. Acad. Sci. U. S. A.* **118**, (2021).

332.   Hernandez, A. *et al.* Immunobiology and application of toll-like receptor 4 agonists to augment host resistance to infection. *Pharmacol. Res.* **150**, 104502 (2019).

333.   Romero, C. D. *et al.* The Toll-like receptor 4 agonist monophosphoryl lipid a augments innate host resistance to systemic bacterial infection. *Infect. Immun.* **79**, 3576–3587 (2011).

334.   Fensterheim, B. A. *et al.* The TLR4 Agonist Monophosphoryl Lipid A Drives Broad Resistance to Infection via Dynamic Reprogramming of Macrophage Metabolism. *J. Immunol.* **200**, 3777–3789 (2018).

335.   Bohannon, J. K. *et al.* Role of G-CSF in monophosphoryl lipid A-mediated augmentation of neutrophil functions after burn injury. *J. Leukoc. Biol.* **99**, 629–640 (2016).

336.   Awate, S., Babiuk, L. A. & Mutwiri, G. Mechanisms of action of adjuvants. *Front. Immunol.* **4**, 114 (2013).

337.   Cipolla, L., Gabrielli, L., Bini, D., Russo, L. & Shaikh, N. Kdo: a critical monosaccharide for bacteria viability. *Nat. Prod. Rep.* **27**, 1618–1629 (2010).

338.   Pulendran, B. Modulating TH1/TH2 responses with microbes, dendritic cells, and pathogen recognition receptors. *Immunol. Res.* **29**, 187–196 (2004).

339.   Xia, S., Chen, Z., Shen, C. & Fu, T.-M. Higher-order assemblies in immune signaling: supramolecular complexes and phase separation. *Protein Cell* **12**, 680–694 (2021).

340.   Ubanako, P., Xelwa, N. & Ntwasa, M. LPS induces inflammatory chemokines via TLR-4 signalling and enhances the Warburg Effect in THP-1 cells. *PLoS One* **14**, e0222614 (2019).

341.   Ito, F., Sono, Y. & Ito, T. Measurement and Clinical Significance of Lipid Peroxidation as a Biomarker of Oxidative Stress: Oxidative Stress in Diabetes, Atherosclerosis, and Chronic Inflammation. *Antioxidants (Basel)* **8**, (2019).

342.   Dunkhunthod, B. *et al.* Gymnema inodorum (Lour.) Decne. Extract alleviates oxidative stress and inflammatory mediators produced by RAW264.7 macrophages. *Oxid. Med. Cell. Longev.* **2021**, 8658314 (2021).

343.   Schrödinger, LLC. Schrödinger Release 2020–2:Maestro, Schrödinger. Preprint at (2020).

344.   Harder, E. *et al.* OPLS3: A Force Field Providing Broad Coverage of Drug-like Small Molecules and Proteins. *J. Chem. Theory Comput.* **12**, 281–296 (2016).

345.   Schrödinger, LLC. The PyMOL Molecular Graphics System, Version 2.0. Preprint at (2015).

346.   Frisch, M. J. *et al.* Gaussian 09. Preprint at (2009).

347.   Case, D. *et al. Amber 16, University of California, San Francisco.* (2016).

348.   Wang, J., Wang, W., Kollman, P. A. & Case, D. A. Automatic atom type and bond type perception in molecular mechanical calculations. *Journal of Molecular Graphics and Modelling* vol. 25 247–260 Preprint at https://doi.org/10.1016/j.jmgm.2005.12.005 (2006).

349.   Bayly, C. I., Cieplak, P., Cornell, W. & Kollman, P. A. A well-behaved electrostatic potential based method using charge restraints for deriving atomic charges: the RESP model. *The Journal of Physical Chemistry* vol. 97 10269–10280 Preprint at https://doi.org/10.1021/j100142a004 (1993).

350.   Wang, J., Wolf, R. M., Caldwell, J. W., Kollman, P. A. & Case, D. A. Development and testing of a general amber force field. *Journal of Computational Chemistry* vol. 25 1157–1174 Preprint at https://doi.org/10.1002/jcc.20035 (2004).

351.   Kirschner, K. N. *et al.* GLYCAM06: a generalizable biomolecular force field. Carbohydrates. *J. Comput. Chem.* **29**, 622–655 (2008).

352.   Dickson, C. J. *et al.* Lipid14: The Amber Lipid Force Field. *Journal of Chemical Theory and Computation* vol. 10 865–879 Preprint at https://doi.org/10.1021/ct4010307 (2014).

353.   Essmann, U. *et al.* A smooth particle mesh Ewald method. *The Journal of Chemical Physics* vol. 103 8577–8593 Preprint at https://doi.org/10.1063/1.470117 (1995).

354.   Maier, J. A. *et al.* ff14SB: Improving the Accuracy of Protein Side Chain and Backbone Parameters from ff99SB. *Journal of Chemical Theory and Computation* vol. 11 3696–3713 Preprint at https://doi.org/10.1021/acs.jctc.5b00255 (2015).

355.   Roe, D. R. & Cheatham, T. E., 3rd. PTRAJ and CPPTRAJ: Software for Processing and Analysis of Molecular Dynamics Trajectory Data. *J. Chem. Theory Comput.* **9**, 3084–3095 (2013).

356.   Case, D. A. *et al. AMBER 2015, University of California, San Francisco*. (2015).

357.   Humphrey, W., Dalke, A. & Schulten, K. VMD: visual molecular dynamics. *J. Mol. Graph.* **14**, 33–8, 27–8 (1996).

358.   Martínez, L., Andrade, R., Birgin, E. G. & Martínez, J. M. PACKMOL: a package for building initial configurations for molecular dynamics simulations. *J. Comput. Chem.* **30**, 2157–2164 (2009).

359.   Journal of infectious diseases, T. & 2019. Conjugation of different immunogenic enterococcal vaccine target antigens leads to extended strain coverage. *academic.oup.com* (2019).

360.   Pérez-Enciso, M. & Tenenhaus, M. Prediction of clinical outcome with microarray data: a partial least squares discriminant analysis (PLS-DA) approach. *Hum. Genet.* **112**, 581–592 (2003).

361.   Breiman, L., Friedman, J., Stone, C. J. & Olshen, R. A. *Classification and Regression Trees*. (Chapman and Hall/CRC, 1984).

362.   Mohamed, H. T. *et al.* Infrared microspectroscopy and imaging analysis of inflammatory and non-inflammatory breast cancer cells and their GAG secretome. *Molecules* **25**, 4300 (2020).

Appendix I

Supplementary information of CHAPTER I

Additional Experimental section of results reported in Chapter I

Chemistry

All reagents and solvents were purchased from commercial sources and used without further purifications, unless stated otherwise. Reactions were monitored by thin-layer chromatography (TLC) performed over Silica Gel 60 F254 plates (Merck®). Flash chromatography purifications were performed on silica gel 60 60-75μm from commercial source.

^{1}H and ^{13}C NMR spectrum were recorded with Bruker Advance 400 with TopSpin® software, or with NMR Varian 400 with Vnmrj software. Chemical shifts are expressed in ppm respect Me4Si; coupling constants are expressed in Hz. The multiplicity in the ^{13}C spectra was deducted by APT experiments.

Exact masses were recorded with Agilent 6500 Series Q-TOF LC/MS System. Purity of final compounds was about 95% as assessed by quantitative NMR analysis.

All compounds are >95% pure by HPLC analysis.

Computational Methods

i.   Computational studies of TLR4 in complex with β-FP20, β-FP22, and β-FP24.

Macromolecule preparation. 3D coordinates from the X-ray structure of the human (TLR4/MD-2/E. coli LPS)2 ectodomain (PDB ID 3FXI)1 were retrieved from the Protein Data Bank (www.rcsb.org). Solvent, ligands, and ions were removed. Hydrogen atoms were added to the X-ray structure using the pre-processing tool of the Protein Preparation Wizard of the Maestro package[343]. The protein structure went through a restrained minimization under the OPLS3 force field[344] with a convergence parameter to root-mean-square-deviation (RMSD) for heavy atoms kept default at 0.3 Å.

Construction and optimization of the ligands. The 3D structures of the FP ligands (FP20, FP22 and FP24) were built with PyMOL molecular graphics and modelling package[345] using as a template the E. coli lipid A (PDB ID 3FXI)1 with the builder tool implemented in PyMOL. The resulting structures were first refined at the AM1 level of theory and then optimized at the Hartree-Fock (HF) level (HF/6-311G**) with Gaussian09.[346]

All-atom parametrization of the ligands. The parameters of the ligands needed for MD simulations were obtained using the standard Antechamber procedure implemented in Amber16.[347] The partial charges were derived from the HF calculations and formatted for AmberTools15 and Amber16 with Antechamber[348], using RESP charges[349], and assigning the general Amber force field (GAFF) atom types.[350] Later, the atom types of the saccharide atoms in FP compounds were changed to the GLYCAM06 force field[351]

tom types, and the atoms constituting the lipid chains to the Lipid14 force field[352] tom types.

Molecular dynamics simulations of FP compounds in water. FP structures were subjected to MD refinement in aqueous solvent, prior to docking. The structures were submitted to all-atom MD simulations during 100 ns in the Amber16 suite.[347] The simulation box was designed such as the edges were distant of at least 10 Å of any atom. The system was solvated with the TIP3P water molecules model. Na+ ions were added to counterbalance the eventual charges of the FP molecules. All the simulations were performed with the same equilibration and production protocol. First, the system was submitted to 1000 steps of the steepest descent algorithm followed by 7000 steps of the conjugate gradient algorithm. A 100 kcal·mol-1·A-2 harmonic potential constraint was applied to the ligand. In the subsequent steps, the harmonic potential was progressively lowered (respectively to 10, 5, and 2.5 kcal·mol-1·A-2) for 600 steps of the conjugate gradient algorithm each time, and then the whole system was minimized uniformly. Next, the system was heated from 0 to 100 K using the Langevin thermostat in the canonical ensemble (NVT) while applying a 20 kcal·mol-1·A-2 harmonic potential restraint on the protein and the ligand. Finally, the system was heated up from 100 to 300 K in the isothermal-isobaric ensemble (NPT) under the same restraint condition as the previous step, followed by simulation for 100 ps with no harmonic restraint applied. At this point, the system was ready for the production run, which was performed using the Langevin thermostat under the NPT ensemble, at a 2 fs time step. Long-range electrostatics were calculated using the Particle Mesh Ewald method.[353]

Docking calculations. To avoid the limitation of using only one scoring function, AutoDock Vina 1.1.2 [217] and AutoDock 4.2 [217] were used for the docking of the FP compounds (FP20, FP22 and FP24) in the TLR4 agonist X-ray structure from PDB ID 3FXI. Preliminary docked poses were obtained with AutoDock Vina, and the best-predicted docked poses were redocked with AutoDock 4. AutoDockTools 1.5.6 program[345] was used to assign the Gasteiger-Marsili empirical atomic partial charges to the atoms of both the ligands and the receptor. Non-polar hydrogens were merged for the ligands. The structure of the receptor and the ligands were set rigid and flexible, respectively. In AutoDock 4.2, the Lamarckian evolutionary algorithm was selected, and all parameters were kept default except for the number of genetic algorithm runs that was set to 100 to enhance the sampling. The box spacing was set to the default value of 1 Å in AutoDock Vina, and 0.375 Å in AutoDock 4. The size of the box was set to 33.00, 40.50, and 35.25 Å in the x, y, z-axes, respectively, with the box centre located equidistant to the mass centre of residues Arg90 (MD-2), Lys122 (MD-2), and Arg264 (TLR4), in both docking programs. The structure of the receptor was always kept rigid, whereas the structure of the ligands was set partially flexible by providing freedom to some carefully selected rotatable bonds.

Molecular dynamics simulations of TLR4/ligand complexes.

Selected docked complexes were submitted to all-atom MD simulations during 200 ns in the Amber16 suite.[347] The protein was described by the ff14SB all-atom force field.[354] For the FP ligands, the monosaccharide backbone was described using the GLYCAM06 force field[351], and the lipid chains with the Lipid14 force field.[352] The simulation box was designed such as the edges were distant of at least 10 Å of any atom. The systems were solvated with the TIP3P water molecules model. Na+ ions were added to counterbalance the eventual charges of the protein-ligand systems when needed. All the simulations were performed with the same equilibration and production protocol. First, the system was submitted to 1000 steps of the steepest descent algorithm followed by 7000 steps of the conjugate gradient algorithm. A 100 kcal·mol-1·A-2 harmonic potential constraint was applied to both the proteins and the ligand. In the subsequent steps, the harmonic potential was progressively lowered (respectively to 10, 5, and 2.5 kcal·mol-1·A-2) for 600 steps of the conjugate gradient algorithm each time, and then the whole system was minimized uniformly. Next, the system was heated from 0 to 100 K using the Langevin thermostat in the canonical ensemble (NVT) while applying a 20 kcal·mol-1·A-2 harmonic potential restraint on the protein and the ligand. Finally, the system was heated up from 100 to 300 K in the isothermal-isobaric ensemble (NPT) under the same restraint condition as the previous step, followed by simulation for 100 ps with no harmonic restraint applied. At this point, the system was ready for the production run, which was performed using the Langevin thermostat under the NPT ensemble, at a 2 fs time step. Long-range electrostatics were calculated using the Particle Mesh Ewald method.[353]

Analysis. Trajectory analysis was performed using the cpptraj module[355] of AmberTools15.[356]

Root mean square deviation (RMSD) was computed with backbone α-carbons for proteins, and heavy atoms for ligands with respect to the first frame using the rms tool.

The vector tool was used to calculate the angle between two vectors associated to two pairs of atoms. To follow the orientation of the ligands along the simulation we computed the angle between two arbitrarily selected vectors, one from the α-carbon (CA) of Thr115 to the CA of Phe121, residues located at MD-2 β-sheet 7, and the other from the C1 to the C3 carbons of FP glucosamine group. To follow the orientation of MD-2 Phe126 side chain we computed the angle between two arbitrarily selected vectors, one from the CA to the ζ-carbon (CZ) of Phe126, and the other from the CA of Phe126 to the CA of Ser33.

With the distance tool we tracked interatomic distances. For polar interactions of FP compounds to (TLR4/MD-2)2 in type-A orientation we computed interatomic distances between the P atom of phosphate group C4 to selected atoms of TLR4 residues (ζ-nitrogen (NZ) of Lys341, NZ of Lys362, and CZ of Arg264), and to selected atoms of MD-2 (η-oxygen (OE) of Tyr102, δ-carbon (CD) of Glu92), between the O atom of hydroxyl C6 group to selected atoms of TLR4* residues (CD of Gln436*, CA of Ser415*), and MD-2 residues (NZ of Lys122 and CZ of Arg90); and between C2

glucosamine atom to selected atoms of MD-2 rim residues (CA of Ser120, CA of Ser118, CA of Arg90, and CA of Glu92). For polar interactions of FP compounds to (TLR4/MD-2)2 in type-B orientation we computed interatomic distances between the P atom of phosphate group C4 to selected atoms of TLR4 residues (NZ of Lys341, and NZ of Lys362), TLR4* residues (CD of Gln436* and CD of Glu439*), and MD-2 residues (NZ of Lys122, and CZ of Arg90), between the O atom of hydroxyl C6 group to selected atoms of TLR4 residues (NZ of Lys341, NZ of Lys362, and CZ of Arg264), and MD-2 residues (CD of Glu92), and between C2 glucosamine atom to selected atoms of MD-2 rim residues (CA of Ser120, CA of Ser118, CA of Arg90, and CA of Glu92).

The nativecontacts tool was used to get minimum distances between sets of atoms. For hydrophobic interactions of fatty acid (FA) chains of FP compounds to residues within the MD-2 pocket we computed minimum distance from any carbon atom of FA chains 1,2 and 3 of FP compounds to any heavy atom of side chains of Val82, Phe141 and Val113.

Molecular visualization and graphics were generated using visual molecular dynamics (VMD) software[357],and PyMOL molecular graphics and modelling package.

ii. Molecular dynamics (MD) simulations of α-FP20 and β-FP20 self-assembly.

Initial systems set up. Initial configurations for molecular dynamics simulations were built using the freely distributed Packmol package.[358] Two simplistic systems were created, each of them consisting of a water cubic box of (80) Å3 with 128 molecules of either α-FP20 or β-FP20 and Na+ counterions. All the molecules were randomly distributed.

Molecular dynamics simulations. Based on our previously reported studies on the self-aggregation of other FP analogs,[353]he systems were simulated at 350 K to minimize the simulation time while increasing the assembly speed. Within the NpT ensemble pressure was handled both isotropically (to trigger the self-assembly). Thus, the systems were first simulated in isotropic conditions at 350 K for 200 ns. The MD protocol used was the same as the one described for the simulations of the docking poses except for the temperature value (350 K instead of 300 K).

Analysis. Trajectory analysis was performed using the cpptraj module[355] of AmberTools15. Molecular visualization and graphics were generated using visual molecular dynamics (VMD) software[357] and PyMOL molecular graphics and modelling package.[345]

Area of the bilayer: the area was calculated as follows: Area per lipid = (box X dimension × box Y dimension). The periodic box dimensions were extracted from the trajectory using cpptraj and following the Lipid14 tutorial at the Amber16 website (https://ambermd.org/tutorials/advanced/tutorial16/).

Murine Immunization Experiments

Animal protocols were approved by CIC bioGUNE's Animal Research Ethics Board in accordance with Spanish and European guidelines and regulations. Thirty-eight

female C57BL/6J mice were purchased from Charles River Laboratories (Lyon, France). Upon arrival, animals were maintained under 12-hour light/dark cycles while receiving food and water ad libitum and were rested for two weeks prior to immunization.

MPLA (InvivoGen), FP18, and FP20 were reconstituted in DMSO (Sigma-Aldrich) at a concentration of 1 mg/mL. EndoFit ovalbumin (InvivoGen) was utilized for immunizations. Inoculations were formulated OVA, adjuvant (or vehicle), and PBS to achieve the appropriate dosages. Immunizations began at approximately 9 weeks of age. At day 0, mice received subcutaneous injections of 10 µg OVA with or without 10 µg of adjuvant. Mice were boosted with identical injections at day 21. Bleeding was performed the day before the first and second immunizations. At day 42, mice were euthanized by carbon dioxide followed by cervical dislocation, and blood was collected via intracardiac puncture. Blood collected in serum separator tubes (BD) was centrifuged at 10,000 RPM for 5 minutes, and serum was stored at -80ºC until use.

Antibody responses were measured by capture ELISA. NUNC plates (ThermoFisher) were coated overnight with 100 µL of coating buffer, containing 0.5 ug/mL OVA in 0.2 M sodium bicarbonate at pH 9.6. Following four washes with 200uL of 0.05% TWEEN-PBS wash buffer in an automatic plate washer (BioTek), plates were blocked for one hour with filtered 1% BSA-PBS assay diluent. Wells were aspirated, and serial dilutions (2-fold) of the sera, starting at 1/100 were applied, followed by an incubation of 1 h. Horseradish peroxidase-conjugated goat anti-mouse secondary antibodies against IgG (Jackson ImmunoResearch), IgG1, IgG2b, IgG2c, and IgG3 (SouthernBiotech) were diluted 1:1000 in assay diluent. After six washes with wash buffer, 100uL of secondary antibody was added to each well for 45 minutes. Plates were washed eight times with 200 µL wash buffer, then two times with 400 µL PBS. One hundred uL of 3,3′,5,5′-tetramethylbenzidine peroxidase substrate solution (TMB, Sera Care) was added to each well and incubated for 30 minutes. After stopping the reaction with 100 µL of 2 M sulfuric acid, samples were measured with a microplate reader (BioTek Epoch) at 450 nm.

Additional SI, such as details on computational methods are available at https://pubs.acs.org/doi/10.1021/acs.jmedchem.2c01998.

Chemistry

Compound 2a

2-dodecanamido-2-deoxy-α,β-D-glucopyranose
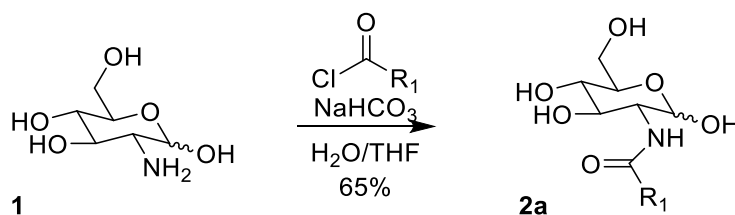
^{1}H NMR (400 MHz, DMSO) δ 7.66 (d, J = 8.0 Hz, 1H, NHβ), 7.49 (d, J = 7.7 Hz, 4H, NHα), 6.44 (d, J = 6.2 Hz, 1H, 1-OHβ), 6.39 – 6.33 (m, 4H, 1-OHα), 4.95 – 4.91 (m, 5H, H-1α+6-OHβ), 4.89 (d, J = 5.2 Hz, 4H, 4-OHα), 4.79 (d, J = 4.8 Hz, 1H, 4-OHβ), 4.59 (d, J = 5.1 Hz, 4H, 3-OHα), 4.51 (t, J = 5.8 Hz, 1H, 3-OHβ), 4.42 (dt, J = 11.5, 5.5 Hz, 5H, H-1β+6-OHα), 3.67 (dd, J = 11.8, 4.6 Hz, 1H, H-3β), 3.62 (dd, J = 5.1, 2.1 Hz, 1H), 3.61 – 3.40 (m, 14H, sugar ring), 3.11 (ddd, J = 9.7, 8.2, 5.1 Hz, 4H, H-6α), 3.08 – 3.03 (m, 2H, H-6β), 2.08 (dt, J = 10.9, 7.4 Hz, 10H, CH$_2$α chains), 1.47 (q, J = 7.0 Hz, 11H, CH$_2$β chains), 1.24 (s, 80H, chains bulk), 0.90 – 0.82 (m, 15H, chain ends).

^{13}C NMR (101 MHz, DMSO) δ 173.31, 172.82, 96.11, 91.05, 77.21, 74.74, 72.49, 71.59, 71.32, 70.83, 61.58, 57.57, 54.73, 40.59, 40.38, 40.17, 39.96, 39.75, 39.54, 39.33, 36.18, 35.74, 31.77, 29.53, 29.49, 29.43, 29.37, 29.23, 29.18, 29.14, 25.78, 22.56, 14.42.

HRMS (ESI- Q-TOF): m/z [M+Na+] calculated for C18H35NNaO6+: 384.2361. Found: 384.2364.

Compound 3a

2-dodecanamido-2-deoxy-6-O-tert-butyldimethylsilyl-α,β-D-glucopyranose
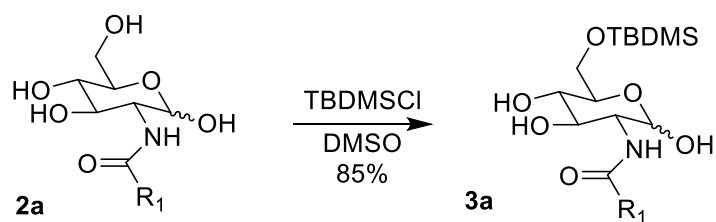
¹H NMR (400 MHz, DMSO) δ 7.62 (d, J = 7.9 Hz, 1H; NH), 6.43 (d, J = 6.4 Hz, 1H; 1-OH), 4.90 (d, J = 6.5 Hz, 1H; 4-OH), 4.77 (d, J = 9.1 Hz, 1H; 3-OH), 4.42 (t, J = 7.0 Hz, 1H; H-1), 3.86 (d, J = 10.8 Hz, 1H; H-6), 3.66 (dd, J = 11.0, 4.6 Hz, 1H; H-6), 3.30 (d, J = 7.9 Hz, 2H; H-2 + H-3), 3.14 – 2.98 (m, 2H; H-4 + H-5), 2.06 (t, J = 7.4 Hz, 2H CH₂α chain), 1.48 (s, 2H; CH₂β chains), 1.24 (s, 20H; chain bulk), 0.94 – 0.74 (m, 12H 3x chain ends + 9x tBu-Si), 0.05 (d, J = 3.0 Hz, 6H; Me-Si).

¹³C NMR (101 MHz, DMSO) δ 173.21, 95.93, 77.09, 74.83, 70.82, 63.61, 57.54, 40.61, 40.40, 40.20, 39.99, 39.78, 39.57, 39.36, 36.20, 31.78, 29.54, 29.51, 29.45, 29.39, 29.20, 29.14, 26.41, 25.76, 22.57, 18.64, 14.41, -4.66, -4.67.

HRMS (ESI- Q-TOF): m/z [M+Na+] calculated for $C_{24}H_{49}NNaO_6Si^+$: 498.3226. Found: 498.3223.

Compound 4a

1,3-di-O-dodecanoyl-2-dodecanamido-2-deoxy-6-O-tert-butyldimethylsilyl-β-D-glucopyranose
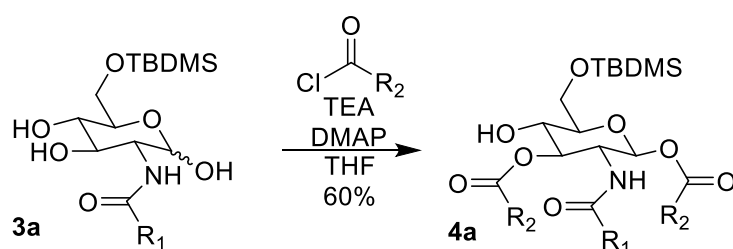
¹H NMR (400 MHz, DMSO) δ 7.80 (d, J = 9.5 Hz, 1H; NH), 5.56 (d, J = 8.9 Hz, 1H; H-1), 5.38 (d, J = 5.9 Hz, 1H; 3-OH), 4.92 (dd, J = 10.6, 8.6 Hz, 1H; H-3), 3.83 (dd, J = 10.4, 5.8 Hz, 2H; H-2 + H-6), 3.76 – 3.70 (m, 1H; H-6), 3.38 (dd, J = 14.3, 8.5 Hz, 2H; H-4 + H-5), 2.30 – 2.14 (m, 7H; CH₂α chains), 1.94 (t, J = 7.3 Hz, 2H; CH₂α chain),

1.44 (dd, J = 25.9, 6.4 Hz, 10H; CH$_2$β chains), 1.24 (d, J = 2.4 Hz, 75H; chains bulk), 0.90 – 0.81 (m, 24H; 9x chain ends + 9x tBu-Si), 0.07 – -0.01 (m, 6H; Me-Si).

^{13}C NMR (101 MHz, DMSO) δ 174.93, 172.72, 172.34, 171.74, 92.49, 77.48, 75.66, 67.73, 62.54, 52.26, 40.65, 40.44, 40.23, 40.02, 39.82, 39.61, 39.40, 36.08, 34.13, 33.94, 31.78, 31.74, 29.59, 29.52, 29.50, 29.44, 29.39, 29.35, 29.30, 29.19, 29.00, 28.93, 28.75, 26.26, 25.70, 24.95, 24.77, 22.55, 18.54, 14.39, 14.36, -4.71, -4.78.

HRMS (ESI- Q-TOF): m/z [M+Na+] calculated for C48H93NNaO8Si+: 862.6567. Found: 862.6569.

Compound 5a

1,3-di-O-dodecanoyl-2-dodecanamido-2-deoxy-4-O-(dibenzyl)phospho-6-O-tert-butyldimethylsilyl-β-D-glucopyranose
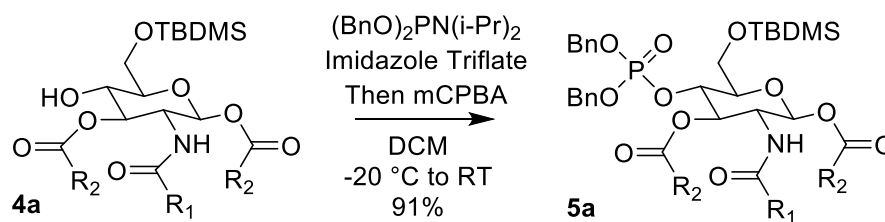
^{1}H NMR (400 MHz, CDCl3) δ 7.34 – 7.25 (m, 10H; aromatic), 5.61 (d, J = 8.7 Hz, 1H; H-1), 5.44 (d, J = 9.6 Hz, 1H; NH), 5.16 (dd, J = 10.8, 9.1 Hz, 1H; H-3), 5.00 (dd, J = 8.1, 2.8 Hz, 2H; CH$_2$-Ph), 4.96 – 4.91 (m, 2H; CH$_2$-Ph), 4.53 (q, J = 9.2 Hz, 1H; H-4), 4.23 (dt, J = 10.8, 9.5 Hz, 1H; H-5), 3.91 (dd, J = 11.9, 1.8 Hz, 1H; 1xH-6), 3.78 (dd, J = 11.9, 4.6 Hz, 1H; 1xH-6), 3.56 (ddd, J = 9.6, 4.4, 1.7 Hz, 1H; H-2), 2.31 (td, J = 7.5, 3.5 Hz, 2H; CH$_2$α chain), 2.19 (t, J = 7.7 Hz, 2H; CH$_2$α chain), 2.07 – 2.01 (m, 2H; CH$_2$α chain), 1.61 – 1.37 (m, 6H; CH$_2$β chains), 1.33 – 1.10 (m, 50H; chain bulk), 0.92 – 0.83 (m, 18H; 9x chain ends + 9x tBu-Si), 0.03 – -0.03 (m, 6H; Me-Si)

^{13}C NMR (101 MHz, CDCl3) δ 174.43, 172.75, 172.40, 135.52, 128.60, 128.56, 127.88, 127.83, 92.59, 77.31, 77.00, 76.68, 76.23, 76.16, 72.94, 72.89, 69.56, 69.51, 69.46, 61.63, 52.79, 36.76, 34.08, 33.94, 31.89, 29.65, 29.60, 29.49, 29.47, 29.43, 29.37, 29.33, 29.25, 29.11, 29.01, 25.82, 25.58, 24.63, 24.58, 22.66, 18.32, 14.07, -5.19, -5.32.

HRMS (ESI-Q-TOF): m/z [M+Na+] calculated for C62H108NNaO11PSi+: 1122.7237. Found: 1123.7234.

Compound 6a

1,3-di-O-dodecanoyl-2-dodecanamido-2-deoxy-4-O-(dibenzyl)phospho-β-D-glucopyranose
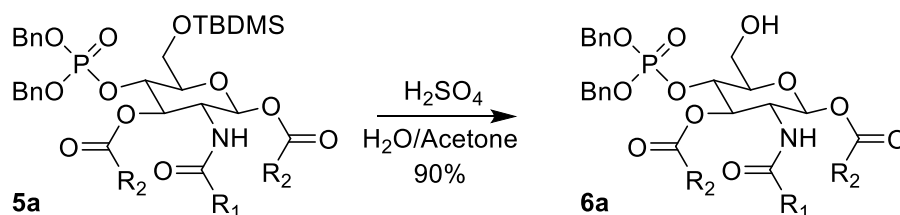
^{1}H NMR (400 MHz, CDCl3) δ 7.40 – 7.27 (m, 10H; aromatics), 5.63 (d, J = 8.8 Hz, 1H; H-1), 5.45 (d, J = 9.6 Hz, 1H; NH), 5.18 (dd, J = 10.7, 9.3 Hz, 1H; H-3), 5.08 – 4.91 (m, 4H; CH$_2$-Ph), 4.54 (q, J = 9.5 Hz, 1H; H-4), 4.26 (dd, J = 19.9, 9.3 Hz, 1H; H-2), 3.87 – 3.74 (m, 2H; H-6), 3.47 (d, J = 9.7 Hz, 1H; H-5), 2.40 – 2.24 (m, 2H; CH$_2$α chain), 2.10 – 1.91 (m, 4H; CH$_2$α chains), 1.61 – 1.46 (m, 4H; CH$_2$β chains), 1.46 – 1.33 (m, 2H; CH$_2$β chain), 1.33 – 1.01 (m, 51H; chains bulk), 0.92 – 0.83 (m, 9H; chains ends).

^{13}C NMR (101 MHz, CDCl3) δ 174.11, 172.77, 172.49, 128.94, 128.84, 128.72, 128.66, 128.26, 127.95, 92.61, 77.33, 77.01, 76.69, 75.90, 75.87, 72.46, 72.42, 72.15, 72.10, 70.23, 70.17, 70.10, 60.23, 52.78, 36.71, 34.03, 33.71, 31.90, 29.67, 29.62, 29.49, 29.44, 29.38, 29.34, 29.32, 29.26, 29.23, 29.04, 29.01, 25.56, 24.59, 24.48, 22.66, 14.09.

HRMS (ESI-Q-TOF): m/z [M+Na+] calculated for C59H92NNaO11P+: 1008.6305. Found: 1008.6309.

Compound FP20

1,3-di-O-dodecanoyl-2-dodecanamido-2-deoxy-4-O-phospho-β-D-glucopyranose
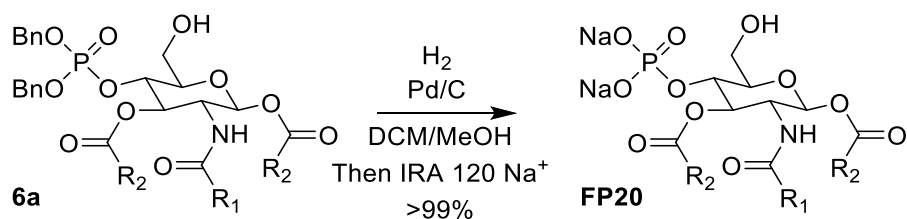
^{1}H NMR (400 MHz, cd3od) δ 5.75 (d, J = 8.9 Hz, 1H; H-1), 5.28 (t, J = 9.8 Hz, 1H; H-3), 4.28 (q, J = 9.7 Hz, 1H; H-4), 4.06 (t, J = 9.6 Hz, 1H; H-2), 3.89 – 3.74 (m, 2H; H-6), 3.62 (t, J = 9.2 Hz, 1H; H-5), 2.42 – 2.25 (m, 4H; CH$_2$α chains), 2.09 (t, J = 7.6 Hz, 2H; CH$_2$α chain), 1.56 (d, J = 6.4 Hz, 7H; CH$_2$β chains), 1.29 (s, 53H; chains bulk), 0.90 (t, J = 6.6 Hz, 9H; chains ends).

^{13}C NMR (101 MHz, MeOD) δ 174.69, 173.32, 172.00, 92.16, 76.22, 76.17, 72.81, 72.78, 72.20, 72.14, 60.30, 52.82, 48.23, 48.02, 47.81, 47.59, 47.38, 47.17, 46.96, 36.05, 33.64, 33.55, 31.67, 31.66, 29.45, 29.39, 29.38, 29.35, 29.26, 29.20, 29.19, 29.14, 29.07, 29.05, 29.02, 28.92, 28.74, 25.58, 24.38, 22.31, 13.00.

HRMS (ESI-Q-TOF): m/z [M-] calculated for C42H80NO11P-: 805.5469. Found: 805.5472.

Compound 7

1,3-di-O-dodecanoyl-2-dodecanamido-2-deoxy-6-O-tert-butyldimethylsilyl-α-D-glucopyranose
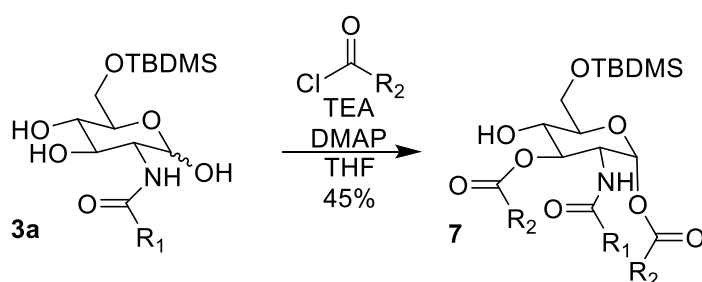
Compound **3a** (2.0 g, 4.2 mmol, 1 eq.) was dissolved in anhydrous THF (84 ml, 0.05 M) under Ar atmosphere. Triethylamine (2.4 ml, 17.2 mmol, 4.1 eq.), 4-dimethylaminopyridine (1.1 g, 9.2 mmol, 2.2 eq.) and lauroyl chloride (2.2 ml, 9.2 mmol, 2.2 eq.) were added to the solution at 0 °C. Reaction was subsequently heated to 30 °C

and stirred over 2h, then controlled by TLC (EtPet/AcOEt 6:4). Subsequently, solution was diluted in AcOEt and washed with 1M HCl. Organic phase thus obtained was dried with Na_2SO_4 and solvent was removed by rotavapor. Raw product thus obtained (4 g) was purified using Biotage® Isolera LS System (Tol/AcOEt 99:1 to 88:12 over 10 CV). After purification, 1.59 g of compound **7** were obtained, in a 45% yield.

^{1}H NMR (400 MHz, CDCl3) δ 6.13 (d, J = 3.6 Hz, 1H, H-1), 5.60 (d, J = 8.6 Hz, 1H, NH), 5.16 (dd, J = 11.1, 9.2 Hz, 1H, H-3), 4.30 (ddd, J = 11.2, 8.7, 3.6 Hz, 1H, H-3), 3.93 (dd, J = 9.8, 3.7 Hz, 1H, H-6a), 3.86 (t, J = 9.1 Hz, 1H, H-4), 3.75 (dd, J = 9.9, 6.6 Hz, 1H, H-6b), 3.72 – 3.68 (m, 1H, H-5), 2.44 – 2.27 (m, 4H, CH$_2$α chains), 2.08 (td, J = 7.4, 2.5 Hz, 2H, CH$_2$α chain), 1.72 – 1.57 (m, 6H, CH$_2$β chains), 1.56 – 1.47 (m, 2H, CH$_2$β chains), 1.36 – 1.19 (m, 53H, chains bulk), 0.91 – 0.83 (m, 20H, 9x chain ends + 9x tBu-Si), 0.10 – 0.06 (m, 6H, Me-Si).

HRMS (ESI- Q-TOF): m/z [M+Na+] calculated for C48H93NNaO8Si+: 862.6567. Found: 862.6565.

Compound 8

1,3-di-O-dodecanoyl-2-dodecanamido-2-deoxy-4-O-(dibenzyl)phospho-6-O-tert-butyldimethylsilyl-α-D-glucopyranose
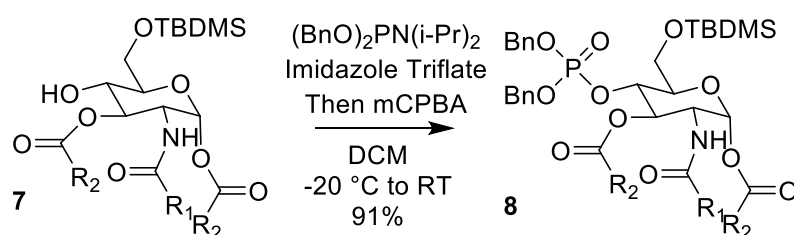
Compound **7** (1.59 g, 1.8 mmol, 1 eq.) and imidazole triflate (1.0 g, 4.0 mmol, 2.25 eq.) were dissolved in DCM (90 mL, 0.02 M) under inert atmosphere. Dibenzyl N,N-diisopropylphosphoramidite (1.38 g, 4.0 mmol, 2.2 eq) was added to the solution at 0 °C. Reaction was monitored by TLC (EtPet/acetone 9:1); after 30 min, substrate depletion was detected. Solution was then cooled at -20 °C and a solution of meta-chloroperbenzoic acid (1.24 g, 7.2 mmol, 4 eq.) in 12 ml of DCM was added dropwise. After 30 min the reaction was allowed to return to RT and left stirring overnight.

After TLC analysis, reaction was quenched with 15 ml of a saturated NaHCO₃ solution and concentrated by rotavapor. The mixture was then diluted in AcOEt and washed 3 times with a saturated NaHCO₃ solution and three times with a 1 M HCl solution. The organic phase was recovered, dried with Na₂SO₄ and solvent was removed by rotavapor.

Crude thus obtained was purified by flash column chromatography (EtPet/acetone 9:1). 1.80 g of pure compound **8** were obtained as a yellow oil in a 91% yield.

^{1}H NMR (400 MHz, CDCl3) δ 7.37 – 7.26 (m, 10H, aromatics), 6.18 (d, J = 3.6 Hz, 1H, H-1), 5.53 (d, J = 8.7 Hz, 1H, NH), 5.32 (dd, J = 11.1, 9.2 Hz, 1H, H-3), 5.01 (dd, J = 8.1, 3.3 Hz, 2H, CH₂-Ph), 4.95 (dd, J = 7.7, 0.9 Hz, 2H, CH₂-Ph), 4.59 (q, J = 9.2 Hz, 1H, H-4), 4.31 (ddd, J = 11.1, 8.7, 3.7 Hz, 1H, H-2), 3.88 – 3.74 (m, 3H, H-5, H-6), 2.43 – 2.35 (m, 2H, CH₂α chain), 2.20 (t, J = 7.7 Hz, 2H, CH₂α chain), 2.06 (td, J = 7.4, 2.4 Hz, 2H, CH₂α chain), 1.65 (p, J = 7.4 Hz, 2H, CH₂β chain), 1.58 – 1.38 (m, 5H, CH₂β chains), 1.37 – 1.12 (m, 51H, chains bulk), 0.93 – 0.81 (m, 19H, 9x chain ends + 9x tBu-Si), 0.01 (d, J = 7.4 Hz, 6H, Me-Si).

^{13}C NMR (101 MHz, CDCl3) δ 175.10, 172.84, 171.44, 135.59, 135.54, 135.51, 135.47, 128.61, 128.57, 128.23, 127.90, 127.79, 90.22, 73.13, 73.06, 72.91, 72.85, 70.93, 69.57, 69.51, 69.48, 69.42, 61.45, 51.34, 36.53, 34.15, 33.99, 31.89, 29.65, 29.60, 29.53, 29.47, 29.43, 29.39, 29.35, 29.33, 29.29, 29.27, 29.24, 29.21, 29.10, 25.80, 25.49, 24.84, 24.59, 23.81, 22.66, 18.26, 14.08, -5.26, -5.34.

HRMS (ESI-Q-TOF): m/z [M+Na+] calculated for C62H108NNaO11PSi+: 1122.7237. Found: 1123.7239

Compound 9

1,3-di-O-dodecanoyl-2-dodecanamido-2-deoxy-4-O-(dibenzyl)phospho-α-D-glucopyranose
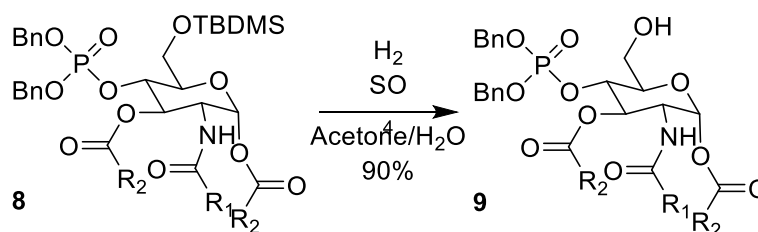
Compound **8** (1.80 g, 1.6 mmol, 1 eq.) was dissolved in acetone (32 mL, 0.05 M) and 320 µL (1% v/v) of a 5% v/v solution of H_2SO_4 in H_2O was added at RT. Solution was left stirring for 8 h and monitored by TLC (EtPet/Acetone 8:2). After reaction completion, solution was diluted in AcOEt and washed three times with a saturated $NaHCO_3$ solution. Organic phase thus obtained was dried with Na_2SO_4 and solvent was removed by rotavapor. Raw product thus obtained was purified by flash column chromatography (EtPet/Acetone 85:15). After purification (1.4 g) of compound **9** was obtained as a white solid in a 90% yield.

^{1}H NMR (400 MHz, CDCl3) δ 7.40 – 7.28 (m, 10H, aromatics), 6.17 (d, J = 3.7 Hz, 1H, H-1), 5.45 (d, J = 8.9 Hz, 1H, NH), 5.32 – 5.25 (m, 1H, H-3), 5.09 – 4.94 (m, 4H, CH_2-Ph), 4.58 (q, J = 9.5 Hz, 1H, H-4), 4.40 (ddd, J = 11.0, 8.9, 3.7 Hz, 1H, H-2), 3.84 (dd, J = 13.2, 2.8 Hz, 1H, H-6a), 3.78 – 3.72 (m, 1H, H-6b), 3.72 – 3.67 (m, 1H, H-5), 2.38 (dd, J = 7.9, 7.1 Hz, 2H, $CH_2α$ chain), 2.05 (dtd, J = 15.3, 8.0, 4.3 Hz, 4H, $CH_2α$ chains), 1.65 (p, J = 7.3 Hz, 2H, $CH_2β$ chain), 1.52 (td, J = 8.3, 3.9 Hz, 2H, $CH_2β$ chain), 1.45 – 1.36 (m, 2H, $CH_2β$ chain), 1.35 – 1.06 (m, 50H, chains bulk), 0.88 (td, J = 6.9, 2.5 Hz, 9H, chain ends).

^{13}C NMR (101 MHz, CDCl3) δ 174.73, 172.74, 171.42, 135.18, 135.15, 135.12, 135.08, 128.94, 128.82, 128.72, 128.66, 128.23, 127.94, 90.43, 77.33, 77.01, 76.69, 72.74, 72.70, 72.17, 72.11, 70.53, 70.49, 70.20, 70.15, 70.09, 70.03, 60.25, 51.07, 36.51, 34.14, 33.79, 31.90, 29.64, 29.61, 29.58, 29.49, 29.46, 29.34, 29.31, 29.26, 29.22, 29.08, 29.05, 25.46, 24.84, 24.61, 22.66, 14.09.

HRMS (ESI-Q-TOF): m/z [M+Na+] calculated for C59H92NNaO11P+: 1008.6305. Found: 1008.6308.

Compound α-FP20

1,3-di-O-dodecanoyl-2-dodecanamido-2-deoxy-4-O-phospho-α-D-glucopyranose
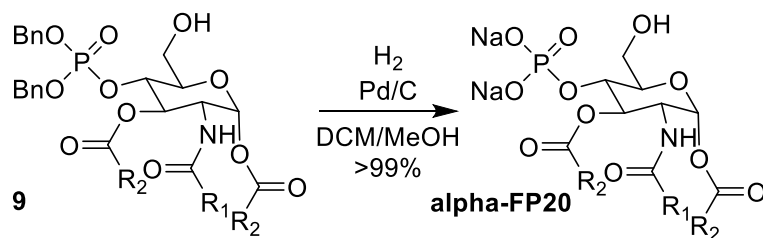
Compound **9** (50 mg, 0.05 mmol, 1 eq.) was dissolved in a mixture of DCM (2.5 mL) and MeOH (2.5 mL) and put under Ar atmosphere. Pd/C catalyzer (10 mg, 20% m/m) was then added to the solution. Gases were then removed in the reaction environment, which was subsequently put under H_2 atmosphere. The solution was allowed to stir for 2 h, then H_2 was removed and reaction monitored by TLC (EtPet/acetone 8:2).

Triethylamine (100 µL) was then added to the reaction, which was stirred for 15 min. Solution was subsequently filtered on syringe filters PALL 4549T Acrodisc 25 mm with GF/0.45 µm Nylon to remove Pd/C catalyzer and solvents were evaporated by rotavapor. Crude product was resuspended in a DCM/MeOH solution and IRA 120 H^+ was added. After 30 min stirring, IRA 120 H^+ was filtered, solvents were removed by rotavapor, the crude resuspended in DCM/MeOH and IRA 120 Na^+ was added. After 30 min stirring, IRA 120 Na^+ was filtered and solvents were removed by rotavapor.

Raw product was purified through reverse chromatography employing a C4 functionalized column (PUREZZA-Sphera Plus Standard Flash Cartridge C4 - 25um - Size 25 g) in the Biotage® Isolera LS System (gradient: H_2O/THF 70:30 to 15:85 over 10 CV with 1% of an aqueous solution of Et_3NHCO_3 at pH 7). (45 mg) of **α-FP20** were obtained as a white powder in a quantitative yield.

^{1}H NMR (400 MHz, MeOD) δ 6.13 (d, J = 3.8 Hz, 1H, H-1), 5.36 (dd, J = 11.0, 9.1 Hz, 1H, H-3), 4.42 – 4.33 (m, 2H, H-2 and H-4), 3.88 – 3.83 (m, 1H, H-5), 3.83 – 3.78 (m, 2H, H-6), 2.51 (t, J = 7.4 Hz, 2H, $CH_2α$ chain), 2.47 – 2.30 (m, 2H, $CH_2α$ chain), 2.17 (dd, J = 9.6, 5.5 Hz, 2H, $CH_2α$ chain), 1.68 (dt, J = 13.9, 6.9 Hz, 2H, $CH_2β$ chain), 1.64 – 1.52 (m, 4H, $CH_2β$ chain), 1.41 – 1.25 (m, 58H, chains bulk), 0.96 – 0.89 (m, 9H, chains ends).

^{13}C NMR (101 MHz, MeOD) δ 175.07, 173.60, 172.19, 90.10, 73.40, 73.35, 72.30, 72.24, 70.64, 60.20, 50.74, 48.24, 48.02, 47.81, 47.60, 47.38, 47.17, 46.96, 35.48, 33.73, 33.32, 31.69, 31.67, 29.44, 29.42, 29.39, 29.36, 29.35, 29.29, 29.27, 29.20, 29.18, 29.10, 28.96, 28.92, 28.78, 25.63, 24.43, 24.37, 22.34, 13.04.

HRMS (ESI-Q-TOF): m/z [M-] calculated for C42H80NO11P-: 805.5469. Found: 805.5463.

Compound 10

1,3-di-O-dodecanoyl-2-dodecanamido-2-deoxy-4,6-di-O-(dibenzyl)phospho-β-D-glucopyranose
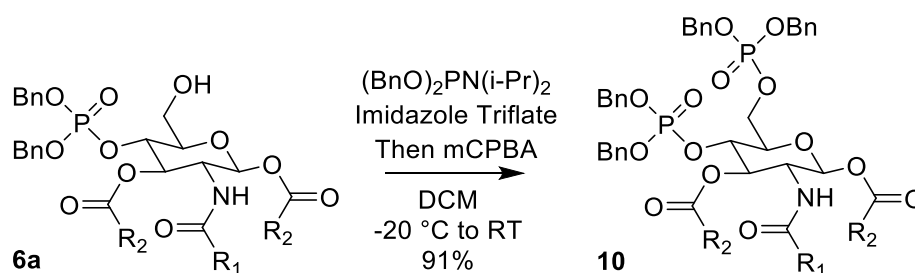
Compound **6a** (2.36 g, 2.4 mmol, 1 eq.) and imidazole triflate (1.4 g, 5.4 mmol, 2.25 eq.) were dissolved in DCM (121 mL, 0.02 M) under inert atmosphere. Dibenzyl N,N-diisopropylphosphoramidite (1.83 g, 5.3 mmol, 2.2 eq) was added to the solution at 0 °C. Reaction was monitored by TLC (EtPet/acetone 9:1); after 30 min, substrate depletion was detected. Solution was then cooled at -20 °C and meta-chloroperbenzoic acid (1.66 g, 9.7 mmol, 4 eq.), dissolved in 17 ml of DCM, was added dropwise. After 30 min the reaction was allowed to return to RT and left stirring overnight.

After TLC analysis, reaction was quenched with 15 ml of a saturated NaHCO₃ solution and concentrated by rotavapor. The mixture was then diluted in AcOEt and washed 3 times with a saturated NaHCO₃ solution and three times with a 1 M HCl solution. The organic phase was recovered, dried with Na₂SO₄ and solvent was removed by rotavapor.

Crude thus obtained was purified by flash column chromatography (EtPet/acetone 9:1). 2.41 g of pure compound **10** were obtained as a yellow oil in a 91% yield.

^{1}H NMR (400 MHz, CDCl3) δ 7.33 – 7.18 (m, 21H; aromatics), 5.66 (d, J = 8.8 Hz, 1H; H-1), 5.51 (d, J = 9.5 Hz, 1H; NH), 5.18 (dd, J = 10.6, 9.2 Hz, 1H; H-3), 5.02 (dd, J = 10.8, 3.3 Hz, 4H; CH$_2$-Ph), 5.00 – 4.95 (m, 2H; CH$_2$-Ph), 4.94 – 4.88 (m, 2H; CH$_2$-Ph), 4.49 – 4.43 (m, 1H; H-4), 4.42 – 4.36 (m, 1H; H-6), 4.25 (dd, J = 19.8, 9.3 Hz, 1H; H-2), 4.16 (ddd, J = 11.8, 7.1, 5.0 Hz, 1H; H-6), 3.74 (dd, J = 9.5, 4.2 Hz, 1H; H-5), 2.19 (dt, J = 15.9, 7.0 Hz, 5H; CH$_2$α chains), 2.07 – 2.01 (m, 2H; CH$_2$α chain), 1.49 (dt, J = 14.0, 7.1 Hz, 4H; CH$_2$β chains), 1.45 – 1.36 (m, 2H; CH$_2$β chain), 1.34 – 1.11 (m, 54H; chains bulk), 0.88 (t, J = 6.8 Hz, 10H; chains ends).

^{13}C NMR (101 MHz, CDCl3) δ 174.22, 172.82, 172.17, 135.79, 135.72, 135.39, 135.33, 135.25, 128.67, 128.65, 128.62, 128.58, 128.54, 128.52, 128.47, 128.44, 128.05, 128.00, 127.96, 127.94, 92.44, 74.11, 72.59, 72.53, 72.41, 72.39, 69.92, 69.86, 69.79, 69.74, 69.44, 69.38, 69.32, 65.30, 52.68, 36.73, 33.93, 31.89, 29.56, 29.53, 29.51, 29.48, 29.46, 29.44, 29.41, 29.39, 29.35, 29.29, 29.21, 29.18, 29.11, 25.57, 24.57, 24.43, 22.66, 14.08.

HRMS (ESI-Q-TOF): m/z [M+Na+] calculated for C70H105NNaO14P2+: 1268.6907. Found: 1268.6908.

Compound FP200

1,3-di-O-dodecanoyl-2-dodecanamido-2-deoxy-4,6-di-O-phospho-β-D-glucopyranose
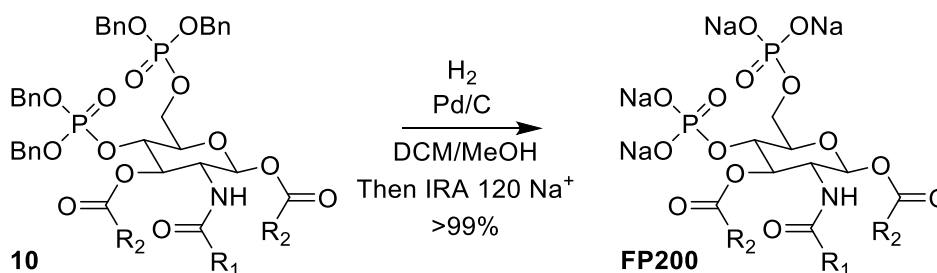
Compound **100** (57 mg, 0.05 mmol, 1eq.) was dissolved in a mixture of DCM (2.5 mL) and MeOH (2.5 mL) and put under Ar atmosphere. Pd/C catalyzer (10 mg, 20% m/m) was then added to the solution. Gases were then removed in the reaction environment, which was subsequently put under H$_2$ atmosphere. The solution was

allowed to stir for 2 h; then H_2 was removed and reaction monitored by TLC (EtPet/acetone 8:2).

Triethylamine (100 µL) was then added to the reaction, which was stirred for 15 min. Solution was subsequently filtered on syringe filters PALL 4549T Acrodisc 25 mm with GF/0.45 µm Nylon to remove Pd/C catalyzer and solvents were evaporated by rotavapor. Crude product was resuspended in a DCM/MeOH solution and IRA 120 H^+ was added. After 30 min stirring, IRA 120 H^+ was filtered, solvents were removed by rotavapor, the crude resuspended in DCM/MeOH and IRA 120 Na^+ was added. After 30 min stirring, IRA 120 Na^+ was filtered and solvents were removed by rotavapor.

(45 mg) of **FP200** were obtained as a white powder in a quantitative yield.

^{1}H NMR (400 MHz, MeOD) δ 5.77 (d, J = 8.8 Hz, 1H; H-1), 5.32 – 5.23 (m, 1H; H-3), 4.39 (dd, J = 18.9, 9.5 Hz, 1H; H-4), 4.21 (d, J = 9.7 Hz, 3H; H-6), 4.10 – 4.00 (m, 1H; H-2), 3.80 (d, J = 9.2 Hz, 1H; H-5), 2.44 – 2.24 (m, 6H; $CH_2\alpha$ chains), 2.09 (t, J = 7.6 Hz, 2H; $CH_2\alpha$ chain), 1.55 (dd, J = 13.5, 6.9 Hz, 10H; $CH_2\beta$ chains), 1.39 – 1.24 (m, 79H; chains bulk), 0.96 – 0.82 (m, 33H; chains ends).

^{13}C NMR (101 MHz, MeOD) δ 174.87, 173.81, 91.22, 72.86, 72.80, 71.25, 68.94, 68.86, 68.80, 64.65, 64.61, 52.10, 48.24, 48.03, 47.82, 47.61, 47.39, 47.18, 46.97, 36.10, 35.63, 33.76, 33.64, 33.55, 33.40, 31.69, 31.63, 29.26, 29.22, 29.18, 29.15, 29.11, 29.06, 29.03, 28.98, 28.84, 28.78, 25.68, 25.62, 24.69, 24.63, 24.38, 22.35, 22.32, 13.06, 13.03, 7.82.

HRMS (ESI-Q-TOF): m/z [M-] calculated for $C_{42}H_{81}NO_{14}P_2^-$: 885.5132. Found: 885.5133.

NMR Spectra

Compound FP20
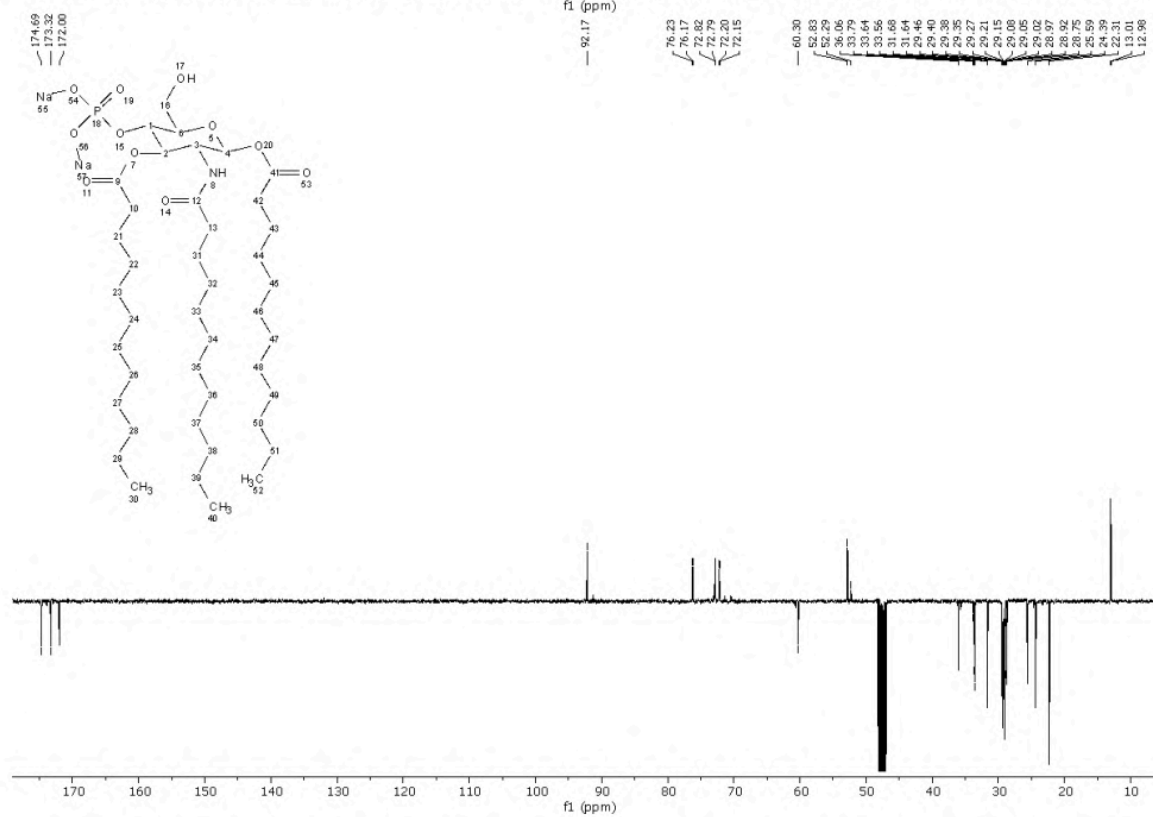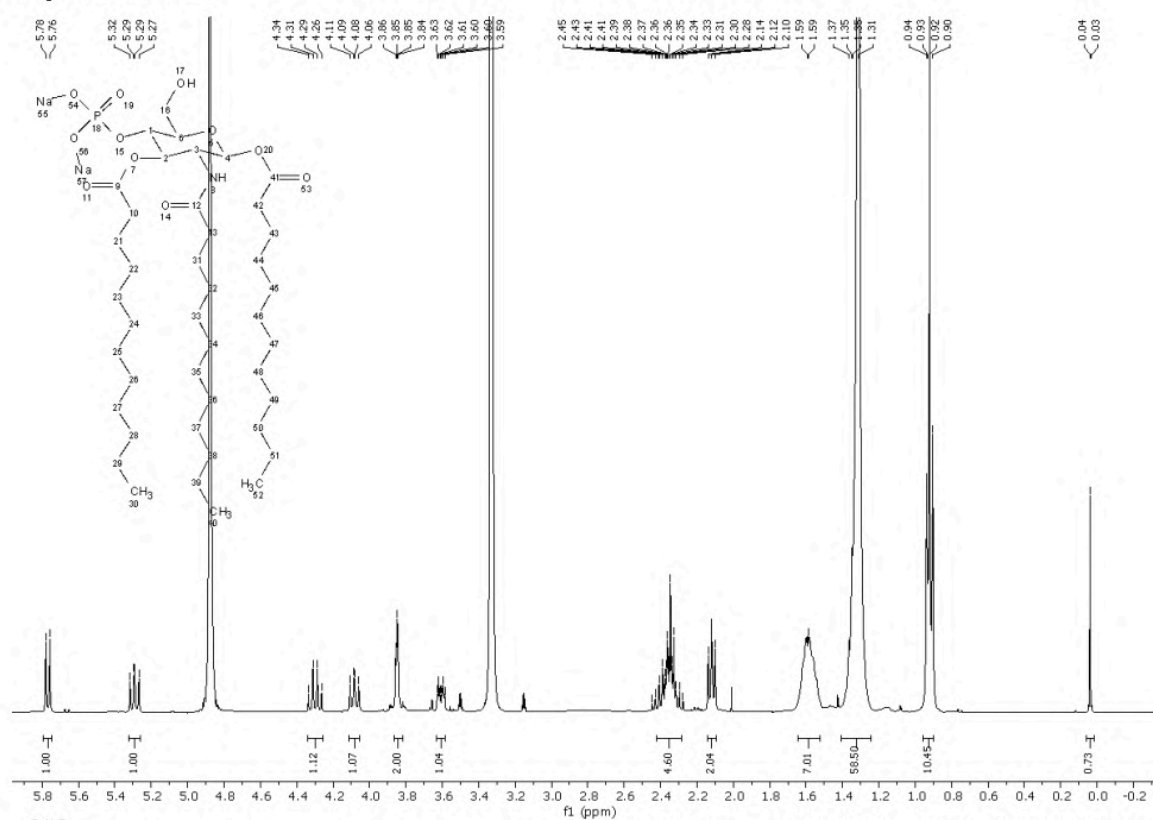
Compound FP21
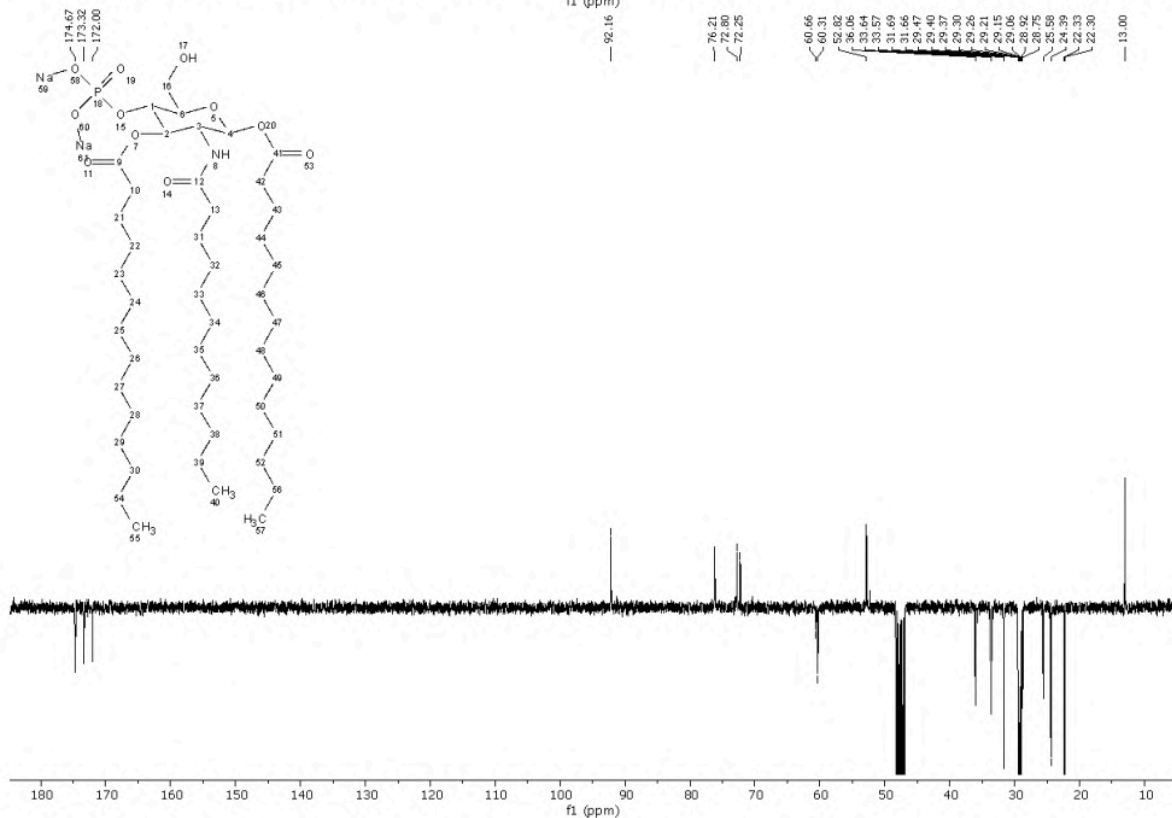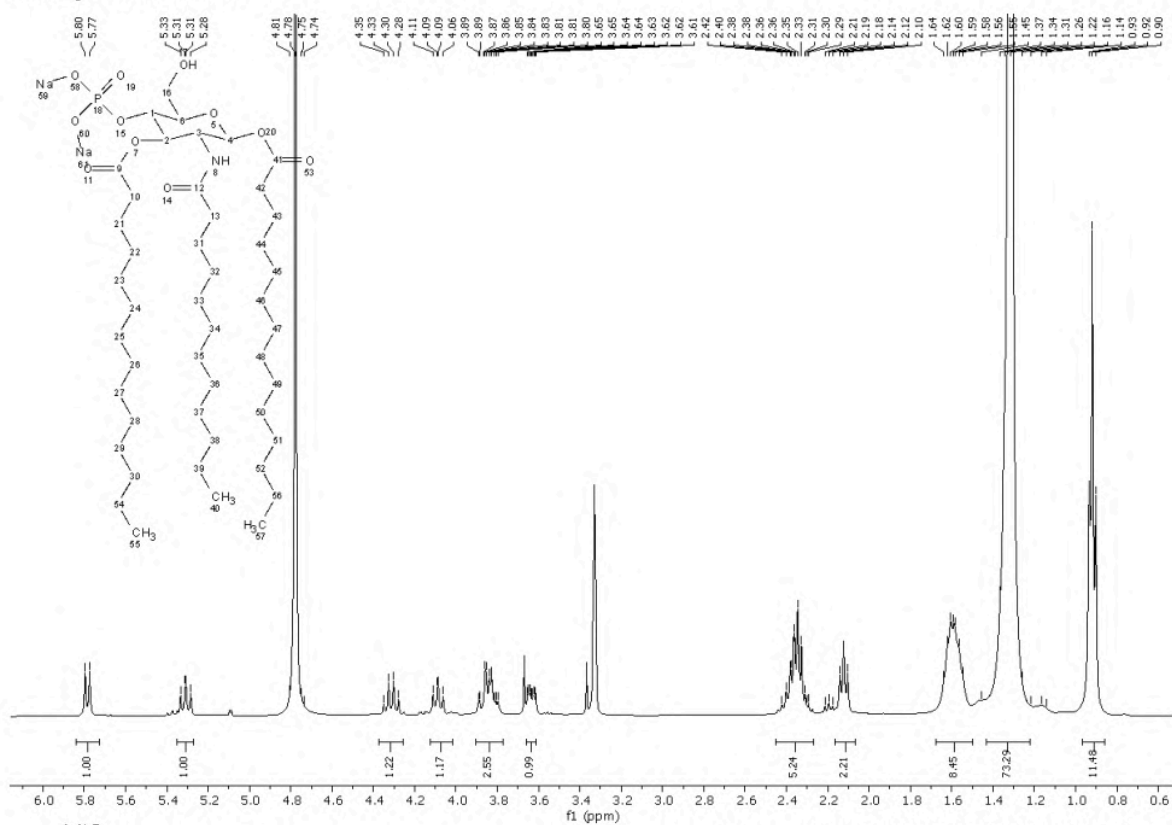
Compound FP22
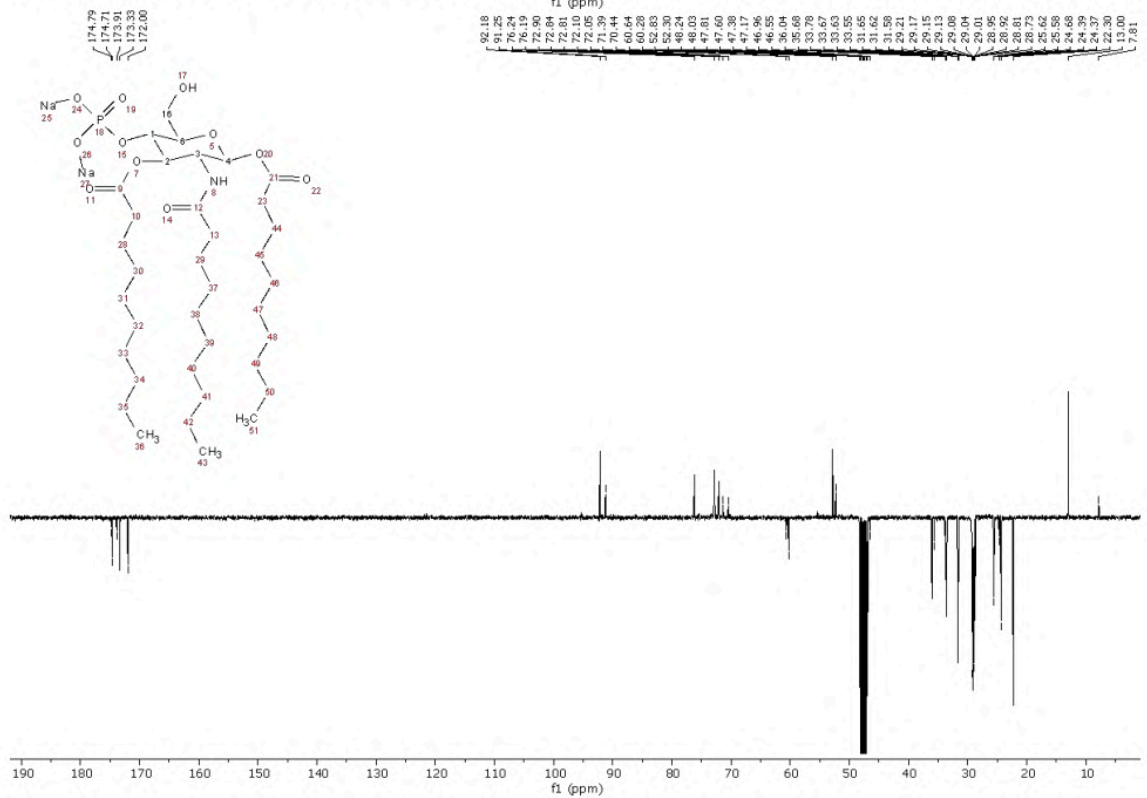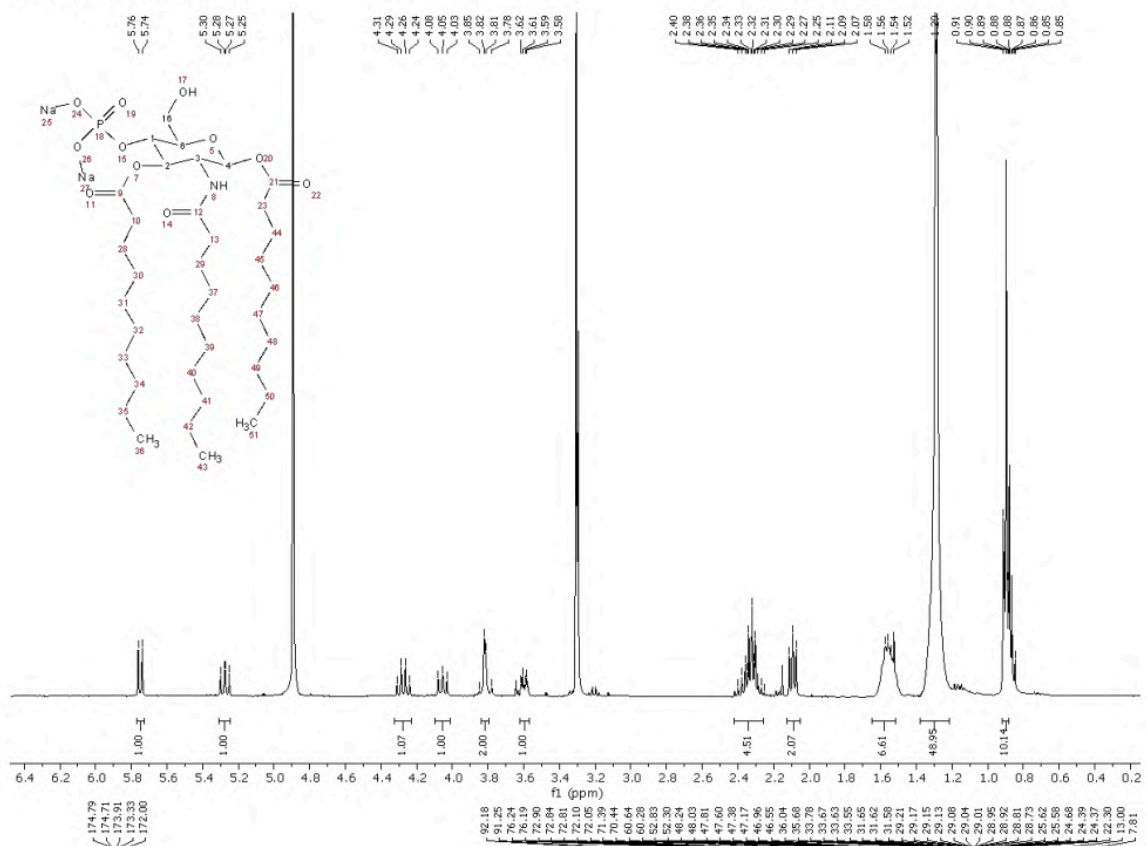
Compound FP23
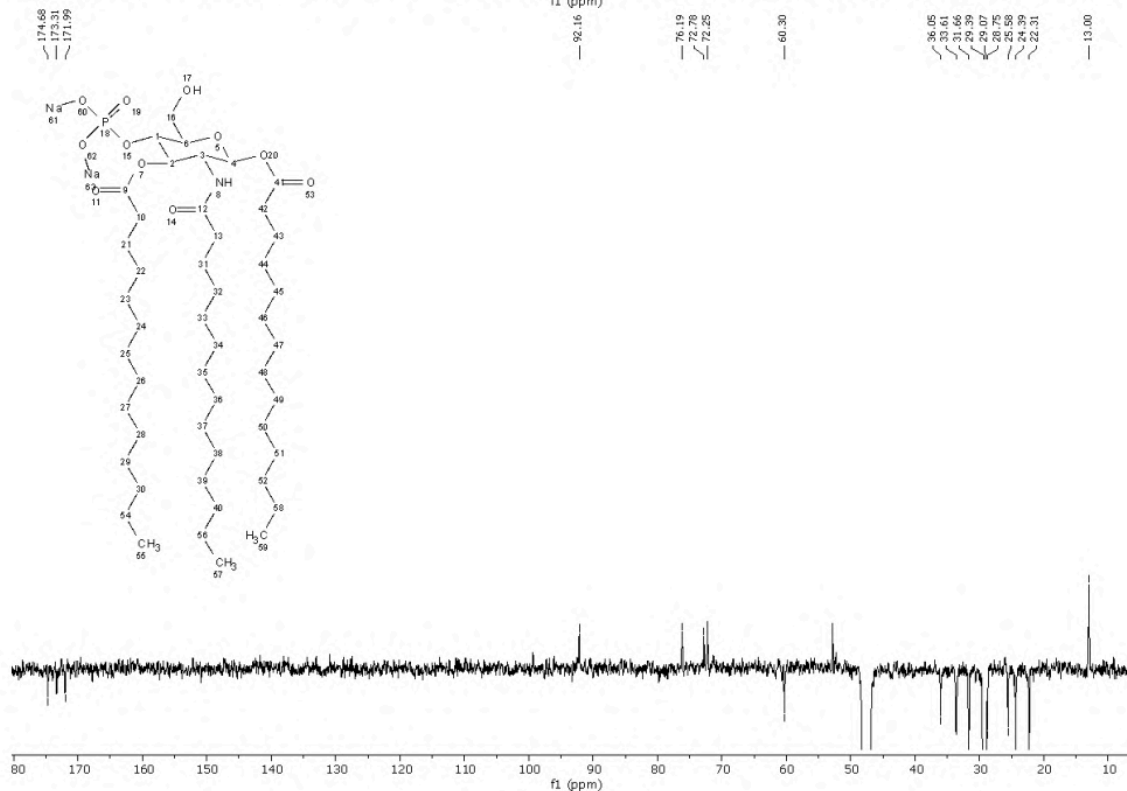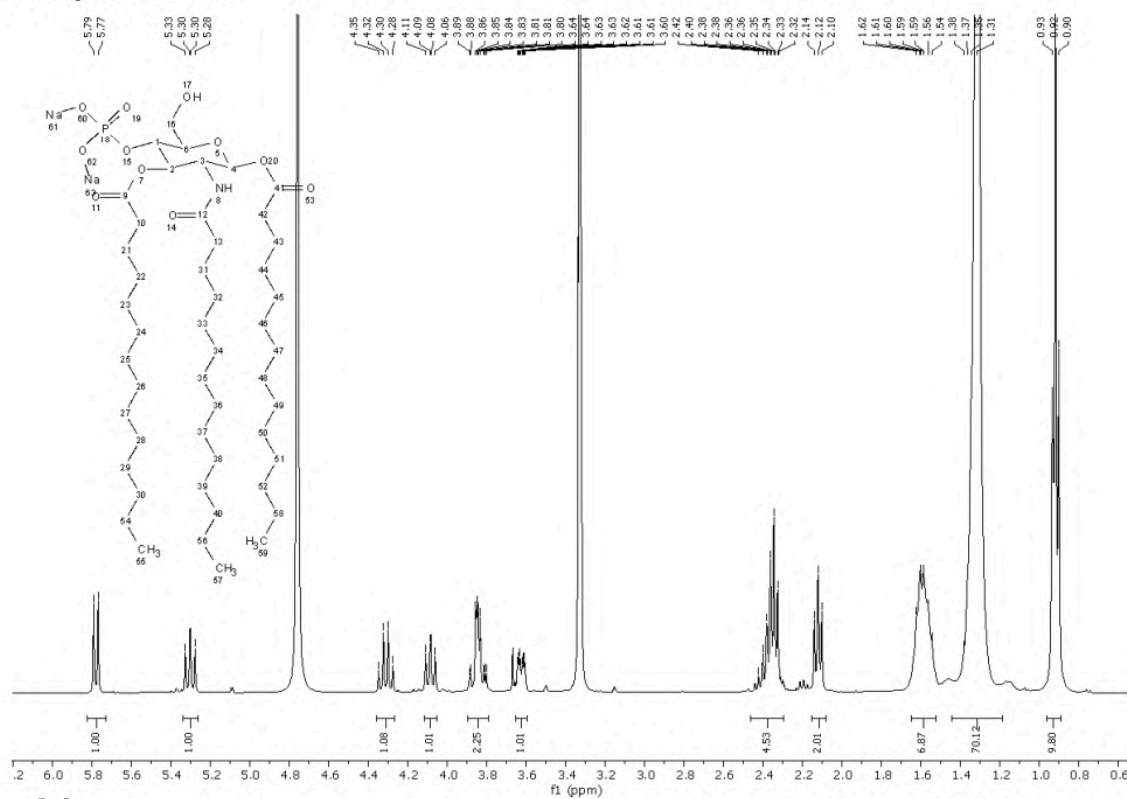
Compound FP24
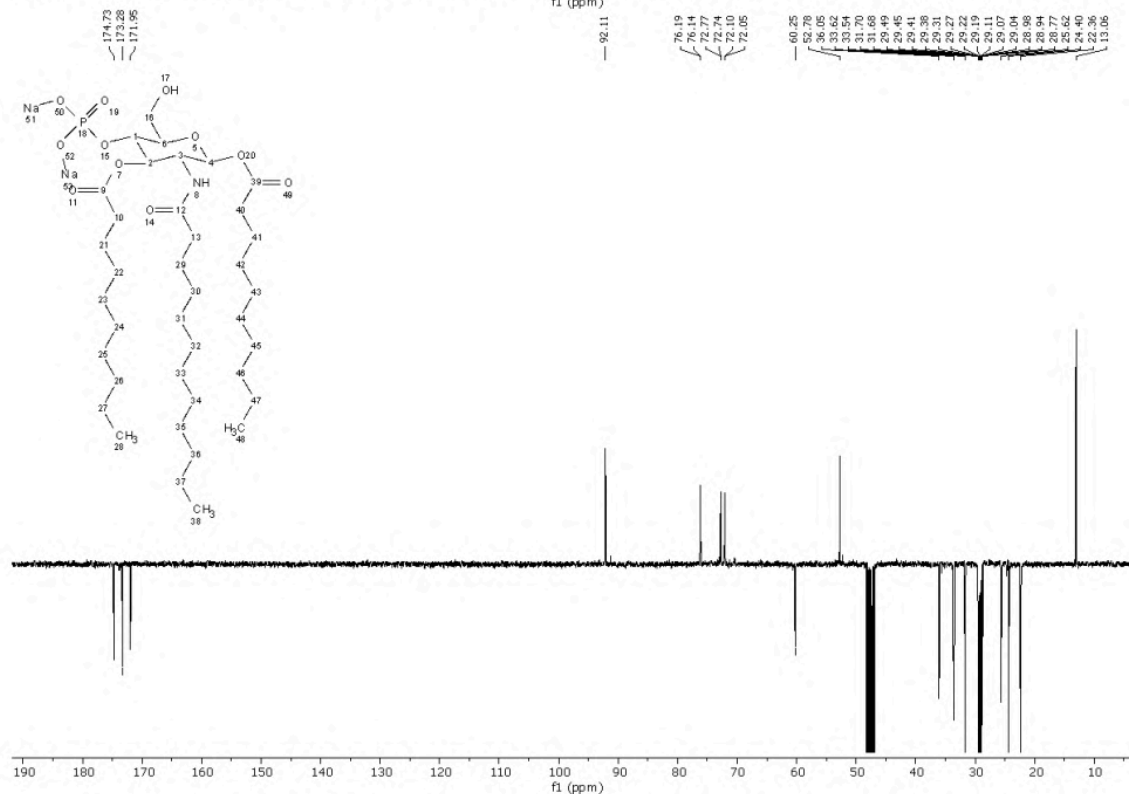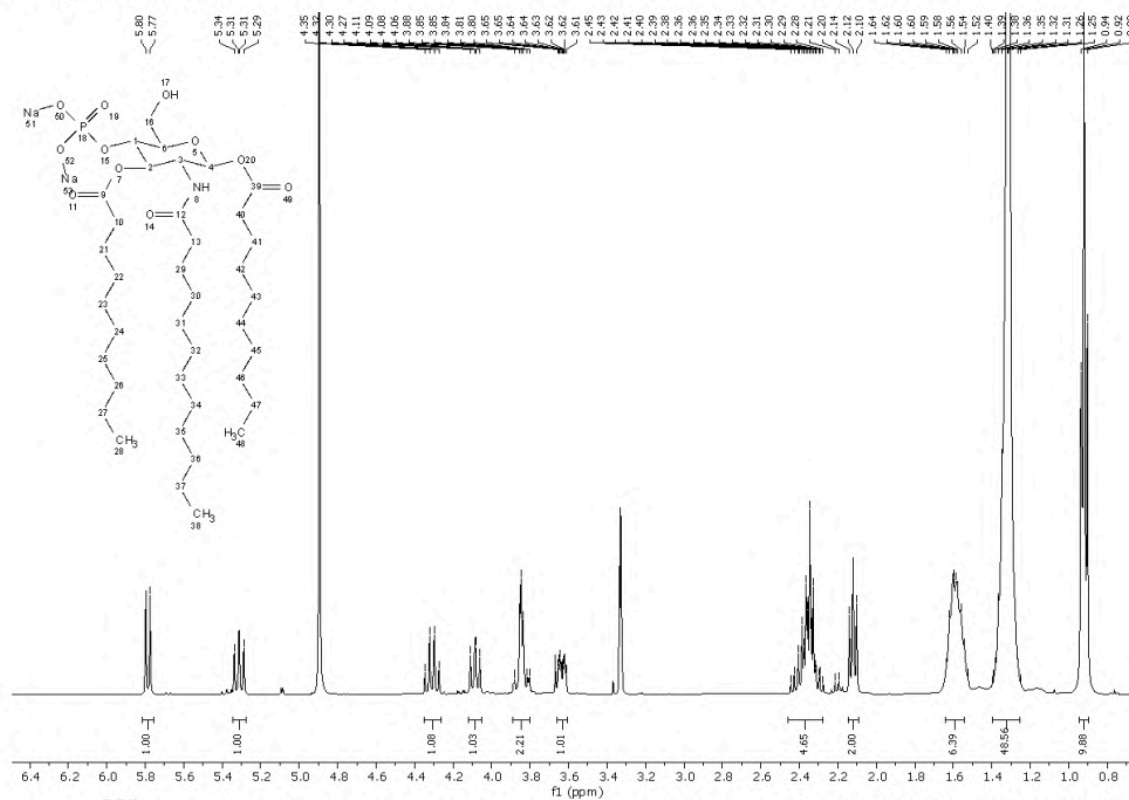
Compound α-FP20
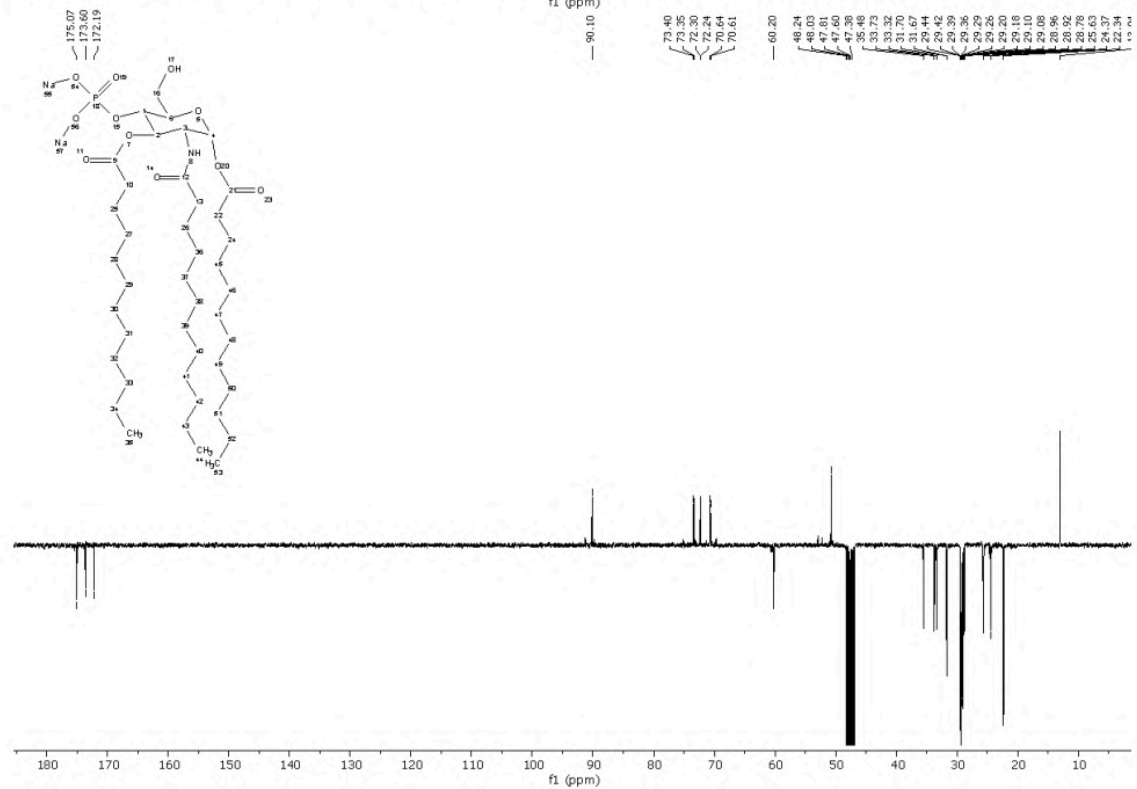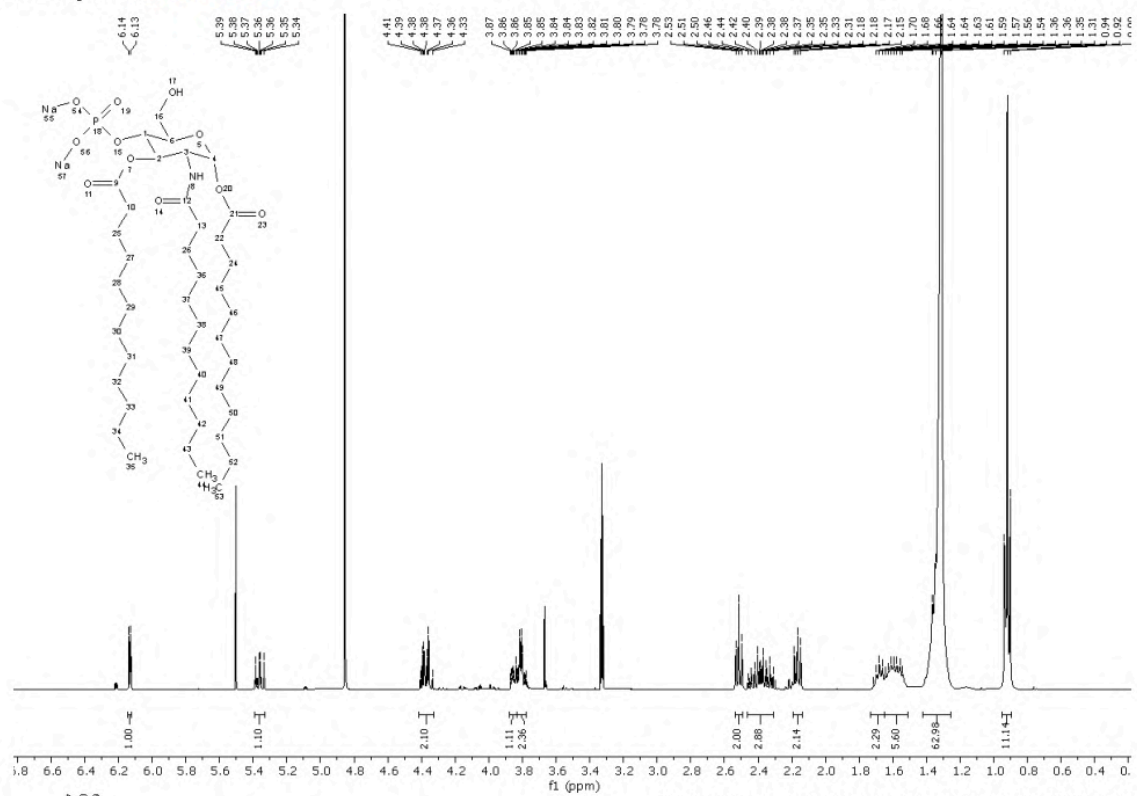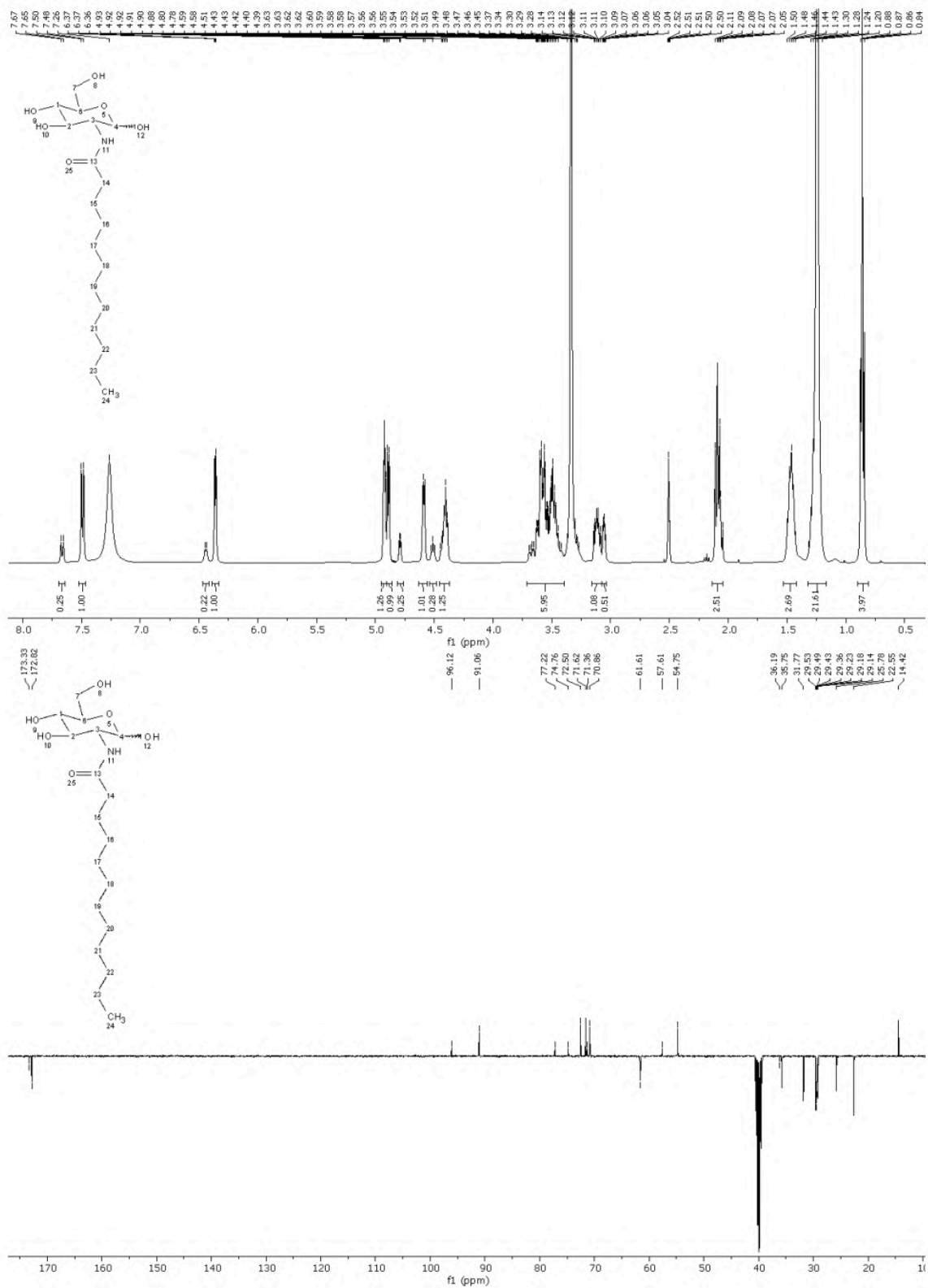
Compound 2a

Compound 3a
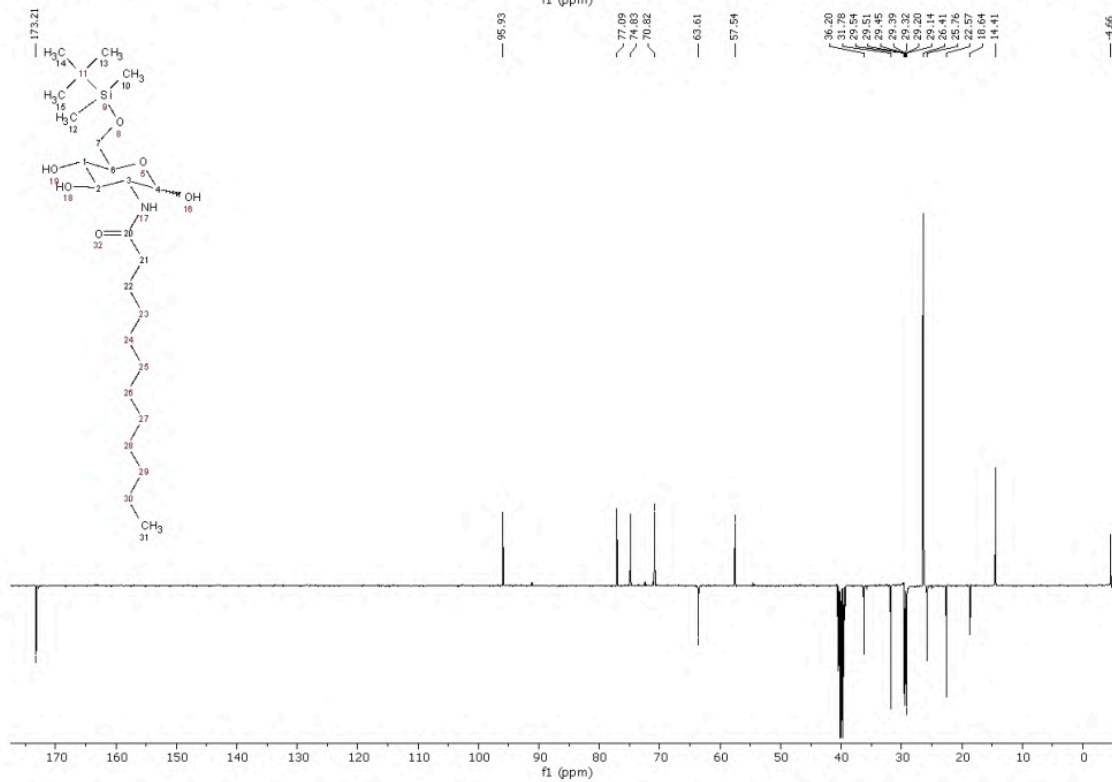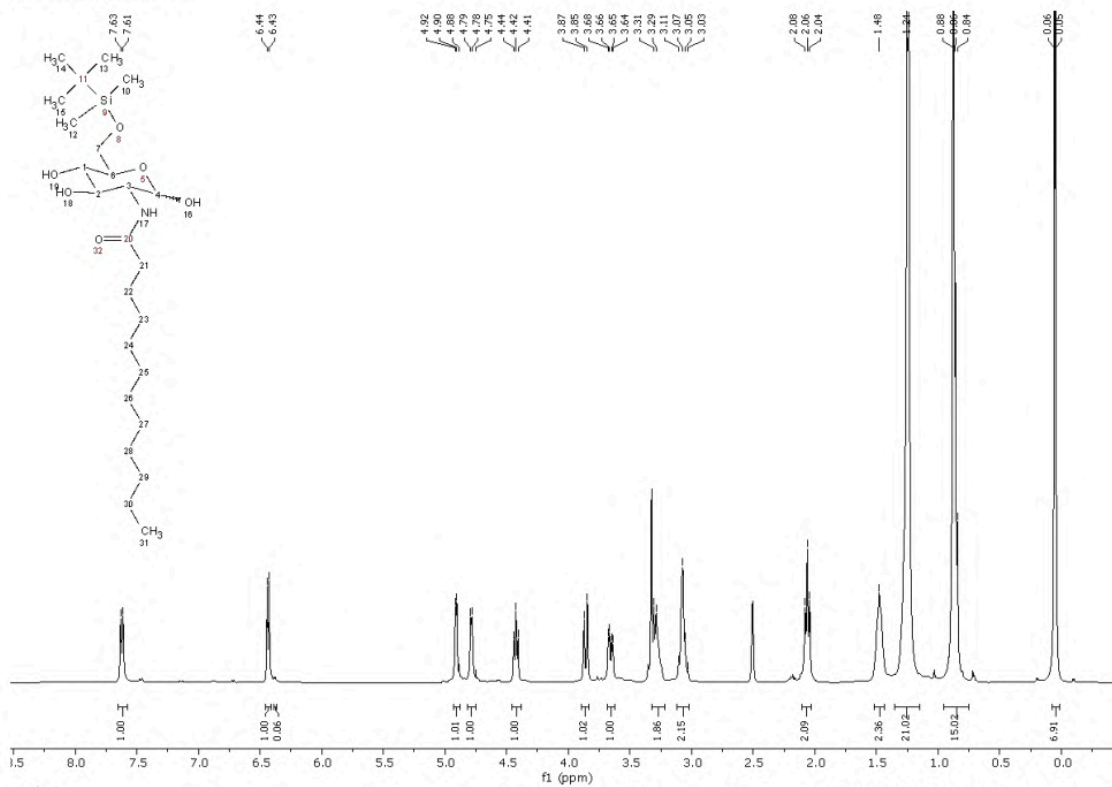
Compound 4a
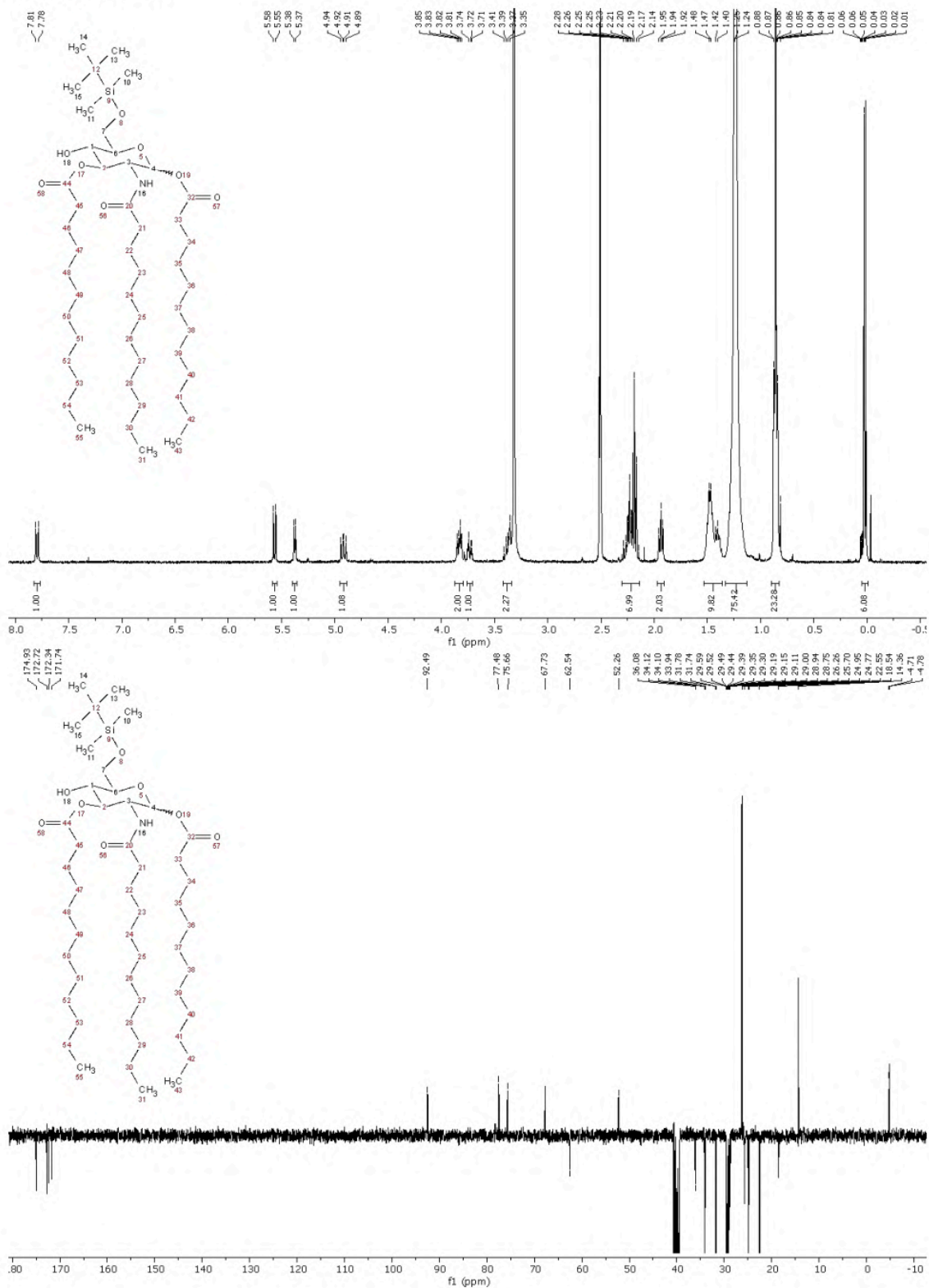
Compound 5a
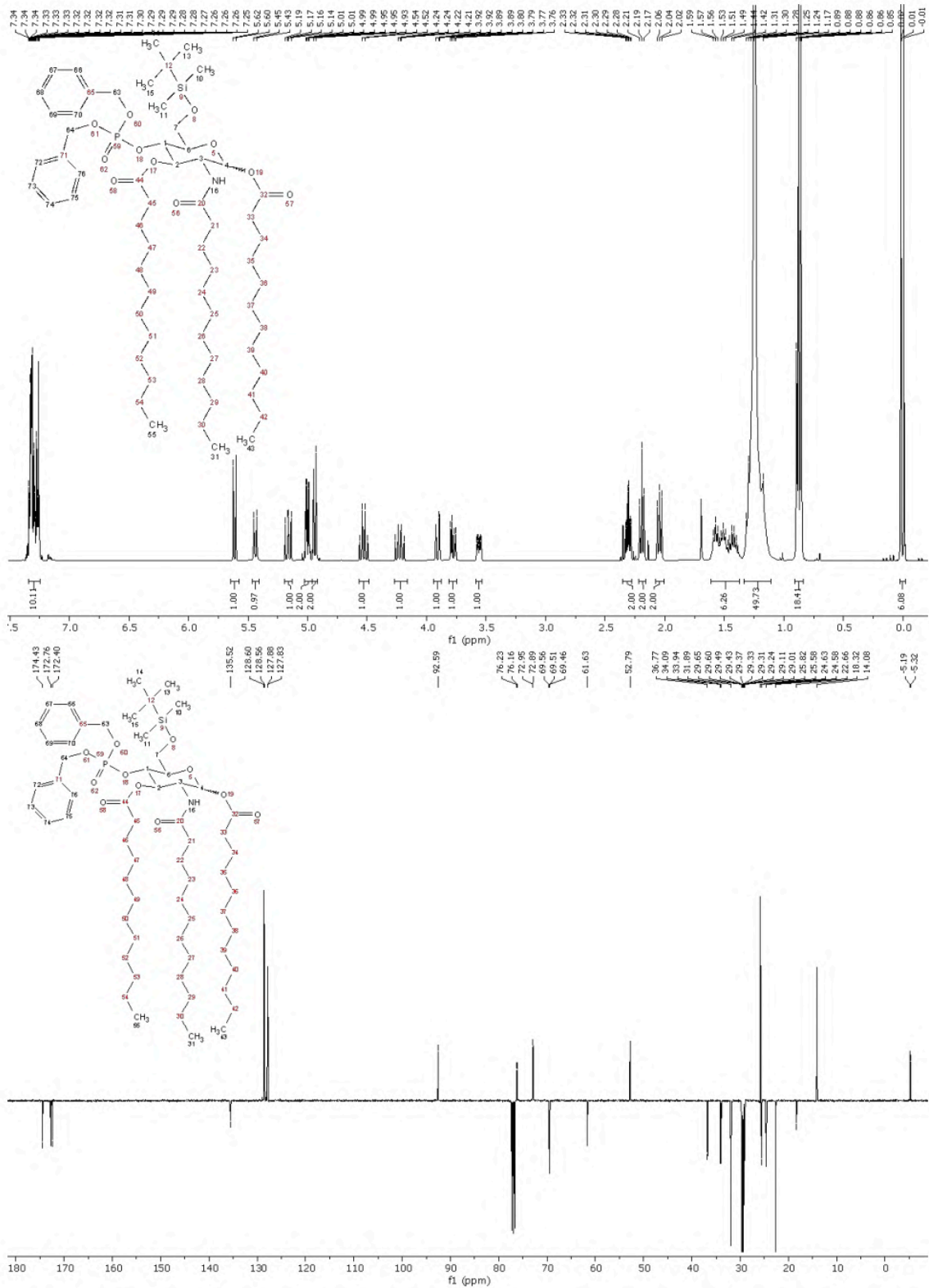
Compound 6a
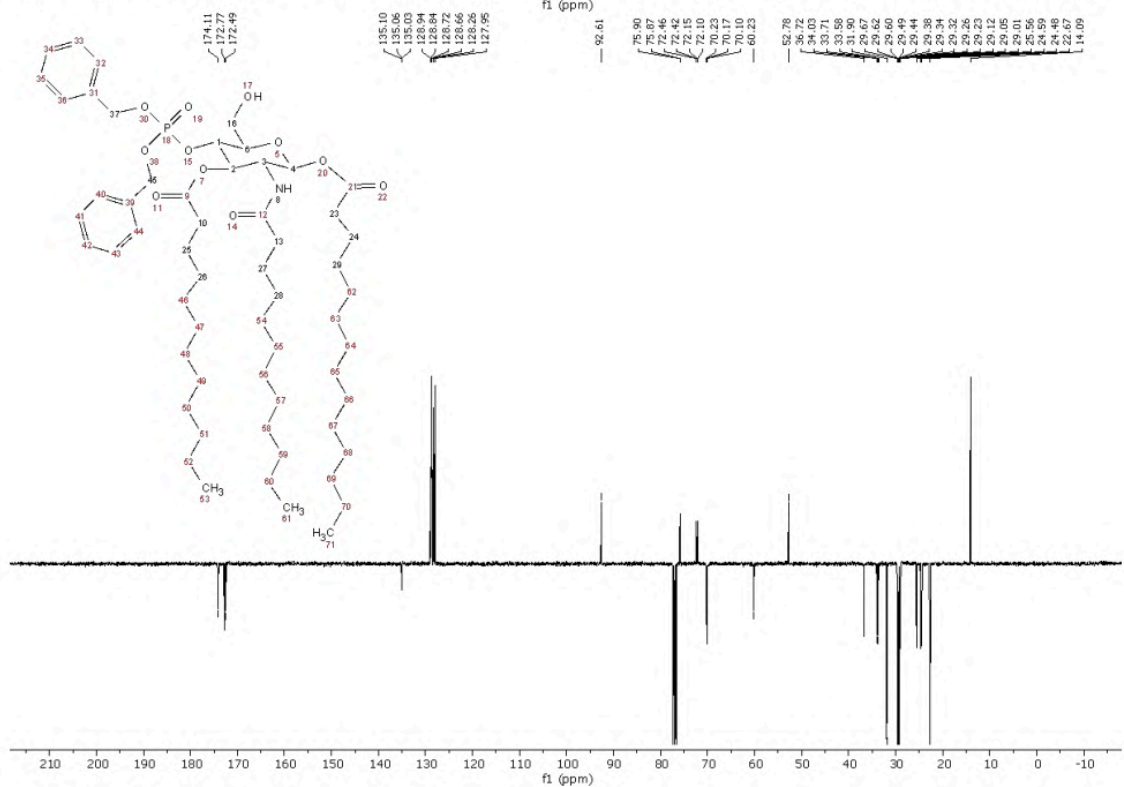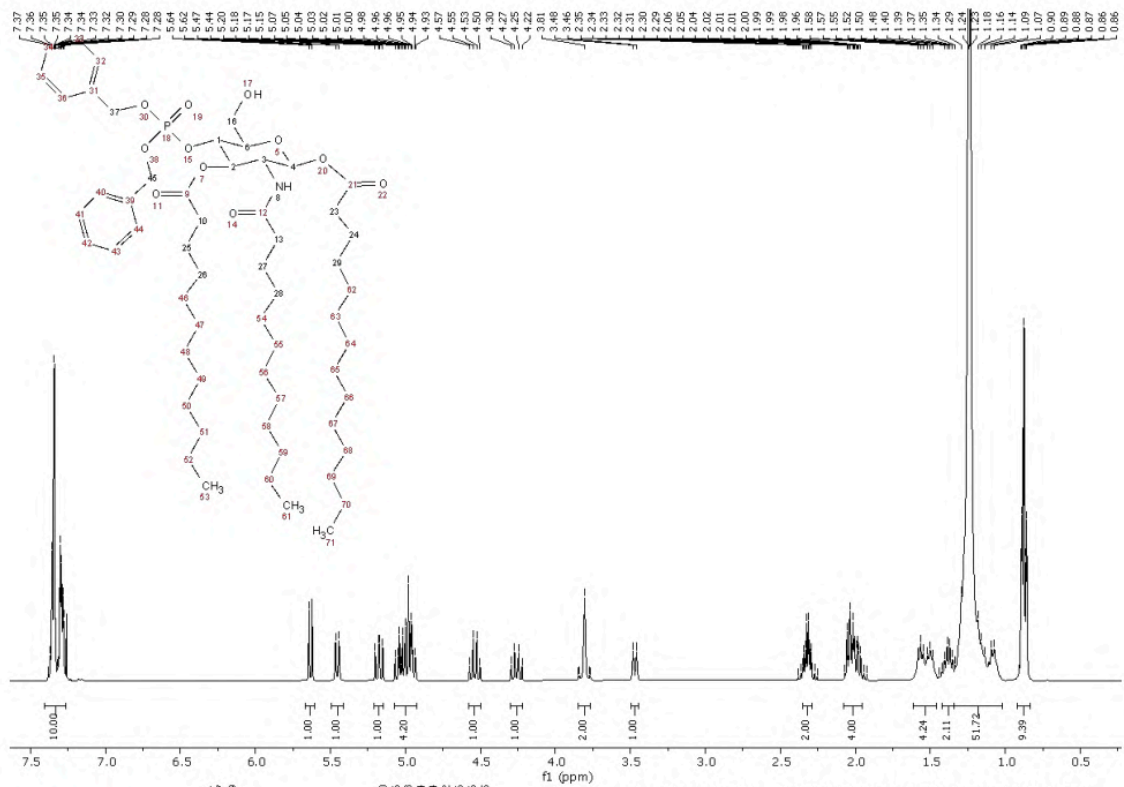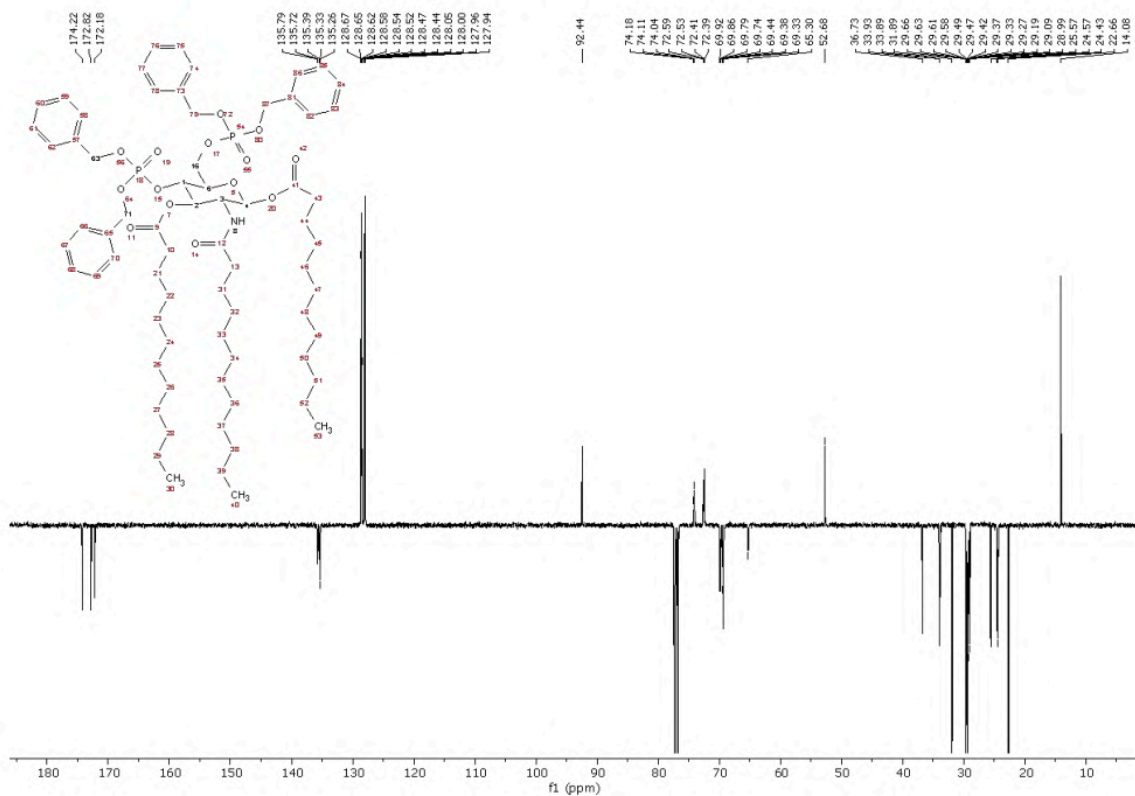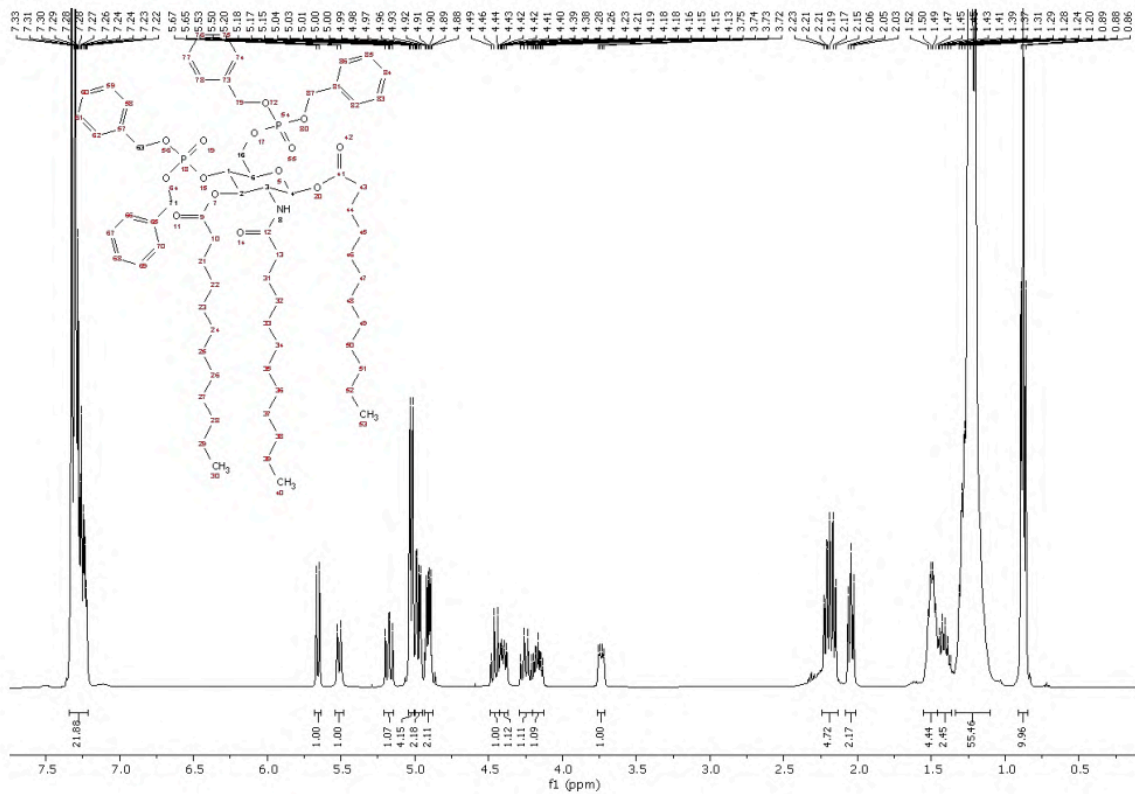
Compound 7
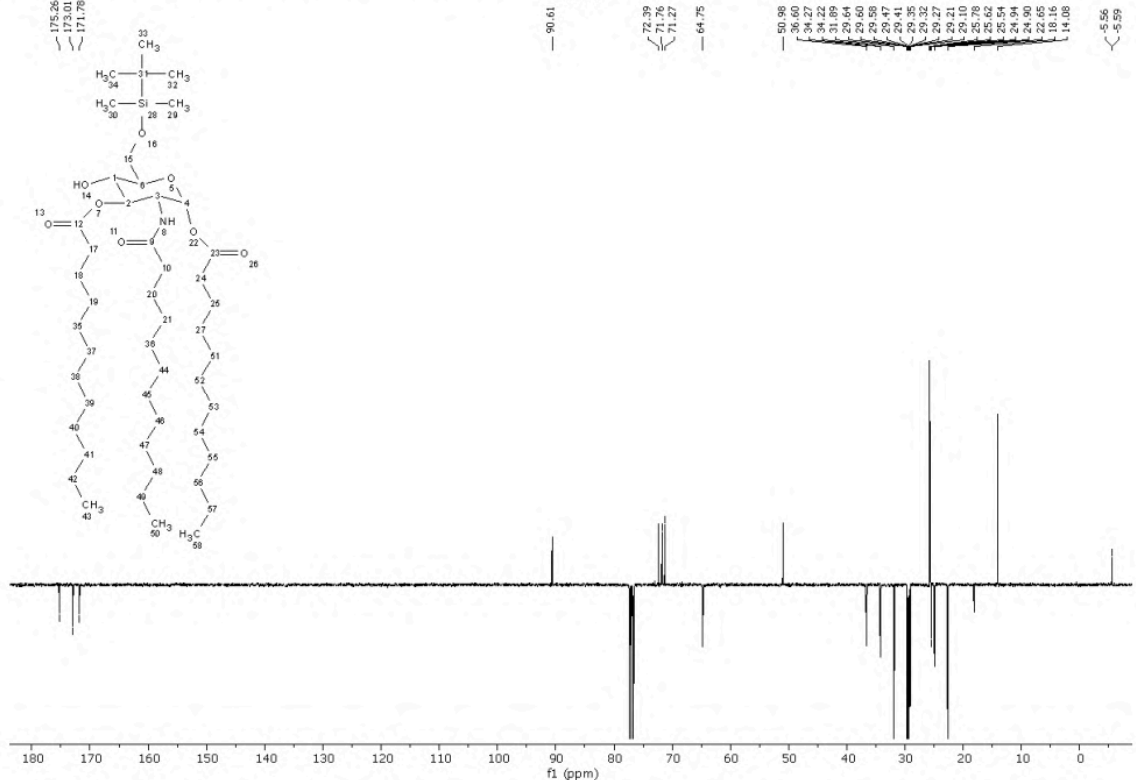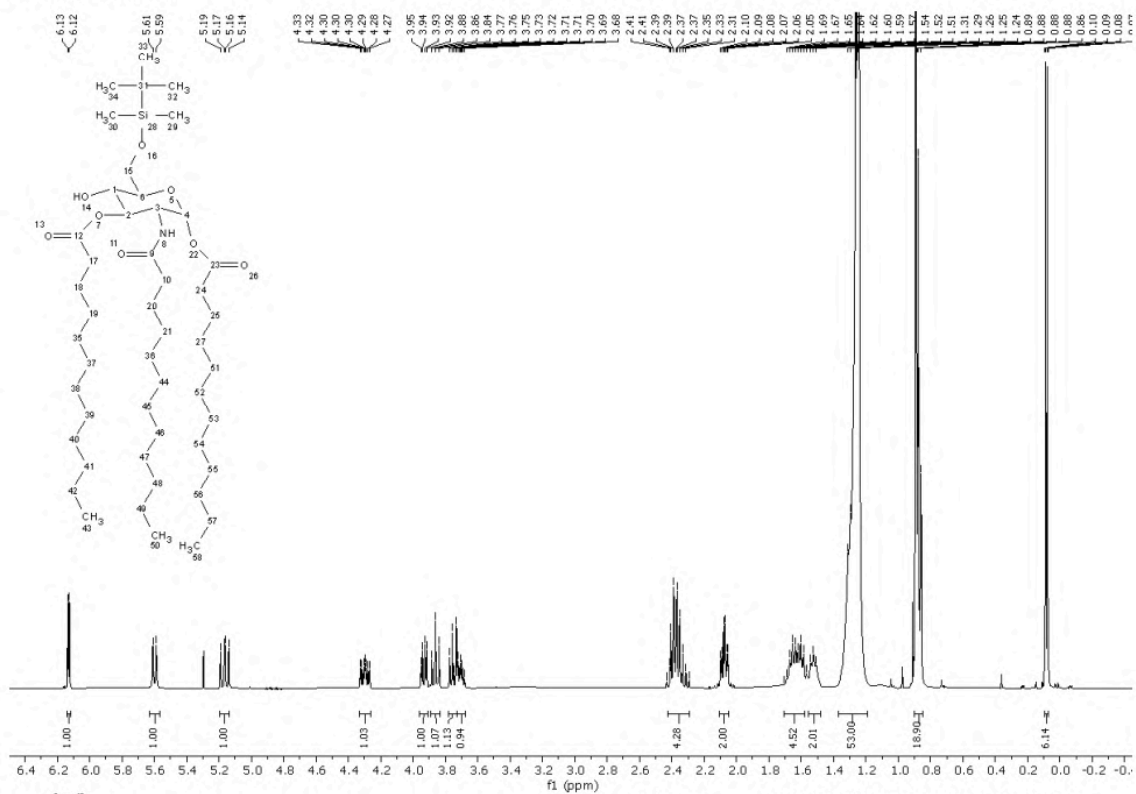
Compound 8
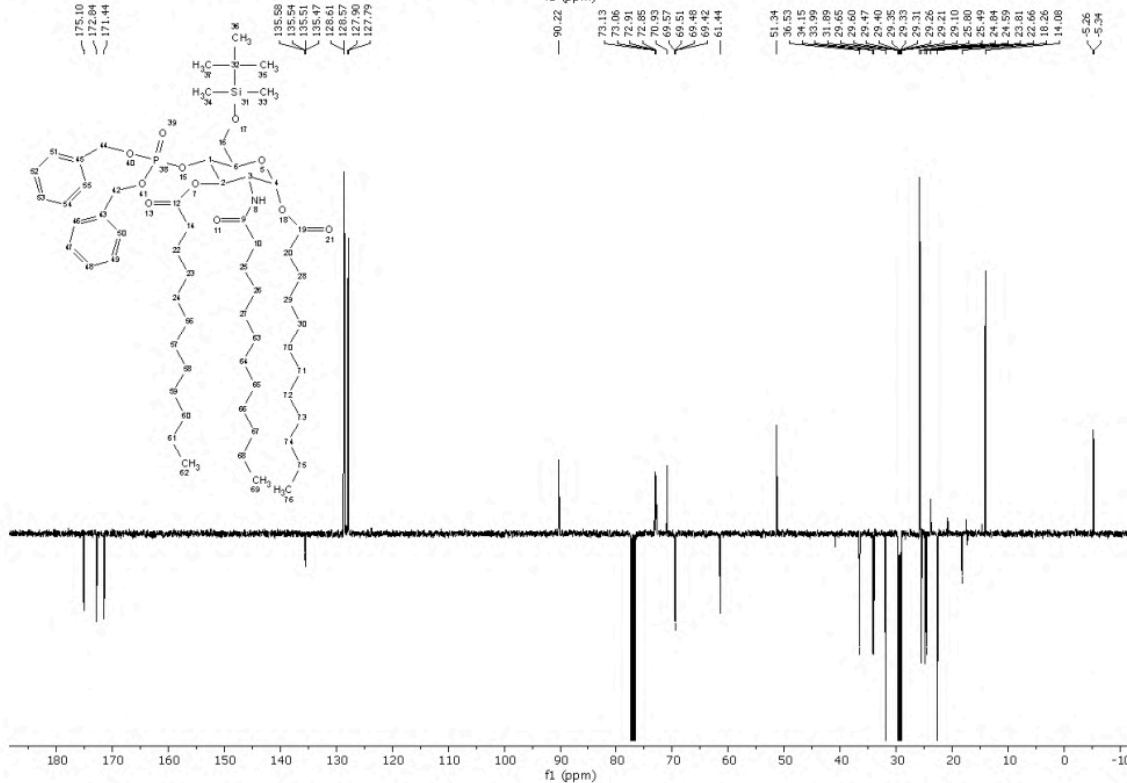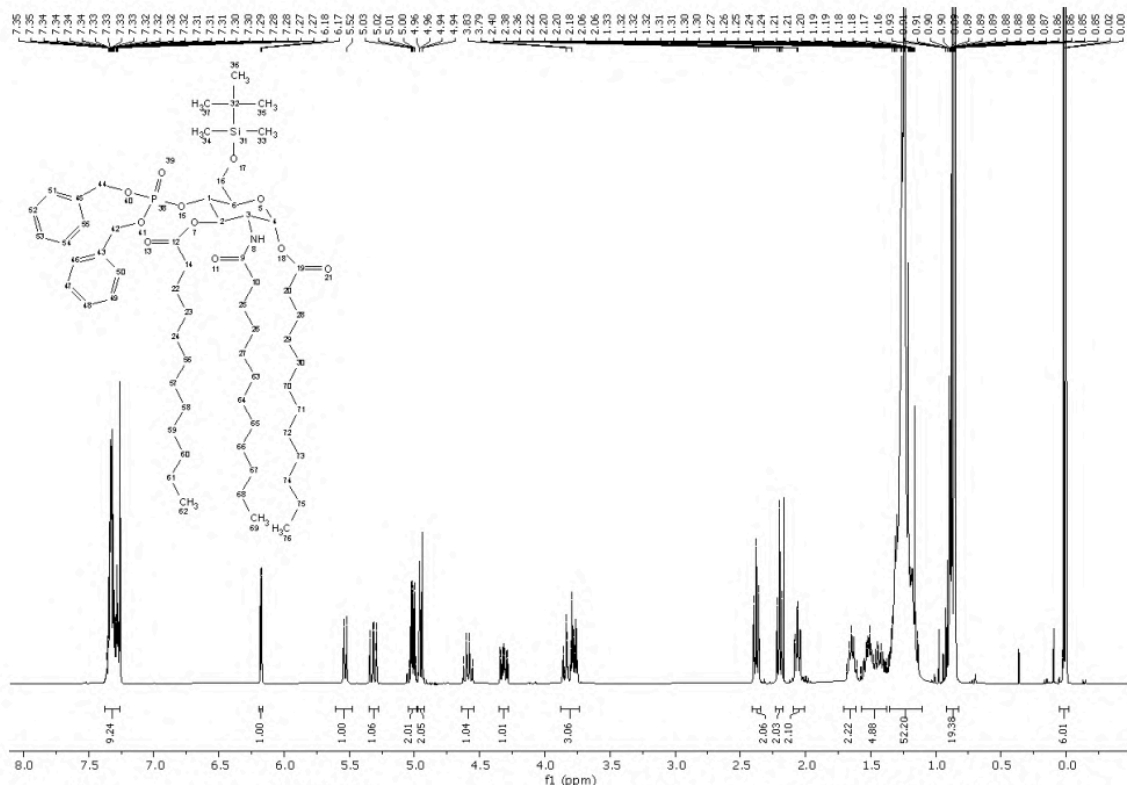
Compound 9
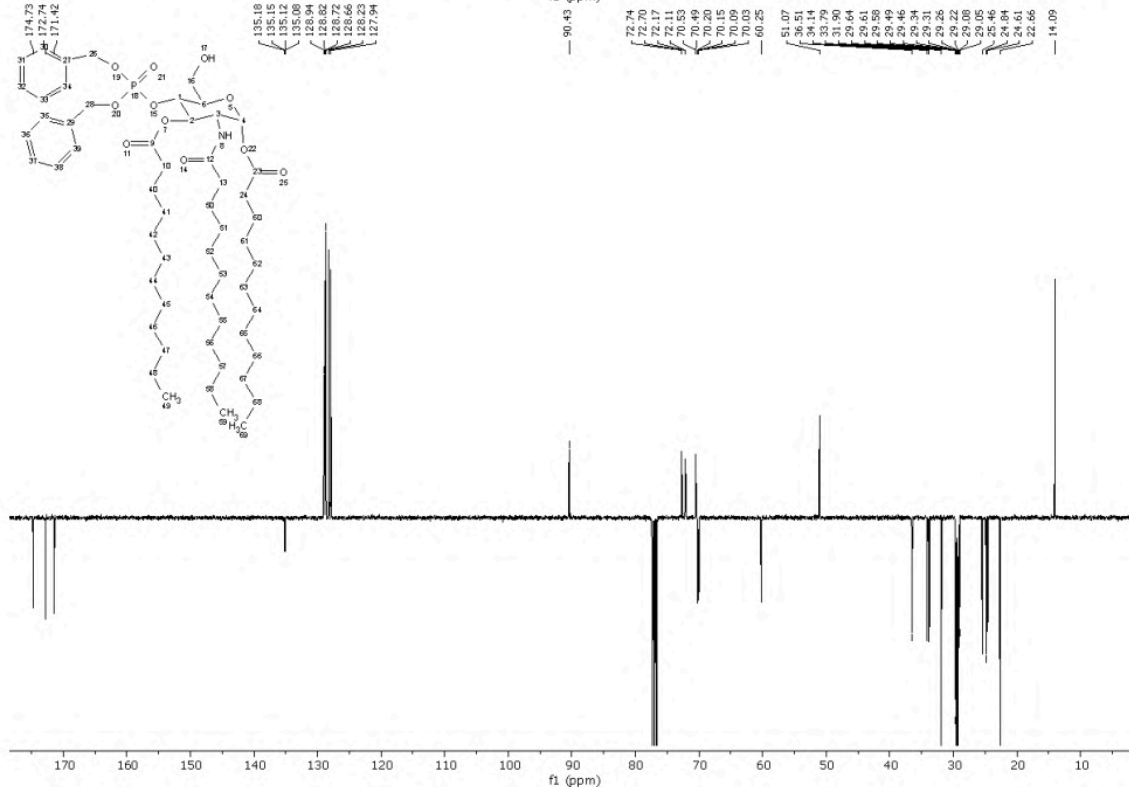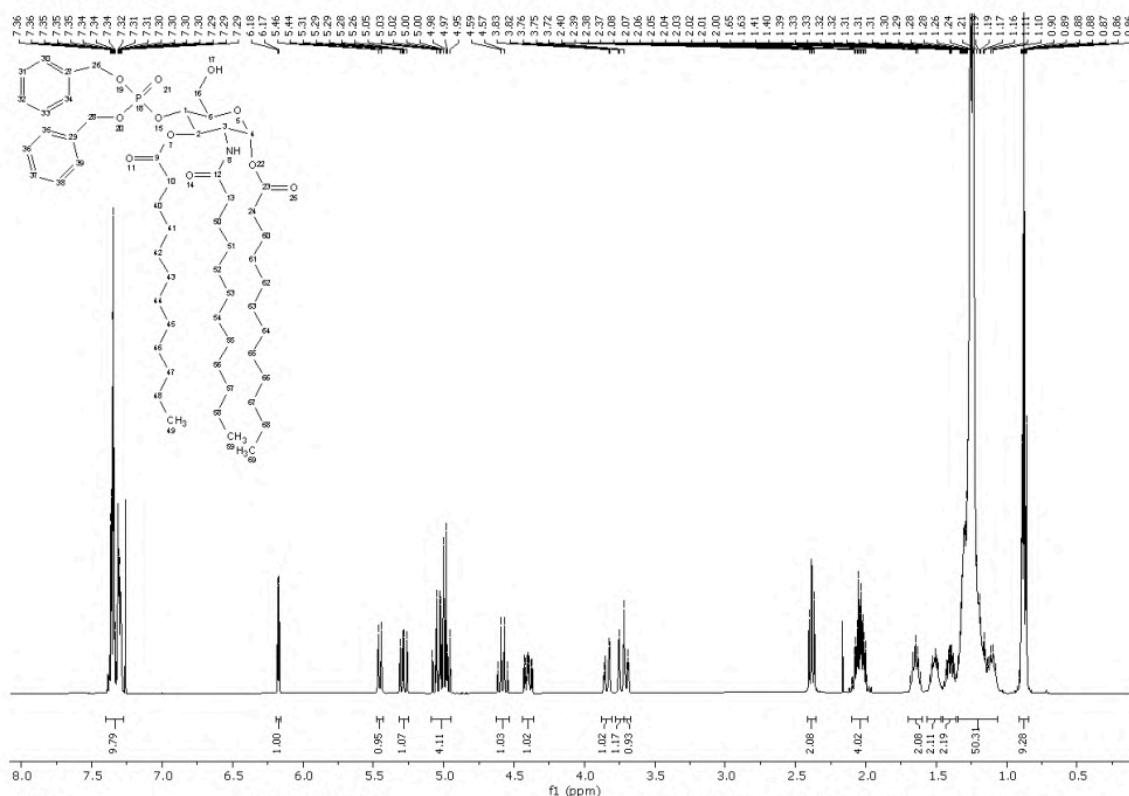
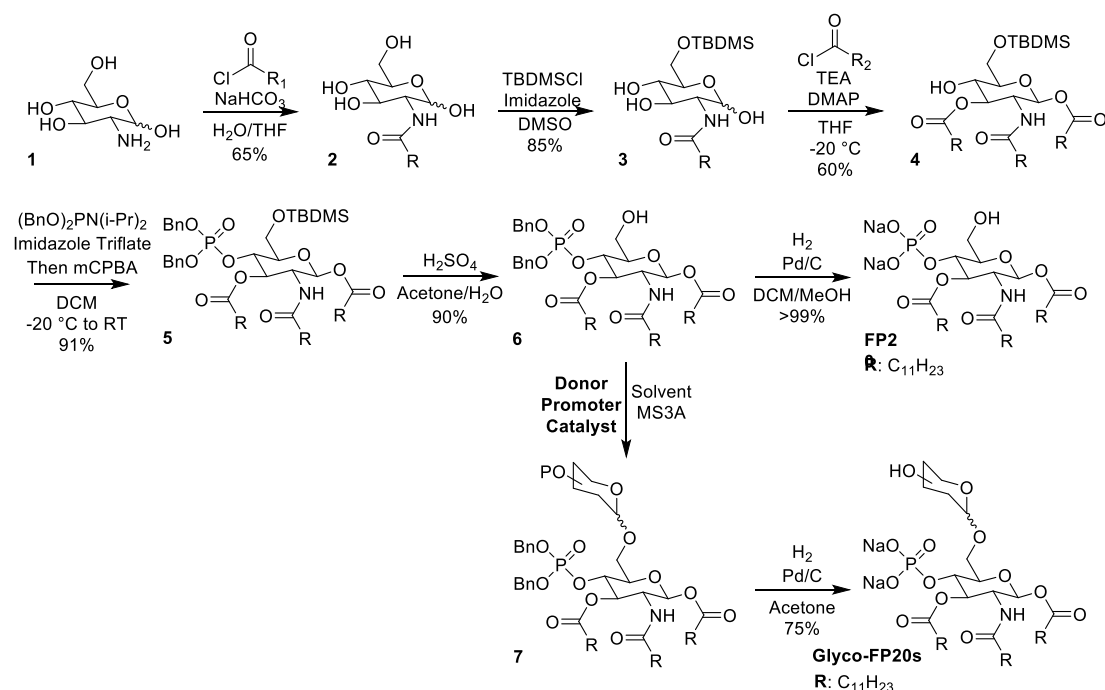## Compound 10

Appendix II

Supplementary information of CHAPTER II

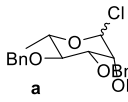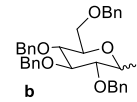# Additional Experimental section of results reported in Chapter II

Chemistry

General

All reagents and solvents were purchased from commercial sources and used without further purifications, unless stated otherwise. Reactions were monitored by thin-layer chromatography (TLC) performed over Silica gel 60 F254 plates (Merck). Flash chromatography purifications were performed on Silica gel 60 60−75 μm from a commercial source or using Biotage Isolera LS Systems. ^{1}H and ^{13}C NMR spectra were recorded with Bruker Advance 400 with TopSpin software, or with NMR Varian 400 with VnmrJ software. Chemical shifts are expressed in ppm with respect to Me$_4$Si; coupling constants are expressed in Hz. The multiplicity in the ^{13}C spectra was deducted by APT experiments. Exact masses were recorded with Agilent 6500 Series Q-TOF LC/MS system.

Scheme S1 Synthesis of FP20s and Glyco-FP20s compounds. To minimize the number of steps and maintain the high yield of the synthesis, we performed the glycosylation immediately before the final hydrogenation, using intermediate **6** as our substrate.

Donors		Entry	Donor (Eq)	Solvent (M)	Promoter (Eq)	Catalyst (Eq.)	Time (h)	Yield (%)
		1	a (1.2)	Tol (0.1)	Ag$_2$O (2)	TfOH (0.4)	24	60
		2	b (1.2)	Tol (0.1)	Ag$_2$O (2.5)	TfOH (0.4)	48	18
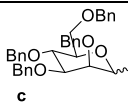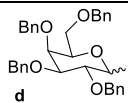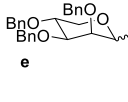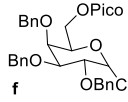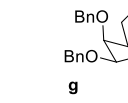
			Donor	Solvent	Silver salt	Acid		
		3	c (1.2)	Tol (0.1)	Ag$_2$O (2.5)	TfOH (0.4)	48	20
c / d		4	d (1.2)	Tol (0.1)	Ag$_2$O (2.5))	TfOH (0.4)	20	15
		5	e (1.2)	Tol (0.1)	Ag$_2$O (2.5)	TfOH (0.4)	18	25
		6	d (1.2)	Tol (0.05)	Ag$_2$SO$_4$ (2.5)	TfOH (0.5)	16	15
e / f		7	d (1.2)	Tol (0.05)	AgOTf (2.0)	N/A	24	21
		8	d (1.2)	Tol (0.05)	AgOTf (2.0)	N/A	7	29
		9	d (1.2)	DCM (0.05)	Ag$_2$SO$_4$ (2.5-> 5)	TfOH (0.5->2.0)	48	11
g		10	f (1.2)	DCM (0.05)	Ag$_2$SO$_4$ (2.5-> 5)	TfOH (0.5->2.0)	48	38
		11	g (1.2)	DCE (0.05)	Ag$_2$SO$_4$ (1.5); I$_2$ (1.5)	TfOH (0.2)	5	42
		12	G (1.2)	DCM (0.05)	Ag$_2$SO$_4$ (2.5)	TfOH (2.0)	20	25

Table S1 Screening of FP20 glycosylation using different glycosyl donors and silver salts.

General Method A: Silver Salts and Acid Catalyst
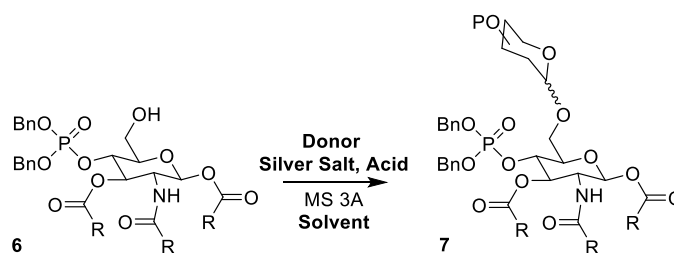
A suspension of compound **6** (0.10 mmol, 1.0 Eq.), glycosyl **donor** (0.12 mmol, 1.2 Eq.) and freshly activated 3 Å molecular sieves (300% m/m) in anhydrous **solvent** under inert atmosphere was stirred for 1 h at room temperature. Then, the mixture was cooled to 0 °C and the appropriated silver salt promoter (1.5-2.5 Eq.) and acid catalyst (0.50-2.5 Eq.) were added. Reaction was allowed to slowly return to room temperature and monitored *via* TLC (Tol/AcOEt 75:25 or Hex/Acetone 75:25).

Upon reaction completion, the mixture was filtered over Celite pad to remove the solids. Solution was diluted with ethyl acetate and washed three times with NaHCO$_3$. The organic layer was recovered, dried over Na$_2$SO$_4$ and excess solvent removed by rotavapor.

Crude product thus obtained was purified by flash chromatography (Tol/AcOEt 75:25 or EtPet/Acetone 75:25). Final compound was obtained as a pink syrup.
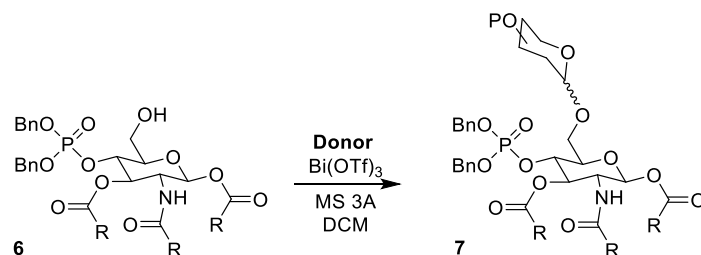
General Method B: Bismuth Triflate

A suspension of compound **6** (0.10 mmol, 1.0 Eq.), glycosyl **donor** (0.12 mmol, 1.2 Eq.) and flame activated 3 Å molecular sieves (300% m/m) in anhydrous DCM under inert atmosphere was stirred for 1 h at room temperature. Then, the mixture was cooled to 0 °C and Bi(OTf)$_3$ (0.35-0.90 Eq.) was added. Reaction was allowed to return to room temperature and monitored *via* TLC (Tol/AcOEt 6:4 or Hex/Acetone 7:3).

Upon reaction completion, the mixture was filtered over celite pad to remove heavy metals. Solution was diluted in ethyl acetate and washed three times with NaHCO$_3$. The organic layer was recovered, dried over Na$_2$SO$_4$ and excess solvent removed by rotavapor.

Crude product thus obtained was purified through flash chromatography (Tol/AcOEt 6:4 or EtPet/Acetone 7:3). Final compound was obtained as a pink oil.

O-(2,3,4-Tri-O-benzyl-6-O-picoloyl-D-glucopyranosyl)-(1→6)-2-deoxy-4-O-(dibenzyl)phospho-2-dodecamido-1,3-di-O-dodecanoyl-β-D-glucopyranose.

^{1}H NMR (400 MHz, CDCl$_3$) δ 8.76 (d, *J* = 4.8 Hz, 1H), 8.75 – 8.72 (m, 0H), 8.01 (t, *J* = 8.1 Hz, 1H), 7.83 (td, *J* = 7.8, 1.7 Hz, 1H), 7.77 (td, *J* = 7.8, 1.7 Hz, 1H), 7.49 – 7.41 (m, 2H), 7.40 – 7.15 (m, 39H), 5.63 (dd, *J* = 8.8, 5.9 Hz, 1H), 5.40 (d, *J* = 9.6 Hz, 1H), 5.35 (d, *J* = 9.5 Hz, 1H), 5.16 (ddd, *J* = 12.6, 9.2, 3.9 Hz, 2H), 5.01 – 4.90 (m, 7H), 4.86 (s, 2H), 4.85 (d, *J* = 3.5 Hz, 1H), 4.80 – 4.67 (m, 4H), 4.61 (tt, *J* = 10.3, 6.0 Hz, 4H), 4.55 – 4.41 (m, 4H), 4.35 – 4.16 (m, 3H), 4.09 – 3.97 (m, 2H), 3.81 (q, *J* = 8.1 Hz, 4H), 3.73 – 3.41 (m, 7H), 2.26 (t, *J* = 7.6 Hz, 2H), 2.18 (t, *J* = 7.8 Hz, 2H), 2.12 (d, *J* = 8.0 Hz, 2H), 2.03 (q, *J* = 8.6 Hz, 3H), 1.50 (q, *J* = 7.2 Hz, 5H), 1.45 – 1.37 (m, 3H), 1.22 (d, *J* = 16.0 Hz, 66H), 0.88 (dp, *J* = 6.9, 2.3 Hz, 12H).

^{13}C NMR (101 MHz, CDCl$_3$) δ 174.3, 174.1, 172.8, 172.8, 172.3, 172.1, 164.6, 149.9, 147.8, 138.7, 138.5, 138.4, 138.1, 138.0, 137.8, 137.3, 137.1, 135.4, 135.3, 128.8, 128.7, 128.7, 128.6, 128.6, 128.6, 128.5, 128.5, 128.4, 128.3, 128.1, 128.1, 128.0, 127.9, 127.9, 127.8, 127.7, 127.7, 127.6, 127.0, 125.5, 125.3, 104.1, 96.9, 92.6, 92.5, 84.5, 82.0, 81.9, 79.9, 77.4, 77.2, 77.0, 76.7, 75.8, 75.0, 75.0, 74.9, 74.7, 73.2, 72.9, 72.8, 69.8, 69.8, 68.9, 68.8, 65.5, 64.3, 52.9, 36.8, 36.8, 34.0, 34.0, 33.9, 33.9, 31.9, 29.7, 29.6, 29.5, 29.5, 29.4, 29.4, 29.3, 29.3, 29.2, 29.1, 29.0, 29.0, 25.6, 25.6, 24.6, 24.5, 24.4, 22.7, 14.1.

HRMS (ESI-Q-TOF): m/z [M+Na$^+$] calculated for C$_{89}$H$_{123}$NNaO$_{17}$P$^+$: 1545.8452. Found: 1545.8487.

O-(2,3,4-Tri-O-benzyl-6-O-picoloyl-D-galactopyranosyl)-(1→6)-2-deoxy-4-O-(dibenzyl)phospho-2-dodecamido-1,3-di-O-dodecanoyl-β-D-glucopyranose.

^{1}H NMR (400 MHz, CDCl$_3$) δ 8.73 (td, J = 10.7, 4.7 Hz, 2H), 8.05 (t, J = 8.5 Hz, 2H), 7.95 (d, J = 7.9 Hz, 1H), 7.92 – 7.85 (m, 1H), 7.78 (dd, J = 8.2, 6.5 Hz, 1H), 7.50 – 6.99 (m, 64H), 5.63 (d, J = 8.8 Hz, 1H), 5.53 (d, J = 8.8 Hz, 1H), 5.32 (dd, J = 17.9, 9.3 Hz, 2H), 5.11 (q, J = 9.7 Hz, 2H), 5.05 – 4.56 (m, 22H), 4.53 – 4.48 (m, 1H), 4.46 – 4.19 (m, 10H), 4.17 – 3.94 (m, 5H), 3.92 – 3.73 (m, 7H), 3.71 – 3.60 (m, 2H), 3.51 (dd, J = 9.8, 2.8 Hz, 1H), 2.47 – 1.95 (m, 13H), 1.55 – 1.34 (m, 13H), 1.24 (s, 102H), 0.88 (td, J = 5.7, 2.9 Hz, 19H).

^{13}C NMR (101 MHz, CDCl$_3$) δ 174.2, 172.7, 172.3, 164.6, 149.9, 147.9, 138.5, 138.3, 137.1, 128.7, 128.6, 128.4, 128.3, 128.3, 128.1, 128.0, 127.9, 127.7, 127.6, 127.5, 126.9, 125.4, 104.0, 97.3, 92.6, 81.9, 77.3, 77.0, 76.7, 76.3, 75.2, 74.6, 73.6, 73.2, 71.9, 68.8, 65.2, 65.0, 64.0, 52.8, 36.8, 34.0, 31.9, 29.7, 29.6, 29.5, 29.4, 29.4, 29.3, 29.1, 29.1, 25.6, 24.6, 24.6, 22.7, 14.1, -0.0.

HRMS (ESI-Q-TOF): m/z [M+Na$^+$] calculated for C$_{89}$H$_{123}$NNaO$_{17}$P$^+$: 1545.8452. Found: 1545.8468.

O-(2,3,4-Tri-O-benzyl-6-O-picoloyl-D-mannopyranosyl)-(1→6)-2-deoxy-4-O-(dibenzyl)phospho-2-dodecamido-1,3-di-O-dodecanoyl-β-D-glucopyranose.

^{1}H NMR (400 MHz, CDCl$_3$) δ 8.76 (dd, J = 11.5, 4.7 Hz, 2H), 7.99 (t, J = 8.1 Hz, 2H), 7.64 (td, J = 7.7, 1.8 Hz, 2H), 7.53 – 7.12 (m, 59H), 5.62 (dd, J = 8.8, 3.8 Hz, 2H), 5.55 (d, J = 9.6 Hz, 1H), 5.44 (d, J = 9.6 Hz, 1H), 5.19 (ddd, J = 10.9, 9.1, 4.9 Hz, 2H), 5.01 – 4.87 (m, 12H), 4.87 – 4.72 (m, 2H), 4.72 – 4.43 (m, 14H), 4.38 (q, J = 9.3 Hz, 1H), 4.27 (q, J = 10.1 Hz, 3H), 4.18 – 3.90 (m, 6H), 3.90 – 3.81 (m, 2H), 3.81 – 3.72 (m, 2H), 3.70 – 3.65 (m, 1H), 3.61 (dd, J = 11.6, 6.2 Hz, 1H), 3.51 (td, J = 8.6, 3.0 Hz, 2H), 2.30 (td, J = 7.1, 4.1 Hz, 4H), 2.27 – 2.11 (m, 5H), 2.11 – 2.03 (m, 4H), 1.62 – 1.37 (m, 13H), 1.26 (d, J = 9.5 Hz, 100H), 0.97 – 0.80 (m, 20H).

^{13}C NMR (101 MHz, CDCl$_3$) δ 174.4, 174.2, 172.9, 172.3, 164.5, 150.0, 147.9, 139.0, 138.4, 138.3, 138.2, 138.1, 137.1, 136.9, 128.8, 128.8, 128.7, 128.7, 128.7, 128.6, 128.4, 128.4, 128.4, 128.3, 128.2, 128.1, 128.0, 127.9, 127.8, 127.8, 127.7, 127.7, 127.6, 127.3, 126.7, 125.5, 125.3, 102.1, 98.2, 92.6, 82.2, 80.1, 77.3, 77.0, 76.7, 75.1, 74.7, 74.2, 74.0, 73.9, 73.6, 73.5, 72.7, 72.7,

72.2, 71.3, 70.3, 69.7, 69.7, 64.8, 64.4, 52.8, 36.8, 36.8, 34.0, 34.0, 33.9, 31.9, 29.7, 29.7, 29.6, 29.6, 29.5, 29.5, 29.5, 29.4, 29.4, 29.3, 29.2, 29.1, 29.0, 25.6, 24.6, 24.5, 24.5, 22.7, 14.1.

HRMS (ESI-Q-TOF): m/z [M+Na$^+$] calculated for C$_{89}$H$_{123}$NNaO$_{17}$P$^+$: 1545.8452. Found: 1545.8536.

General Method C: NIS and HOFox
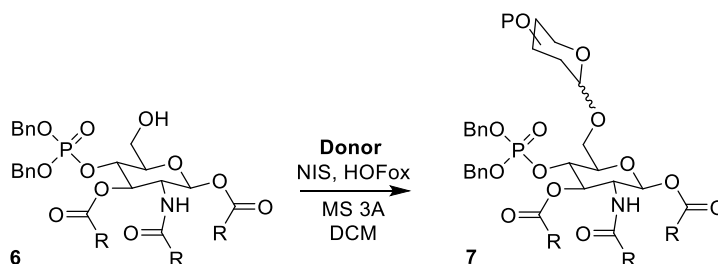
A suspension of compound **7** (0.10 mmol, 1.0 Eq.), glycosyl **donor** (0.20 mmol, 2.0 Eq.) and flame activated 3 Å molecular sieves (300% m/m) in anhydrous **solvent** under inert atmosphere was stirred for 1 h at room temperature. Then, N-hydroxysuccinimide (2.0 Eq.) and HOFox (0.5 Eq.) were added. Reaction was allowed to return to room temperature and monitored *via* TLC (Tol/AcOEt 75:25 or EtPet/Acetone 75:25).

Upon reaction completion, the mixture was filtered over celite pad to remove heavy metals. Solution was diluted in ethyl acetate and washed three times with NaHCO$_3$. The organic layer was recovered, dried over Na$_2$SO$_4$ and excess solvent removed by rotavapor.

Crude product thus obtained was purified through flash chromatography (Tol/AcOEt 75:25 or EtPet/Acetone 75:25). Final compound was obtained as a pink oil.

O-(2,3,4-Tri-O-benzyl-L-rhamnopyranosyl)-(1→6)-4-O-(dibenzyl)phospho-2-deoxy-2-dodecamido-1,3-di-O-dodecanoyl-β-D-glucopyranose.

^{1}H NMR (400 MHz, CDCl$_3$) δ 7.50 – 7.20 (m, 38H), 5.65 (d, *J* = 8.8 Hz, 0H), 5.61 (s, 1H), 5.48 (d, *J* = 9.3 Hz, 0H), 5.40 (s, 1H), 5.21 (dd, *J* = 10.9, 9.1 Hz, 0H), 5.14 (s, 1H), 4.91 (d, *J* = 11.6 Hz, 9H), 4.69 (s, 2H), 4.62 (d, *J* = 2.2 Hz, 4H), 4.57 – 4.34 (m, 2H), 4.23 (s, 1H), 3.99 – 3.79 (m, 4H), 3.75 – 3.49 (m, 6H), 2.37 – 2.28 (m, 3H), 2.16 – 2.11 (m, 2H), 2.05 (s, 3H), 1.57 (s, 6H), 1.47 – 1.35 (m, 4H), 1.29 (s, 77H), 0.88 (td, *J* = 6.9, 1.2 Hz, 13H).

^{13}C NMR (101 MHz, CDCl$_3$) δ 174.2, 172.8, 172.4, 138.7, 138.6, 135.3, 135.2, 128.7, 128.7, 128.7, 128.6, 128.5, 128.4, 128.3, 128.3, 128.2, 128.1, 128.1, 128.0, 127.9, 127.9, 127.7, 127.6, 127.6, 127.6, 127.5, 127.4, 127.4, 98.6, 92.5, 82.1, 80.4, 79.7, 77.3, 77.0, 76.7, 75.4, 75.0, 72.8,

72.8, 72.5, 71.9, 69.7, 69.7, 69.6, 69.6, 68.1, 65.0, 52.7, 36.8, 34.0, 33.9, 31.9, 30.9, 29.7, 29.6, 29.6, 29.5, 29.5, 29.4, 29.3, 29.3, 29.3, 29.2, 29.1, 29.0, 25.6, 24.6, 24.5, 22.7, 18.0, 17.9, 14.1.

HRMS (ESI-Q-TOF): m/z [M+Na$^+$] calculated for $C_{83}H_{120}NnaO_{15}P^+$: 1424.8288. Found: 1424.8342.

***O*-(2,3,4,6-Tetra-*O*-benzyl-D-glucopyranosyl)-(1→6)-4-*O*-(dibenzyl)phospho-2-deoxy-2-dodecamido-1,3-di-*O*-dodecanoyl-β-D-glucopyranose**.

^{1}H NMR (400 MHz, CDCl$_3$) δ 7.40 – 7.20 (m, 32H), 7.11 (ddd, J = 13.3, 6.8, 2.7 Hz, 2H), 5.62 (dd, J = 8.8, 3.8 Hz, 1H), 5.34 (d, J = 9.5 Hz, 1H), 5.27 (d, J = 9.6 Hz, 0H), 5.13 (td, J = 10.9, 8.9 Hz, 1H), 5.00 – 4.85 (m, 6H), 4.79 (dd, J = 10.9, 2.5 Hz, 1H), 4.73 (d, J = 11.0 Hz, 1H), 4.70 – 4.64 (m, 2H), 4.63 – 4.54 (m, 2H), 4.53 – 4.45 (m, 1H), 4.44 – 4.21 (m, 4H), 3.93 (t, J = 9.3 Hz, 1H), 3.87 – 3.75 (m, 3H), 3.70 – 3.51 (m, 5H), 3.46 – 3.33 (m, 1H), 2.22 (t, J = 7.6 Hz, 1H), 2.13 (dt, J = 17.2, 7.7 Hz, 3H), 2.03 (q, J = 7.3 Hz, 3H), 1.50 (s, 3H), 1.40 (p, J = 7.1 Hz, 3H), 1.22 (d, J = 16.1 Hz, 52H), 0.88 (t, J = 6.7 Hz, 10H).

^{13}C NMR (101 MHz, CDCl$_3$) δ 172.7, 172.2, 139.0, 138.2, 138.0, 128.7, 128.7, 128.6, 128.5, 128.3, 128.3, 128.2, 128.1, 128.0, 127.9, 127.9, 127.8, 127.8, 127.7, 127.7, 127.6, 127.5, 127.4, 103.9, 97.3, 92.7, 84.5, 81.9, 79.8, 77.6, 77.5, 77.3, 77.0, 76.7, 75.6, 74.9, 74.6, 73.4, 73.3, 73.3, 72.8, 72.7, 70.2, 69.7, 68.4, 52.9, 36.8, 34.0, 33.9, 31.9, 29.7, 29.6, 29.5, 29.5, 29.4, 29.4, 29.3, 29.1, 29.0, 25.6, 24.6, 24.5, 24.4, 22.7, 14.1.

HRMS (ESI-Q-TOF): m/z [M+Na$^+$] calculated for $C_{90}H_{126}NnaO_{16}P^+$: 1530.8706. Found: 1530.8759.

***O*-(2,3,4,6-Tetra-*O*-benzyl-D-mannopyranosyl)-(1→6)-4-*O*-(dibenzyl)phospho-2-deoxy-2-dodecamido-1,3-di-*O*-dodecanoyl-β-D-glucopyranose.**

^{1}H NMR (400 MHz, CDCl$_3$) δ 7.43 – 7.08 (m, 35H), 5.60 (d, J = 8.8 Hz, 1H), 5.46 – 5.38 (m, 1H), 5.15 (ddd, J = 10.5, 9.0, 1.0 Hz, 1H), 5.00 – 4.82 (m, 7H), 4.71 (s, 2H), 4.63 (d, J = 12.1 Hz, 1H), 4.59 – 4.43 (m, 6H), 4.26 (dt, J = 10.9, 9.2 Hz, 1H), 4.02 (t, J = 9.5 Hz, 1H), 3.93 – 3.70 (m, 7H), 3.70 – 3.60 (m, 2H), 2.31 – 2.23 (m, 2H), 2.18 (t, J = 7.7 Hz, 2H), 2.06 (dd, J = 8.7, 6.8 Hz, 2H), 1.53 (ddt, J = 12.0, 6.6, 3.1 Hz, 5H), 1.41 (h, J = 7.5 Hz, 3H), 1.35 – 1.09 (m, 59H), 0.92 – 0.81 (m, 12H).

^{13}C NMR (101 MHz, CDCl$_3$) δ 174.4, 172.8, 172.3, 138.7, 138.6, 138.5, 138.3, 135.5, 135.4, 135.4, 135.4, 128.6, 128.6, 128.3, 128.3, 128.2, 128.2, 128.2, 127.9, 127.9, 127.9, 127.8, 127.8, 127.8, 127.7, 127.7, 127.6, 127.6, 127.4, 127.4, 127.4, 98.4, 92.6, 80.1, 77.3, 77.0, 76.7, 75.1, 74.7, 74.7, 74.4, 73.3, 73.2, 73.1, 72.7, 72.5, 72.1, 72.0, 69.6, 69.6, 69.6, 69.6, 69.1, 64.7, 52.8, 36.8, 34.0, 33.9, 33.5, 31.9, 29.7, 29.6, 29.6, 29.5, 29.5, 29.5, 29.4, 29.3, 29.3, 29.2, 29.1, 29.0, 25.6, 24.8, 24.6, 24.5, 22.7, 14.1.

HRMS (ESI-Q-TOF): m/z [M+Na$^+$] calculated for C$_{90}$H$_{126}$NnaO$_{16}$P$^+$: 1530.8706. Found: 1530.8765.

O-(2,3,4,6-Tetra-O-benzyl-D-galactopyranosyl)-(1→6)-4-O-(dibenzyl)phospho-2-deoxy-2-dodecamido-1,3-di-O-dodecanoyl-β-D-glucopyranose.

^{1}H NMR (400 MHz, CDCl$_3$) δ 7.40 – 7.27 (m, 25H), 5.56 (d, *J* = 8.8 Hz, 1H), 5.32 (d, *J* = 9.5 Hz, 1H), 5.12 (dd, *J* = 10.9, 8.9 Hz, 1H), 5.00 – 4.90 (m, 4H), 4.90 (s, 1H), 4.80 – 4.61 (m, 5H), 4.56 – 4.47 (m, 1H), 4.46 – 4.34 (m, 2H), 4.25 (dt, *J* = 10.9, 9.1 Hz, 1H), 4.06 – 3.99 (m, 2H), 3.98 – 3.91 (m, 1H), 3.92 – 3.84 (m, 1H), 3.80 (d, *J* = 7.3 Hz, 2H), 3.49 (d, *J* = 6.6 Hz, 2H), 2.26 – 2.20 (m, 2H), 2.17 – 2.13 (m, 2H), 2.05 (t, *J* = 7.7 Hz, 3H), 1.68 – 1.57 (m, 7H), 1.55 – 1.47 (m, 3H), 1.32 – 1.15 (m, 77H), 0.92 – 0.84 (m, 13H).

^{13}C NMR (101 MHz, CDCl$_3$) δ 174.3, 172.7, 172.3, 139.0, 138.8, 138.6, 138.2, 135.5, 129.9, 128.6, 128.6, 128.3, 128.3, 128.3, 128.2, 128.1, 128.1, 128.0, 128.0, 127.8, 127.7, 127.6, 127.5, 127.4, 127.4, 127.3, 126.0, 97.7, 92.6, 78.9, 77.3, 77.0, 76.7, 76.4, 75.2, 74.9, 74.7, 73.5, 73.3, 73.2, 73.0, 72.8, 69.8, 69.7, 69.7, 69.6, 69.2, 68.9, 65.4, 52.8, 36.8, 34.0, 33.9, 31.9, 29.7, 29.6, 29.6, 29.5, 29.5, 29.4, 29.3, 29.3, 29.3, 29.1, 29.0, 25.6, 24.6, 24.5, 22.7, 21.3, 14.1.

HRMS (ESI-Q-TOF): m/z [M+Na$^+$] calculated for C$_{90}$H$_{126}$NnaO$_{16}$P$^+$: 1530.8706. Found: 1530.8763.

O-(2,3,4-Tri-O-benzyl-D-lyxopyranosyl)-(1→6)-4-O-(dibenzyl)phospho-2-deoxy-2-dodecamido-1,3-di-O-dodecanoyl-β-D-glucopyranose.

^{1}H NMR (400 MHz, CDCl$_3$) δ 7.42 – 7.10 (m, 35H), 5.60 (d, *J* = 8.8 Hz, 1H), 5.46 – 5.39 (m, 1H), 5.20 – 5.10 (m, 1H), 5.00 – 4.82 (m, 6H), 4.71 (s, 2H), 4.63 (d, *J* = 12.1 Hz, 1H), 4.59 – 4.42 (m, 6H), 4.26 (dt, *J* = 10.9, 9.2 Hz, 1H), 4.02 (t, *J* = 9.5 Hz, 1H), 3.91 – 3.72 (m, 7H), 3.69 – 3.60

(m, 2H), 2.31 – 2.24 (m, 2H), 2.18 (t, J = 7.7 Hz, 2H), 2.06 (dd, J = 8.7, 6.8 Hz, 2H), 1.53 (ddq, J = 11.7, 6.2, 3.5 Hz, 5H), 1.41 (h, J = 7.4 Hz, 3H), 1.36 – 1.07 (m, 60H), 0.94 – 0.80 (m, 12H).

^{13}C NMR (101 MHz, CDCl$_3$) δ 174.4, 172.8, 172.3, 138.7, 138.6, 138.5, 138.3, 135.5, 135.4, 135.4, 135.4, 128.6, 128.6, 128.3, 128.3, 128.2, 128.2, 128.2, 127.9, 127.9, 127.9, 127.8, 127.8, 127.8, 127.7, 127.7, 127.6, 127.6, 127.4, 127.4, 127.4, 98.4, 92.6, 80.1, 77.3, 77.0, 76.7, 75.1, 74.7, 74.7, 74.4, 73.3, 73.2, 73.1, 72.7, 72.5, 72.1, 72.0, 69.6, 69.6, 69.6, 69.6, 69.1, 64.7, 52.8, 36.8, 34.0, 33.9, 31.9, 29.7, 29.6, 29.6, 29.5, 29.5, 29.5, 29.4, 29.3, 29.3, 29.2, 29.1, 29.0, 25.6, 24.6, 24.5, 22.7, 14.1.

HRMS (ESI-Q-TOF): m/z [M+Na$^+$] calculated for C$_{82}$H$_{118}$NNaO$_{15}$P$^+$: 1410.8131. Found: 1410.8142.

General Method D: Catalytic Hydrogenation
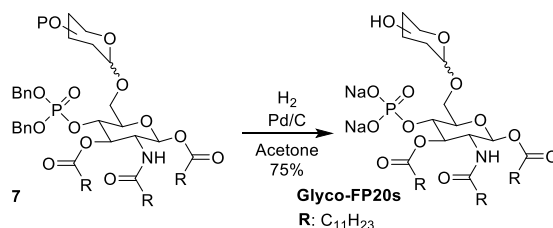
Compound **7** (0.05 mmol, 1 eq.) was dissolved in anhydrous, degassed acetone (5 mL, 0.01 M) and put under inert atmosphere. Pd/C catalyst (50% m/m) was then added to the solution. Gases were then removed in reaction environment, which was subsequently put under H$_2$ atmosphere. The solution was allowed to stir 4.5 h, then H$_2$ was removed, and reaction monitored by TLC (EtPet/Acetone 7:3).

Triethylamine (100 µL, 2% v/v) was then added to the reaction, which was stirred for 15 min. Solution was subsequently filtered on syringe filters PALL 4549T Acrodisc 25 mm with GF/0.45 µm Nylon to remove Pd/C catalyst and solvents were removed by rotavapor. Crude product was resuspended in a DCM/MeOH solution and IRA 120 H$^+$ was added. After 30 min stirring, IRA 120 H$^+$ was filtered, solvents were removed by rotavapor, the crude resuspended in DCM/MeOH and IRA 120 Na$^+$ was added. After 30 min stirring, IRA 120 Na$^+$ was filtered and solvents were removed by rotavapor.

Raw product was purified through reverse chromatography employing a C18 functionalized column (PUREZZA-Sphera Plus Standard Flash Cartridge C18 – 25-35 µm – 100A – Size 12 g) in the Biotage® Isolera LS System (gradient: H$_2$O/THF 90:10 to 15:85 over 10 CV with 1% of an aqueous solution of Et$_3$NHCO$_3$ at pH 7). The compound thus obtained was treated again with IRA 120 H$^+$ and IRA 120 Na$^+$ as before, obtaining the final **Glyco-FP20** as a white powder in a 75% yield.

O-(*L-Rhamnopyranosyl*)-(1→6)-2-deoxy-2-dodecamido-1,3-di-O-dodecanoyl-4-O-phospho-β-D-glucopyranose.

^{1}H NMR (400 MHz, MeOD) δ 5.76 (dd, *J* = 8.8, 5.1 Hz, 1H), 5.27 (dd, *J* = 10.5, 8.9 Hz, 1H), 4.58 (d, *J* = 0.9 Hz, 0H), 4.38 (dq, *J* = 26.0, 9.5 Hz, 1H), 4.16 – 4.01 (m, 2H), 4.00 – 3.94 (m, 1H), 3.91 (dd, *J* = 3.5, 1.7 Hz, 1H), 3.83 – 3.61 (m, 4H), 3.43 – 3.34 (m, 1H), 2.50 – 2.23 (m, 5H), 2.12 (dd, *J* = 8.4, 6.8 Hz, 2H), 1.58 (dt, *J* = 14.0, 8.0 Hz, 7H), 1.31 (s, 62H), 0.98 – 0.85 (m, 11H).

^{13}C NMR (101 MHz, MeOD) δ 174.7, 173.4, 172.0, 101.0, 92.1, 75.1, 73.0, 72.7, 71.7, 70.9, 70.6, 68.5, 65.7, 52.7, 48.2, 48.0, 47.9, 47.8, 47.6, 47.4, 47.2, 47.0, 36.1, 33.7, 33.6, 31.7, 31.7, 29.5, 29.4, 29.4, 29.4, 29.3, 29.3, 29.2, 29.2, 29.1, 29.1, 29.0, 28.8, 28.5, 25.6, 24.7, 24.4, 22.3, 22.3, 16.6, 13.0.

HRMS (ESI-Q-TOF): m/z [M$^-$] calculated for $C_{48}H_{89}NO_{15}P^-$: 950.5975. Found: 950.5961.

O-(*D-Glucopyranosyl*)-(1→6)-2-deoxy-2-dodecamido-1,3-di-O-dodecanoyl-4-O-phospho-β-D-glucopyranose.

^{1}H NMR (400 MHz, MeOD) δ 5.77 (dd, J = 8.9, 1.1 Hz, 1H), 5.31 (dd, J = 10.6, 9.1 Hz, 1H), 4.91 (d, J = 3.8 Hz, 1H), 4.51 (q, J = 9.5 Hz, 1H), 4.46 – 4.36 (m, 1H), 4.25 (d, J = 10.3 Hz, 0H), 4.08 (ddd, J = 12.7, 10.6, 8.8 Hz, 1H), 3.96 (dd, J = 11.6, 4.9 Hz, 1H), 3.92 – 3.79 (m, 3H), 3.75 – 3.64 (m, 2H), 3.41 – 3.36 (m, 1H), 3.28 (tt, J = 9.0, 3.1 Hz, 2H), 2.48 – 2.29 (m, 4H), 2.12 (t, J = 7.6 Hz, 2H), 1.66 – 1.49 (m, 6H), 1.31 (s, 44H), 0.97 – 0.85 (m, 8H).

^{13}C NMR (101 MHz, MeOD) δ 174.7, 173.4, 172.0, 98.8, 92.1, 76.6, 74.9, 73.5, 73.2, 72.8, 72.5, 72.2, 70.5, 65.4, 61.3, 52.8, 48.2, 48.0, 47.8, 47.6, 47.4, 47.2, 47.0, 36.1, 33.6, 33.4, 31.7, 29.4, 29.3, 29.2, 29.1, 29.0, 28.8, 28.8, 25.6, 24.7, 24.6, 24.4, 22.4, 13.1.

HRMS (ESI-Q-TOF): m/z [M$^-$] calculated for $C_{48}H_{89}NO_{16}P^-$: 966.5924. Found: 966.5935.

***α*-O-(*D-Galactopyranosyl*)-(1→6)-2-deoxy-2-dodecamido-1,3-di-O-dodecanoyl-4-O-phospho-β-D-glucopyranose**.

^{1}H NMR (400 MHz, MeOD) δ 5.77 (d, J = 8.9 Hz, 1H), 5.31 (dd, J = 10.6, 9.0 Hz, 1H), 4.91 (d, J = 3.9 Hz, 2H), 4.45 (q, J = 9.4 Hz, 1H), 4.10 (dd, J = 10.6, 8.9 Hz, 1H), 4.02 – 3.94 (m, 2H),

3.92 – 3.80 (m, 4H), 3.79 – 3.65 (m, 3H), 2.47 – 2.28 (m, 4H), 2.12 (t, J = 7.6 Hz, 2H), 1.65 – 1.51 (m, 6H), 1.31 (s, 53H), 0.97 – 0.89 (m, 10H).

^{13}C NMR (101 MHz, MeOD) δ 176.3, 174.9, 174.8, 174.0, 99.0, 91.3, 79.8, 74.3, 73.4, 71.5, 70.8, 70.0, 69.7, 69.2, 65.6, 61.6, 52.2, 48.3, 48.0, 47.8, 47.6, 47.4, 47.2, 47.0, 36.1, 35.7, 33.8, 33.6, 33.4, 31.7, 31.7, 31.7, 29.5, 29.4, 29.4, 29.4, 29.4, 29.3, 29.3, 29.3, 29.2, 29.2, 29.1, 29.1, 29.1, 29.0, 29.0, 29.0, 28.9, 28.8, 25.7, 25.6, 24.7, 24.6, 24.4, 22.4, 22.3, 13.1, 13.1.

HRMS (ESI-Q-TOF): m/z [M$^-$] calculated for C$_{48}$H$_{89}$NO$_{16}$P$^-$: 966.5924. Found: 966.5942.

α-O-(*D-Mannopyranosyl*)-(*1→6*)-2-deoxy-2-dodecamido-1,3-di-O-dodecanoyl-4-O-phospho-*β*-D-glucopyranose.

^{1}H NMR (400 MHz, MeOD) δ 5.72 (d, J = 8.8 Hz, 1H), 5.28 – 5.19 (m, 1H), 4.79 (s, 1H), 4.30 (d, J = 9.3 Hz, 1H), 4.06 – 3.44 (m, 16H), 2.34 (ddt, J = 28.9, 21.7, 7.8 Hz, 6H), 2.09 (t, J = 7.6 Hz, 3H), 1.54 (d, J = 18.7 Hz, 11H), 1.29 (s, 94H), 0.99 – 0.78 (m, 18H).

^{13}C NMR (101 MHz, MeOD) δ 172.1, 100.1, 92.2, 75.2, 73.3, 72.9, 71.1, 70.7, 67.6, 65.6, 61.5, 52.8, 48.2, 48.0, 47.8, 47.6, 47.4, 47.2, 47.0, 36.1, 33.7, 33.6, 33.6, 31.7, 29.5, 29.3, 29.3, 29.2, 29.1, 29.0, 28.8, 25.6, 24.7, 24.5, 24.4, 22.3, 13.0.

HRMS (ESI-Q-TOF): m/z [M$^-$] calculated for C$_{48}$H$_{89}$NO$_{16}$P$^-$: 966.5924. Found: 966.5912.

### *α*-O-(*D-Lyxopyranosyl*)-(*1→6*)-2-deoxy-2-dodecamido-1,3-di-O-dodecanoyl-4-O-phospho-*β*-D-glucopyranose.

^{1}H NMR (400 MHz, MeOD) δ 5.73 (d, J = 8.7 Hz, 1H), 5.22 (dd, J = 10.6, 8.9 Hz, 1H), 4.27 – 4.19 (m, 1H), 4.08 (dd, J = 10.6, 8.8 Hz, 1H), 4.00 (dd, J = 11.4, 2.2 Hz, 1H), 3.91 (dd, J = 11.4, 6.5 Hz, 1H), 3.82 (t, J = 2.9 Hz, 1H), 3.79 – 3.72 (m, 3H), 3.64 – 3.58 (m, 2H), 2.51 – 2.30 (m, 5H), 2.15 – 2.07 (m, 2H), 1.66 – 1.51 (m, 8H), 1.31 (s, 63H), 0.94 – 0.90 (m, 10H).

^{13}C NMR (101 MHz, MeOD) δ 174.7, 173.4, 172.0, 100.7, 92.1, 73.1, 71.1, 70.1, 67.3, 65.9, 62.9, 61.6, 48.2, 48.0, 47.8, 47.6, 47.4, 47.2, 47.0, 36.1, 33.7, 33.6, 32.3, 31.7, 29.4, 29.1, 28.8, 26.7, 25.6, 24.4, 22.3, 13.0.
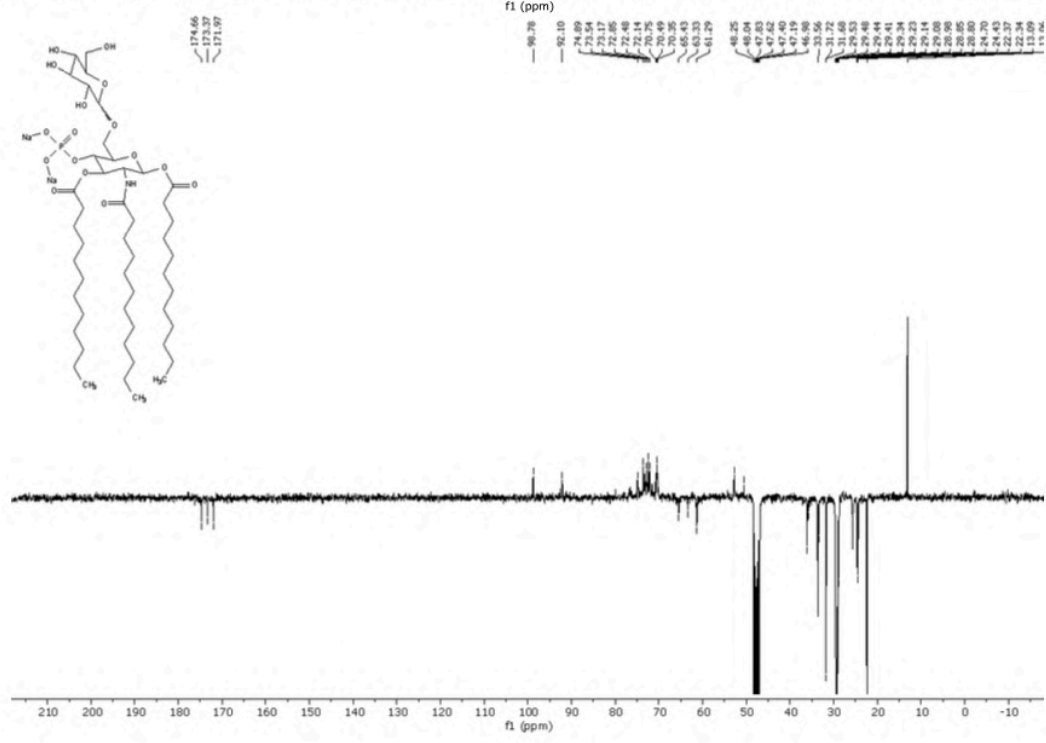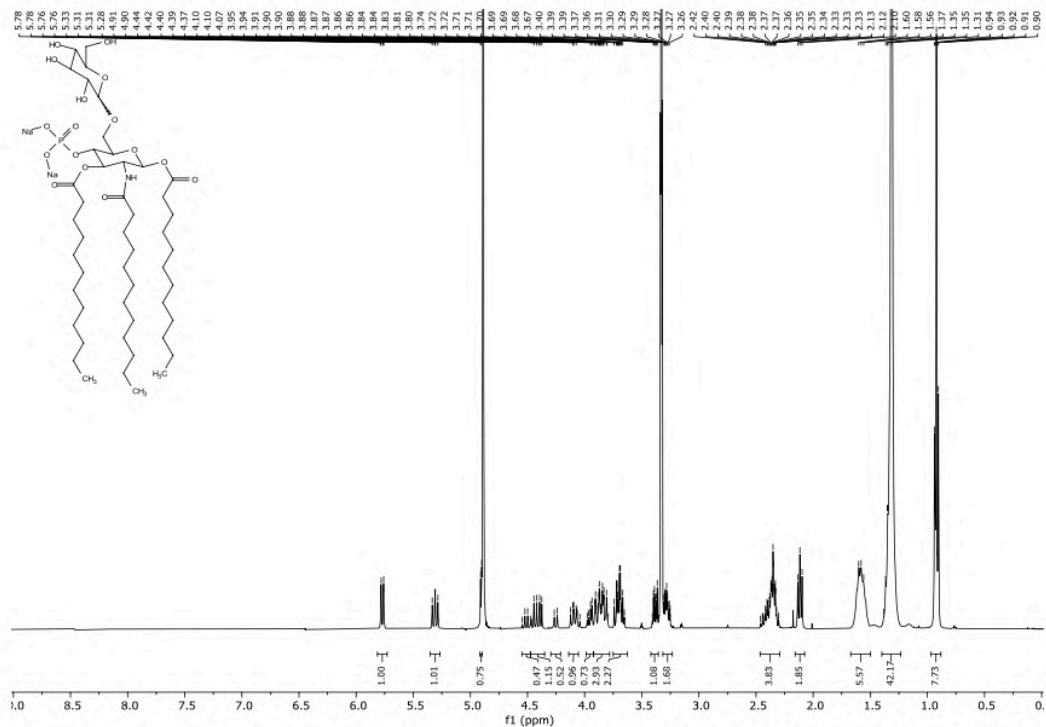
HRMS (ESI-Q-TOF): m/z [M$^-$] calculated for C$_{47}$H$_{87}$NO$_{15}$P$^-$: 936.5819. Found: 936.5832.

NMR Spectra of Final Compounds
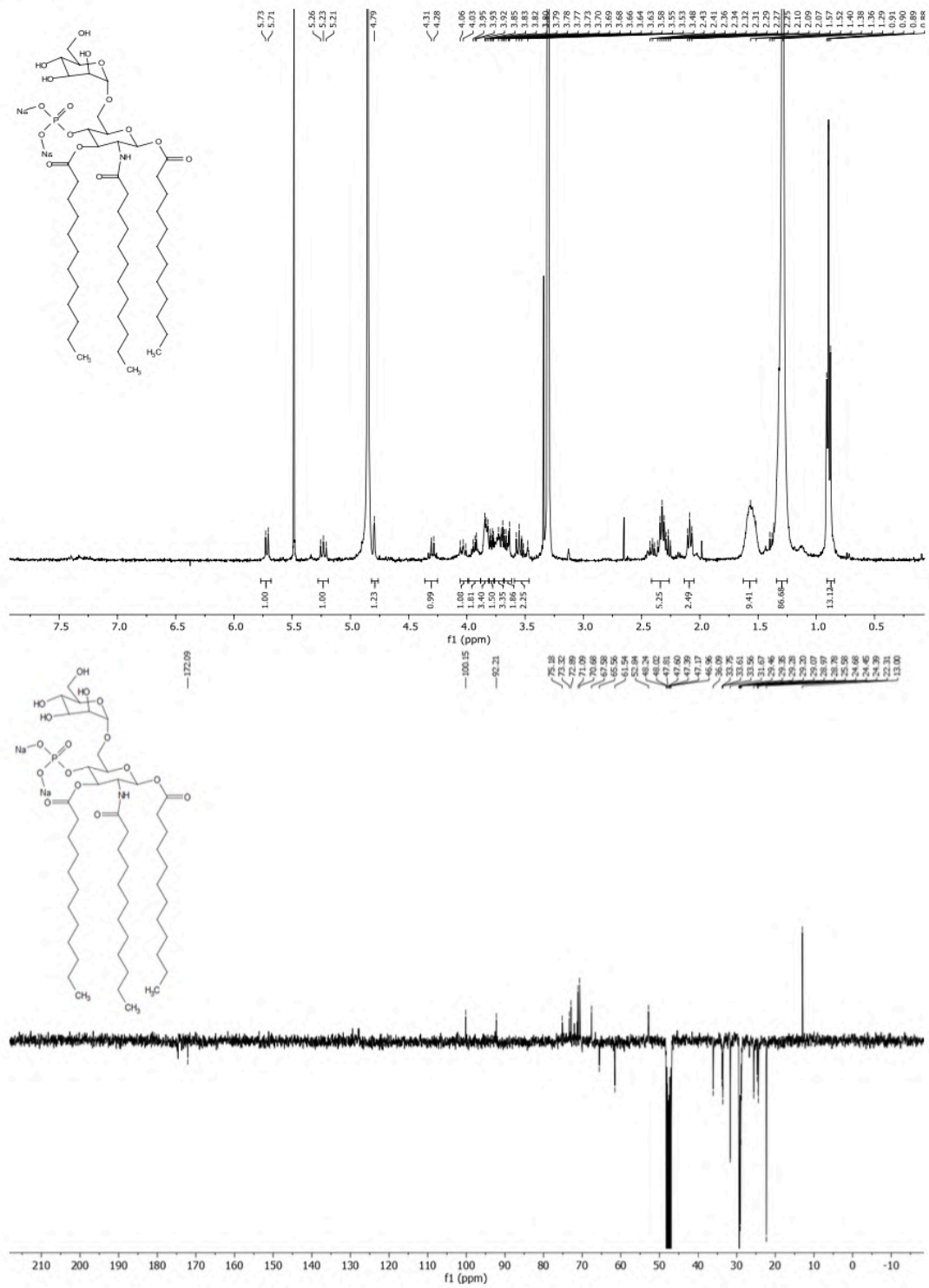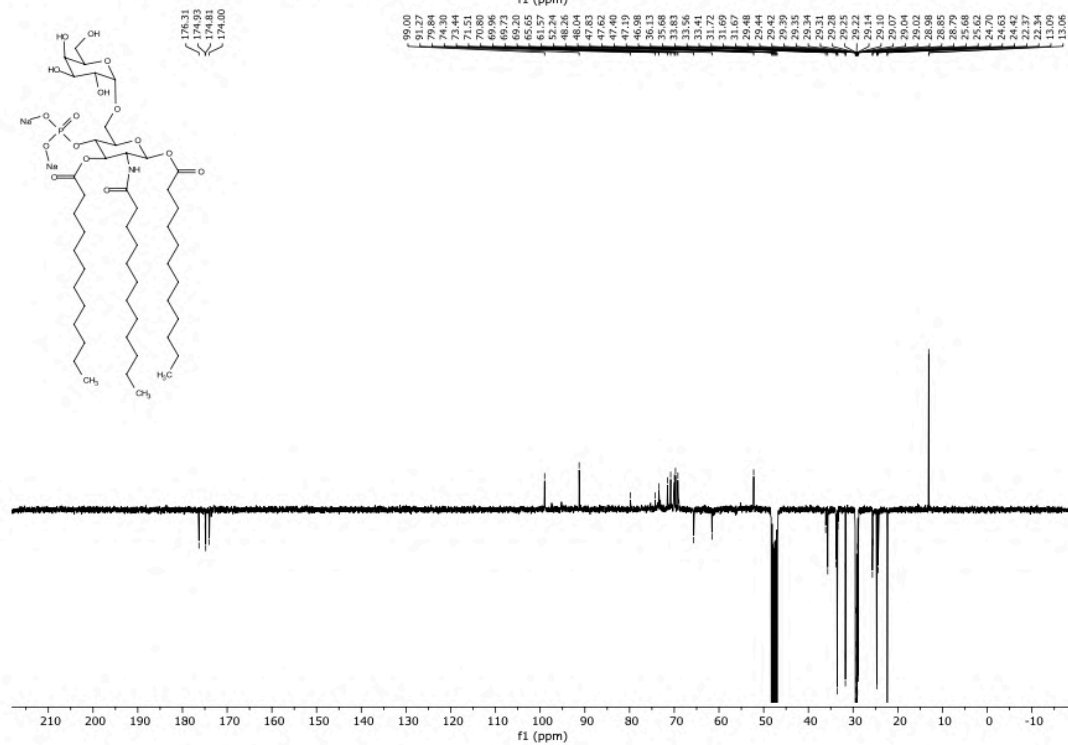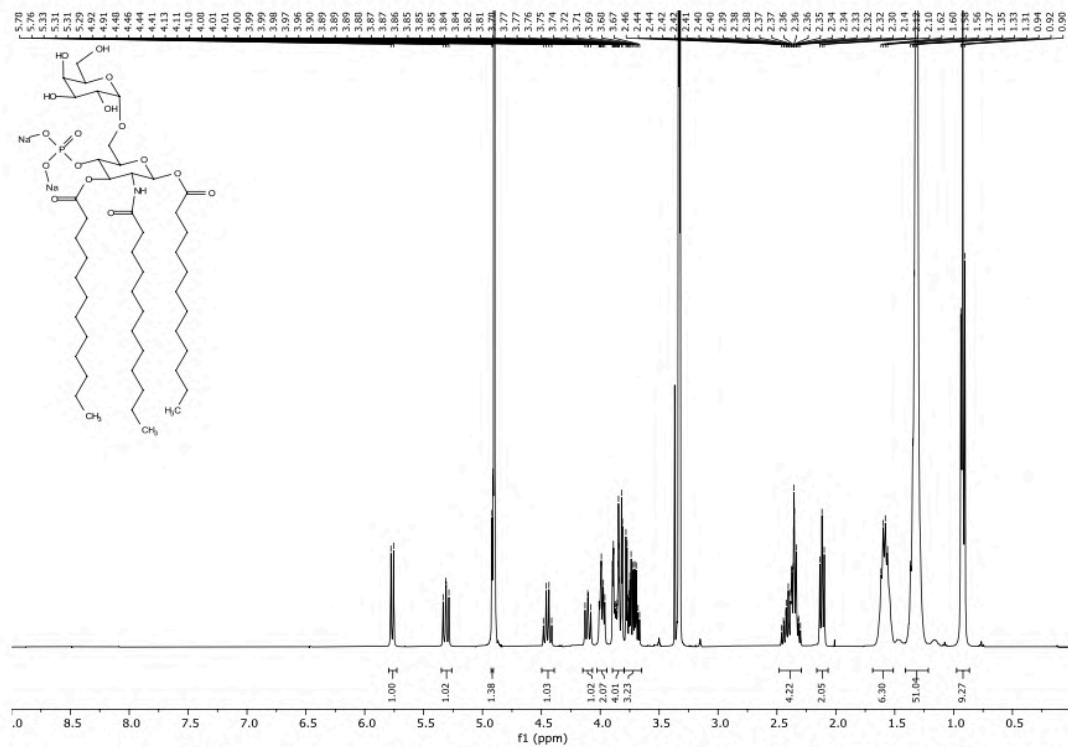
FP20Rha
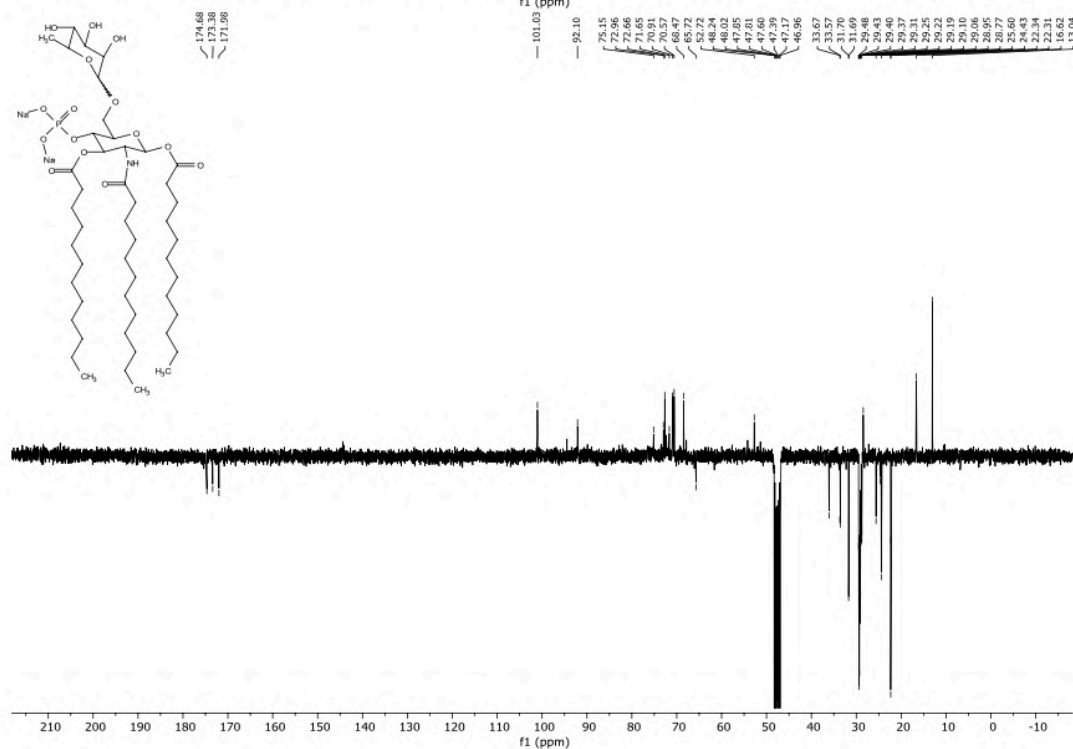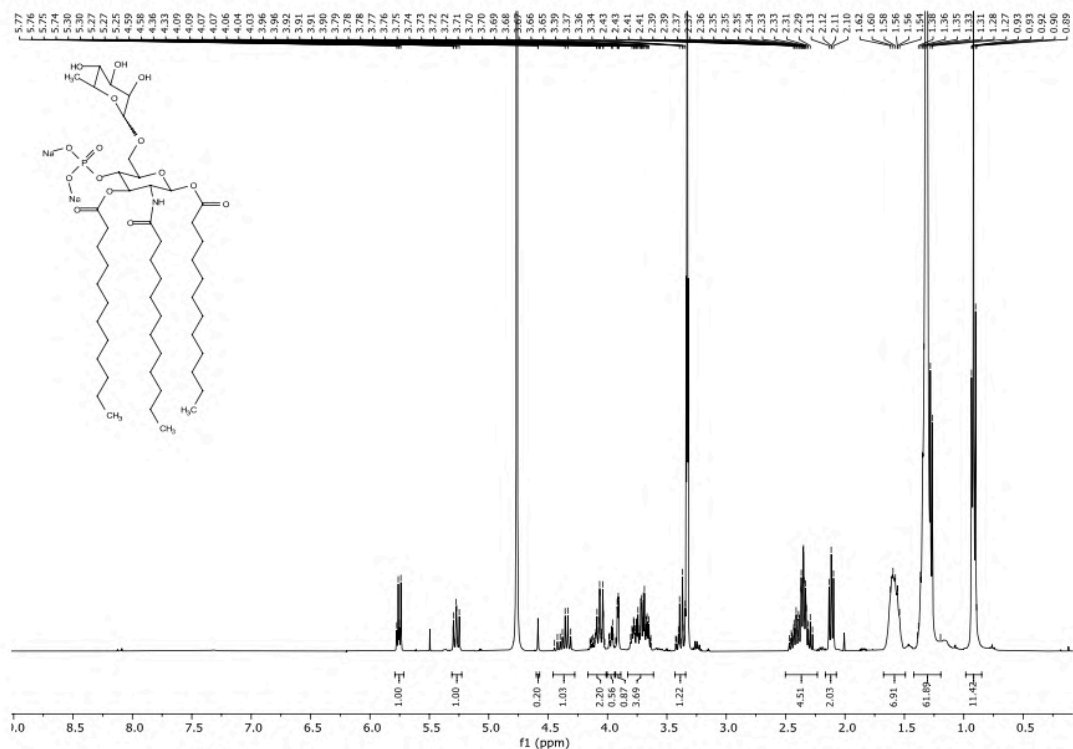
FP20Glc

FP20Man

FP20Gal

FP20Lyx

Appendix III

Supplementary information of CHAPTER III

# Additional Experimental section of results reported in Chapter III

Chemistry

All reagents and solvents were purchased from commercial sources and used without further purifications, unless stated otherwise. Reactions were monitored by thin-layer chromatography (TLC) performed over Silica gel 60 F254 plates (Merck). Flash chromatography purifications were performed on Silica gel 60 60–75 μm from commercial sources or using Biotage Isolera LS Systems.

^{1}H and ^{13}C NMR spectra were recorded with Bruker Advance 400 with TopSpin software. Chemical shifts are expressed in ppm with respect to Me$_4$Si; coupling constants are expressed in Hz. The multiplicity in the ^{13}C spectra was deducted by APT experiments.

Tested compound purity was higher than 95% as assessed by ^{1}H qNMR experiment using trimethylsilyl propanoic acid as standard.

Exact masses were recorded with Xevo G2-XS Q- TOF System.
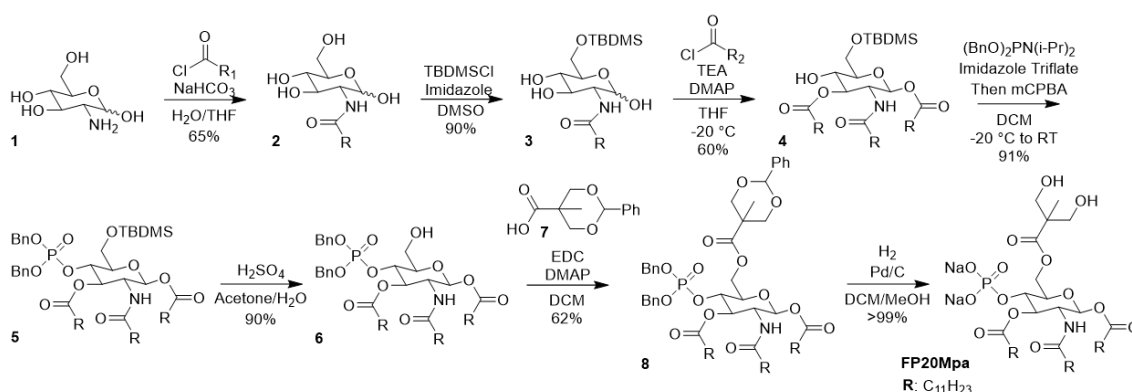
Synthesis of 8

4-O-(dibenzyl)phospho-2-deoxy-2-dodecamido-1,3-di-O-dodecanoyl-6-O-(5-Methyl-2-phenyl-1,3-dioxane-5-carboxylate)-β-D-glucopyranose.

Compound **6** (100 mg, 0.11 mmol, 1 eq.) and compound **7** (48 mg, 0.11 mmol, 1.1 eq.) were dissolved in dry DCM (1 ml, 0.1 M) under Ar atmosphere. Then, EDC (23 mg, 0.12 mmol, 1.2 eq.) and DMAP (0.112 mg, 0.01 mmol, 0.1 eq.) were added to the solution at 0° C. Subsequently, the solution was allowed to return at room temperature and stirred overnight. Reaction, monitored by TLC (Hep/Acetone 8:2), was then stopped and the solution concentrated under reduced pressure. Then it was diluted with AcOEt and washed three times with HCl. Organic phase thus obtained was dried with Na$_2$SO$_4$ and solvent was removed by rotavapor. Raw product thus obtained (550 mg) was purified

using flash column chromatography (Hep/Acetone 85:15). After purification, 96.5 mg of compound **8** were obtained, in 62% yield.

^{1}H NMR (400 MHz, CDCl$_3$) δ 7.43 (dd, J = 6.8, 3.0 Hz, 2H, aromatics), 7.35 – 7.27 (m, 9H, aromatics), 7.23 (dd, J = 6.8, 2.9 Hz, 3H, aromatics), 5.60 (d, J = 8.7 Hz, 1H, H-1), 5.45 (s, 1H, Ph-C*H*(OR)$_2$ HMP), 5.36 (d, J = 9.5 Hz, 1H, NH), 5.15 (dd, J = 10.8, 9.0 Hz, 1H, H-3), 4.98 (d, J = 8.6 Hz, 2H, CH$_2$-Ph), 4.93 – 4.85 (m, 2H, CH$_2$-Ph), 4.73 – 4.62 (m, 3H, H-6a, CC*H$_2$*OH HMP), 4.51 (q, J = 9.4 Hz, 1H, H-4), 4.26 – 4.18 (m, 2H, H-2, H-6b), 3.79 (dd, J = 9.9, 4.0 Hz, 1H, H-5), 3.64 (dd, J = 11.5, 1.6 Hz, 2H, CC*H$_2$*OH HMP), 2.29 (td, J = 7.5, 3.2 Hz, 2H, CH$_2$α Chains), 2.18 – 2.12 (m, 2H, CH$_2$α Chains), 2.07 – 2.02 (m, 2H, CH$_2$α Chains), 1.52 – 1.34 (m, 5H, CH$_2$β Chains), 1.25 (d, J = 4.3 Hz, 52H, Chains bulk), 1.04 (s, 3H, CH$_3$ HMP), 0.88 (td, J = 6.7, 1.4 Hz, 9H, CH$_3$ chains).

^{13}C NMR (101 MHz, CDCl$_3$) δ 175.3, 174.3, 174.2, 174.1, 173.3, 172.9, 172.9, 172.8, 172.5, 172.3, 138.0, 137.9, 135.3, 135.2, 134.9, 134.9, 134.5, 129.7, 129.0, 128.9, 128.9, 128.8, 128.8, 128.7, 128.7, 128.7, 128.6, 128.6, 128.6, 128.6, 128.3, 128.1, 128.1, 128.1, 128.0, 127.9, 126.2, 126.1, 101.8, 101.6, 92.5, 92.5, 77.3, 77.0, 76.7, 73.5, 73.5, 73.3, 73.3, 73.1, 72.5, 72.3, 72.3, 70.2, 70.1, 70.1, 70.0, 69.9, 69.9, 69.8, 69.8, 69.7, 69.7, 67.3, 67.3, 62.2, 62.0, 61.5, 52.7, 52.7, 50.5, 42.5, 41.1, 36.7, 34.0, 33.9, 33.8, 33.7, 33.5, 31.9, 29.7, 29.6, 29.6, 29.5, 29.5, 29.5, 29.4, 29.3, 29.3, 29.3, 29.3, 29.2, 29.1, 29.1, 29.0, 25.6, 25.6, 24.6, 24.5, 22.7, 19.1, 17.9, 17.4, 14.1.

HRMS (ESI-Q-TOF): m/z [M+Na$^+$] calculated for C$_{68}$H$_{104}$NNaO$_{14}$P$^+$: 1212.7092. Found: 1212.7078.

Synthesis of FP20Hmp

6-O-(2,2-bis(hydroxymethyl)propionoyl)-2-deoxy-2-dodecamido-1,3-di-O-dodecanoyl-4-O-phospho-β-D-glucopyranose.

Compound **8** (90 mg, 0.08 mmol, 1 eq.) was dissolved in anhydrous acetone (9 ml, 0.01 M) under Ar atmosphere. Then, Pd/C catalyst (45 mg), 50% m/m) was added always under inert atmosphere. Then, the hydrogen was added, and the reaction stirred overnight at room temperature. The reaction was monitored by TLC (Hep/Acetone 8:2), then stopped. The hydrogen was completely removed, and the Ar atmosphere restored. Triethylamine (180 μl, 2% v/v) was added to the solution, which was stirred for 15 minutes. Then, the catalyst was removed by filtration on syringe filters PALL 4549T Acrodisc 25 mm with GF/0.45 μm Nylon and solvents were evaporated by rotavapor. The compound was resuspended in DCM/MeOH 1:1 and IRC 120 H$^+$ (500% m/m) was added to the solution. After 15 minutes stirring, the acid resin was removed by filtration and

solvents were removed by rotavapor. The compound was again suspended in DCM/MeOH and IRC 120 Na$^+$ (750% m/m) was added. The solution was stirred again for 45 minutes; then the resin was removed by filtration and solvent was removed by rotavapor. Crude product thus obtained was dissolved in acetone and crystallized at -20 °C. The compound was then filtered obtaining 54 mg of compound **FP20Hmp** as a white powder, in 75% yield.

^{1}H NMR (400 MHz, MeOD) δ 5.77 (d, J = 8.9 Hz, 1H, H-1), 5.31 (dd, J = 10.6, 9.0 Hz, 1H, H-3), 4.48 (dd, J = 12.3, 2.2 Hz, 1H, H-6a), 4.41 (q, J = 9.6 Hz, 1H, H-4), 4.32 (dd, J = 12.2, 4.7 Hz, 1H, H-6b), 4.10 (dd, J = 10.7, 8.9 Hz, 1H, H-2), 3.90 (ddd, J = 9.9, 4.7, 2.3 Hz, 1H, H-5), 3.78 (d, J = 11.1 Hz, 1H, CC*H₂*OH HMP), 3.70 (s, 2H,CC*H₂*OH HMP), 3.65 (d, J = 11.1 Hz, 1H, CC*H₂*OH HMP), 2.48 – 2.29 (m, 4H, CH₂α Chains), 2.12 (t, J = 7.6 Hz, 2H, CH₂α Chains), 1.65 – 1.53 (m, 6H CH₂β Chains), 1.31 (d, J = 2.2 Hz, 52H, Chains bulk), 1.20 (s, 3H, CH₃ HMP), 0.95 – 0.89 (m, 9H, CH₃ Chains).

13C NMR (101 MHz, MeOD) δ 174.8, 174.8, 173.5, 172.2, 92.1, 78.0, 77.7, 77.4, 73.2, 72.7, 72.3, 64.7, 64.6, 62.1, 52.5, 50.5, 48.6, 48.4, 48.2, 47.9, 47.7, 47.5, 47.3, 36.2, 33.7, 33.7, 31.8, 31.7, 29.6, 29.5, 29.5, 29.5, 29.4, 29.4, 29.4, 29.3, 29.3, 29.2, 29.2, 29.2, 29.1, 29.0, 28.8, 25.7, 24.5, 22.4, 16.2, 13.4.

HRMS (ESI-Q-TOF): m/z [M-H$^-$] calculated for C$_{47}$H$_{87}$NNaO$_{14}$P$^-$: 920.5864. Found: 920.5873.

Murine Immunization Experiments

C57BL/6 J mice were purchased from Charles River Laboratories (Lyon, France). Upon arrival, animals were maintained under 12 h light/dark cycles while receiving food and water ad libitum and were rested for 2 weeks prior to immunization.

MPLA (InvivoGen) and FP20Hmp were reconstituted in DMSO (Sigma-Aldrich) at a concentration of 1 mg/mL. EndoFit ovalbumin (InvivoGen) was utilized for immunizations. Inoculations were formulated OVA, adjuvant (or vehicle), and PBS to achieve the appropriate dosages. Immunizations began at approximately 9 weeks of age. At day 0, mice received subcutaneous injections of 10 ug OVA with or without 10 μg of adjuvant. Mice were boosted with identical injections at day 21. Bleeding was performed the day before the first and second immunizations. At day 42, mice were euthanized by carbon dioxide followed by cervical dislocation, and blood was collected via intracardiac puncture. Blood collected in serum separator tubes (BD) was centrifuged at 10,000 RPM for 5 min, and serum was stored at −80 °C until use.

Antibody responses were measured by capture ELISA. NUNC plates (Thermo Fisher) were coated overnight with 100 μL of coating buffer, containing 0.5 μg/mL OVA in 0.2 M sodium bicarbonate at pH 9.6. Following four washes with 200 μL of 0.05%

Tween-PBS wash buffer in an automatic plate washer (BioTek), plates were blocked for 1 h with filtered 1% BSA-PBS assay diluent. Wells were aspirated, and serial dilutions (twofold) of the sera, starting at 1/100, were applied, followed by an incubation of 1 h. Horseradish peroxidase-conjugated goat anti-mouse secondary antibodies against IgG (Jackson ImmunoResearch), IgG1, IgG2b, IgG2c, and IgG3 (SouthernBiotech) were diluted 1:1000 in assay diluent. After six washes with wash buffer, 100 μL of secondary antibody was added to each well for 45 min. Plates were washed eight times with 200 μL wash buffer, and then two times with 400 μL PBS. One hundred microliters of 3,3′,5,5′-tetramethylbenzidine peroxidase substrate solution (TMB, SeraCare) was added to each well and incubated for 30 min. After stopping the reaction with 100 μL of 2 M sulfuric acid, samples were measured with a microplate reader (BioTek Epoch) at 450 nm.

Bacterial strains and culture conditions

Enterococcus faecium 1236/1[359], a vancomycin-resistant Enterococcus, was grown in Tryptic Soy Broth, and Agar (TSB/TSA) at 37°C without agitation. For recombinant production of PpiC, we used *Escherichia coli* M15, harboring pRep4 and pQE30PpiC[59], grown in Luria Bertani (LB) containing kanamycin at 25μg/ml and ampicillin at 100μg/ml, at 37°C with agitation.

Rabbit immunization

PpiC was recombinantly produced in *E. coli* M15 harboring pRep4 and the previously genetically engineered pQE30PpiC[59]. The production and purification of PpiC was performed as described by Romero-Saavedra et al. (2015)[359]. Briefly, after reaching an optical density at 600nm of 0,5, the bacterial culture was induced with the addition of isopropyl β-D-1-thiogalactopyranoside at 0,05mM for two hours at 37°C. Following the induction of the expression, the bacterial culture was placed in lysis buffer (50mM NaH_2PO_4, 300mM NaCl, pH 8) containing lysozyme at 10mg/ml for an enzymatic lysis and with glass beads to mechanically break the bacteria. The his-tagged protein was purified by affinity chromatography. Amicon Ultra-15 Centrifugal Filter Unit of 10,000 MWCO was used for desalting and concentrating.

New Zealand rabbits were divided into groups of three. The first group was immunized with FP20Hmp and acted as a negative control. The second group with the recombinantly produced PpiC. Group 3 was immunized with a formulation containing PpiC and MPLA to have a positive control to assess the antibodies produced by the fourth group, immunized with PpiC and FP20Hmp. Every group was immunized following the immunization schedule presented in Table X1. One of the rabbits immunized with PpiC and FP20Hmp was a non-responder and was therefore excluded from this study.

Sera from all the rabbits were collected on day 28. Pre-immune sera, as well as terminal bleeds were heat-inactivated for 30 minutes at 56°C and then stored frozen at -20°C. Table X2 lists the different rabbit sera used in this study.

Immunodetection of specific antibodies by ELISA

Enzyme-linked ImmunoSorbent Assay (ELISA) were performed following the protocol previously described by Romero-Saavedra at al. (2019)[61]. The recombinant PpiC at 1µg/ml was used to coat Nunc-immuno MaxiSorp 96-well plates overnight. After washing, blocking of the plates was done with PBS-BSA (phosphate buffer saline with 3% of Bovine Serum Albumin) for one hour. 100µl of polyclonal antibodies was added to the plates after dilution of each serum from immunized rabbits in PBS-BSA following a 2-fold dilution from 1:50 to 1:51 200. After incubation for 1 h, alkaline phosphatase conjugated anti-rabbit IgG produced in goat was diluted at 1:1000 and added to the plates for a one-hour incubation. After extensive washing, Ortho-nitrophenyl-b-D-galactopyranoside at 1mg/ml was added to the plates as substrate and the quantity of bound IgGs was assessed by checking absorbance at 405nm after two hours.

Whole-bacterial-cell ELISA

Immunoreactivity towards *E. faecium* 11236/1 was performed as described before[61]. After growing *E. faecium* 11236/1 until OD650nm reached 0.4, cells were harvested and washed twice with PBS. Bacteria were resuspended in 8% paraformaldehyde and incubated for two hours at 4°C. After washing with PBS, fixed cells were resuspended in 10ml of coating buffer (0.2 M Sodium carbonate / bicarbonate buffer, pH 9.4) and used to coat plates overnight at 4°C. The following day, after extensive washing, plates were incubated with PBS-BSA for a 24-hour blocking time. After, binding of IgG to the whole bacterial surface was assessed as described above, following the same protocol as for the classical ELISA. Absorbances were measured after 360 minutes. Enrichment of *E. faecium*-specific antibodies was calculated by subtracting the absorbance obtained with the pre-immune serum of each rabbit diluted at 1:50 to the corresponding terminal bleed, at the same dilution.

Ethics statements

Animal (mice) protocols were approved by CIC bioGUNE's Animal Research Ethics Board in accordance with Spanish and European guidelines and regulations. Development of polyclonal rabbit sera was performed by the company Biogenes GmbH in Berlin (Germany), in compliance with the German animal protection law (TierSchG).

NMR Spectra

Compound 8
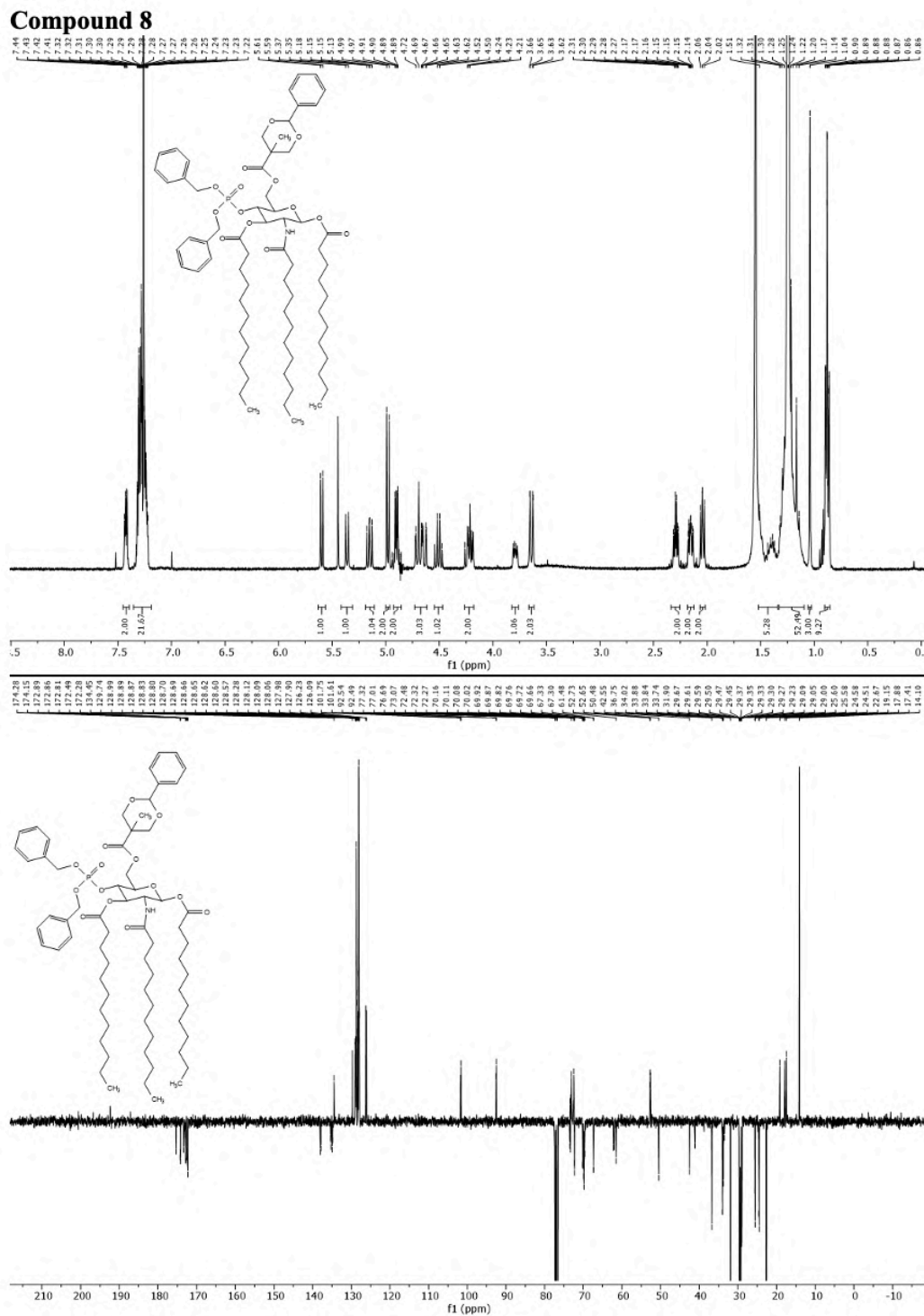
FP20Hmp
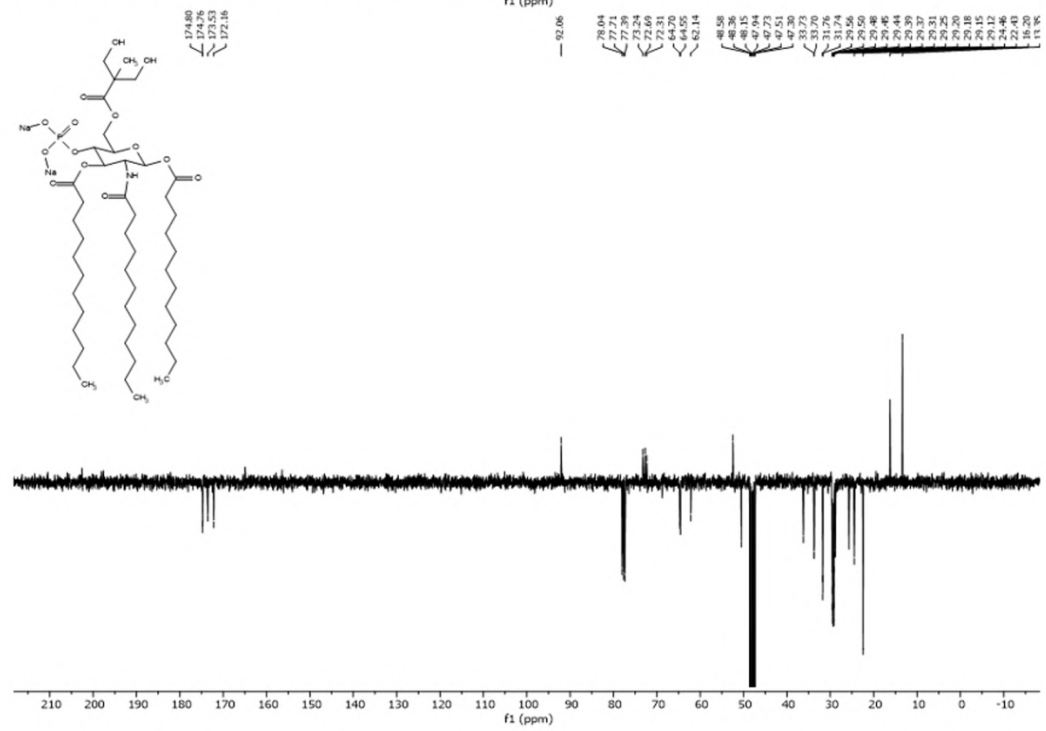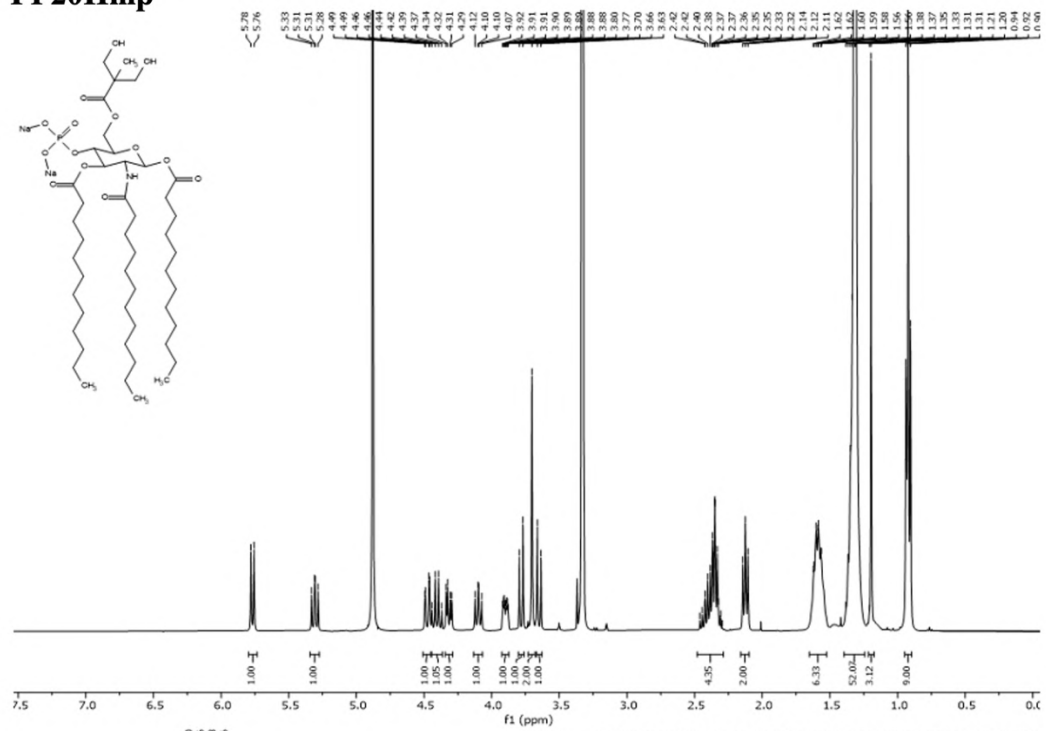
Appendix IV

Supplementary information of CHAPTER IV

Additional Experimental section of results reported in Chapter IV

3.5. Multivariate Analysis

Multivariate analysis has been performed using R version 3.6.3. FTIR spectra have been split into five spectral regions and partial least square discriminant analysis (PLS-DA) has been applied on each region, as previously described[309].

PLS-DA is a widely used multidimensional linear regression method, which is a variant of the classical partial least square method when the dependent variable is categorical[360]. To assess the predictive discrimination and avoid over-fitting, for each method a 3-time repeated 5-fold cross-validation was applied; so, for each method, 15 models were trained. Since each sample has multiple spectra, folds have been created at the sample level, ensuring that all spectra for a given sample are either in the training or in the test set. More specifically, having N samples each with m_N spectra, on every round of cross-validation, the samples have been partitioned into 5 folds. Four folds (containing N*4/5 samples) have been used to train the model, and the remaining fold (containing N*1/5 samples) was used to test the model. Folds are complementary (i.e., no repeated samples in different folds) and the samples are randomly chosen. The training of the model is repeated 5 times, each time varying the test partition. The 5-fold cross-validation is then repeated 3-times to lower the risk of partition-dependent artefacts. The best model has been selected using the "one standard error rule". In this case, the model with the best performance value is identified, and using resampling, we can estimate the standard error of performance. The final model used was the simplest model within one standard error of the (empirically) best model[361]. As a performance measure the root mean square error (RMSE) was used. For the PLS-DA method the variable importance measure here is based on weighted sums of the absolute regression coefficients[361]. Each PLS-DA model includes the following 3 classes: NT-T 0 h, NT-Tn, LPS-Tn. Different models have been created for each time: 15 min, 3 h, and 24 h. The discrimination accuracy among the classes was evaluated using the classification accuracy, e.g., the proportion of true results (true positive + true negative) over the total number of samples.

The distribution of distances between TDM cells treated with LPS and untreated has been obtained by computing the Euclidean distance between all pairs of spectra (in the low dimensional PLS score space), between group T 0 h and Tn for NT and for LPS, that is:

$$D(K)_{i,j} = \frac{1}{L}\sqrt{\sum_{c=1}^{C}(x_i^c - x_j^c)^2}$$

where i is the i-th spectra belonging to the initial time (T 0 h) group, while j is the j-th spectra belonging to the Tn (where n = 15 min, 3 h, 24 h) group. L is the number of PLS scores, and c is the C-th PLS component. K is either NT or LPS. In order to assess the statistical significance of the difference between the distances in NT and LPS and in the time factor, a two-ways repeated measurement ANOVA has been performed.
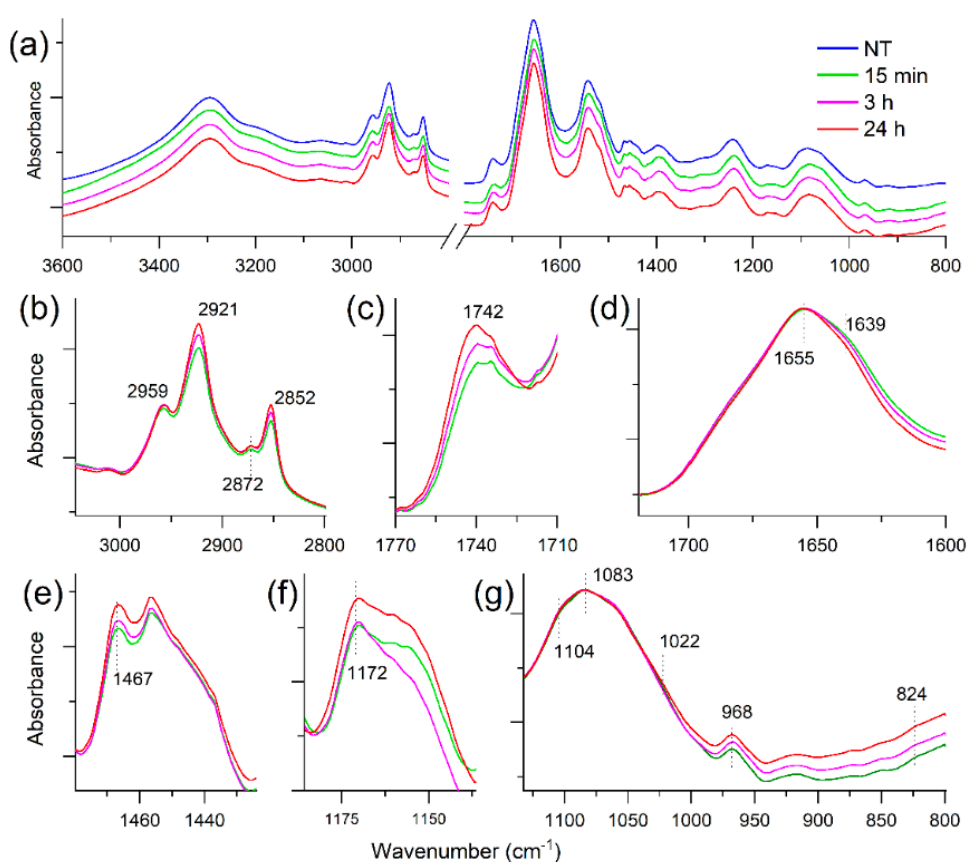
Mean absorption spectra for each experimental group. (a) Mean absorption spectra of non-treated (NT) and LPS-treated cells at different time points (15 min, 3 h, 24 h) are displayed in the whole measured range. (b-g) Mean absorption spectra of LPS-treated cells at different time points in selected spectral ranges. The average absorption spectra are reported after normalization at the Amide I band area of the measured spectra, therefore, the absorbance is in arbitrary units and spectra have been offset for the clarity of the figures (a-g).
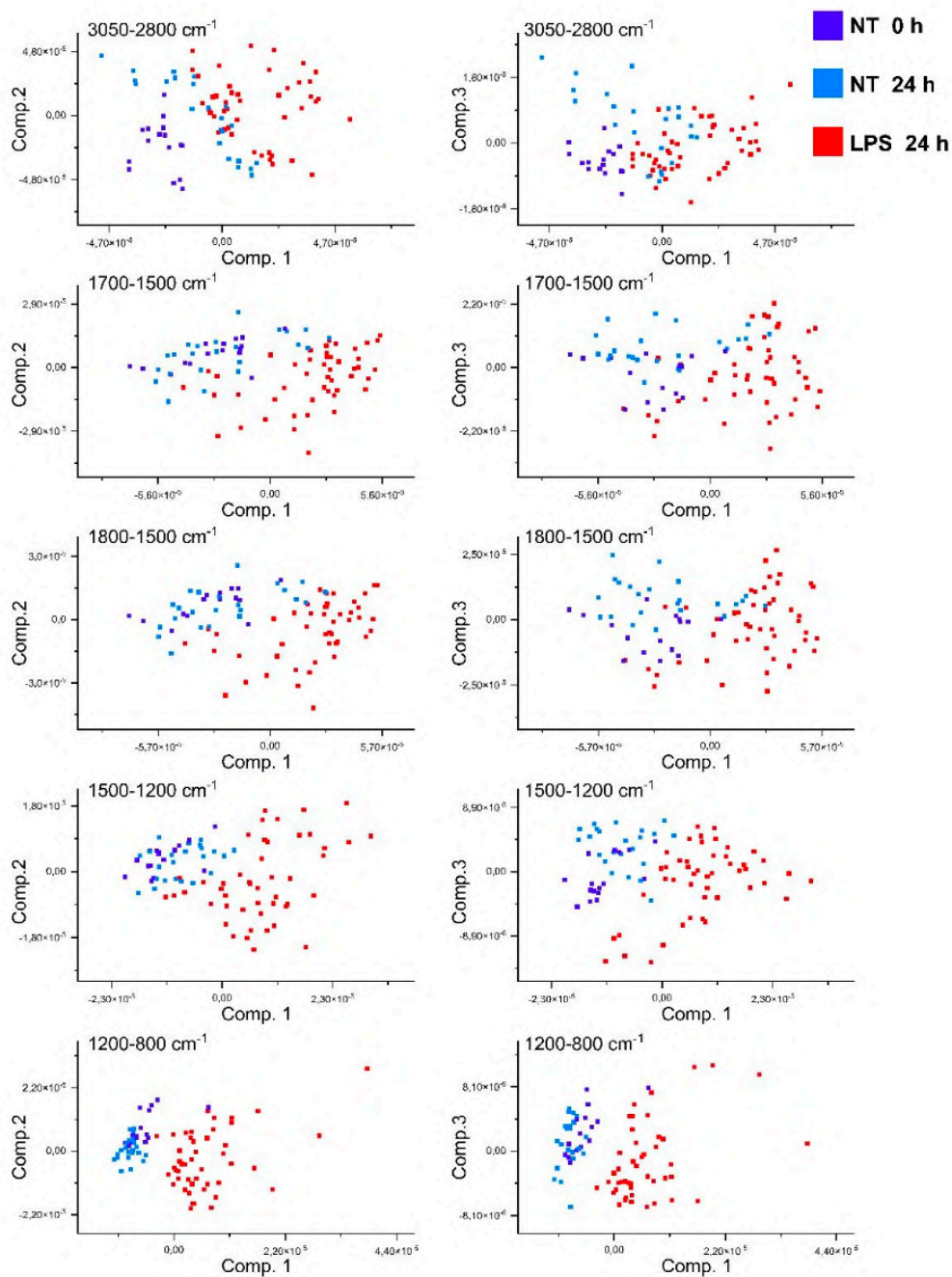
PLS-DA score plots. The score plots of Component 2 versus Component 1 and of Component 3 versus Component 1 were reported for the PLS-DA analysis of non-treated TDM cells at 0 h and 24 h and LPS treated TDM cells for 24 h. The PLS-DA analysis was performed in the indicated spectral ranges.
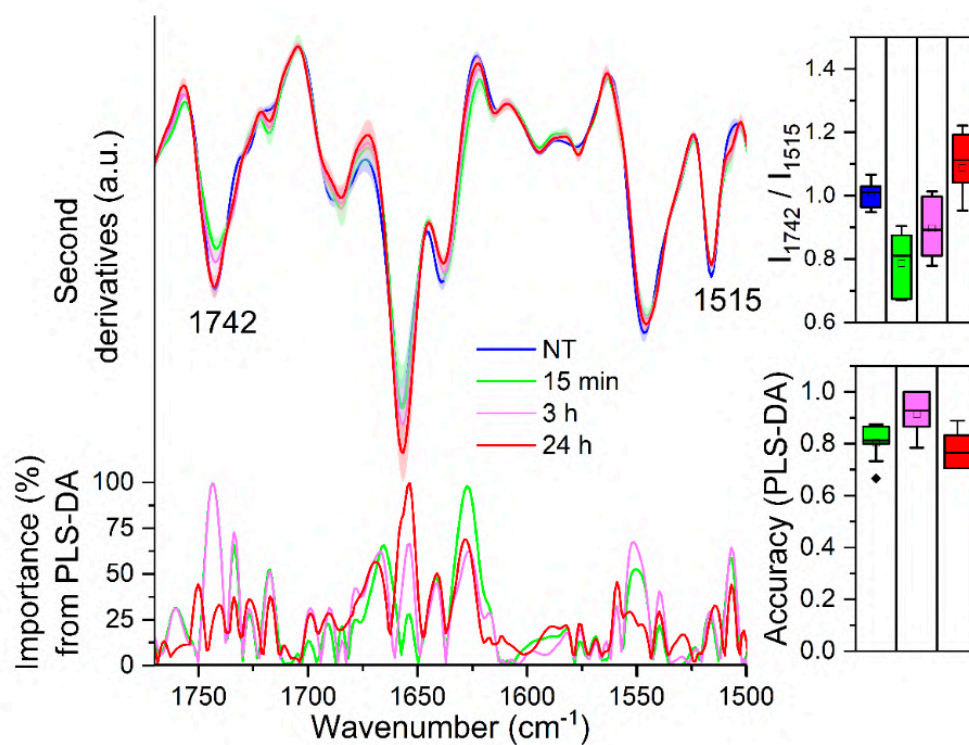
Mean second derivative spectra in the 1760-1500 cm^{-1} range of TDM cells before (NT) and at different time points after LPS administration. Standard deviation has also been displayed as a shadowed area. In the inset, the intensity ratio between the C=O band at ~ 1742 cm^{-1} and the tyrosine peak at ~ 1515 cm^{-1} is illustrated. Below, the wavenumber importance for PLS-DA discrimination performed in the 1800-1500 cm^{-1} spectral range is shown. The PLS-DA discrimination accuracy has been also reported.

Peak positions (cm^{-1})	Assignment	References
~2921	CH2 antisymmetric stretching	299,305,306
~2852	CH2 symmetric stretching	299,305,306
~1742	C=O stretching from lipid ester groups	299,305,306
~1655	α-helices/random coils	298,299
~1639-1628	β-sheets	298,299
~1467	CH2 and CH3 bending, mainly from lipid hydrocarbon chains	299,305,306
~1172	CO-O-C stretching, mainly from phospholipids; carbohydrates: C-OH, C-C stretching and C-O-H bending; SO4, C-O-S stretching mainly from GAGs	299,305,317–319,362

~1104	Polysaccharide ring vibrational modes; GAG ring vibrations.	319,326
~1083-1073	Polysaccharide ring vibrational modes; GAG ring vibrations; P=O symmetric stretching PO^{2-} mainly from phospholipids and SM	299,305,306,319,326
~1022	Polysaccharides: mainly ring vibrations and stretching vibrations of C-OH of side groups and C-O-C of glycosidic bonds; GAG pyranose ring	317–319,323,324
~968	N(CH3)3 asymmetric stretching of PC and SM; C-C stretching of the DNA backbone and/or of RNA ribose-phosphate main chain vibrations	305,307
~834-824	Glycosidic linkages of polysaccharides (mainly C1-H ring); C-O-S from GAGs	318,327–329

Assignment of the relevant IR components. The peak positions from second derivative spectra have been reported for the spectral components identified by PLS-DA. The main assignment to the cell biomolecules has been indicated.